BRNO UNIVERSITY OF TECHNOLOGY

Faculty of Electrical Engineering
and Communication

DOCTORAL THESIS

Brno, 2024 Ing. Ivana Labounková

BRNO UNIVERSITY OF TECHNOLOGY
VYSOKÉ UČENÍ TECHNICKÉ V BRNĚ

FACULTY OF ELECTRICAL ENGINEERING AND COMMUNICATION
FAKULTA ELEKTROTECHNIKY A KOMUNIKAČNÍCH TECHNOLOGIÍ

DEPARTMENT OF BIOMEDICAL ENGINEERING
ÚSTAV BIOMEDICÍNSKÉHO INŽENÝRSTVÍ

ANALYSIS OF IMAGE RETINAL SEQUENCES FROM EXPERIMENTAL OPHTHALMOSCOPE
TITLE OF STUDENT'S THESIS

DOCTORAL THESIS
DIZERTAČNÍ PRÁCE

AUTHOR — Ing. Ivana Labounková
AUTOR PRÁCE

ADVISOR — doc. Ing. Radim Kolář, Ph.D.
VEDOUCÍ PRÁCE

EXPERT ADVISOR — Assoc. Prof. MUDr. Igor Nestrašil, Ph.D.
ŠKOLITEL SPECIALISTA

BRNO 2024

ABSTRACT

Partly verified hypothesis is that ophthalmological and all systemic diseases affecting cardiovascular system imprints pathophysiological features into retinal hemodynamics. Retinal hemodynamics are easy to non-invasively access through the eye lens via optical imaging sensitive to blood volume or flow. Today, functional retina imaging (fRI) is an emerging field trying to identify candidates for non-invasive biomarkers of various diseases. The overall objective of this doctoral thesis was to push the state-of-the-art in fRI methods and employ the methods in pioneering biomedical applications.

The first part of the thesis summarizes the fRI state-of-the-art including (i) retina anatomy and physiology; (ii) etiology of retinal pulsatile phenomena such as spontaneous venous pulsation (SVP); (iii) fRI principles and methods; (iv) image analysis in fRI; (v) multivariate statistics promising for fRI; and (vi) pitfalls.

The second part contains original research that has been peer-reviewed, presented at international conferences, and published as original research articles (in the IEEE Transactions on Medical Imaging and the Communications Biology). Here, the thesis presents a novel implementation of automated and data-driven principal (PCA) and independent (ICA) component analyses in fRI utilized via video-ophthalmoscopy. Both, PCA and ICA, detected SVP with higher detection rate than previous literature. Moreover, PCA and ICA identified optic cup pulsation (OCP) pattern, hypothesized to be of arterial origin, and components potentially related to respiratory induced effects. Neither OCP nor respiratory induced effects were widely reported before. Further, SVP and OCP morphology was identified to be correlated to heart rate and ageing. The correlations were identified on pilot dataset acquired in Erlangen, Germany and confirmed on re-test dataset acquired in Minneapolis, USA. The video-ophthalmoscope (VO) device has been synchronized with a hub enabling simultaneous acquisition of non-invasive and invasive biosignals, such as electrocardiogram, electrooculogram, finger plethysmography, respiratory plethysmography, and intracranial pressure (ICP). Mobile bedside cart with joystick-driven and motorized VO positioning system has been designed and assembled. Preliminary simultaneous fRI-ICP dataset has been acquired and research project investigating in vivo predictive fRI power to ICP has been initiated.

In conclusion, implementation of PCA and ICA improved state-of-the-art of SVP, OCP and respiratory pattern imaging. The thesis also demonstrates that heart rate and age are important biological factors which needs to be considered in study designs investigating retinal hemodynamics. Finally, the thesis initiated a pioneering research project which has a potential to develop non-invasive and non-contact ICP measurement technology.

KEYWORDS

Principal component analysis, independent component analysis, retina imaging, video-ophthalmoscope, retinal pulsatile pattern, spontaneous venous pulsation, optic cup pulsation, retina

ABSTRAKT

Předpokládá se, že nejen oftalmologické, ale i některé systémové nemoci ovlivňující kardiovaskulární systém (např. diabetes mellitus), mění hemodynamiku cévního řečiště sítnice. Cévní řečiště sítnice včetně projevů metabolických procesů je snadno pozorovatelné neinvazivními metodami, např. optickými soustavami optimalizovanými pro pozorování objemových změn krve. Tento rychle se vyvíjející obor funkčního zobrazování sítnice se snaží identifikovat a definovat biomarkery různých nemocí získané na základě neinvazivního měření. Cílem této doktorské práce je rozšířit a obohatit pole funkčního zobrazování retiny a uplatnit metody v biomedicínských aplikacích.

První část této práce popisuje dosavadní vývoj oboru funkčního zobrazování retiny včetně kapitol (i) anatomie a fyziologie sítnice; (ii) původ pulzací v cévním řečišti sítnice včetně samovolných žilních pulzací v oblasti optického disku (SVP, z aj. spontaneous venous pulsation); (iii) metody a principy funkčního zobrazování sítnice; (iv) metody zpracování obrazu ve funkčním zobrazování sítnice; (v) metody vícerozměrné statistiky aplikovatelné v oboru; (vi) nedostatky v oboru funkčního zobrazení sítnice a prostor pro vylepšení.

Druhá část této doktorské práce představuje originální výzkum, který byl recenzován a představen na mezinárodních konferencích, a publikován v časopisech IEEE Transactions on Medical Imaging, a Communications Biology. Zde doktorská práce představuje inovativní implementaci, datasetem řízenou analýzu hlavních komponent a analýzu nezávislých komponent ve funkčním zobrazení retiny, aplikovanou na video-oftalmoskopická data. Obě metody detekovaly přítomnost SVP ve vyšší míře než předchozí studie. Metody navíc identifikovaly další pulzující složky sítnice - pulzace intenzity poháru optického disku (OCP, z aj. optic cup pulsation) zřejmě arteriálního původu, a složku vykazující pulzaci o nízké frekvenci vzniklou vlivem dýchání. Žádná s těchto dvou složek nebyly zaznamenány v předchozích studiích. Dále bylo zjištěno, že morfologie jednotlivých pulzů SVP a OCP jsou korelovány s tepovou frekvencí a věkem. Tyto korelace byly zjištěny v datasetech sekvenčních snímků sítnice získaných na oční klinice v Erlangenu (Německo) a na University of Minnesota, Minneapolis (USA). Pro akvizici obou datasetů byl použit unikátní video-oftalmoskop (Tornow, 2015). Poslední část této práce popisuje návrh a realizaci prvního simultánního měření sekvenčních snímků sítnice, neinvazivního měření biosignálů (tj. elektrokardiogram, elektrookulogram, prstová pletysmografie), a invazivního měření intralebního tlaku. Pojízdný stůl s ramenem, nesoucí video-oftalmoskop s polohováním ovládaným joystickem, byl navrhnut a sestrojen pro potřeby pacientů umístěných na jednotkách neurologické intenzivní péče. Byl získán první dataset simultánního měření funkčního zobrazování sítnice a intralebního tlaku. Tento mezník představuje počátek pro následné studie zabývající se odhadem intralebního tlaku bezkontaktně na základě sekvenčních snímků sítnice.

Závěrem, tato práce rozšířila dosavadní vývoj funkčního zobrazení sítnice o automatickou analýzu a identifikaci jevů samovolných žilních pulzací v optickém disku, pulzací optického disku a projevu dýchání v sítnici. Tato práce dále identifikuje tepovou frekvenci jako důležitý faktor pro další klinické studie zabývající se hemodynamikou v sítnici. A nakonec, tyto teze představily první simultánní měření sekvenčních snímků sítnice a intralebního tlaku.

KLÍČOVÁ SLOVA

Analýza hlavních komponent, analýza nezávislých komponent, zobrazování sítnice, video-oftalmoskop, pulsační složky sítnice, spontánní žilní pulsace, pulsace poháru optického disku, sítnice

ROZŠÍŘENÝ ABSTRAKT

Pozorování patofyziologických jevů oční sítnice in vivo započaly již na konci 19. století, kdy byl sestaven první oftalmoskop. Dnes jsou k dispozici variace optických i jiných soustav zachycující nejen statické fotografie, ale i sekvence snímků sítnice zobrazující především hemodynamické změny. Obor funkčního zobrazování sítnice je relativně nový a rozvíjí se především v posledních dvou desetiletích, kdy byla představena různá hardwarová řešení zobrazování (oftalmoskopické metody, interferometrické metody, aj.) a algoritmy pro digitální zpracovaní statických i dynamických snímků.

Předmětem funkčního zobrazování sítnice je především sledování hemodynamických změn, tj. prokrvení tkáně, tok krve, arteriální pulzace a žilních pulzací hlavní a vedlejších větví centrální retinální žíly. Pulzace centrální retinální žíly v oblasti optického disku je dlouhodobě sledovaný fenomén, o jehož původu se vedou diskuze. Jedna z novějších akceptovaných teorií vysvětluje jev jako výsledek vzájemného působení tlaků vnitřního prostředí oka a mozkomíšního moku (kde hodnota tlaku mozkomíšního moku se předpokládá stejná jako hodnota intralebního tlaku). Oba tlaky působí na centrální retinální žílu na obou stranách membrány lamina cribrosa sclaera, rozdělující prostředí oka a optického nervu. Výsledný tlakový gradient pak vytváří žilní pulzace v oblasti optického disku. Klinické studie pak nasvědčují tomu, že absence pulzace centrální retinální žíly je spojeno se zvýšenými hodnotami intralebního tlaku. Nicméně metodologie přesného odhadu intralebního tlaku na základě žilních pulzací v sítnici je stále v řešení. Změny v parametrech žilní pulzace v hlavní i vedlejších větvích je pak spojeno i s dalšími fyziologickými faktory (např. stárnutí). Autoři dalších klinických studií spojují hemodynamické změny v sítnici s vlivem patologických procesů a nemocí (např. diabetes mellitus, diabetická retinopatie, glaukom, Alzheimerova choroba, apod.). Pro identifikaci a kvantifikaci takových hemodynamických změn je potřeba vhodných akvizičních metod, metod zpracování obrazu a správné určení klinických biomarkerů.

Kvantifikace hemodynamických změn v sítnici a srovnání výsledků mezi klinickými studiemi zůstává problematické, jelikož neexistuje žádný zlatý standard jak v oblasti akvizičních metod tak v oblasti algoritmů zpracování obrazu či parametrizace. Existuje spousta přístrojů pro akvizici sekvenčních snímků sítnice, popř. jejich vrstev, poskytující časový průběh měřených veličin vyznačujících se pulsacemi (tj. objem krve či cévní průměr v čase v případě oftalmoskopických metod, nebo tok a rychlost krve v případě interferometrických metod, atd.). V zaměření na nejrozšířenější oftalmoskopické metody, ještě nedávné klinické studie používaly subjektivní hodnocení žilní pulzace, kdy pozorovatel klasifikoval změny průměru žil do čtyř kategorií (Hedgesova škála). Subjektivní hodnocení začínají nahrazovat přesná měření průměrů a intenzit vybraných žil prostřednictvím metod zpracování

obrazu. Tyto algoritmy jsou převážně semi-automatické a vyžadují vstupy určené uživatelem/pozorovatelem. Semi-automatické analýzy jsou poskytovány i v rámci některých komerčních přístrojů určených pro akvizici sekvenčních snímků sítnice (Imedos, Německo, XyCam , USA). Přidružený software vyžaduje výběr části cévy pro následnou analýzu. Jelikož cévní větvení sítnice je unikátní pro každé individuum, subjektivní výběr může vést k chybám a zkreslení výsledků.

Pro automatickou analýzu a identifikaci hemodynamických změn v sekvenčních snímcích sítnice se nabízí metody slepé separace zdrojů (z aj. blind source separation), např. metody analýz hlavních a nezávislých komponent. Metody analýz hlavních a nezávislých komponent byly již úspěšně implementovány v oboru funkčního zobrazení mozku magnetickou rezonancí za účelem lokace anatomických částí s různými fyziologickými funkcemi. Podobný charakter dat z funkční magnetické rezonance a dat sekvenčních snímků sítnice vede k předpo-kladu úspěšné aplikace analýzy hlavních a nezávislých komponent i v oboru funkčního zobrazení sítnice za účelem identifikace fyziologických celků se specifickým hemodynamickým průběhem. Kromě implementace metod slepé separace zdrojů pro plně automatickou analýzu pulzačních složek v sekvenčních snímcích sítnice, obor funkčního zobrazení sítnice poskytuje prostor pro další vylepšení jak z hlediska zpracování dat (hodnocení kvality videa, potlačení skoků v časových průbězích objemu krve vzniklých v důsledku sakadických pohybů oka či mrknutí), tak z hlediska bazálního výzkumu identifikace fyziologických proměnných ovlivňujících hemodynamické průběhy jednotlivých funkčních částí. V teoretických modelech se objevuje např. faktor tepové frekvence, který ovšem nebyl potvrzen prostřednictvím žádné klinické studie.

Pro podrobnější seznámení s dosavadním vývojem oboru je první část této práce věnována rozsáhlému teoretickému úvodu, který popisuje (i) anatomii a fyziologii sítnice; (ii) původ pulzací v cévním lůžku sítnice (např. samovolné žilní pulzace); (iii) metody a principy funkčního zobrazení sítnice (včetně podrobného posisu nemydriatického video-oftalmoskopu, který byl využit pro akvizici dat analyzovaných v praktické části); (iv) metody zpracování obrazu ve funkčním zobrazení sítnice; (v) metody vícerozměrné statistiky vhodné pro sekvenční snímky sítnice (analýzy hlavních a nezávislých komponent); (vi) nedostatky v oboru funkčního zobrazení sítnice.

Pro praktickou část a vývoj algoritmů byly použity sekvenční snímky sítnice (o délce 10 sekund) zdravých subjektů a subjektů s léčenou oční hypertenzí získaných na oční klinice v Erlangenu, Německo. Sekvenční snímky byly pořízeny speciálním video-oftalmoskopem (zdroj světla o vlnové délce 574 nm, 25 snímků za sekundu) při současném rozšíření zornic subjektů (0.1% roztok tropicamide). V rámci praktické části dizertační práce byly splněny následující cíle.

Byl sestaven algoritmus pro potlačení skoků v hemodynamických průbězích fyzio-

logických celků sítnice vzniklých důsledkem sakadických pohybů nebo mrknutím. Algoritmus využívá metody shlukové analýzy časových průběhů intenzitních gradientů. Hlavním jádrem disertační práce je inovativní aplikace metod vícerozměrné statistiky pro automatickou a datasetem řízenou analýzu a separaci fyziologických celků v sekvenčních snímcích sítnice na základě jejich přidružených hemodynamických průběhů. Byly aplikovány metody prostorové analýzy hlavních komponent (PCA) a analýzy nezávislých komponent (ICA). Obě metody, PCA i ICA, detekovaly přítomnost samovolných žilních pulzací v oblasti optického disku ve vyšší míře než uvádí předchozí studie s užitím subjektivních metod. Míra detekce je srovnatelná se studiemi využívajících semi-automatických metod digitálního zpracování obrazu. PCA a ICA dokáží v rámci svých výstupů lokalizovat přítomnost samovolných žilních pulzací do příslušné části obrazu (prostorová hlavní/nezávislá komponenta) a ukázat časový průběh (koeficienty hlavní/nezávislé komponenty) představující hemodynamiku v dané funkční části. Kromě samovolných žilních pulzací (SVP, z aj. spontaneous venous pulsations) v optickém disku, PCA i ICA identifikovaly další komponentu nazvanou pulzace poháru optického disku (OCP z aj. optic cup pulsation), která je prostorově homogenní přes všechny subjekty, a která nebyla zaznamenána v jiných předchozích studiích. Přítomnost této komponenty dosahovala přes 90% ve vyšetřených očích. Novým poznatkem byla i identifikace projevu dýchání v sekvenčních snímcích sítnice. Komponenta identifikována pro dýchání byla rovnoměrně rozprostřena přes daný obraz a časový průběh koeficientů vykazoval frekvenci dýchání (0.2 Hz).

Následná podrobnější analýza časových průběhů koeficientů hlavních komponent identifikovaných jako SVP a OCP ukázala korelaci morfologie jednotlivých pulzů a tepové frekvence nebo stárnutí. Dosud polemizovaný faktor tepové frekvence vyskytující se v teoretických modelech byl potvrzen jako fyziologická proměnná i v klinické studii. Výsledek naznačuje, že tepová frekvence musí být brána v potaz pro následující klinické studie zabývajících se změnou hemodynamiky a pulzací vlivem nemocí. Korelace s věkem je v souladu s předchozí studií.

V disertační práci je představen návrh a realizace simultánní akvizice sekvenčních snímků sítnice a dalších bio-signálů (elektro-kardiogram, elektro-okulogram, pulsní oximetrie, respirační plethysmografie) včetně invazivně měřeného intralebního tlaku. Součástí projektu byl i návrh a sestavení pojízdného vozíku s ramenem a polohováním. Vozík musí být kompatibilní a flexibilní pro potřeby neurologických pacientů umístěných na jednotce neurologické intenzivní péče. Pro propojení a synchronizaci video-oftalmoskopu a dalších biosignálů byl použit systém prezentovaný v Kolar R. et al., Biomedical Optics Express, 14:6, 2023. Pro připojení a synchronizaci signálu z intralební tlakové sondy byl navržen speciální převodník ve spolupráci s externí firmou. Tato práce prezentuje první přesně synchronizované simultánní měření

sekvenčních snímků sítnice a intralebního tlaku. Tento mezník představuje počátek pro následné studie zabývající se odhadem intralebního tlaku bezkontaktně na základě sekvenčních snímků sítnice.

Závěrem, tato práce rozšířila dosavadní vývoj funkčního zobrazení sítnice o automatickou analýzu a identifikaci jevů samovolných žilních pulzací v optickém disku, pulzací poháru optického disku a projevu dýchání v sítnici. Tato práce dále identifikuje tepovou frekvenci jako důležitý faktor pro další klinické studie zabývající se hemodynamikou v sítnici. A nakonec, tyto teze představily první simultánní měření sekvenčních snímků sítnice a intralebního tlaku. Tato disertační práce představuje původní výzkum, který byl recenzován a představen na mezinárodních konferencích, a publikován v časopisech IEEE Transactions on Medical Imaging, a Communications Biology.

LABOUNKOVÁ, Ivana. *Analysis of image retinal sequences from experimental ophthalmoscope*. Brno: Brno University of Technology, Faculty of Electrical Engineering and Communication, Department of Biomedical Engineering, 2024, 182 p. Doctoral thesis. Advised by doc. Ing. Radim Kolář, Ph.D., and by Assoc. Prof. MUDr. Igor Nestrašil, Ph.D.

Author's Declaration

Author:	Ing. Ivana Labounková
Author's ID:	136480
Paper type:	Doctoral thesis
Academic year:	2023/24
Topic:	Analysis of image retinal sequences from experimental ophthalmoscope

I declare that I have written this paper independently, under the guidance of the advisor, expert advisor and using exclusively the technical references and other sources of information cited in the paper and listed in the comprehensive bibliography at the end of the paper.

As the author, I furthermore declare that, with respect to the creation of this paper, I have not infringed any copyright or violated anyone's personal and/or ownership rights. In this context, I am fully aware of the consequences of breaking Regulation § 11 of the Copyright Act No. 121/2000 Coll. of the Czech Republic, as amended, and of any breach of rights related to intellectual property or introduced within amendments to relevant Acts such as the Intellectual Property Act or the Criminal Code, Act No. 40/2009 Coll. of the Czech Republic, Section 2, Head VI, Part 4.

Brno ....

author's signature*

*The author signs only in the printed version.

ACKNOWLEDGEMENT

I would like to express my gratitude and special thanks to my supervisor doc. Ing. Radim Kolář, Ph.D. for his dedicated support, guidance, and patience throughout the doctoral program journey. I would also like to express my gratitude to my expert advisor associate prof. Igor Nestrašil, Ph.D. who has been supporting my ideas, helped with their experimental realizations and further development.

Furthermore, I would like to thank my husband Ing. René Labounek Ph.D. for his valuable advice and collaboration in professional life, and consistent personal support in family life. I also thank my parents who always supported and encouraged me in my personal and profesional goals.

Contents

List of Figures

Introduction

In vivo observations of hemodynamic processes in human retinal vascular bed begun already in the 19th century when the first ophthalmoscope was assembled. Nowadays, variations of optical systems and other devices are optimized to acquire both static and dynamic images of human retina and to observe the hemodynamic alterations. Even though the first ophthalmoscope is more than century old, the biggest progression of functional retina imaging is happening in the last two decades with the utilization of new technical solutions, principles (video-ophthalmoscopic methods, interferometric methods, etc.), and algorithms for digital image processing.

Functional retina imaging is focused on hemodynamics, its alterations due to diseases or external stimulation. The mostly observed attributes are blood perfusion, blood flow and velocity, pulsation of arteries, pulsations of central retinal vein (CRV) and its adjacent branches. Pulsations of CRV in area of optic disc, widely called spontaneous venous pulsations (SVP), and its origin have been a subject of many discussions. Widely accepted theory explains the SVP as a result of pressure gradient between the intraocular pressure and cerebrospinal fluid pressure (of the same value as intracranial pressure). Both pressures influence the CRV on both sides of lamina cribrosa sclaera, the mesh structure located posteriorly to optic disc and dividing the area of the eye and optic nerve. Clinical studies demonstrated link between absence of SVP and increased values of intracranial pressure. However, the precise estimation based on SVP is still in progress. The alterations of pulsations of CRV and its adjacent branches are linked to various physiological factors (i.e. age). Other clinical studies link the hemodynamic alterations in retina to pathological processes (diabetes mellitus, diabetic retinopathy, glaucoma, Alzheimer's disease, etc.). However, the proper acquisition and image processing methods are crucial to identify such changes and determine suitable candidates for biomarkers.

Quantification of the hemodynamic changes and following result comparisons and verifications within the clinical studies remain problematic as there is no golden standard in acquisition methods, neither in image processing algorithms nor parametrization. There are various devices acquiring the retinal images sequences providing time-courses of measured attributes, such as blood volume or vessel diameter (while using ophthalmoscopic methods), or blood flow and velocity (in case of interferometric methods). In case of ophthalmoscopic methods, even the recent studies (published in) used subjective methodology to evaluate SVP, i.e. the observer categorized the pulsation into one of four categories (Hedges scale). Lately, subjective evaluation yields the precise measurements of vessel diameter based on image processing methods. However, most of the algorithms are semi-automatic and require the human input. Semi-automatic analyses are provided also within the proprietary

software of commercial devices for acquisition of retinal image sequences (Imedos, Německo, XyCam , USA). The proprietary software requires a selection of the vessel for the analysis. As the retinal vascular bed is unique for each individuum, the subjective selection can lead to fault results.

Methods of blind source separation, i.e. principal component analysis (PCA) and independent component analysis (ICA) seems to be promising as data driven tool for automatic analyses in functional retinal imaging. Both PCA and ICA were already successfully implemented in the field of functional magnetic resonance imaging to localize anatomical parts of various physiologic functions. The similar characteristics of datasets of functional retinal imaging and functional magnetic resonance imaging assume the successful utilization of blind source separation techniques in the field of functional retinal imaging in order to identify functionally distinct parts characterized with specific hemodynamics.

Except for the automatic analysis, the functional retinal imaging field lacks also in other areas, i.e. in data processing (video quality assessment, spike suppression filter optimized for time-courses of retinal hemodynamics), and in basal research and identification of factors affecting retinal hemodynamics (e.g. heart rate as a factor in models yet never proven in any clinical study).

This doctoral thesis introduces into the state of the art of the functional retinal imaging within its first chapter which includes (i) retina anatomy and physiology; (ii) etiology of retinal pulsatile phenomena such as spontaneous venous pulsation (SVP); (iii) principles and methods of functional retinal imaging; (iv) image analysis in the field; (v) multivariate statistics promising for functional retinal imaging; and (vi) pitfalls.

The second and third chapters defines and addresses the pitfalls and advance the functional retinal imaging field. The main outcomes are as follows. The blind source separation technique was successfully utilized in functional retinal imaging field to automatically separate functionally distinct parts of human retina. The spikes in hemodynamic time-courses were suppressed via designed algorithm. Heart rate was verified as a factor influencing retinal hemodynamics via analyzing human retina image sequences acquired in eye clinic in Erlangen (Germany) and in University of Minnesota (USA). The last part introduces the first precise simultaneous measurement of retinal image sequences and intracranial pressure along with other biosignals (i.e. electrocardiogram, finger plethysmography, electrooculography). The research here is also presented via related original research articles that were published in journals IEEE Transactions on Medical Imaging and Communications Biology.

1 State of the Art

1.1 Brief Physiology of the Posterior Eye Segment and Retinal Pulsation Phenomena

Eye is an important sensory organ providing visual perceptions. Its main function is light collection, focusing and transformation into electrochemical neural signal which is transferred by neurons into the *cortex*. About 55% of the whole *cortex* is processing just the visual information [243]. Till the light is transformed into electrochemical energy by retinal photoreceptors, the light is trespassing several optical media including *cornea*, anterior chamber, optical lens, posterior chamber, vitreous chamber and is focused on *retina*. The optical path and eye anatomy is visualized in **Figure 1.1**.

For purposes of this thesis (focused mainly on ophthalmoscopic methods and retinal sequence processing), the brief anatomy and physiology description will be limited to posterior eye segment including layers of *retina*, *choroidea*, and physiologic parts *fovea*, optic nerve head (ONH) visible as optic disc (OD) in fundus images, retinal and choroidal vasculature providing blood supply.

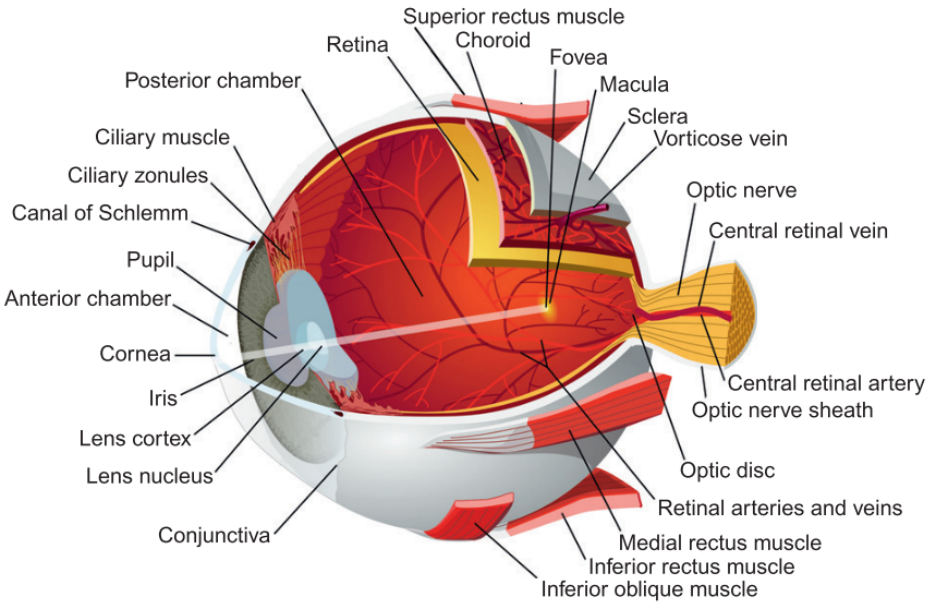

Fig. 1.1: Eye Anatomy [243]

1.1.1 Retina

Retina, an essential part enabling vision, is the most inner layer of an eye bulb lining the vitreous (gel filling the eye inner space). Retina covers approximately 65% of the eye bulb inner wall. Posteriorly, retina borders with ONH, and continues anteriorly till it reaches the ciliary body at *ora serrata*.

Retina is a multi-layer system which can be divided into retinal pigment epithelium and neuroretina (including nine layers)[101, 257]. Neuroretina enables phototransduction - transformation of light into electrochemical neural signal. The process of phototrunsduction and signal transfer involves several cell types distributed over the neuroretinal layers.

Retinal cell types. There are approximately 55 distinct cell types in mammalian retina [197]. Depending on function, the cells can be divided into following groups - retinal pigment epithelium cells, photoreceptors (rods, cones), interneuron cells (bipolar cells, horizontal cells, amacrine cells, interplexiform cells), ganglion cells (midget ganglion cells, parasol ganglion cells), glial cells (Müller cells, astrocytes, oligodendrocytes, microglia) [101, 243, 257]. The most important are photoreceptor cells - sensors that enable the phototransduction. There are two classes of photoreceptors - rods, cones. In human retina are 77-107 million rods and 4-5 million cones [257]. Each photoreceptor has his outer segment, inner segment (including cell organelles), nucleus and synaptic terminal securing the connection and signal transfer to interneuron cells (bipolar cells in particular). Outer segment contains the membrane discs enclosing the photopigment consisting of a membrane protein *opsin* and chromophore molecule *11-cis-retinal* [101, 243, 257]. Rods and cones differ in the structure (i.e. disc morphology [257], chromophore molecules rhodopsin/photopsins) and the response to light. Rods contain chromophore molecule rhodopsin (absorption peak at 496 nm). Rods are more photon-sensitive and generate the neural signal in response to one photon [101, 257], therefore the rods are used in scotopic conditions. Rods provide lower vision resolution. Higher resolution vision is expected by cones. Each cone contains one of three different types of chromophore molecule to response the light of different wavelengths. Depending on absorption peaks of the chromophore molecules, the cones are red (558 nm), green (531 nm) and blue (419 nm) sensitive. Red-sensitive cones comprehends 63% of all cones, green 32% and blue 6% [257]. The blood supply and metabolic support of photoreceptors are provided by choriocapillaris (part of choroid) through retinal pigment epithelium cells [101, 243, 257]. Except for the metabolic function, the retinal pigment epithelium cells sustain vision acuity as it prevents backscatter of light by absorption of the photons that passed through the photoreceptor layer [243]. Photoreceptors transfer the generated signal through its synaptic terminal to bipolar cells, the most

important interneurons, that process neural signal and transfer it to ganglion cells responsible for the signal transmission to brain through their axons. The function of the glial cells is mostly supporting as the cells maintain the inner environment.

Retinal layers. The retinal cells are distributed over the retinal layers, i.e. retinal pigment epithelium layer and layers of neuroretina - photoreceptor layer, external limiting membrane, outer nuclear layer, outer plexiform layer, inner nuclear layer, inner plexiform layer, ganglion cell layer, retinal nerve fiber layer (RNFL) and internal limiting membrane. All the layers are shown in **Figure 1.2** with graphic demonstration of the cells and layer description seen in ultra-high resolution optical coherence tomography (OCT) image [101, 125]. The most outer part - the retinal pigment epithelium - creates outer blood retina barrier preventing blood leaking from choriocapillaris into photoreceptor layer [257]. The most inner part, the nerve fiber layer, is created by the axons of ganglion cells that transmit the visual signal to brain. The ganglion axons creates axonal bundles that lead to ONH. The axons coming from ganlion cell in fovea (retinal anatomical structure) lead to ONH directly in straight trajectory in papillomacular bundle [243]. The axons of the other ganglion cells leads to ONH through arch trajectories above or below the papillomacular bundle.

Retinal topography and composition. The cell distribution in the neuroretinal layers, the width or even the presence of each neuroretinal layer itself vary over the eye inner surface. Retina is approximately 0.4 mm thick in the edge of

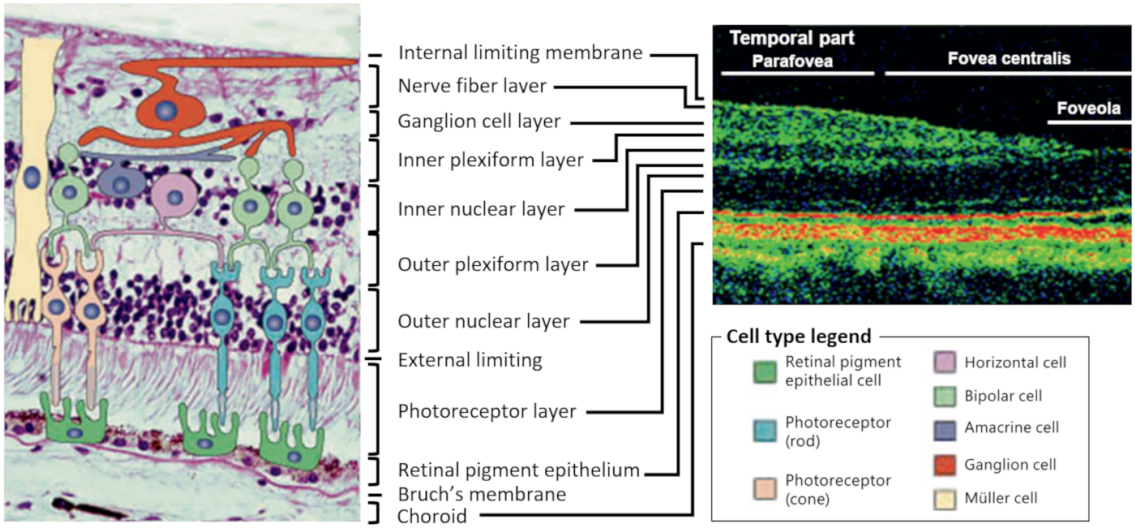

Fig. 1.2: Retina Layers: **left,** Photomicrograph of the retina (magnification x200) with ilustrated retinal cells[101]. **right,** Ultra-high resolution optical coherence tomography of macula (temporal part only)[125]

ONH and is thinning out anteriorly to 0.14 mm at *ora serrata* in the periphery [101]. The retina can be divided into central and peripheral area. The peripheral part includes the retina outside the temporal retinal arteries. This rod-dominant area is characterized by a single ganglion layer, thin retinal nerve fiber layer and thicker retinal pigment epithelium layer (up to 60 μm) [101, 257]. The central area, located in posterior pole between the temporal retinal vessels, is characterized by thin retinal pigment epithelium layer (14 μm) and thick ganglion layer (up to 80 μm). This area comprises the most important structure for the vision - *macula*, located approximately 3 mm temporal to ONH. The macula is a circular area (4.5-5.5 mm in diameter [243, 257]) that includes concentric parts - perifovea, parafovea, and fovea (1.5 mm in diameter, including foveal slope and foveola) [101, 243, 257]. From perifovea to foveola the cone density rises (from $5,000/mm^2$ in macula border to $199,000/mm^2$ in the foveola) and the rod density is dropping. The rods are fully excluded from foveola as well as the blue cones. In the foveola are the cones and Müller cells only so the whole retinal layer in this area is thin enough (0.18 μm) to be supplied by choriocapillaris only. Therefore the retinal vessels are missing in central foveolar area, called foveal avascular zone (0.5 mm in diameter). Three milimeters nasal to macula is located ONH that collects all the axons of ganglion cells. The layer of ganglion axons, RNFL, is the thickest in the border of ONH and can measure up to 300 μm in upper and lower temporal regions.

1.1.2 Optic Nerve

The optic nerve is a confluence of retinal ganglion cell axons [272] and comprises 1.2 million neural axons (approximately 40 times more than included in acoustic nerve) [243]. Optic nerve can be divided into two parts - intraocular and retrobulbar. Intraocular part contains retinal nerve fiber layer and retinal ganglion cell layer which forms a cone as leaving the eyeball through posterior scleral foramen [272]. The narrow part of the ganglion cone is clinically visible part of optic nerve, termed optic disc (OD) in retina fundus images (**Figure 1.3b**). OD is a bright, pink oval of average size $2.69mm^2$ (horizontal diameter 1.76 mm, vertical diameter 1.92 mm) [141, 257, 272] and situated 3-4mm nasally from fovea [141]. OD surface is flat or mildly elevated on the periphery - this part is termed neuroretinal rim [272], and depressed in the middle - this part is termed optic cup (OC) and takes approximatelly a third of the whole OD (0.83 mm horisontal diameter and 0.77 mm vertical diameter) [141]. OD and OC is also visually described in **Figure 1.3a** and OC depression is clearly demonstrated by OCT images in clinical practice **Figure 1.3c**. The OD is surrounded by a scleral ring termed peripapillary ring of Elschnig (oval measuring 1.75 mm high and 1.5 mm wide in average) [222, 272]. OD part in

retina misses the photoreceptors typical for the retina.

Optic nerve continues posteriorly from eye bulb into intraorbital space through posterior scleral foramen and the network of pores and tunnels in scleral canal, termed *lamina cribrosa sclerae*. In the intraorbital space, the optic nerve is myelized by oligodendrocytes [243, 272] and its length is 5mm bigger than the eye bulb-to-orbital apex distance due to eye bulb movements [243]. Then, optic nerve goes through optic channel into *chiasma opticum*, where the retinal ganglion cell axons merge with axons of contralateral optic nerve continuing as *tractus opticus* into *thalamus*[243, 272].

1.1.3 Retinal and ONH Blood Supply

Two thirds of the whole eye blood supply is provided by *arteria ophthalmica* (first branch of *carotid internal*) [106, 109, 110, 111, 112, 243] and its branches. *Arteria ophthalmica* goes through optic channel along the optic nerve. There are two groups of its branches - supplying the whole eye bulb (short and long posterior ciliary arteries PCAr, anterior ciliary arteries, muscle arteries, central retinal arterie CRA), and supplying other orbital structures (including arterie ethmoidal, nasal, frontal and supraorbital).

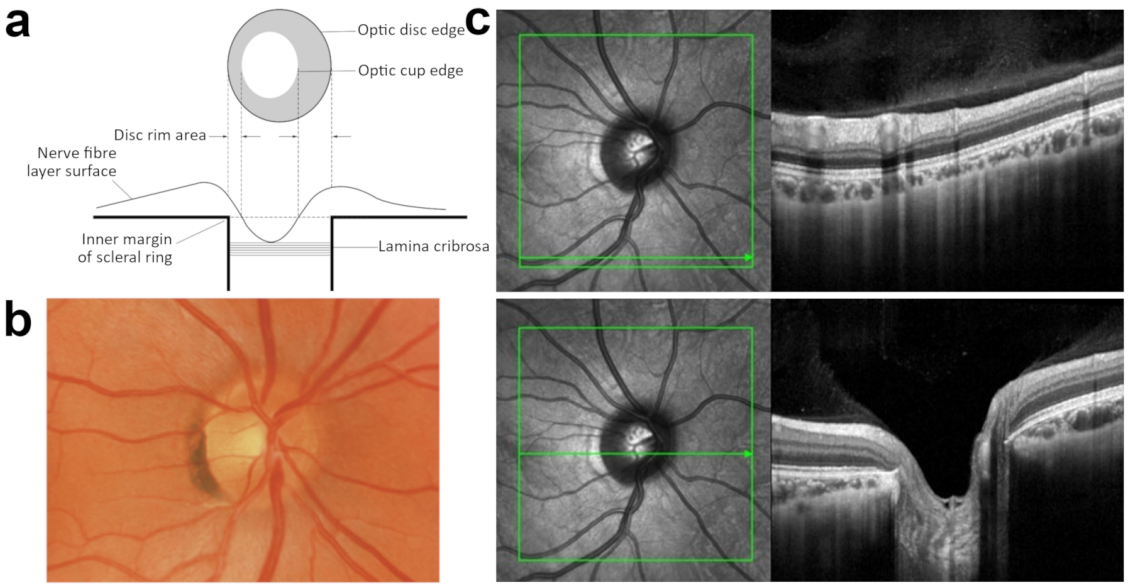

Fig. 1.3: ONH clinical visualization and description: **a,** OD morphology description [224] **b,** Fundus camera image of healthy subject ONH [222] **c,** ONH volume scans (exported from the Heidelberg Spectralis HRA+OCT optical coherence tomographer) [33]

The most important branches of *arteria ophthalmica* providing the blood supply for eye bulb are - CRA (blood supply of retina), and PCAr (supplying *uvea* - inner eye part including choroid, iris and *corpus ciliare*; anterior optic nerve; and outer retinal layers). CRA enters the ventral aspect of the optic nerve 5-15 mm behind the eye bulb and goes within the optic nerve through *lamina cribrosa sclerae* till the retinal surface where is divided into four main arteries (*arteriola nasalis retinae superior*, *arteriola nasalis retinae inferior*, *arteriola temporalis retinae superior*, and *arteriola temporalis retinae inferior*) - each responsible for blood supply of corresponding retinal quadrant [19, 106, 222]. These four arterioles with its branches create the retinal vessel tree visible on retinal surface through ophthalmoscopic techniques. The vessel tree is unique for each person and may be used also for biometric identification [248]. Posterior ciliary artery has more branches as it supplies numerous eye bulb parts. Long branches of PCAr are situated outside the eye bulb and provide blood supply to anterior uveal tissues, e.g. iris. Short branches of PCAr goes through sclaera in posterior eye bulb part and supplying peripapillary choroid. Other short branches could create circle (not closed in many cases), called Zinn-Haller circle (OZH) [79, 106].

Between 60 and 80% of the retina and its inner layers are supplied via retinal circulation with CRA [19, 106, 257]. The blood is drained within the central retinal vein (CRV) leading through optic nerve head, lamina cribrosa sclaera, within the optic nerve. Retina is too thick to be supplied by retinal circulation only. Therefore the outer layers including photoreceptors, bipolar cells and retinal pigment epithelium are supplied by the choroidal circulation (originating in PCAr) through choriocapillaris [106, 257]. Choriocapillaris provide blood supply and metabolic support also in retinal superficial layers of foveal avascular zone and retinal periphery where the zones are thin enough to be fully supplied by choroid and where the retinal vessels are missing[257]. The inner retina can be also supplied by cilio-retinal artery - in 10-30% [19, 159, 243, 257] physiologically, or pathologically along with CRA occlusions [110, 111]. In summary, retina is supplied by both retinal and choroidal circulation systems.

As the retinal circulation is a closed system of one input and one output vessel, it is sensitive to external pressure fluctuations (i.e. intraocular pressure, intracranial pressure) [110] leading to changes in intensity of venous pulsations [124], increase in venous pressure [110], or pathological formation of cilio-retinal arteries, etc. Retinal circulation is also self-regulating system independent on perfusion pressure (dependent on local vascular control mechanism, autoregulation factors - locally produced hormon angiotensin 2, local metabolits, etc.) [76, 235].

The layer below retina, choroid, is the most perfused part and receives about 85% of the whole ocular blood [19, 257]. Unlike retina, choroid is an open circulation

system (supplied from several PCAr branches), thus blood flow is dependent also on perfusion pressure and is characterized by weak autoregulation system [19, 76, 257].

The perfusion of anterior segment of optic nerve is divided into four regions - surface neuron layer, prelaminar layer, laminar layer (verging to sclera, formed by net of *lamina cribrosa sclerae*), retrolaminar layer (posteriorly to *lamina cribrosa sclerae*), **Figure 1.4** [19, 106, 109, 110, 111, 243].

Surface retinal neuron layer is perfused mostly by retinal arterioles (CRA branches) going into the middle OD. Temporal part of OD can be perfused also by cilio-retinal artery, if presented [19, 106, 110, 243, 257]. Prelaminar layer is perfused by PCAr branches and by recurrent braches coming from OZH (formed by short PCAr branches, providing blood supply of peripapilary choroid) which goes through choroid into prelaminar layer [76, 106, 109, 222]. Direct perfussion of prelaminar layer with choroidal capillaries was supposed to be minimal [106] until 2019 when Lee at al. found the parapapillary choroid was the important source of prelaminar ONH tissue [180]. Perfussion of laminar layer is provided by branches originated in OZH and by short branches of posterior ciliary artery [76, 106, 109, 111, 222]. Choroidal peripapillary arterioles could also contribute in perfusion of *lamina cribrosa sclaera* [106]. Retrolaminar region has two sources of blood supply, i.e. one originated in *pia mater*, and CRA with its smaller branches within the optic nerve [106, 111, 222].

The whole vessel map providing blood supply of retina, choroid, and anterior segment of optic nerve is shown in the **Figure 1.5**.

1.1.4 Ocular Hemodynamics

Ocular hemodynamics and its changes are very important indicators of pathologies in various medical disciplines, i.e. ophthalmology (glaucoma [320], CRA occlusion, diabetic retinopathy [51, 177, 229, 233], diabetic macular edema [177]), neurology (stroke, Alzheimer's disease [71]), systemic diseases (diabetes [233]), cardiology [312].

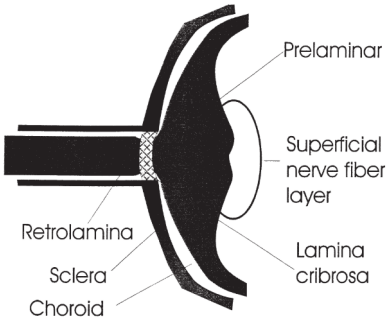

Fig. 1.4: Perfusion regions of optic nerve anterior segment [106]

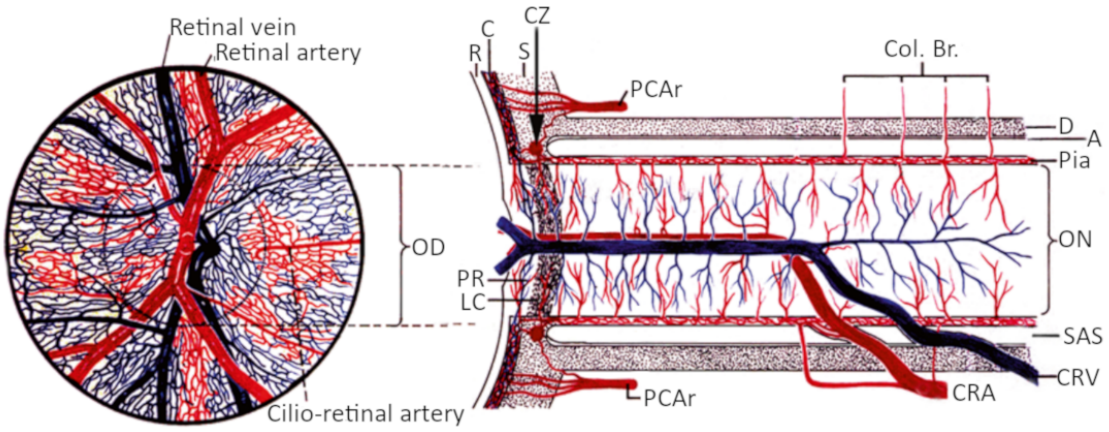

Fig. 1.5: Blood supply of optic nerve anterior segment [111]. A - arachnoid, C-choroid, Col. Br. - collateral branches, CRA - central retinal artery, CRV - central retinal vein, CZ - Zinn-Haller circle, D - dura, LC- lamina cribrosa OD - optic disc, ON - optic nerve, Pia - pia mater, PCAr - posterior ciliary artery, PR - prelaminar region, R - retina, S - sclera, SAS - subarachnoidal space

Ocular hemodynamics can be examined by various techniques, i.e. Doppler velocimetry, laser Doppler flowmetry, laser speckle flowgraphy, techniques based on blue field entoptic phenomenon, fluorescein and indocyanine green (ICG) angiography fundus camera based video-ophthalmoscopy (as retinal vessel analyzer), etc. [106, 242, 327].

The ocular hemodynamics is the most frequently assessed by blood flow Q. Mathematically, blood flow can be calculated with numerous equations based on various available measures, e.g. blood volume (blood flow as a differentiation of total blood volume in time [168], blood velocity (blood flow as vessel crossectional area multiplied by blood velocity [275, 332]), or pressure gradients. The most common equation in ocular physiology is based on pressure gradients. This relation is expressed by Hagen-Poisseuille law (**Equation 1.1**) saying that blood flow in tubular vessel is a ratio of pressure gradient between the ends of the vessel and vascular resistance R within ocular vascular bed (**Equation 1.2**, where the vascular resistance depends on blood viscosity (η) and vessel dimensions, i.e. vessel diameter r and length l) [111, 275, 332]. In case of ocular blood flow, the pressure gradient is represented by ocular perfusion pressure (OPP), closely describe in the next paragraph. Then, the ocular blood flow Q is calculated as a ratio of OPP and vascular resistance according to **Equation 1.3**. In summary, blood flow levels depends mathematically mainly on three factors - perfusion pressure, intraocular pressure (IOP) and blood resistance.

$$Q = \frac{\Delta P}{R} \tag{1.1}$$

$$R = \frac{8\eta l}{\pi r^4} \tag{1.2}$$

$$Q = \frac{OPP}{R} \tag{1.3}$$

Perfusion pressure. In general, the Hagen Poisseuille law uses pressure gradient between the ends of the vessel. In case of blood flow in vascular beds, the pressure gradient of one vessel is replaced with the difference between mean arterial pressure (MAP) and venous pressure forming so-called perfussion pressure. Ocular perfussion pressure (OPP) is a special case of the perfussion pressure that is characterized with difference between MAP in ophthalmic artery and venous or intraocular pressure (of the same values) [19, 111, 275]. The measurements of venous pressure and blood pressure in ophthalmic artery are mostly unavailable, therefore their approximations are used instead. As the venous pressure and IOP are supposed to be of the same value, the easily measurable IOP substitutes the venous pressure. Approximation of MAP in ophthalmic artery is based on standard pressure measurement in brachial artery, i.e. MAP in ophthalmic artery is equal to two thirds of MAP in brachial artery due to hydrostatic effects [150, 254]. Therefore, the most accepted formulation of OPP is expressed as two thirds of MAP minus IOP (**Equation 1.4**) [275]. The calculation of MAP is based on levels of systolic and diastolic pressures (as shown in **Equation 1.5**) [19, 111].

$$OPP = \frac{2}{3}MAP - IOP \tag{1.4}$$

$$MAP = BP_{diast} + \frac{1}{3}(BP_{syst} - BP_{diast}) \tag{1.5}$$

Blood Resistance. Blood resistance is a function of blood viscosity, the length of measured vasculaure, its branching pattern and radius of the vessels of the measured vasculature [275]. This function is expressed by Hagen-Poisselle's law that says the resistance is inversely proportional to the fourth power of the radius of a vessel and indirectly proportional to the blood viscosity[19] (**Equation 1.2**) as noted above. Retinal vascular system is geometrically distributed and the influence of branching pattern is expressed by Murray's law [257]: the cube of the radius of the vessel is equal to the sum of the cubes of the radii of bifurcated blood vessels. Thus the resistance increases with each bifurcation and local blood flow decreases. Besides these laws, others laws known in fluid mechanics may be applied, i.e. Bernoulli principle, Laplace law [332], etc.

Intraocular Pressure. Intraocular pressure is an important factor in ocular hemodynamics influencing choroidal and retinal blood flow. Physiological levels of IOP primarily maintains proper refractive properties of the eye and corneal curvature

[43]. IOP is determined by the pressure exerted by the contents of the eye (aqueous humour, vitreous, blood) outwards against the scleral compliance and extraocular muscle tone exerting inward pressure [43]. The physiological range of IOP is 16±5 mmHg and the values above 25 mmHg are considered pathological [43]. The IOP levels varies about 2-3 mm Hg according to a day period. The highest levels of IOP are usually in the mornings and lowest levels at nights [43, 150]. Besides diurnal fluctuations, the continuous IOP measurement demonstrates the variations along the cardiac cycles[306] characterized with ocular pulse amplitude parameter. The values of ocular pulse amplitude were reported 2.0-3.9 mmHg [48, 116, 147, 306] (varying according to used methodology [271, 336], posture [306], IOP level [48]). The IOP levels depends mainly on four factors, i.e. extraocular muscle tone modulated through central nervous system, vitreous humour, balance of aqueous humour, and ocular blood volume and flow.

IOP-venous pressure relationship. As noted above, IOP represents a good approximation of intraocular venous pressure. This is a result of general vein characteristics and mutual pressure interactions inside the eye. Due to high compliability of the veins [25] and levels of venous pressure (10-15 mmHg), the intraocular veins, exposed to the compression force of IOP, behave as Starling resistors **Figure 1.6**. This means, the venous pressure must be equal to IOP or slightly higher otherwise the veins start to collapse. Once the vein is collapsing, the resistance to flow is increasing in order to increase the venous pressure and balance the negative IOP-venous pressure gradient. In case IOP exceeds the arterial input pressure, the vein collapses completely and the blood flow ceases.

Blood flow and Related hemodynamic parameters. The retinal blood flow demonstrates pulsatile characteristics in both arteries and veins [281, 325, 337] despite the fact the venous flow pulsations in general are considered to be non-observable [32, 185] (except for the jugular veins or particular veins in brain).

The total ocular blood flow was reported 900 μl/min [174], including the total retinal blood flow in range 38-80 μl/min [58, 70, 86, 177, 319, 318, 320]. The total retinal blood flow is 33-35 μl/min in arteries and 34-36 μl/min in veins [57, 263]. Local blood flow varies over the retinal parts and according to local vessel diameter (blood flow increases with the vessel caliber). Blood flow in the temporal part of the retina is reported to be higher than in the nasal part [57]. Considering the diameter, retinal blood flow in each vessel changes according to its diameter: artery blood flow is increasing in range 0.16-6.68 μl/min for arteries of sizes up to 60 μm in diameter and 0.18-4.8 μl/min in veins of sizes up to 50 μm in diameter [233]. Similar values and the same increasing trend of flow with diameter were demonstrated in previous study [281], were the mean flow was in range 0.13-0.45 μl/min for arteries (diameter 100-160 μm) and 0.14-0.3 μl/min for veins (of diameter 37-189 μm) [281]. Trend of

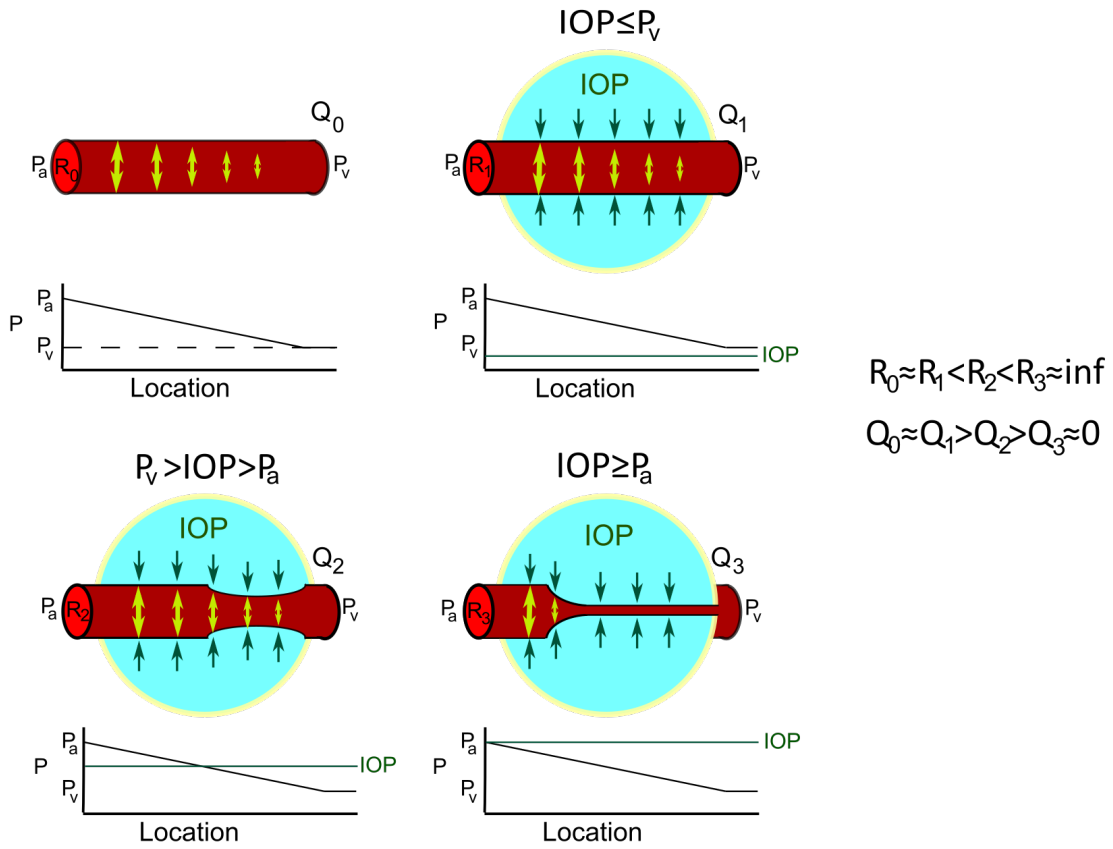

Fig. 1.6: Ocular Starling Resistor [275]. IOP - intraocular pressure, P_a - arterial pressure, P_v - venous pressure, Q_i - blood flow, R_i - vessel resistivity

increasing blood flow with vessel caliber was demonstrated also in [319] where artery blood flow increased from 2.5 to 8.7 μl/min according to artery diameter 33-85 μm, and venous blood flow from 1.8 to 15.8 μl/min for veins of diameter 44-150 μm [319]. This information comply with Murray's law.

The average flow velocities of blood particles is reported 3.4-4.2 mm/s in arteries, 2.9-3 mm/s in retinal veins [29, 340] while in other study reported flow velocity 16-28 mm/s in veins and 38-51 mm/s arteries[319], and capillary flow velocity is 2.89±0.41mm/s [334]. Generally, the absolute values of blood flow and velocity varies according to used methodology, specific tissue and measured atribute (i.e. plasma, red blood cells, leucocytes, etc.) in order to get required parameter (total volumetric blood flow, average blood flow). Particular clinical techniques, including the most recent, demonstrates the relative blood flow, velocity or blood volume changes, i.e. in arbitary units or ratios (laser speckle contrast imaging [253], scanning laser Doppler flowgraphy [229]) or even in alternative quantities (arteriovenous pulse delay) specific to the used methodology, thus the resulted values are not comparable.

Related hemodynamic parameters help describe blood flow and understand the ocular circulation and pathophysiological processes, i.e. arteriovenous passage time (i.e. mean circulation time), arteriovenous pulse delay, pulse wave velocity, blood flow pulsatility, etc. Arteriovenous passage time is oftenly measured via fluorescent dye along with angiography methods and demonstrates the time period between blood filling of arteries and veins, i.e. the first dye appearance in an artery and corresponding vein. The arteriovenous passage time was reported in range 0.87-2.44 s in healthy subjects [74, 167, 334] and can be prolonged in glaucoma patients [74, 241]. The angiography studies with fluorescent dye also help to understand succession of blood filling of particular ocular tissue. It was reported the choroidal blood filling is faster than retinal [110, 339], as blood filling of ONH microvasculature (prelaminar region supplied by choroid[180]) precedes the blood filling of retinal vessels [110]. Technology development made possible measurement of arteriovenous pulse delay, the time period between the pulses in arteries and veins. The delay depend on region, where the vessel is measured. Morgan et al. reported delay 4.4% of cardiac cycle (0.04 s) in lower vein [219]. Gugleta et al. reported delays from 3 spots of lower vein outside the OD, i.e. proximal 76°±58°, middle 31°±60°, distal 2.5°±80.5° phase shift degrees which correspond subsequently to 20%, 8% and 0.7% of cardiac cycle. Although there was a big variability across the subjects, this measurement demonstrated altered pattern of oscillation phase delay for vasospastic subjects [99]. Arteriovenous pulsation delay was also quantified in [294] while using the full-field phase-sensitive swept-source optical coherence tomography, where the delays were 19 ms (measured foot-to-foot) and 99 ms (measured peak to peak). The pulse wave velocity reflecting the pulse propagation within the vessel is one of the biomechanical parameter determining the elasticity of retinal vessel. Pulse wave velocity was quantified to 400 μm/s [163], 20mm/s [165], 600 mm/s [294], measured with retinal vessel analyzer, retinal vessel analyzer and fluorescein angiography and full-field swept-source optical coherence tomography respectively. Another parameter related to blood flow is blood flow pulsatility index/ratio evaluating pulsatility of retinal circulation through CRA or choroidal circulation (evaluated through macular tissue). The pulsatility is usually expressed non-specifically and the values depends on used methodology (i.e. Doppler velocimetry, laser speckle flowgraphy). Changes in pulsatility index are influenced by the vessel resistence as proven in several studies of different fields [117, 230, 308]. Blood flow pulsatility is also a potential clinical marker of age-related macular degeneration (which causes higher choroidal pulsatility) [96].

Auto/regulation. Blood flow is altering according to factors mathematically described above, i.e. IOP, blood resistance, OPP and consequently blood pressure. The relationship between IOP and OPP is mutual as the changes in OPP could

increase/decrease IOP and, vice versa, IOP increase can affect the ocular perfusion. As a result, the impairment in retinal venous outflow leads to retinal volume engorgement and local arterial pressure increase and thus to increased IOP [43, 150]. The moderate reduction of ocular arterial pressure (within physiological ranges) has only a little effect on IOP [43, 106], still in certain range of arterial pressure (<90 mmHg) the IOP decrease might occur [43]. On the other side, an IOP increase due to insufficient outflow of aquous humour decreases the retinal perfusion and retinal blood flow[43, 150] which may lead to retinal ganglion cell axon damage [23, 76]. OPP is also altering with the systemic blood pressure, i.e. OPP increases with increasing blood pressure.

In order to control the blood flow and maintain constant level, the ocular circulation systems (retina, choroid) has the ability of auto/regulation. Besides a system regulation common for various vascular beds of the human body (e.g. autonomic nervous system as sympathetic and parasympathetic innervation, circulating vasoactive hormones and drugs), choroid is also characterized with myogenic autoregulation [275]. Generally, autoregulation of blood flow in a tissue of vascular bed is defined as the ability of the tissue to maintain its blood flow relatively constant despite variations in perfusion pressure [5]. Particularly myogenic autoregulation is the ability of arteries (of corresponding vascular bed) to change the vascular muscle tone in response to vascular wall tension [23, 152]. Other words, choroidal arterial vessels are able of vasoconstriction/vasodilatation in response to a stretching force (caused by arterial pressure) and thus to regulate blood flow. Still, the autoregulation of choroid is very limited.

Unlike choroid, retina does not respond to autonomic control as it does not have parasympathetic and sympathetic innervation [78, 144, 268, 275]. Still, limited systemic regulation is not fully excluded as studies proved the presence of alfa and beta-adrenergic and cholinergic receptors [144]. Neverthless, the question of magnitude of systemic regulation remains unresolved as in vivo studies of retinal vessel reactivity after systemically administered alfa1-adrenergic agonists showed contradictory results [268]. Therefore, retina is characterized with strong local autoregulation systems - myogenic, metabolic, flow-mediated vasodilation, flow control by intercellular conduction. Retinal myogenic autoregulation balance blood flow during increase of mean systemic blood pressure or intraocular pressure. In particular, local autoregulation system decreases the retinal blood flow in response to increased IOP. Yet retinal autoregulation is effective in certain ranges only, i.e. IOP below 30-45 mmHg [19, 332]), mean systemic blood pressure to 41% up to the baseline values [5]. Except the myogenic autoregulation responding to arterial pressure changes, retinal artery walls are able to alter the resistance and vascular tone[238] according to levels of local metabolite production (angiotensinII [76], nitride oxide [111],

adenosin diphosphate [76]) so the blood flow supplying the tissue complies with metabolical demands and local needs. Thus, the blood flow depends on factors as temperature [99], illumination [332], blood gases [68, 78, 115, 144, 155, 232, 277] and postular changes [87]. For example, the blood flow is decreased during the constant illumination while there is 65% increase in retinal blood velocity, 5% increase in venular diameter and up to 82% increase in blood flow in the dark [332]. Effect of illumination is also demonstrated in [166, 226], where the light flicker stimulation was applied. High-frequency flickering stimulation causes different physiological processes creating alterations in ocular blood flow and related vessel diameter (vasodilatation, irregularities in longitudinal vessel profiles [166], increased retinal and ONH perfusion due to increased metabolical demands [5]). Besides the illumination, there is an impact of oxygen level on blood flow and vessel diameter in retinal vascular bed. To maintain blood concentration constant, retina causes an increase in blood flow and vasodilatation in reaction to systemic hypoxia, and causes vasoconstriction and decrease in both blood flow and velocity in reaction to hyperoxia [68, 78, 115, 144, 155, 232, 296]. Retina is more sensitive to changes of oxygen concentration than choroid. It is indicated, that choroid is unaffected by mild systemic hypoxia due to its large volume of oxygenated blood [275]. In case of temperature changes, a faster artery-to-vein pulse wave propagation is demonstrated in subjects exposed to low temperatures [99].

Pulsatile ocular blood flow and the ocular pulse amplitude is influenced also by human measures. As an example, eyes with longer axial lengths, are characterized with lower pulsatile ocular blood flow and ocular pulse amplitude [47]. The blood flow is not influenced only by local measures, but it seems to be affected also by overall body structure as lower ocular pulse amplitude was repored in individuals with higher body mass index [147].

1.2 Retinal pulsation phenomena

Retina provides unique space for non-invasive in-vivo observation of retinal flow. The blood volume is changing periodically along the each cardiac cycle and all these changes may be observable through the most simple ophthalmoscopic methods. The ophthalmoscopy in combination with recording proved the significant changes of blood volume in retinal tissue and geometrical measures of the morphological or structural elements (i.e. vessels or ONH) over the cardiac cycle. With a simple parametrization and further analyses of the recorded images, we can obtain the time-courses of blood flow or volume changes in relative or even absolute values.

Generally, these retinal changes over the cardiac cycle can be marked as retinal pulsation phenomena. This term is not limited to visible vessel diameter change,

total collapse or movements visible through simple ophthalmoscopic methods. The term includes also topics as blood flow/volume pulsations, arterial blood particles velocity pulsations or other atributes depending on particular imaging method. According to morphological structure, we can identify the pulsation of the whole fundus *"fundus pulsation"*, pulsation of the tissue of ONH *"ONH pulsation"*, pulsation of the veins *"spontaneous venous pulsation"* and pulsation of the arteries *"arterial pulsations"* described in the following paragraphs.

These retinal pulsatile phenomena depend on both systemic factors and local retinal autoregulation system. This system has a capability of vasoconstriction or vasodilation to regulate the blood flow in order to fill metabolical demands as described in previous chapter. These contractility/ wall tonus changes may alter the character of retinal pulsation phenomena. Neverthless, contractility changes were mostly demonstrated in extreme conditions (hyperoxia, hypoxia, hypercapnia, extreme temperature). The changes in pulsation character are potential sign of pathologies - both local (e.g., glaucoma [3, 92, 178, 182, 218, 285, 287], CRV occlusion [8, 56, 138, 140, 203]) and others (e.g., internal carotid artery stenosis [312], diabetes [230]), described in the chapter "Clinical significance of retinal pulsation phenomena" in more detail.

Fundus pulsation. The elements of the eye, i.e. retina and cornea, are periodically moving axially back and forth (in amplitude 25-35 μm [149, 291]). The dislocation of the elements are induced by blood filling of ocular tissue (retina, choroid) during systole along each cardiac cycle. These location changes called fundus pulsations are characterized with fundus pulsation amplitude (FPA) defined as mutual distance changes of retina and cornea (app. 4μm [291]).

Research group of L. Schmetterer published several papers about the fundus pulsation and its influencing factors observed with a laser interferometer [274, 276, 277, 278, 279]. The research group described the temporal characteristics of cornea-retina mutual and individual movements. Fundus pulsations were strongly associated with ocular pulse amplitude and pulsatile ocular blood flow [274]. More, Schmetterer and Findl et al. demonstrated variability of FPA as its magnitude depends on the location and tissue composition of certain retinal area. As an example, macula, retinal area where the retinal layer is reduced, changes its volume with choroidal filling only. This results in FPA of 3.4 μm. In contrary, the FPA of optic cup, an area including both choroidal and retinal layers, is 11.2 μm. The smallest FPA were measured in peripheral retina. [75, 274, 279].

The other studies using different technologies also proved the presence of fundus pulsations. K. Singh evaluated both retinal and corneal axial movement along with its mutual distance in time via Fourier domain optical coherence tomography. Retinal and corneal movements were highly correlated, the amplitudes of both tissues

were almost equal. The small phase difference between the both retinal and corneal movements resulted in fundus pulsation amplitude of 4 μm. The phase difference originates in propagation of the pulse wave, as the expansion of the choroid during systole pushes the retina forward and this pressure force reaches cornea with a delay. [290, 291].

The frequency analysis revealed the retina moves axially not only with heart rate, but also at its multiple frequencies [149, 290] (up to 7th harmonic [149]). Yet, any closer etiology remain unclear.

Later studies using laser doppler holography [245, 246, 247] also revealed the pulsations of the retinal tissue outside the vessels. The intensity of the pulsations varied over the all retina according to location (macula, periphery, ONH, peripapillary area of ONH) [245, 247] which is in agreement with previous results of L. Schmetterer.

Fundus pulsation in ONH particularly, reflecting the blood filling in ONH tissue, are described in the following paragraph as ONH pulsation.

ONH pulsation. The ONH tissue is mostly perfused with choroid and partly with retinal vessels. As a result, the pulsation of ONH can be observed in various forms (both the axial dislocation and reflectivity changes).

ONH pulsation seems to be tightly linked to fundus pulsations as ONH is a structural part of retina. However, dysynchronous movement of retinal tissue and ONH was demonstrated as mutual axial distance between retina and cup alters with each cardiac cycle [290]. The ONH axial pulsatile movements were reported in [6, 75, 290, 274] and mathematically modelled in [131]. ONH axial movements are correlated with pulsatile blood flow in CRA [6]. As noted previously, the axial movement (defined with FPA) is larger in ONH than in other areas of retina. FPA in ONH cup is in range 6.3-13.4 μm and FPA in neuroretinal rim 5.1-11.5 μm. As the whole fundus pulsates with the heart rate and at its higher frequencies, the same applies for ONH [290]. Additionally, the ONH pulsations can be also observed as the periodic changes of light reflection of ONH tissue with ophthalmoscopic methods or laser scanning ophthalmoscope [325].

The ONH pulsations (including both the pulsatile movements and changes in reflectivity) could be altered in ocular hypertension [237], or also can be affected by ONH tilting causing deformations of ONH due to horizontal eye movements [315, 316, 317].

Overall, pulsatile changes of ONH reflectivity are not fully understood or described. The possible etiology is in blood filling of ONH prelaminar region via choroidal circulation. This phenomenon and its possible etiology is more described in following chapter as a part of the outcomes of the thesis.

Arterial pulsations. The arterial pulsations were firstly reported by J. Frieden-

wald in 1934 [80]. J. Friedenwald classified the arterial pulsation into serpentine, collapsing/expansile and tonic category and described the main factors influencing the origin and intensity of these pulsations, i.e. artery turtuosity, pulse pressure, systolic pressure, blood viscosity, peripheral resistance, artery wall pliability [80]. Arterial pulse was also noted in book of H. Davson in 1972 [49], where he mentioned arterial collapse under non-physiological conditions (while applying external pressure on eye bulb).

Arteries generally do not collapse due to their high lumen blood pressure and thick walls [81, 104]. Yet, arteries may collapse under pathological conditions (it is suggested that arteries collapse downstream of a stenosis [301]). Regarding retinal studies, the pulsation of arterial diameter was a sign of pathology, e.g. retinal arterial pulse can be manifested during central retinal vein occlusion [8], ocular hypertension [193], external force pressing the eye [135, 137].

However, small periodic alterations of retinal arterial diameter were observed in healthy populations. Studies using dynamic vessel analyzer (DVA) [85, 284] demonstrated periodical changes in retinal artery diameter in healthy subjects [165] as well as study using scanning laser ophthalmoscope with further customed image processing [215], Doppler optical coherence tomography [325] or swept source optical coherence tomography that showed retinal artery thickness pulsation [294].

Except for arterial diameter, also arterial blood flow, volume and velocity demonstrate pulsatile character [117, 165, 187, 219, 247, 312, 319, 325]. Wang et al. enumerated pulsation of blood flow velocity for CRA over the cardiac cycle from the peak systolic velocity 11.8 mm/s to the end diastolic velocity 3.8 mm/s in healthy subjects [312].

Arterial blood flow pulsation represents a great source of information as arterial waveform profile is influenced by the arterial compliance and peripheral resistance [10, 267]. Moreover, retinal blood flow measures represent potential diagnostic parameters for cardiovascular diseases. In particular, the speed of pulse propagation over the retinal artery, called retinal pulse wave velocity, is a direct marker of arterial stiffness and its increased value is associated stroke and hypertension [187]. The retinal pulse wave velocity was reported in range 10-30 mm/s [165, 187] in healthy young subjects, 50 mm/s in subjects with hypertension [187], range 200-300 mm/s in older subjects [165]. However, the contradictory values of retinal pulse wave velocity, i.e. 600 mm/s in healthy subjects, were shown in [294] using swept-source optical coherence tomography declaring the methodology as the first speed and sensitivity-sufficient for this measurement.

In a detail, the retinal arterial flow pulsation are synchronous with choroidal arterial pulsation. More, retinal arterial flow waveform was characterized with a steep slope up and only gentle slope down [153, 247] similarly as the waveform of

choroidal arteries.

Spontaneous venous pulsation. The most visible dynamic phenomenon through ophthalmoscopy is spontaneous venous pulsation (SVP) of CRV inside the OD. SVP is mostly considered as a rythmic changing of CRV diameter due to blood filling and are visible in central part of OD, where CRV is crossing the ONH and leads posteriorly through the lamina cribrosa sclaera outside the eye bulb. SVP presence in human population varies over the research studies from 15-99%[113, 124, 184, 205, 335]. The reported incidence of SVP increases with the imaging tehnology development and its utilization and overall objective assessment.

SVP were observed and reported by Coccius in 1853 for the first time[113, 124, 185]. Since then, many investigators tried to find the right theory or model explaining the SVP etiology (e.g. Bailliart 1917[12], Elliot 1921[62]; Smith 1918[292], Duke-Elder 1926[59], Weinstein 1939[328], Engel 1946[64], Kahn 1950[142]; Baurmann 1925[15]; Walsh 1969[311], Lorentzen 1970[195], Levin 1978[184], Hedges 1994[113]; Levine 1998[185], Jacks & Miller 2003[124], Levine 2016[186], Babbs 2016[11]). The latest widely accepted theory explains the spontaneous venous pulsations of CRV as a result of pressure gradient between IOP and cerebrospinal fluid pressure (CSFP) originated from subarachnoidal space along the retrolaminar segment of optic nerve [124, 185]. Cerebrospinal fluid pressure is considered to be of the same value as intracranial pressure (ICP).

As noted, throughout the last century, the SVP were observed as periodic partial or even full collapses of central retinal vein. Technical development enabled precise quantification of these venous diameter alterations not only in CRV in ONH but also in its branches outside the ONH where the changes are not even visible. The example of rythmic diameter change of the retinal vein inside ONH with its time-course is demonstrated in **Figure 1.7**.

The technical development uncovered the influence of SVP to pulsations of local blood flow, volume and velocity. Various ophthalmoscopy-based methods enabled to measure and evaluate morphological structures of the retina (i.e. vessel diameter alterations) - direct ophthalmoscope [335], slit lamps [143, 219], fundus camera based systems (Retina vessel analyzer ([85, 284]) [86, 89, 92], scanning laser ophthalmoscope [153, 215, 325], custom-build ophthalmoscopes [287, 303]. Except for diameter change, these methods enables to observe the intensity alterations along the vessel lumen [217, 325] which is supposed to correspond to a local blood volume and flow. Except the ophthalmoscopy based methods, others were used for SVP studies - Doppler optical coherence tomography [57, 281, 319, 325, 337], swept-source optical coherence tomography [294], Doppler sonography [209], Doppler holography [245, 247], dynamic angiography [234], laser speckle contrast imaging (implemented in XyCam [253]).

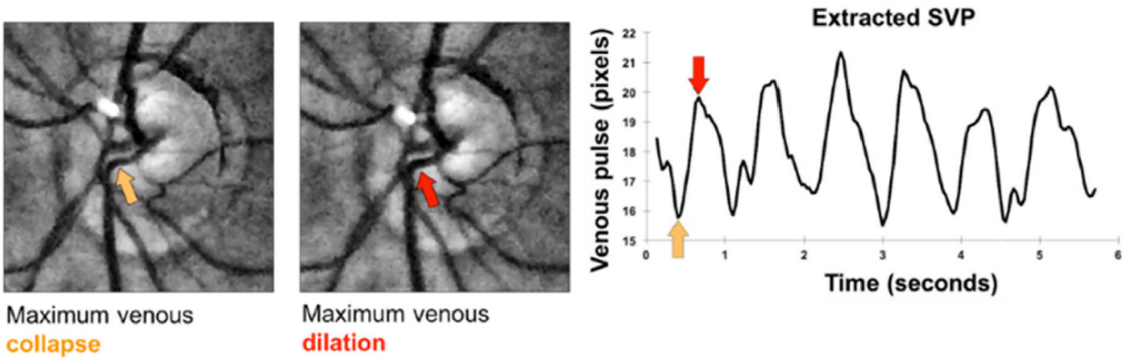

Fig. 1.7: Spontaneous Venous Pulsation [287]. SVP in a form of periodic changes of venous diameter

As noted, different imaging tools provide different measures - flow, velocity, intensity and vessel diameter. Its mutual relationships were explored in [86, 325]. All of the measures have pulsatile character with various phases. It is reported that the pulsatile intensity changes were synchronous with a vessel collapse [325]. The mean flow velocity increases as the vein diameter decreases during each cardiac cycle and the maximum flow velocity seems to be in phase with the vein collapse [86, 325].

Through the past, the studies demonstrated contradictory results about venous collapse. In late 20th century, Chen et al marked the start of venous collapse to early systole, the maximum collapse to early diastole and the total dilation to end diastole [34]. Michelson extended the knowledge about SVP and observed the diameter pulsations are synchronous with IOP pulsations [209]. More, he also evaluated the mean delay of CRV and ICP pulse velocity to 0.024s [209]. However, recent studies utilizing more sophisticated methods with proper measurement demonstrated different timing of SVP occurence: the venous diameter started to decrease at early diastole and reduction persisted until early systole [143, 153]. The synchronicity of IOP and SVP diameter pulse was also refuted. Vein collapse was recorded 40 ms (0.04 cardiac cycles) after IOP minimum [143] and the venous expansion occured 5 ms after IOP maximum [143]. SVP diameter pulsation are supposed to be in phase with intracranial pressure instead [220].

As both arteries and veins demonstrate pulsatile characters of the vessel caliber, flow and velocity, the researchers evaluated differences and delays. The venous collapse was reported 0.13-0.26 cardiac cycles after the minimum of arterial diameter occurence in study [99]; and 0.044 cardiac cycles in [219] which corresponded to 40 ms. However, the study methodology in [219] lacks due to low frame rate 25 fps that only alows to detect the temporal differences of 40 ms. Other study reported that arteriovenous delay in vessel caliber pulsation was reported 19+-4ms [294]. The

venous flow pulsation amplitude is lower in comparison to arterial flow pulsation amplitude [247, 325]. Arterial blood flow maximum corresponds to venous minimum flow.

Spontaneous venous pulsations are altering according to IOP, MAP and other factors described in the previous chapter. Georgevsky et al. demonstrated the postural effects on SVP diameter changes. Increased IOP, decreased SVP diameter amplitude and decreased MAP was reported in supine position in comparison to sitting positions. No significant change was reported during the change from supine to lateral decubitus positon.

1.2.1 Etiology behind the spontaneous venous pulsation

Veins generally do not pulsate in its diameter. However, due to lack of rigidity, their walls are so distensible that even a small change in pressure produces a significant change in diameter. Therefore, the veins may collapse under certain conditions due to their properties that correspond to Starling resistors (decribed previously, **Figure 1.6**). The venous collapse and SVP etiology in general is widely discussed, yet never fully understood. The physiological theories and mathematical models, trying to comprehend this phenomenon, covers several physiological variables - venous pressure, IOP, ICP, autoregulation mechanism, geometry and mechanical properties of lamina cribrosa sclaera and vessels.

Levine's CIVO model. Authors Jacks & Miller (2003) in their clinical study accepted theory of Levine's constant-inflow-variable-outflow (CIVO) model that explains the vein pulsation as a result of fluctuating intravascular pressure gradient between intraocular veins and retrolaminar CRV segment [124, 185, 186]. This theory rejected all previous explanations about SVP etiology and till now, remains the most accepted by the researchers in the field.

The theory covers CRV (its morphology and behaviour) in two surrounding environments - intraocular and retrolaminar, divided by lamina cribrosa sclaera. Intraocular space is characterized with IOP and retrolaminar space with CSFP originating from subarachnoidal space along the CRV in retrobulbar segment of ONH. Cerebrospinal fluid pressure is supposed to be of the same value as ICP. Both ICP and IOP fluctuates with the cardiac cycle in a different level, scale and with a different phase. All these pressure fluctuations are transmitted into the CRV. Regarding the mechanical properties of the capillaries, the inflow of blood into venules is supposed to be non-pulsatile and hence constant. Levine hypothesized that IOP never exceeds pressure in retinal veins. As an implication, IOP fluctuations are transmitted into intravenous pressure of retinal veins, yet never reverse transmural gradient. The hypothesis was in contradiction to previous theory [333] accepted

by many researchers [113, 184, 311] **Figure 1.8**. As a result, the blood flow and intravenous pressure in CRV is pulsatile at the exit of the eye bulb and fluctuates in 3 mmHg amplitude, the same as IOP. In retrolaminar area, the ICP fluctuations are transmitted to CRV so retrolaminar segment of CRV fluctuates in 1mmHg amplitude. This sudden change while crossing the lamina cribrosa sclaera results in pulsatile prelaminar-retrolaminar intravascular pressure gradient of 2 mmHg amplitude (when prelaminar intravenous pressure is 1 mmHg higher in systole and 1 mmHg lower in diastole than retrolaminar). Thus considering the constant inflow, the increased outflow during the systole causes CRV collapse. The mutual mechanism of intraocular-retrolaminar intravenous pressure gradient is described in the schema **Figure 1.9** [124]. [124, 185]

The venous system was modeled as semi-infinite cylindrical tube of constant radius with resistance and capacitance per unit length. The model supposed constant inflow and variable outflow represented with a Fourier series with a fundamental frequency equal to heart rate. According to model, the biggest diameter pulsation is in CRV at the exit point of retina and it is simulated with equation (**Equation 1.6**) based on pulsatile flow given with Fourier series, were f is heart rate, H_n is maximum value of the n-th harmonic of the flow, R is venous wall resistance to blood flow, C is venous capacitance, φ_n is a phase angle of n-th harmonics, x is the location on vessel where the pulsations are measured in time t. Venous radius r is oscillating about base value r_0. [185]

$$r^2(x,t) = r_0^2 - \frac{1}{2\pi^2 f}\sum_{n-1}^{\infty}\frac{H_n}{n}e^{x\sqrt{\pi n f RC}} \times \cos\{2\pi n f(t-\varphi_n) + x\sqrt{\pi n f RC}\} \quad (1.6)$$

Model demonstrated that the length of the pulsating segment decreases with increasing heart rate, venous resistance and capacitance. More, the amplitude of

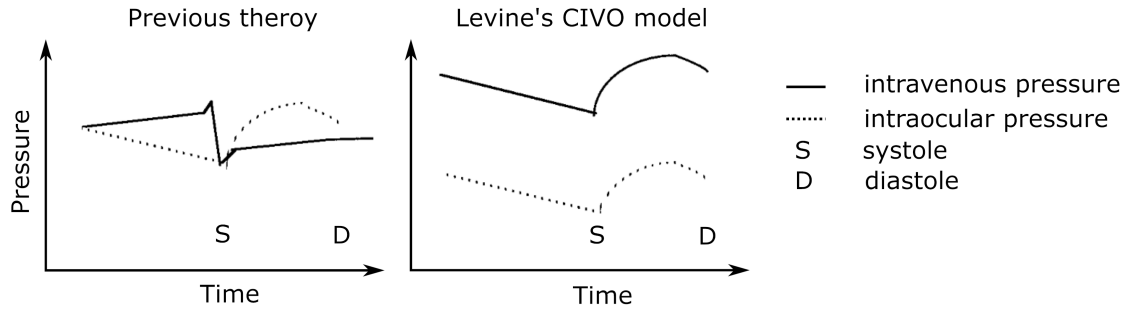

Fig. 1.8: Levine's CIVO hypothesis [185]. CIVO hypothesis suggests the intraocular pressure never exceeds intravenous pressure which is contrary to previous theory where the transmural gradient reverses during cardiac cycle.

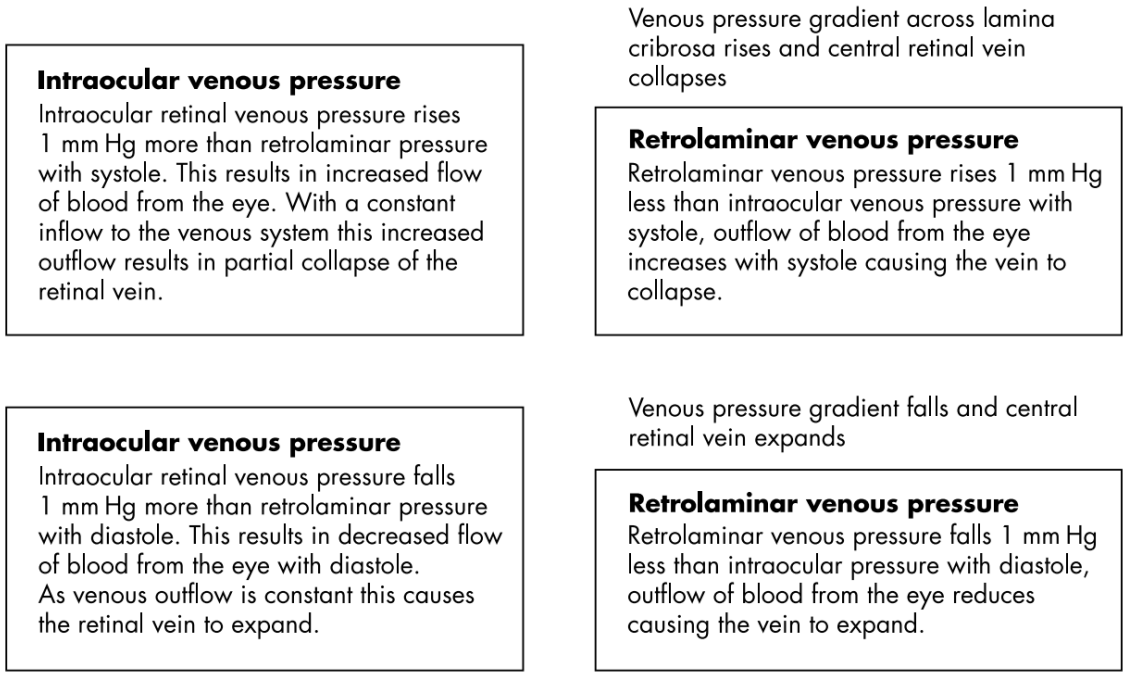

Fig. 1.9: Practical interpretation of Levine's CIVO model [124].

CRV diameter pulsation decreases with increasing heart rate as shown in (**Equation 1.6**). The diameter pulsation amplitude dependency to heart rate has been omitted factor in many basic clinical studies investigating SVP etiology and timing, yet heart rate could be the reason behind the diameter amplitude variability and overall contradictory results in SVP incidence. Additionally, implementation of heart rate as a factor in research studies,that link the SVP to various pathologies (glaucoma, ICP hypertension, etc.), has a potential to bring more accuracy to clinical evaluation and possible biomarker definitions.

Although Levine's theory offers rather a complex mathematical description of SVP etiology, the model does not cover all the possible factors influencing SVP.

Levine's extended CIVO model. Throughout the years, the timings of venous collapse, venous pressure and IOP pressure pulsations were questionable. More, the original CIVO theory and its results were often misinterpreted in other studies [220]. Therefore, Levine published extended CIVO model to clarify the phase relationship between IOP and venous collapse, and more, he extended this model with lamina cribrosa and retrobulbar segment of CRV. [186]

Levine demonstrated that both amplitude and phase of CSFP and IOP oscillations has significant impact on timing of the vein collapse and venous diameter oscillation in general **Figure 1.10**. Graphs in this figure demonstrate the diameter oscillation through one ocular cycle (0°-360°) regarding the phase difference between

IOP and CSFP (-60°-60°). Left graph shows the phase of venous diameter minima in case the CSFP amplitude exceeds IOP amplitude, and the right graph for the opposite case. [186]

Even through model extension, Levine admits the limits of the model as he did not consider the fact that resistance and capacitance changes with the vessel diameter. Moreover, the model of CRV in retrobulbar area is only a rough approximation as it is not clear how much the rigid surroundings may restrict the CRV to change its diameter.

Guidoboni's retinal blood flow model. Guidoboni et al. (2014), as first research group implemented retinal blood flow autoregulation mechanism with blood pressure as factors in the retinal hemodynamics and IOP model. The model uses hydraulic analogy to Ohm's law. The whole retinal system was modeled as a three-segment multicompartment Windkessel model **Figure 1.11** [124]. [100]

Subsequent compartments represent elements of retinal vessel system (CRA, arterioles, capillaries, venules, CRV) in three anatomical regions (intraocular, translaminar, retrobulbar). Each compartment includes resistors, capacitors - the resistors represents a resistance of vessel wall to blood flow and capacitors define the ability of vessel wall to dilate due to changing blood volume. Blood flow autoregulation mechanism, causing vasocontriction/vasodilation, was simulated through variable resistances. Input to this model is temporal waveform of the blood pressure and output is retinal blood flow and velocities in CRA, CRV and microvasculature.

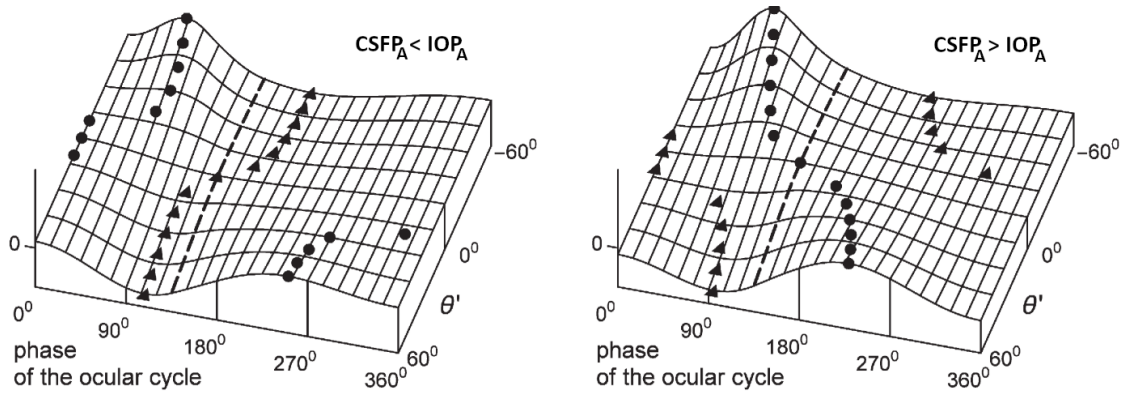

Fig. 1.10: The CRV diameter waveform through ocular cycle (0°-360°) as a function of phase difference between IOP and CSFP [186] for two cases - amplitude of CSFP is lower than IOP amplitude, and amplitude of CSFP exceeds IOP amplitude. The CRV diameter minima is marked as triangle, CRV diameter maxima is marked as circle. $CSFP_A$ - cerebrospinal fluid pressure amplitude, IOP_A - intraocular pressure amplitude.

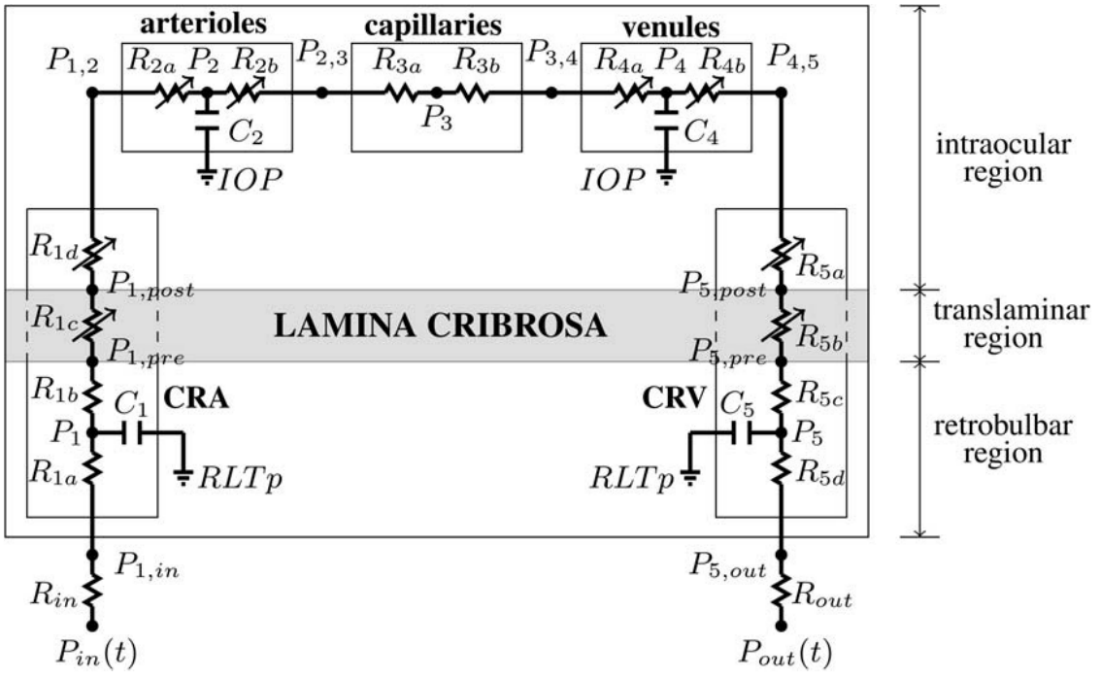

Fig. 1.11: Guidoboni's three-segment multicompartment Windkessel model [100].

[100]

The model was validated when calculated levels of velocities and flow followed the clinically measured values in healthy subjects. Model described the response of retinal blood flow to increasing IOP while active or absent autoregulation. More, model also demonstrated temporal waveform of intraluminal pressure pulse in each compartment for different levels of IOP. The intraluminal pressure base level and its pulsation amplitude decreased with each subsequent compartment, so the venous pressure demonstrated lowest base level and amplitude. With IOP increase, the resistance to blood flow increases, so the intraluminal pressure pulse increases too. This effect of increasing IOP is most significant in the veins due to its properties causing sensitivity to extravascular pressure changes. [100]

Although this model simulates blood flow pulsations and velocity, the cardiac cycle induced changes of venous diameter were not evaluated. The authors admitted the model is lacking due to limited number of compartments representing the retinal vasculature, and inaccurate description of lamina cribrosa geometry. Despite the limitations, this model is another step to better understanding of SVP etiology and its associations to disease as glaucoma, age-related macular degeneration and diabetes. [100]

Babbs model of retinal venous pulsations biomechanics. Ch. Babbs utilized three-segment Windkessel model similarly as the Guidoboni et al. and linked

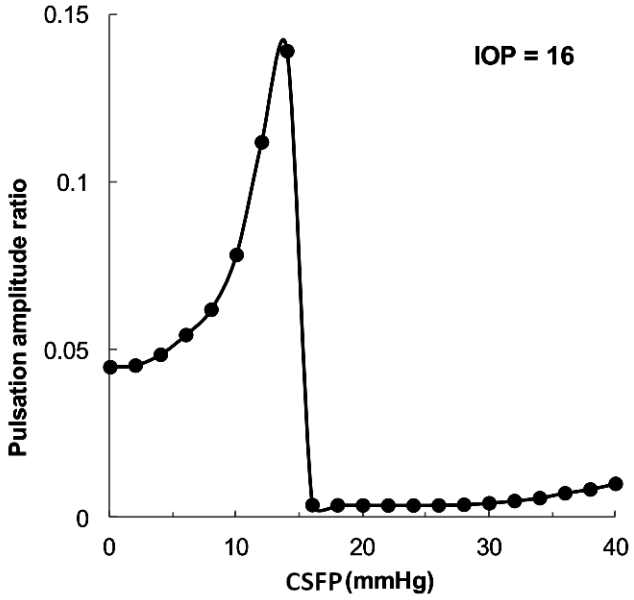

Fig. 1.12: CRV diameter pulsation amplitude as a function of CSFP in specific IOP level [11].

the SVP to intracranial pressure.

Still, Babbs included a few changes as the model considers resistance representing capillary bed in paralell connection. More, Ch. Babbs came up with innovating theory including non-linear compliance and bending deformation. Non-linear compliance is characteristic for veins while transmural pressure varies from positive to negative. Vessel is deforming from circular to oval shape in cross-section, i.e. flattening, while the transmural pressure reverse to negative. [11]

Babbs model uses values from Gray's anatomy as input values. The modelled fluctuations of flow, pressure, blood volume and diameter in each compartment is demonstrated for various conditions - active and disabled non-linear compliance, varying CSFP, IOP and venous pressure, varying arteriolar resistances. Pressure, flow and volume were in phase with arterial pressure. Compartment corresponding to CRV exiting the eyebulb demonstrated flattening and its diameter waveform shape indicated increased diameter with reduced blood volume. Interesting output is the graph describing the dependence of CRV pulsation amplitude on CSFP in specific IOP level **Figure 1.12**. The CRV pulsation amplitude is rising steeply till CSFP is almost equal to IOP. When CSFP is equal to IOP, the pulsation amplitude is minimal. Then, with increasing CSFP, the pulsation amplitude is slightly increasing again. [11] CRV diameter pulsation disappears when venous pressure is equal or exceeds CSFP.

Babbs model offers quite a complex solution while considering all the possible

variables and demonstrates its mutual relationships. However, Ch. Babbs did not demonstrated any influence of possible heart rate induced changes. As previous model, also Babb's model includes limited number of compartments and represents only a rough approximation of the whole retinal vascular system. Additionally, the lamina cribrosa geometry is not modelled accurately and the possible phase differences of CSFP and IOP are not discussed.

Jin's model. The importance of heart rate influence on ocular pulse and fundus pulsations is described in recent Jin's model. The model includes the mathematical descriptions of eye bulb tissues, i.e. sclera, choroid, neural tissue etc., which were previously described with other models. The main innovation is an implementation of a mathematical description of lamina cribrosa sclerae's viscoelastic properties. The viscoelastic properties were defined based on experimental measurements of seven porcine eyes. [131]

The model considers both IOP and CSFP baseline levels of 15 mmHg and 11.3 mmHg respectively and constant venous pressure of 15 mmHg. Ophthalmic artery pressure was considered pulsatile from 71-93 mmHg. The heart rate is changing in range 60-120 beat per minute (bpm) in order to explore its influence on ocular pulse amplitude, choroidal volume and ONH deformation. [131]

As a result, the ocular pulse amplitude and the pulse volume decreased with increasing heart rate by 0.04 mmHg (2.7%) and 0.13 μl (2.8%). Moreover, the model demonstrated pulsations of *lamina cribrosa sclerae* (**Figure 1.13a-c**) and fundus pulsations (particularly ONH and parapapillary retina anterior-posterior movements through cardiac cycle, **Figure 1.13d-f**). ONH pulsated in amplitude of 5.8 μm and decrerased by 0.1 μm for every 10 bpm heart rate increment (**Figure 1.13f**). The ONH displacement follows the measured ONH pulsations in Singh's study [290]. The model also demonstrated that lamina cribrosa is becoming stiffer with a higher heart rate. [131]

Although this model innovatively considers viscoelastic properties of *lamina cribrosa sclerae*, the model is simplified and omits pulsatility of the CSFP, and overall blood circulation over retina.

In summary, the dynamic phenomena of the retina as SVP or other pulsation are investigated for its diagnostic impact in various fields of medicine as described in the next section. To properly observe these pulsation phenomena and prove the hypothetical models, the various current and developing hardware tools along with data processing methods are utilized in research. The most common methods are described in the following sections.

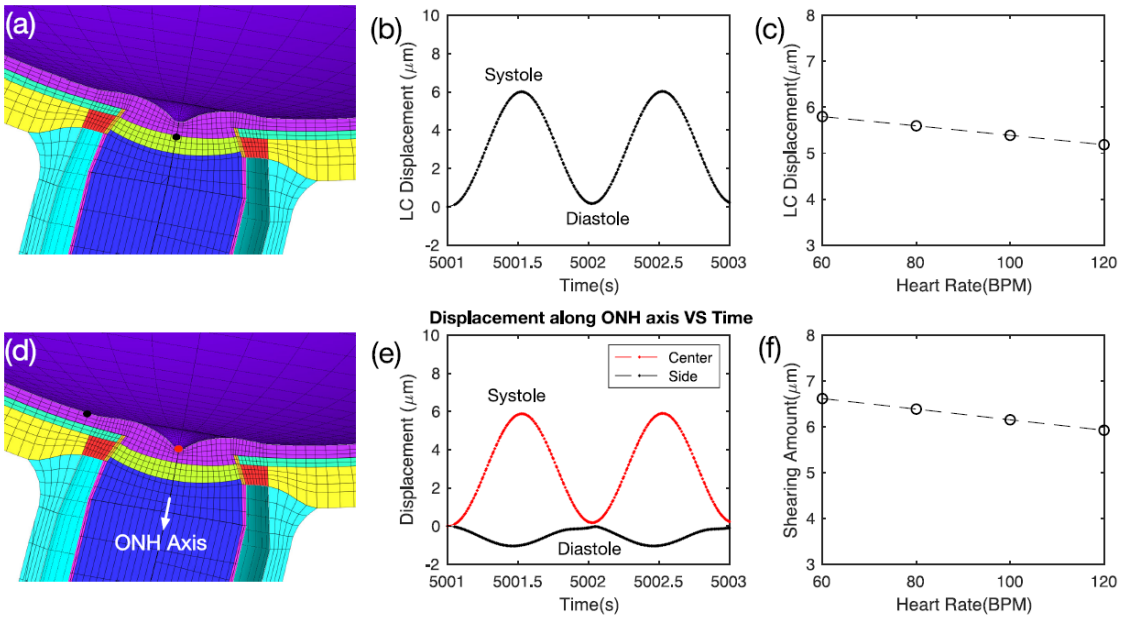

Fig. 1.13: Anterior-Posterior displacement of *lamina cribrosa sclerae* (a-c) and ONH (d-f) and its dependency on heart rate [131].

1.2.2 Clinical significance of retinal pulsation phenomena and biological factors influencing retinal pulsation phenomena

Clinically standard ophthalmology examinations focused on retina rely on both subjective observations and objective quantified markers. Clinically used biomarkers in opthalmology are mostly derived from a static 2D/3D image captured with either a standard fundus camera or optical coherence tomography. The marker examples are cup-to-disc ratio (C/D ratio), retinal neural fiber layer (RNFL) thickness and arteriolar caliber that are attributed with diagnosis of glaucoma. However, the static image cannot be used for detection of any abnormalities in retinal hemodynamics, which are important factors in development of ocular diseases such as glaucoma [93, 329], age related macular degeneration [221] and diabetic retinopathy [280], etc.

The pulsatility of ocular tissues and vessels, as a direct implication of periodic cardiac cycle induced hemodynamic changes, is potentially altered in response to different kinds of pathologies, i.e. local (glaucoma, age-related macular degeneration, giant cell arteritis), other pathologies (diabetes mellitus, carotid artery stenosis, Alzheimers disease, atherosclerosis), and to biological factors (age, sex). The following paragraphs describe the research findings linking the pulsation phenomena and various diseases, pathologies and biological factors.

Glaucoma. The hemodynamic changes, such as reduced ocular blood flow, were reported in glaucoma[75, 97, 283]. In addition, the reduction in pulsatile ocular

blood flow and pulse amplitude were observed in glaucoma [151, 282]. These findings indicate further potential changes in pulsatility of various ocular structures as both pulse amplitude and pulsatile ocular blood flow is highly correlated with FPA [274]. The association of retinal pulsation phenomena with glaucoma disease was proven in the following studies.

In 2012, Singh et al. focused on FPA in subjects with glaucoma disease. This research group measured the change in axial distance between the peripapillary retina and the base of the optic disc cup throughout the cardiac cycle. The significant increase in pulsatile change of the axial distance was measured in nasal part of glaucomatous patients in comparison to healthy subjects ($14.9\pm5.6\mu m$, $10.7\pm2.1\mu m$, respectively, $p = 0.03$).

The absence of SVPs in association with glaucoma was reported in [3, 178, 182, 218, 285]. In 2004, Morgan et al. evaluated prevalence of SVPs in 94 glaucoma patients, 105 glaucoma suspects and in 41 normal subjects to be 54%, 75% and 98% respectively [218]. In 2009, research group of U. Legler observed the presence/absence of SVPs in 352 healthy participants and 84 patients with chronic open-angle glaucoma and determined the prevalence 75.3% and 64.1% respectively [182]. In 2012, Seo at al. reported that SVPs are more frequently found in glaucoma suspects than in patients with primary open angle glaucoma (86.3% vs 53.3%, $p < 0.0001$) based on study including 229 glaucoma patients (primary open angle glaucoma) and 205 glaucoma suspects [285]. In 2013, Pinto et al. found SVP less prevalent in glaucoma patients including both normal tension and primary open angle glaucoma than in healthy subjects, i.e. 51%, 50% and 82% respectively [3]. In this study, the prevalence of SVPs' in normal tension glaucoma group decreased with increased glaucoma damage. Yet this statement did not apply to primary open angle glaucoma group. In 2017, Lee investigated also the presence/absence of SVPs in healthy participants and patients with unilateral primary open angle glaucoma with low IOP [178]. Lee reported the smaller prevalence of SVPs in glaucomatous eyes with 50.5% in comparison to healthy controls 81.7%. All in all, the SVPs' prevalence was lower in glaucoma patients in comparison to healthy controls in all mentioned studies [3, 178, 182, 218, 285]. Importantly, the evaluation of SVPs' presence/absence was done subjectively by observers in all these studies.

The SVPs' association to glaucoma is studied also in the work of S. Shariflou [287]. He evaluated the SVP's presence subjectively and reported SVPs' in 67% of glaucoma suspects and in 62% of glaucoma patients and the results are in agreement with the previous work with subjectively evaluated SVPs. However, he also run computer analysis that revealed the presence of SVPs' in 100% of participants (including both glaucoma suspects and glaucoma patients). The computer analysis quantified the average SVP amplitude to be larger in glaucoma patients than in glaucoma sub-

jects (43±10.7% vs 34±6.7%). [287] Also, this work reports that SVP's amplitude is correlated with the thickness of RNFL ($r = 0.49, p = 0.006$) proving the association of SVPs with neurodegenerative disease of glaucoma [287]. The SVP-RNFL correlation is also in agreement with previous study using the semi-automatic algorithm and objective SVP quantification [92] where Golzan et al. reported decreasing SVP amplitude with increasing RNFL loss. Golzan et al. also suggested the magnitude of SVP as an indicator of glaucoma severity [92].

Other diseases. The spontaneous venous pulsations in a form of diameter change are reported in up to 99% of healthy population. However, the prevalence of SVPs is significantly reduced in people with optic disc edema regardless the intraocular and intracranial pressure [204].

The direct association of IOP and SVPs is proven in study of J. Jonas [136], where Jonas used outside pressure on eye bulb to increase the IOP and consequently induce and enhance the SVP. The outside force measured with a pressure sensor enabled to determine vein collapse pressure in moment of SVP appearance [136]. This ophthalmodynamometric method was used in following studies linking the SVP with both local (optic disc excavation [13]) and other pathologies (such as thyroid-associated orbiopathy [139] and giant cell arteritis [137]). The study of J. Jonas [139] found the central retinal vein collapse pressure is higher in patients with thyroid-associated orbiopathy than in control group. The second study found a significant difference in central retinal artery collapse pressure between the patients with giant cell arteritis and patients with nonarteritic anterior ischaemic optic neuropathy [137]. These studies prove the importance of retinal hemodynamics along with its induced structural changes in neurological, neuro-ophthalmological and orbital diseases [139].

The SVPs are reported altered also in certain vascular pathologies - local (CRV occlusion [8, 56, 138, 140, 203]) and others (internal carotid artery stenosis [312]). Particularly, ophthalmodynamometric method of J. Jonas was used to differantiate the patients with CRV occlussion of ischemic type, patients with CRV occlussion of non-ischemic type, patients with branch retinal vein occlussion, patients with retinal venous stasis and healthy controls [138, 140]. J. Jonas reported the largest CRV pressure in patient group with CRV occlusion of ischemic type, followed by group with CRV occlusion of nonischemic type, group with branch retinal vein occlusion, and with control group with the lowest CRV pressure [138, 140]. In following study, McAllister indicates worsening prognosis of the CRV occlussion in patients with higher levels of retinal venous pressure [203]. Additionally, the study demonstrates a correlation of retinal venous pressure and worsening visual acuity [203]. In 2020, N. Arej observed the spontaneous retinal arterial pulsations in CRV occlusion via infrared video sequence of ONH. Arej reported higher best corrected visual acuity in patients with presence of retinal arterial pulsations, and indicated a faster recovery

for this patient group [8].

Not only local vascular pathologies are reflected in ocular pulsation phenomena. The studies indicates also the changes in ocular hemodynamics that resulted from the pathologies in vessels outside the eye bulb [154, 157, 191, 240, 312]. Particularly in patients with internal carotid stenosis, there is significantly lower peak systolic and end diastolic velocity in CRA and PCAr [312], significant perfusion changes in superficial vascular layer of retina [191], abnormalities in intraocular pressure and pulse amplitude [157, 240]. The direct proofs of influence of stenosis in vascular system outside the eye bulb towards the pulsation phenomena were presented in works of M. Rina [260] and R. Tornow [305]. M. Rina found changes in parameters describing the pulse waveform of blood flow in ONH vessels measured via laser speckle flowgraphy. Particularly the parameters, i.e. blowout time and blowout score, were significantly associated with mean intima-media thickness and plaque score of carotids internal and common [260]. In 2017, R. Tornow used custom-build video-ophthalmoscope [304] utilizing photoplethysmography to measure hemodynamic changes in ONH. The eyes in the patient with macroangiopathy and plaque of the carotid communis (both sides) demonstrated asymmetry in timing and waveform of pulses derived from outer rim area - the pulse in the left eye preceded pulse measured in the right eye (40 ms time difference) [305].

The worsening vascular condition affecting the ocular blood flow and associated retinal pulsation phenomena may originate also from another multi-systemic disorder - diabetes mellitus. It is known, the diabetes mellitus cause hardening of the arteries throughout the whole body and may progress into diabetic vascular disease and diabetic retinopathy. The alterations in retinal hemodynamics (blood flow velocity in CRV, blood flow in retinal microvasculature) were reported in patients with diabetic retionopathy [102, 229, 233]. In 1997, the reduced FPA was found in patients with proliferative diabetic retinopathy [278]. In 2013, the changes in retinal arterial pulsations (diameter oscillations) were observed in diabetic (type 2) patients via dynamic vessel analyzer [16]. The analysis revealed a reduction in high frequency oscillations of retinal arterial pulsations [16]. In 2021, the blood flow pulsatility ratio of retinal artery was reported significantly higher in patient with diabetes (type 2) receiving the insulin treatment than in patients with diabetes (type 2) without treatment [230].

Biological factors. One of the most important factors directly influencing pulsation phenomena is IOP. If the amplitude of IOP, i.e. ocular pulse amplitude, is higher than 1.2 mmHg, the SVPs are reported to be visible on fundoscopy [297]. Also, SVPs are changing with IOP level. Reduced IOP causes reduction in SVP amplitude, which was observed in IOP experiment with utilization of pharmacological intervention [89]. Additionally, the ling between IOP and SVP is proven via

ophthalmodynamometric method of J. Jonas mentioned previously [136]. via IOP manipulation experiment with utilization of pharmacological intervention

The main biological factor influencing the overall body is the age. Generally, the retinal vasculature demonstrates decrease in blood flow [63, 235], metabolic demands [235] and vascular autoregulation [129, 235] in elder population. Additionally, vascular compliance, stiffness and systemic vascular resistance changes with the age [83, 128, 175, 179, 194, 206]. This indicates the potential changes also in retinal pulsation phenomena. Kotliar et al. studied the retinal diameter pulse changes along the vessel axis via retinal vessel analyzer [165, 166]. Kotliar demonstrates the age-related changes in vessel response to flicker stimulation - less regular longitudinal vessel profiles were found in elder population [166]. In the next study, Kotliar found the pulse wave (vessel diameter change) is transferred through the vessel with a higher velocity in elders which indicates also lower vascular compliance [165]. The other connection between the vascular compliance and retinal vascular pulse (measured via modified photoplethysmography) was studied in work of Abdul-Rahman [2]. Additionally, N. Luft demonstrated the pulse waveform measured with laser speckle flowgraphy alters with age [196].

The another factor influencing overall body is the body position. It is known, that body position alters the systemic blood pressure and IOP values [146, 181, 202, 244]. Also, higher levels of ocular perfusion pressure were found in recumbent position in comparison to sitting position [146, 181]. Hence, the changes in retinal pulsation phenomena may be expected. The influence of postural effects on SVP were studied by D. Georgevsky. She demonstrated significant reduction in SVP amplitude from sitting to supine position [87].

The studies demonstrated higher pulsatile ocular blood flow in women [4, 151] which marks the gender as another potential biological factor influencing retinal pulsation phenomena. Besides gender, also body mass index may potentially affects the retinal pulsations, as R. Karadag found decreased ocular pulse amplitude in subjects with higher body mass index [147]. Yet, according to my knowledge, neither gender nor body mass index was inspected as a factor influencing the retinal pulsation phenomena.

ICP predictor. The alteration or disappearance of SVPs due to elevated ICP [11, 27, 91, 90, 124, 220, 335] has been a known physical diagnostic finding for many years. In theory, SVPs originate from a varying pressure gradient between the intraocular space and cerebrospinal fluid (CSF) [90, 124, 185]. Both intraocular and intracranial pressures affect retinal vessel hemodynamics. The central retinal vein collapses when intraocular pressure (IOP) is higher than the venous outflow pressure, i.e., the pressure within the optic nerve. Then, the central retinal pulsatility (i.e., SVPs) is clearly visible if the IOP and venous outflow pressure are equal. In case

of higher venous outflow pressure, the pulsatility disappears [341]. SVPs' absence, or a change from presence to absence, can indicate elevated ICP [46, 124] Yet, the empirical relationship between continuous SVPs and ICP waveforms is currently not fully explored [124, 184, 335, 341].

Pitfalls of state of the art of clinical significance. The retinal pulsation phenomena has a tremendous potential in a diagnostic field of ophthalmology, neurology, cardiology and endocrinology. However, the biological factors and its influence must be identified properly prior any utilization in diagnostics. As there is no standard in retinal function imaging and parametrization, the essential identification of biological factors along with its influence on extracted parameters remain unexplored. In focus on ophthalmoscopic methodology, there is no study demonstrating the influence of the age on the amplitude of vessel pulsation in retina, despite Kotliar's studies demonstrated the changes in pulse wave propagation. And, the increase of stiffness in elders indirectly indicates the altered reaction to cardiac induced changes of blood volume. Hence the factor of age and its impact is not fully investigated yet.

As age has a serious impact on overall body condition, it also changes the mechanism maintaining the cardiac output of an individual. It was found that the increased cardiac output in elders is achieved with a lower heart rate and higher stroke volume [266]. In other words, the higher heart rate allows less time for ventricle to fill, hence the stroke volume is reduced. This information reflects the Frank-Starling law. In focus on ophthalmoscopy and retinal vessels, the changes in amplitudes of vessel pulses with the heart rate are expected. Levine in his CIVO models included heart rate as a factor impacting the SVP amplitude [185, 186]. And yet, heart rate has remained to be omitted factor in clinical studies.

1.3 Functional Retina Imaging and Ocular Hemodynamic Assessment

The retinal hemodynamics and its changes has tremendous potential in diagnostics of various diseases. Except for the opththalmology diagnostics (CRA occlusion, diabetic retinopathy, glaucoma), the hemodynamic changes in retina reflects also neudegenerative diseases (Alzheimer disease, multiple sclerosis, stroke) or cardiovascular diseases and pathologies (coronary heart disease, hypertension, diabetes and higher arterial stiffness).

The potential of functional retinal imaging exceeds the potential of classic single photography as the additional temporal dimension may provide the information about blood flow, velocity, and overall vascular condition. Additionaly, in combina-

tion with the further stimuli, dynamic retinal imaging is revealing the deeper view into neurovascular coupling mechanism.

Continuous temporal measurements of ocular hemodynamics revealed pulsation characteristics of its specific features, such as blood flow, red blood cell velocity, etc. These pulsations imply also blood concentration and structural changes, i.e., vessel caliber changes detectable mainly via dynamic recordings of e.g. ophthalmoscopy-/OCT-based methods.

Throughout last two decades, there were attempts to assemble tool covering ocular hemodynamics and retinal pulsation phenomena, i.e. the temporal structural, volumentric and blood concentration changes, through various different kinds of techniques. Examples of such devices focusing on retinal pulsation phenomena are commercially available ophthalmoscopy-based retinal/dynamic vessel analyzer (RVA/DVA, Jena, Germany), XyCam (Vasoptic Medical, Inc., Baltimore, USA) and OCT-based HRA+SLO (Heilderberg Spectralis, Heidelberg, Germany), or custom-built ophthalmoscopy-based prototypes including experimental ophthalmoscope developed in colaboration of Alexander-Fridrich University (Erlangen, Germany) and Brno University of Technology (Brno, Czech Republic) closely described in following chapter.

Yet no technique is considered as a gold standard for functional retinal imaging and overall hemodynamics assessment [75, 196].

In the next chapters, the methodologies assessing ocular hemodynamics and retinal pulsation phenomena manifesting in certain retinal pulsatile patterns (RPP) will be introduced from the oldest - ophthalmoscopy-based techniques to newer interferometry-based methods and their various combinations.

1.3.1 Ophthalmoscopy based methods

Ophthalmoscopy-based methods are the oldest techniques for retina examination and hemodynamic observation. Till now, the ophthalmoscopic methods remained the most commonly used in clinical ophthalmology either in their upgraded forms or in combinations with other methodologies based on different principles (e.g. Doppler effect).

The first attempts of ocular hemodynamics assesment started already in the fifties of 19th century, when Coccius as first observed SVPs while using the first direct ophthalmoscope. [113, 124, 185]

Nowadays, there are various forms of the direct and indirect ophthalmoscopes, slit lamps, fundus cameras, scanning laser ophthalmoscopes, and other advanced ophthalmoscopy-based tools providing a direct observation, digitalized single image or even an image sequence with a dynamic information about retinal structure.

Angiographic imaging. In late 50s and 60s, ophthalmoscopic methods while contrast dye administration (fluorescein angiography, indocyanine green angiography) defined angiographic imaging of ocular hemodynamics and structure [110, 115, 250]. For the objective assessment of retinal hemodynamics, arterio-venous delay and mean circulation time were defined as parameters. However, the term *objective* is not accurate as the observer subjectively assessed the time-points to mark down and calculate the parameters.

With technical development, the angiographic imaging was combined with video-recording devices which enabled further data analysis through image processing, and hence proper quantitative evaluation of the parameters. More, commonly used classic fundus cameras or slit lamps yielded scanning laser ophthalmoscopes (SLOs) enhancing image contrast, temporal and spatial resolution.

The combination of SLO and angiography methods was popular for ocular hemodynamic studies in 90s [74, 334]. However, the imaging methodology is invasive as pupil dilation and dye injections are needed. More, the interpretation of the results is difficult. The angiographic methods using SLO to assess the hemodynamics are used till the present. Commercially available SLOs covers operating modes for various needs of angiography imaging, and also other operating modes for non-invasive static/dynamic imaging.

Scanning laser ophthalmoscope. Scanning laser ophthalmoscope (SLO) was introduced already in early 80s [326]. Unlike the classic slit lamp or a fundus camera acquiring the whole image of the retina at one time, this electro-optical imaging device uses a high collimated laser beam scanning retina point by point.

To compare both principles in more detail, fundus cameras use the majority of the aperture area, i.e. pupil, for light entry and only a small part for the exit of reflected light. The utilization of the high collimated laser beam yielded a revolutionary concept of inverted ratio of entering and exiting light. Hence, SLO uses only a small, 0.5 mm^2, area for entering beam and the rest, cca 49 mm^2 of the dilated pupil, for the reflected light to exit. The laser beam scans the retina in a raster pattern 'point by point' illuminating only 20 μm diameter spot at one time. The laser beam is moved by two mirrors mounted on galvanometers - with frequency of 60 Hz vertically and 7875 Hz horizontally. The total retinal irradiance was limited to 50 μW. As a result, the retina was illuminated with much smaller light levels with SLO than with concurrent devices. More, the output image reduced the reflections and light scattering commonly presented in concurrent devices. [326]

The examples of commercial SLO devices using SLO are F10 SLO (Nidec, Inc., San Jose, California, USA), Spectralis series products - Heidelberg Retinal Angiography (HRA), Heidelberg Retinal Tomography (HRT), HRT+OCT (Heidelberg Engineering, Heidelberg, Germany), etc. All SLO devices work in various modes

and operate in specific wavelengths accordingly. In angiography imaging mode, the shorter wavelengths (blue, cca 500 nm) are used to excite the fluorescence. Generally used wavelength for retinal vessel imaging is 550-640 nm, and 640 nm and higher wavelengths are the most convenient for imaging of deeper retinal layers.

Most commonly used device in research of retinal hemodynamics, and spontaneous venous pulsation in particular, is Spectralis HRA, used in [153, 215, 285, 325]. All noted studies used near-infrared imaging (820 nm), 8-10 fps, 5-20 s of acquisition time, resolution up to 768x768 px in 15° field of view. Wartak et al. utilized SLO for analysis of both vessel diameter and intensity fluctuations (**Figure 1.14**) and compared the time-courses and the peak timing with OCT measurements as described in the following paragraphs focused on OCT.

Although Spectralis HRA in a simple SLO mode has a potential in static retinal imaging, in dynamic imaging lacks in frame rate for proper dynamic analysis. In [285], authors admits limited frame rate that had to be compensated with interpolation method. More, Kotliar et al. stated that even frame rate of 25 fps is insufficient for research of retinal pulsation phenomena and its timings [165]. Additionally, the tool includes no further software for following detailed dynamic analyses. Therefore, mainly clinicians struggles in evaluation of retinal pulsation phenomena and uses subjective evaluation methods (e.g. [45, 285]).

Retinal vessel analyzer. Retinal vessel analyzer (RVA) (Imedos, Jena, Germany), also called dynamic vessel analyzer (DVA), is a fundus camera based system with a vessel tracking software providing video-recording of retinal hemodynamics along with a semiautomatic detection and analysis of retinal vessel diameter.

The system was introduced in 2002 [284] and it is the most common hardware used for detection and analysis of retinal blood vessel pulsations in research of various pathological conditions (glaucoma, diabetic retinopathy, Alzheimer's disease, etc.).

The overall RVA/DVA design is demonstrated in the **Figure 1.15A**. The system is based on fundus camera (Zeiss Jena, Germany), halogen bulb as the source of illumination, and a computational unit for the analysis. Inserted filter in illumination pathway transmits only the green light close to 500 nm which creates the optimal contrast of the erythrocytes in vessel lumen and surrounding tissues (according to extiction coefficients for oxy/deoxy hemoglobin **Figure 1.21 A**).

The main principle of the RVA/DVA is that the hemoglobin absorbs the wavelengths in range of 400-620 nm while the surrounding tissues are more reflective to this light. Therefore the light detected on fundus camera CCD detector includes mostly the reflected light of the surrounding tissues, and the resulted brightness profile of the vessel column is demonstrated in **Figure 1.15B**. In reality, the brightness profile is not ideal due to reflections on the vessel surface or shadowing structures.

The included algorithm is monitoring the image quality and vessel atributes to

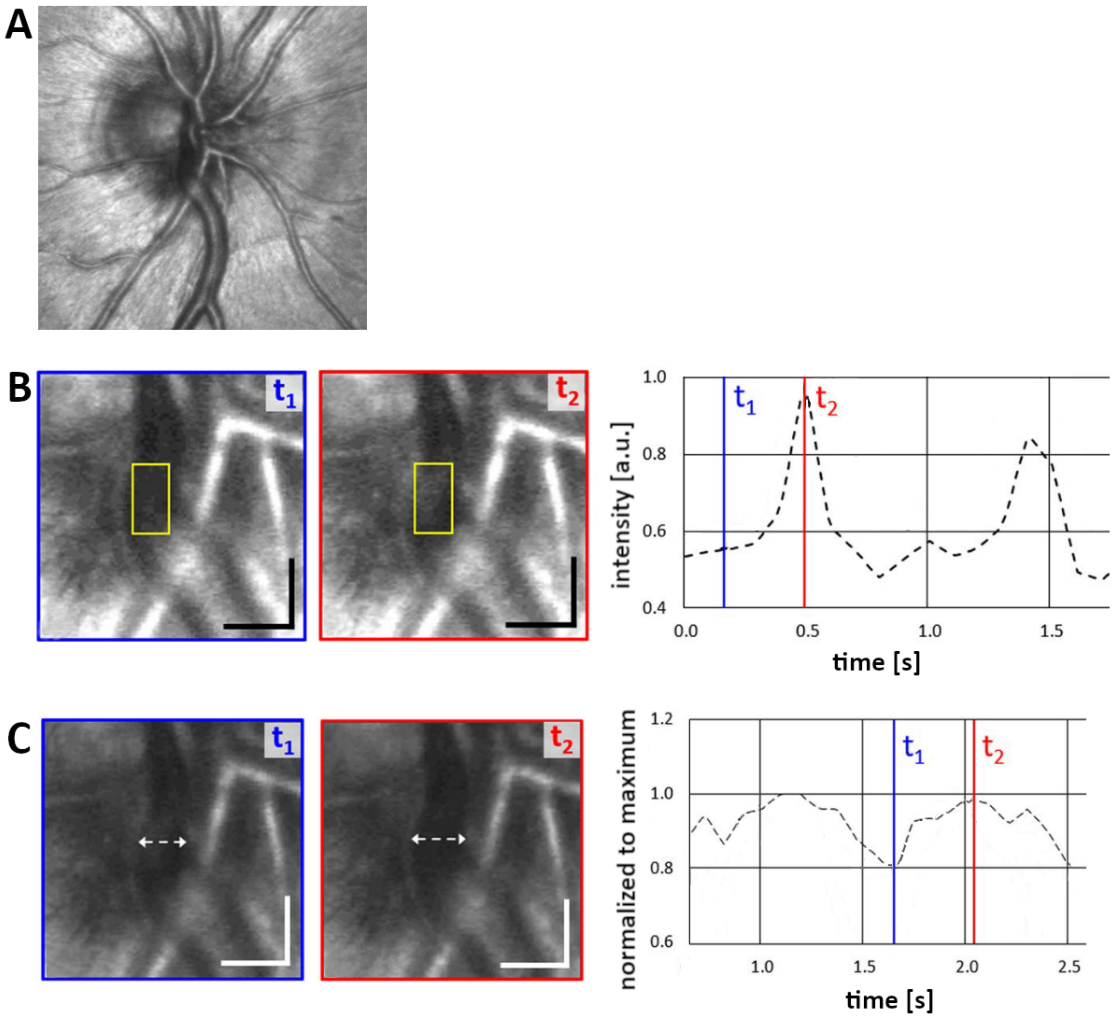

Fig. 1.14: Analysis of Scanning Laser Ophthalmoscope (SLO) video-recording. **A,** Image acquired with SLO **B,** Intensity fluctuations extracted from selected area (vessel) in SLO video-recording **C,** Transversal vessel diameter fluctuations extracted from selected vessel in SLO video-recording. [325]

ensure the correct measurement and results. The algorithm provides the temporal measurements of the vessel diameter in a manually selected fundus area. Once selected, the repeated measurements are evaluated automatically. For the best results, the area for vessel analysis is designated in range of one to two diameters from ONH. The analysis of the vessel diameter is limited to vessels of diameter $> 90\ \mu m$. Also the selected region of interest cannot include two vessels close to each other as the system cannot distinguish them as two separate vessels [85]. Additionally, the RVA requires administration of mydriasis, i.e., eye drops for pupil dilatation.

RVA provides the possibility of flicker stimulation. Flicker stimulation induces

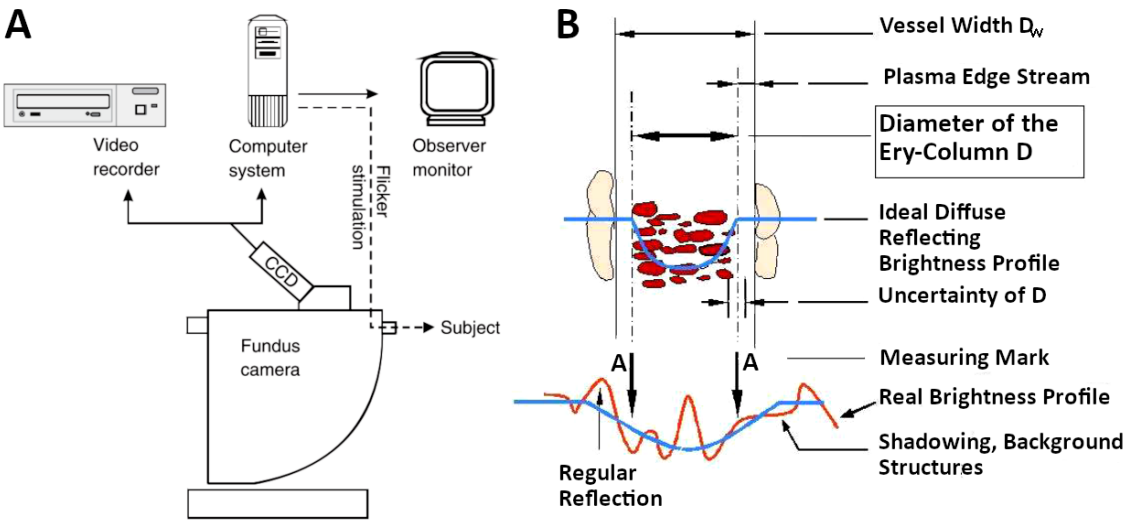

Fig. 1.15: Retinal vessel analyzer. **A,** Design of RVA [85] **B,** Principle of RVA [284].

a vascular dilatation that is altered in various pathological conditions, such as glaucoma [84, 98], diabetes and diabetic retinopathy [176, 189] and Alzheimer's [164, 249], and may lead to neurovascular coupling clarification [324]. The flicker stimulator included in RVA system is based on the optoelectronic shutter device which interrupts illumination generated by fundus camera. The stimulation is set to 12.5 Hz.

Except for the flicker stimulation, the system includes also the interface for synchronized recording of finger pulse plethysmography and electrocardiogram.

For overall summary of presented technical parameters, the video-recordings of the fundus is acquired with 25 fps, measuring resolution $< 1\ \mu m$ and image resolution 10 um in field of view 40°. The examination time is limited up to 10 min.

Retinal vessel analysis applied in healthy subjects reveals correlation of blood velocity and flow with retinal vesssel diameters. [86] Additionally, pulse wave velocity (expressed in mm/s) may be derived. RVA/DVA analyzers are used for observation of both retinal arterial pulsations and spontaneous venous pulsations [89, 91, 92, 165]. The example of the RVA/DVA application and following analysis is demonstrated in **Figure 1.16**

Laser Speckle Imaging (LSI methods). Another way of ocular (retinal and ONH) circulation estimation is via laser speckle imaging methods (LSI) [51, 196, 253, 298]. The general principle of this methodology was introduced already in 1981 when the red blood cells (RBCs) velocity distribution was presented using means of laser speckle photography [73, 196]. The methodology has developed into LSI as known today and represents another way of dynamic retinal imaging. The

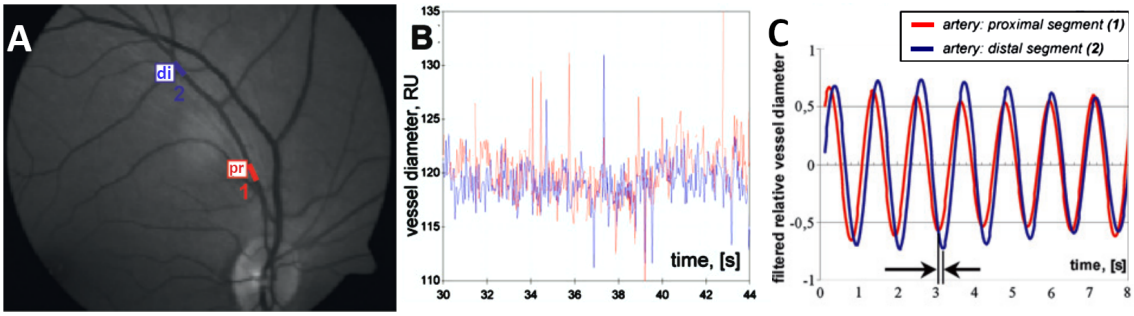

Fig. 1.16: Use of retinal vessel analyzer. **A,** Proximal and distal segments of the retinal artery selected for analysis **B,** Time-courses of vessel diameter measured in relative units (RU) **C,** Filtred time-courses (representative example of healthy young subject) [165].

methodology uses infrared coherent light (approximately 650-830 nm, emitted by a laser) [196, 298] that scatters on diffusing surfaces. The scattered light forms a speckle pattern whose contrast fluctuates according to velocity of moving particles (e.g. blood components as RBCs) in specific location and time. The speckle pattern fluctuations are evaluated statistically only. Derived descriptive parameters are mean and standard deviation of the intensity distribution of a speckle pattern, ratio of standard deviation of the intensity distribution of a speckle pattern to mean intensity of spatio-temporal neighborhood, normalized blur and square blur ratio, where mean blur rate represents relative value of blood flow velocity, normalized blur correlates with blood flow ratio in ONH and retina and square blur ratio represents an information about blood velocity [196, 298]. Thus, LSI generally provides values of the blood velocity in arbitary units only. The link of the output descriptive parameters and absolute values of velocity was established by correlations of outputs with directly measured values via invasive methods - microsphere method, hydrogen gas clearence method [300, 314].

Examples of commercially available devices are LSFG-NAVI (SoftwareCo., Ltd., Fukuoka, Japan) [196] and recently introduced XyCam (Vasoptic Medical, Inc., Baltimore, USA) [44, 51, 145, 252, 253]. Both devices provide dynamic recording of retina up to 5 s long through the dilated pupil. LSFG-NAVI system, more common in Japan, provides 4 s acquisition time with framerate 30 fps, image resolution 750 x 360 px for field of view 30° or 45° ($\sim$ 1.06 x 1.06 mm or 0.72 x 0.72 mm) [196, 298]. The primary evaluated parameter is mean blur rate (expressed in arbitary units) which represents blood flow velocity. The software of the commercial device quantifies the parameters describing the shapes of mean blur rate waveform. In comparison to LSFG NAVI system, XyCam evaluates blood velocity based on laser

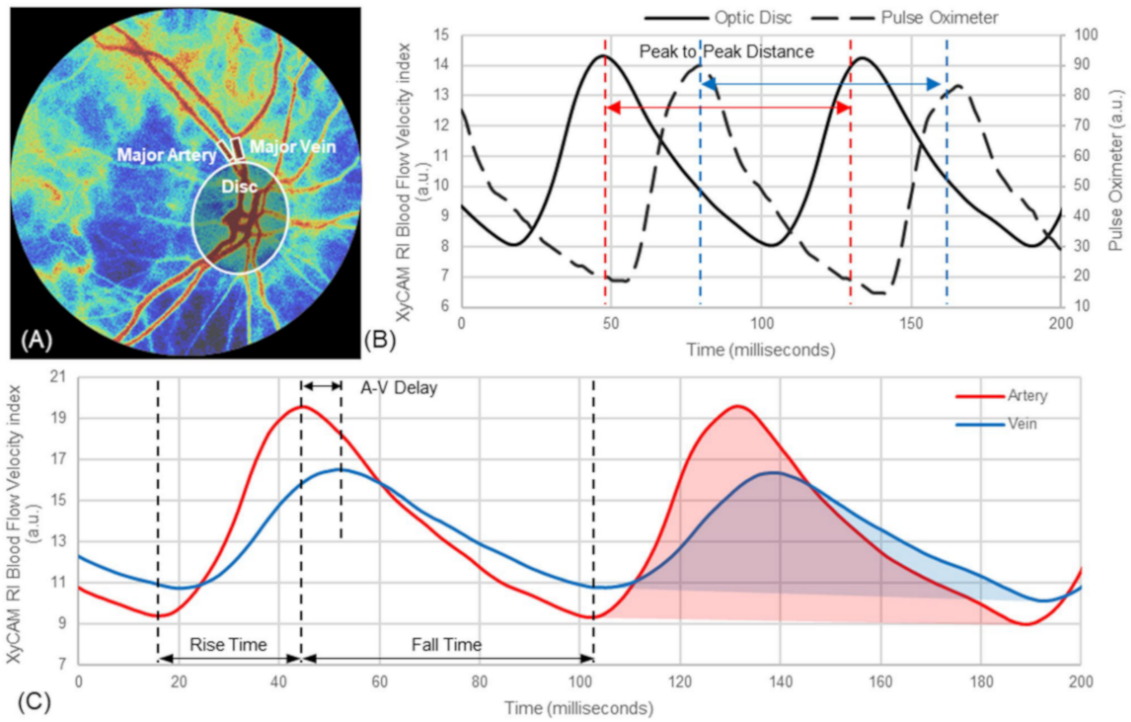

Fig. 1.17: Retinal hemodynamics analyzed with XyCam (LSI method). **A,** Blood flow velocity map covering the fundus **B,** Blood flow velocity time-courses (in arbitary units) of OD compared to finger pulse oximeter **C,** Blood flow velocity time-courses extracted from selected locations of the artery and vein. [37]

speckle contrast, i.e., standard deviation of intensity distribution to intensity mean of spatio-temporal neighborhood [51, 253]. The XyCam system emits light of laser wavelength of 650 nm and CMOS camera detects 120 speckle images at a framerate >60 fps from field of view of 20° [253]. The advantage of the device is in its size, device can be used as handheld or attached to a slit lamp base. XyCam can be connected to finger pulse oximeter and the software monitors, and evaluates the pulsatile time-course of the blood flow in selected location (i.e., artery, vein, the whole optic disc) **Figure 1.17** [37, 51, 145]. However, the main disadvantage of both LSI devices is the evaluation of blood velocity in arbitary units.

Retinal function imager. The retinal function imager (RFI) is based on principle of functional optical imaging of neocortex, widely used in brain research [95]. Research group of A. Grinvald applied this principle to retina and in 2004 the newly developed RFI (Optical Imaging Ltd., Rehovot, Israel) was introduced [94]. This fundus camera-based system is focused mostly on retinal microvasculature imaging [313]. As RFI covers also the retinal functional imaging, RFI maps the blood flow velocities in retinal vessels including the capillaries of 5 μm in diameter.

Additionally, RFI is referred to measure oximetry and metabolic function of retina.

RFI utilizes adjusted fundus camera with a stroboscopic light source generating the flashes at 100 Hz and providing continuous illumination of 75 W. RFI is operating at four different wavelengths switching with a fast filter wheel according to imaging protocols and resulted images are acquired with high-speed digital camera. The imaging parameter of the introduced device in 2004 are as followed: resolution 1024 x 1024, one pixel corresponding to 2-20 μm, field of view 6° - 60°, four optional wavelength in range 450-1100 nm, frame rate up to 50 Hz in full resolution and up to 100 Hz in binned. [94] Nowadays, RFI system is distributed as systems with various fields of view (20°, 35°, or 50° corresponding to 4.3 x 4.3 mm^2, 7.3 x 7.3 mm^2, 10.4 x 10.4 mm^2) [313]. The current base construction is the same as introduced, only software is still continuously improving.

At first, the device included the manual drawing tool to mark the analyzed vessels [36]. Throughout the years, the improvements in rapid automatic processing and blood velocity measurements were done with new algorithms. Since 2016, the software is able of automatic frame alignment, generates vessel topography maps with differentiated arteries and veins and precisely measures vessels diameter [313].The only limitation of RFI is that it cannot distinguish the vascular beds (i.e. retina and choroid) where the vessel originates.

The RFI provides dynamic imaging as the standard measurement captures the sequence of eight images with a mean exposition time of 1 ms and 10-20 ms apart, which creates a video record of 0.122s. RFI detects RBCs in each frame and subsequent image processing determine the local flow velocity as the ratio of traveled distance of RBC between frames and time difference. Resulted image with mapped flow velocities is shown in **Figure 1.18**.

Although the RFI provides dynamic recording of the retinal hemodynamics, the recording is too short for the overall evaluation of retinal pulsations (velocity fluctuations in particular) induced by cardiac cycle. However, these velocity fluctuations are considered in the overall assessment as RFI monitors possible impacts of the pulsation phenomenon with synchronized acquisition of cardiac cycle through a probe (finger/earlobe) while hemodynamics mapping [94, 313]. Therefore the RFI is suitable mainly for microcirculation mapping (as demonstrated in 1.18).

The imaging of detailed retinal vasculature and blood flow velocity mapping is important for early diagnostics therefore RFI was utilized in research of various diseases as diabetic retinopathy, age related macular degeneration or glaucoma, etc. [28, 29, 228]

Other customized devices. Various commercial devices do not meet the demands of researchers. Therefore the researchers come up with various principle-based devices used for retinal pulsation phenomena observations. Regarding oph-

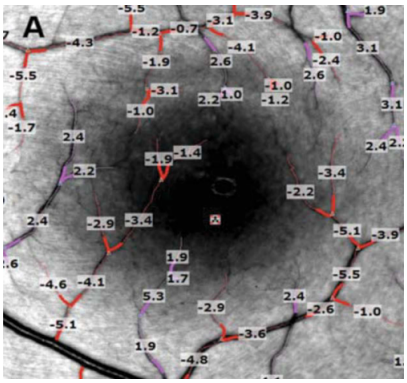

Fig. 1.18: Blood flow velocity map assessed by RFI in macular area [302].

thalmoscopy, Morgan et al.[217, 219, 220], Moret et al.[215]. The most of these devices utilize the commercially available imaging device used for retina in combination with a recording device.

Tablet-based ophthalmoscope. The research group of M. Golzan introduced a new low-cost video-ophthalmoscope in 2020 [287]. The ophthalmoscope can be used in combination of tablet camera (within iOS operating system). The introduced ophthalmoscope requires administration of mydriatic drops a provides the video recording of 30 fps, 77 μm/pixel resolution and 46° field of view. The subsequent off-line analysis in ImageJ uses the green channel only to measure diameter of manually selected vessel. The data processing and diameter variations evaluation were performed in Excel.

Another customized device introduced in 2015 - video-ophthalmoscope [303] (that is in main interest of this chapter) will be fully described later in this chapter.

1.3.2 Doppler Based methods

Commonly used methods for hemodynamic assessment of large retinal vessels, ONH microvasculature and submacular choriocapillaris, are based on Doppler effect (both optical and acoustic). Optical Doppler effect describes the frequency shift induced by a reflection of coherent light from moving particles in the tissue. Detected spectrum of coherent light beam scattered and reflected by a static nonchangeble surface remains the same, while spectrum of the coherent light beam reflected by moving particles broadens. The spectrum of the scattered light is called Doppler shift power spectrum. In application to retinal hemodynamics, the moving particles are RBCs in the vessels and vascularized tissue. Basic Doppler-based methods are laser Doppler velocimetry [262, 265] and laser Doppler flowmetry (single-point Doppler flowmetry, scanning laser Doppler flowmetry) [24, 207, 208, 264].

Doppler flowmetry. The Doppler flowmetry uses optical Doppler effect. As noted previously, the spectrum of the coherent light beams broadens when scattered and reflected by a perfused tissue while spectrum of the coherent light reflected by other tissue (i.e. vessel walls) remains unchanged and serves as a reference. The width of the spectra depends on the velocity of moving particles and also on the angles between the velocity vectors of the moving particles and light propagation vector. As a result, the Doppler shift corresponds to the flow, fraction power of the Doppler shift to volume and velocity is calculated as a ratio of flow and volume. [208]

The Doppler flowmetry principle was utilized in several no longer commercially available devices including Canon Laser Blood Flowmeter, Laser Doppler Flowmeter and Scanning Laser Flowmeter.

The Doppler-based methods can be also combined with scanning laser ophthalmoscope [24, 207, 208]. This combination provides more accurate assessment of blood flow, as the calculation is not based on standard mean value of vessel diameter but utilization of SLO enables to calculate the blood flow based on a measured individual's vessel diameter. Commercially available device combining Doppler flowmetry and confocal scanning laser tomograph is Heidelberg Retinal Flowmeter (HRF; Heidelberg GmbH, Heidelberg, Germany). This laser scanning retinal flowmeter scanned the retina with parameters field of view 10°, 2.7mm x 0.7 mm with a spatial resolution 10 μm, i.e., area of 256 x 64 px. [208].

The effect of cardiac cycle on scanning laser Doppler flowmetry measurements was demonstrated in work of Sullivan et al. while using HRF [299]

Doppler sonography. The Doppler effect is not limited to coherent light but also applies to wave phenomena in general, i.e. to acoustic waves.

Doppler sonography uses acoustic Doppler effect to quantify blood velocities (both peak systolic and end-diastolic) and resistivity indexes in retrobulbar vessels, including central retinal artery, posterior ciliary arteries and ophthalmic artery. Doppler sonography evaluates the Doppler shift in frequency of reflected sound waves. Sonographic B-scans provides the image of ocular anatomy. This methodology includes a Doppler probe that is applied on the closed eyelid. Thus the probe is stressing the eye leading to elevated IOP and improper measurement. Insufficient resolution does not allow to measure the retrobulbar vessel diameters and so the measurement of volumentric blood flow is not possible. [327]

The examples of sonographic devices applicable to retina were Color Doppler Imaging device (Siemens Quantum 2000 system, Siemens, Munich, Germany) and Doppler sonography device (Trancraniell Doppler, EME, Uberlingen, Germany). [107, 209]

1.3.3 Interferometry based methods

The basics of interferometry-based methods were introduced in late 80s and originally were utilized to measure axial lenght of the eye [72]. In 1991 first optical coherence tomograph was introduced [118]. Since then, many commercial and in-house OCTs were assembled. Regarding ocular hemodynamics, Schmetterer et al. were ones of the first focusing on ocular pulsations while laser interferometry utilization [274, 276, 277, 278, 279].

Laser interferometry. Since 1995, group of L. Schmetterer was focused on observation of fundus pulsations via laser interferometry [274, 276, 277, 278, 279]. This methodology was one of the first non-invasive methods estimating pulsatile ocular blood flow. Laser interferometry measures fundus pulsation amplitude which is a maximum distance between cornea and retina.

The methodology uses modified pulsation interferometer connected to a fundus camera. Laser beam of high coherence length (wavelength 783 nm, power of 50-80 μW, beam diameter 1 mm) [276, 278, 279] is partially reflected in cornea and partially in retina. The light reflected from cornea serves as a reference wave. The both reflected waves form interferences which are detected with CCD detector. The mutual distance alterations between cornea and retina are derived from interferograms. The connection of the device to a fundus camera secures the visual inspection of the measurement point (which is approximatelly 20-50 μm in diameter) [276].

To compare laser interferometry with the older methods focusing on pulsatile character of ocular hemodynamics, i.e., pneumotonometry, the output parameters of the both methods (i.e. pulse amplitude and fundus pulsation amplitude FPA) strongly correlates. The disadvantage of both methods is that they evaluate pulsatile ocular blood flow only, not the total volumentric blood flow.

Spectral domain low-coherence interferometry (SD-LCI). K. Singh et al introduced (SD-LCI) approach that represents a custom-build SD-OCT system to measure ocular pulsatility changes and FPA [289, 290, 291]. This methodology overcomes the previous work of Schmetterer [276, 278, 279] as it increased the displacement precision and acquisition speed to 100 Hz and 40 nm respectively. Additionally, in comparison to laser interferometry, the SD-LCI can simultaneously measure the displacements of each ocular layer separately and distinguish their directions.

Similarly as laser interferometry, SD-LCI method is based on Michaelson interferometry. In this case, the interferometer is connected to superluminiscent diode generating coherent light beam of shorter wavelenghts than previous technique to enable better precision in depth resolution. The beam is splitted into two arms, sample and reference. The outer part of the sample beam is focused in cornea while

central part is focused on retina. This configuration enables simultaneous measurement of amplitude and direction of the corneal and retinal displacement. [290, 291]

This SD-LCI technique was utilized to measure pulsatility changes in glaucoma with acquisition parameters of 7μm of depth resolution and 40 fps. In application on human subjects, the spectral analysis of pulsatile movements of retina reveiled the presence of fundamental frequency of the heart rate and more, its harmonics (up to seven)[290, 291].

Optical Coherence tomography (OCT) methods. Optical coherence tomography is a non-invasive method for three dimensional eye imaging commonly used in clinical practice and research for monitoring various eye diseases (e.g. glaucoma [82], age related macular degenerations[225]), and neurology diseases (Parkinson's disease, Alzheimer's disease, multiple sclerosis, intracranial hypertension etc.) [132, 236], etc. The first such device was introduced in early 90s [118].

Optical coherence tomography is an interferometry-based method. Time domain OCT (TD-OCT) was introduced as first. The TD-OCT principle is similar to SD-LCI method noted in previous paragraphs. Basically, the low coherent, near infrared light beam is generated from superluminiscent diode. The beam goes through a beam splitter that splits the beam into the reference and sample beams. The sample beam is partially absorbed by the transparent tissues in anterior segment of the eye. The sample beam is then backscattered and reflected by tissues of interest in posterior segment of the eye. In OCT, the interference of the reflected light beams at the level of photodetector is only possible when the distances traveled by the light in both pathways (reference and sample) are the same. This allows measurement of the echo time delay and also implies the importance of the mechanical shifting of the mirror in reference beam pahtway. Reference mirror is translocated so echo time delays from reference mirror and ocular tissue layers (superficial retinal layer has shorter echo time than deeper choroidal) matches. Then, the axial scan (A-scan) is quantified based on amplitude of occurred interference signal made from reflected sample and reference beams. [273]

Later, the detector was replaced with interferometer capable of analyzing the full spectrum of interference signals at once. This allowed the elimination of mechanically translocated mirror so acquisition time of A-scans was reduced and resolution improved. This was only possible with the utilization of Fourier transform equation, hence this methodology is called Fourier-domain or spectral domain OCT (SD-OCT). SD-OCT is no longer working with echo time delays but evaluates the output interference signal as a function of wavelengths. [273]

OCT technology is getting more advanced and the scan speed was increased with utilization of narrow bandwidth laser as a light source. This technology is called swept source OCT (SS-OCT) [273, 294]. Spahr et al. used full field SS-OCT to

investigate retinal vascular dynamics by measuring the global displacement of the retina due to blood filling. As a result, pulsations of retina thickness near arteries and veins and their mutual delays were presented [294].

Doppler OCT. Functional extension of OCT, i.e. Doppler OCT (DOCT), enabled observation of retinal hemodynamics through cross-sectional imaging of the flow in retinal blood vessels [6, 57, 119, 183, 187, 281, 294, 319, 325, 337].

DOCT is not measuring only amplitudes of the interference signals as conventional OCTs, but also detects Doppler shifts in reflected spectrum induced by moving particles in tissue, similarly as in laser Doppler velocimetry or flowmetry. [337]

Research group of S. Yazdanfar was one of the first observing blood flow in larger retinal vessels with color DOCT technique in time domain. However, the sampling frequency was limited as they acquired 40 sequential images (of 5 depth scans) in 5s, i.e. 8 cross-sectional images per second. In their work, they demonstrated extracted flow velocity profiles of blood flow pulses with fitted parabole curves represented by detected Doppler shift in units of kHz. [337]

Next advances in DOCT were made by research group of Y.Wang when they introduced optical DOCT in spectral domain with ability to measure volumentric flow (in μl/min).

Since 2013, the dual-beam DOCTs were introduced [21, 57]. The single beam systems (used before) suffered from unknown Doppler angle between the sample beam and vessel. Single beam system used to address these issues usually by intensive post-processing calculations. However, the calculated angles suffered from lower accuracy affecting the final determined velocity precision. More, the single-beam systems cannot determine the velocity in cases that the beam is perpendicular to plane of measured area. Dual-beam systems eliminates the dependence on the unknown Doppler angle and secures that the velocity is always possible to determine as two beams illuminates the area of interest under two different angles [57].

Doblhoff-Dier et al. introduced a dual-beam DOCT system combined with DVA for exact determination of vessel diameter so the total retinal blood flow can be measured. As a result, pulsatile character of blood velocity of both arteries and veins were presented and mutual dependency of pulsatile curves of vessel flow velocity and diameters were demonstrated. [57]

Research group of A. Leitbeg, focused on pulsatile ocular blood flow measurement [21, 183, 281], and introduced the dual-beam bidirectional Doppler swept-source DOCT composing the rotating Dove prism. Rotating Dove prism keeps the detection planes of the sample beams parallel to velocity vectors so the angle between them is low. Larger angles lead to errors in determined velocities. More, rotating Dove prism enables measurement duration to decrease. [21] As a result, they presented the pulsatile axial velocity in indicated vessels (**Figure 1.19**).

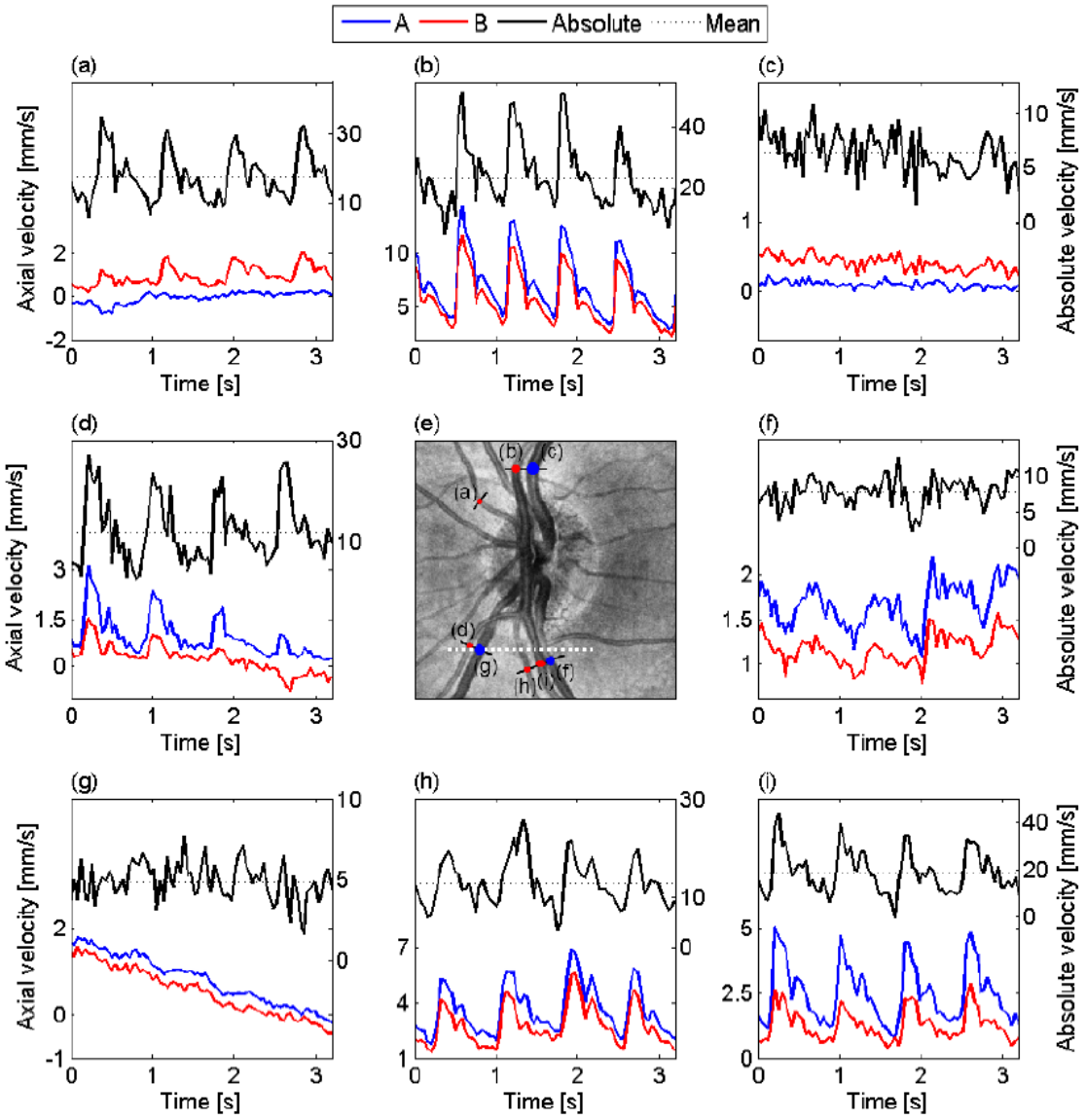

Fig. 1.19: Blood velocity outputs from dual-beam bidirectional Doppler swept-source DOCT. **A-D, F-I** Time courses of blood velocities measured in highlighted areas in **E** while using rotating Dove prism. red and blue - axial velocity for two channels A and B, black - calculated absolute velocity, dotted - mean value of absolute velocity. **E,** En-face mean projection of OCT data set forming the 15° fundus image.[21]

Also the combinations of techniques were used for retinal hemodynamic estimation. Huang et al. [119] presented a technique combined of OCT angiography and DOCT. The research group utilized intensity-based Doppler variance method to perform OCT angiography. Based on custom-programmed algorithm for 3-D

segmentation and vessel boundaries extraction, the Doppler angle was obtained for further angle correction of detected blood velocities. The advantage of this approach for volumentric blood flow evaluation is that this technique is easily applicable for commercial devices without a necessity of technical upgrades. [119]

Lately, Li et al. evaluated pulse wave velocities using a jump-scanning method via phase resolved DOCT [187]. This methodology basically measures the pulse wave transit times from two different indicated scanning areas through "transient jumps". Li in his work used custom built SD-OCT and derived pulse wave velocity, marker of arterial stiffness.

The important work about ocular hemodynamics, and spontaneous retinal venous pulsations in particular, was presented by Wartak et al. [325]. In their work, they analyzed, compared and explored the mutual relationships of pulsatile phenomena characteristics and parameters provided by different tools, i.e. ophthalmoscopy-based method - SLO and conventional intensity-based OCT with Doppler extension (**Figure 1.20**). The research group acquired data of 3 consecutive cardiac cycles with SLO (10 fps), and custom-built OCT (Doppler coss-sectional images with 44 fps, and B-scans with 24 fps where A scan rate was 100 kHz). Wartak et al. reported that the pulsatile intensity changes were synchronous with vessel diameter changes (i.e. vessel collapse). And, as noted in previous chapter, the mean flow velocity increases as the vein diameter decreases during each cardiac cycle and the maximum flow velocity seems to be in phase with the vein collapse. [325]

Overall, most of commercial devices on market combines various types of SLO or IR camera and OCT because SLO/IR camera provides live fundus imaging for quick orientation before OCT measurement. There are many OCT manufacturers on market, i.e. Heidelberg Engineering, Inc., Germany; Carl Zeiss Meditec, Inc., Jena, Germany; Topcon, Tokyo, Japan; Optovue; Fremont, California, USA; Nidek, Inc. San Jose, California, USA; Optos, Inc., Dunfermline, United Kingdom; etc. The most commonly used in medical research is Spectralis OCT+HRA (Heidelberg Engineering, Inc. Heidelberg, Germany).

Laser Doppler Holography. The laser Doppler holography (LDH) is interferometry-based full-field imaging method originating in OCT and inspired by laser Doppler flowgraphy. This method measures primarily Doppler power spectrum density from the interference of reflected beams - holographic reference beam and Doppler broadened beam backscattered by the retina. Optical field formed by a reference beam beats against Doppler-shifted sample beam. Optical field power can be increased in order to use shorter exposure time. Thus, the temporal resolution could be as low as 1.6 ms. Then, detected interferograms are analyzed and holograms are reconstructed. [245, 246, 247]

Methodology brought many advantages, i.e. Doppler spectral broadening of

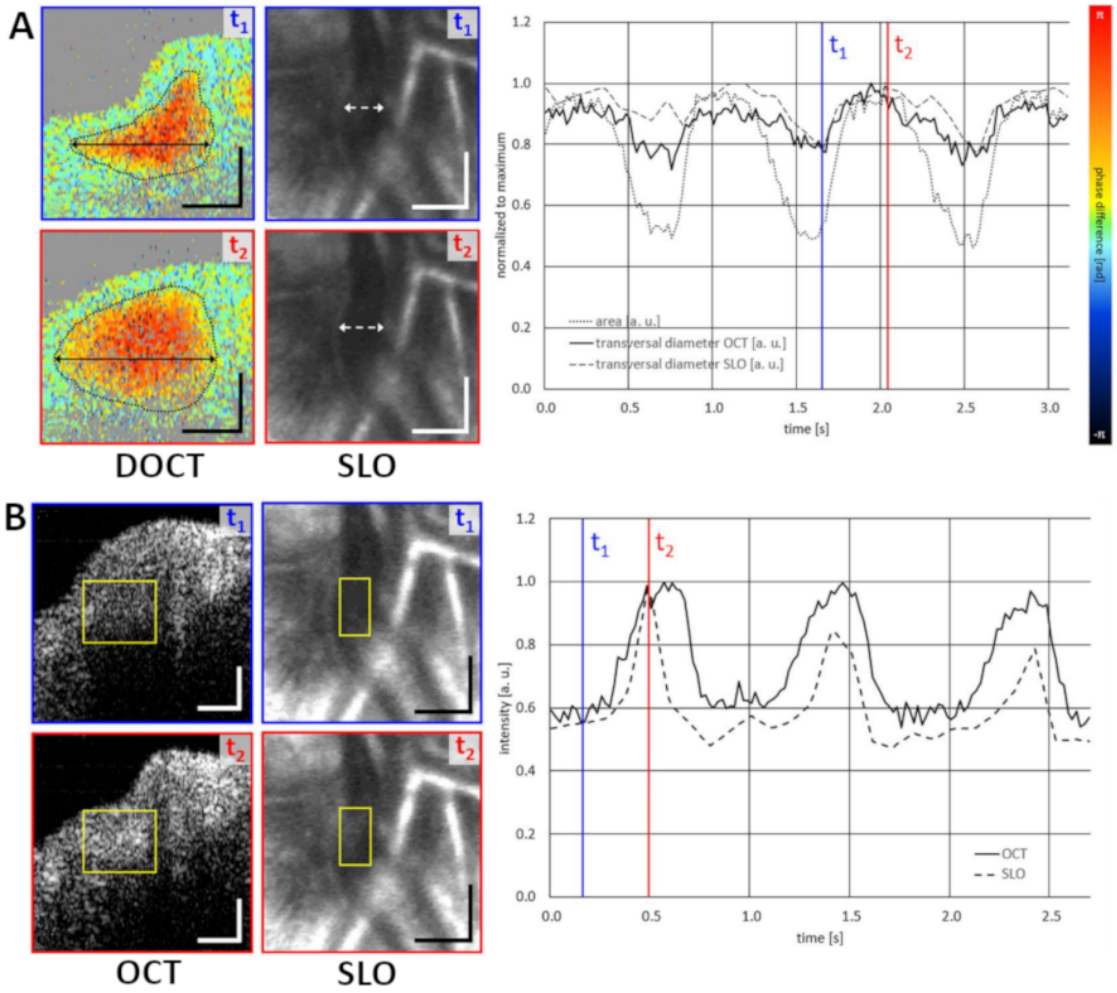

Fig. 1.20: SVP evaluation and comparison between DOCT/OCT and SLO techniques. **A** SVP area evaluation of DOCT (total area, tranversal diameter) and SLO (transversal diameter) over 3 cardiac cycles. Data were acquired within consecutive sessions. **B,** SVP intensity evaluation of OCT tomograms and SLO images within indicated region of interests withi three cardiac cycles.[325]

backscattered light enabled the contrast of the same level as in OCT angiography methods in much lower exposure time than current methods. The exposure time of this level (i.e. 1.6 ms) may provide the proper analysis of blood flow. [245, 246, 247]

Using LDH, the blood flow, velocity and volume can be evaluated from Doppler amplitudes and shifts. The research group of L. Puyo analyzed the pulsatile character of blood flow in retinal vessels using LDH. However, the resulted data suffered from artifacts originated from saccadic eye movements and axial movements of choroid and retina due to blood filling. Later, these movements were successfully filtered out by utilizing singular value decomposition methods. Singular value de-

composition helped identify high powered components (i.e. saccadic eye movements) so only low powered components were preserved.[245, 246, 247]

1.3.4 Other technologies recording retinal pulsation phenomena

Ophthalmodynamometry. Ophthalmodynamometry is an older method determining the collapse pressure in retinal vessels. Besides evaluation of ocular perfussion, the method was clinically used to detect carotid stenosis, thus gives the important information about perfussion of both eye and brain. Current ophthalmodynamometric examinations utilize slit lamp for biomicroscopic observation of ONH while Goldmann contact lenses and pressure sensor are applied [136]. The example of commercial device was ODM - Saugnapfdynamometer (Fa. Boucke taberna pro medicum, Luneburg, Germany) [223].

Pneumotonometry. Methodology uses pneumatic applanation tonometer to measure changes in IOP caused by rhythmic filling of intraocular vessels. These changes in IOP are parametrized with pulse amplitude (maximum IOP change during cardiac cycle) and pulsatile ocular blood flow (POBF) parameter as an output. Examples of commercial pneumotonometric system were OBF System 3000 (OBF Labs, Malmesbury, UK), Ocular Blood Flow Analyzers (Paradigm Medical Industries, Salt Lake City ,USA). [274, 327]

1.3.5 Experimental video-ophthalmoscope

The main focus of this chapter is the device of the experimental video-ophthalmoscope (VO) [303]. The VO acquired retinal video-sequences that were used for analyses and algorithm development in published journal articles introduced in chapter *Results*. The video-ophthalmoscope [303] is the in-house built ophthalmoscope developed in collaboration of Department of Biomedical Engineering in Brno University of Technology (Brno, Czech Republic) and Erlangen University Hospital in Erlangen (Germany). This prototype of non-mydriatic VO was introduced in 2015 in [303].

Video-ophthalmoscope [303] innovatively uses the inner part of the pupil as an entry for light emitted by the light source and outer part of the pupil for the light reflected by the retina. Classic fundus cameras use the opposite approach. The used approach enables simple construction of the VO regarding the location of the light source. The light source is placed in the optical path between the detector and eye in comparison to fundus camera, where the light source is placed out of optical path and the light is deflected by the optical system of mirrors into the eye. [303]

The wavelength of the light is determined based on Lambert-Beer law so the light is sensitive to hemodynamic changes in retina. Lambert-Beer law defines intensity

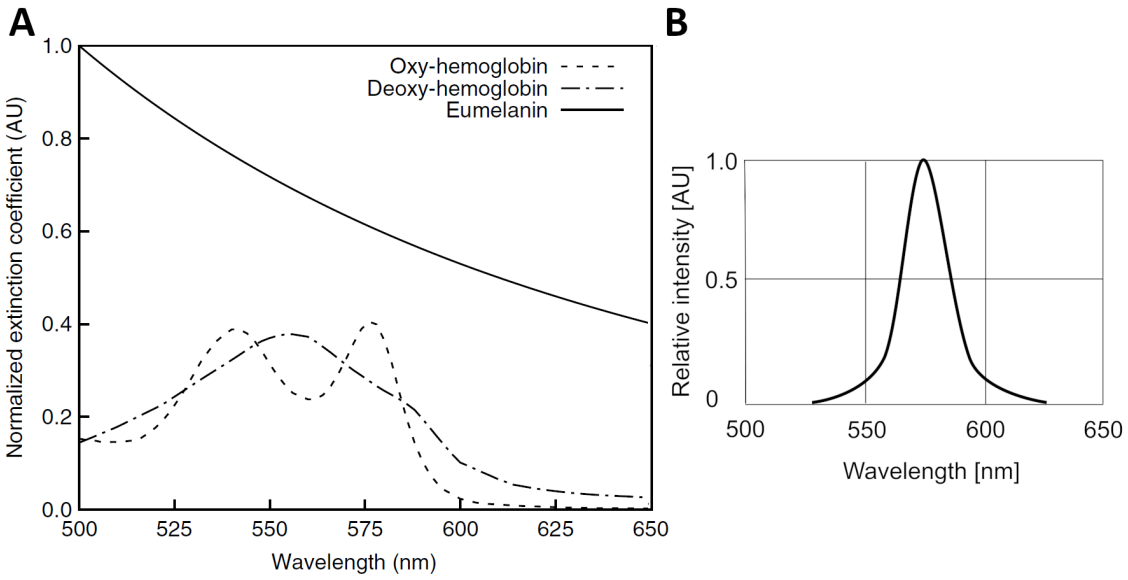

Fig. 1.21: A, Extiction coefficients as a function of wavelength for chromophores - melanin, oxy- and deoxy-hemoglobin [88]. B, LED diode characteristics.

of light after transmission through specific tissue (**Equation 1.7**)

$$I = I_0 e^{\mu_a(\lambda)L} \tag{1.7}$$

where I_0 is intensity of light source, L is length of optical path through specific tissue, and μ_a is absorption coefficient ($[\mu_a] = cm^{-1}$) determining the ability of the tissue to absorb the light of specific wavelength. The absorption coefficient is directly proportional to extinction coefficient which is demonstrated as a function of wavelength for three different kinds of matter (i.e. oxy- and deoxy- hemoglobin, melanin) in **Figure 1.21 A**. Melanin, oxy- and deoxy- hemoglobin are the most important chromophores in the optical path in retina imaging. The extinction coefficient function indicates the absorption coefficient for hemoglobin is the highest in wavelength range of 525-575 nm. More, oxy- and deoxy hemoglobin may be distinguished while utilizing the light with wavelength of 575 nm. The high concentration of melanin, which is characterized with high absorption coefficient, may impact the intensity of output image. [40, 88, 148]

The main advantage of the VO is that it enables non-mydriatic approach as various kinds of mydriasis may cause side effects (i.e. long-term dilation, eye irritation, hypertension). Another advantage is long-term (non-limited) data acquisition due to low light intensity source meeting the conditions for long-term light exposure. Additionally, besides stated frame rate of 25 frames per second (fps), the detector enables options of higher frame rate, e.g. 50 fps. The detected image is of lower

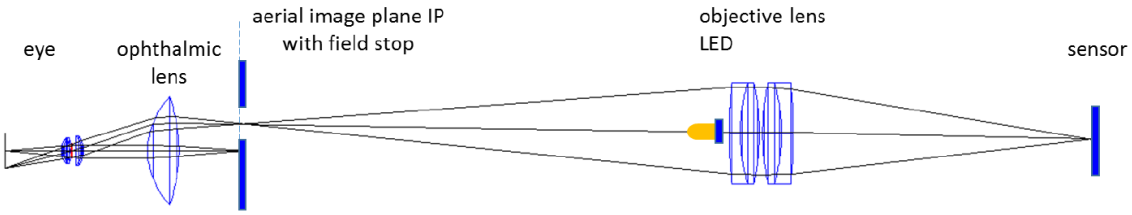

Fig. 1.22: Schema of experimental video-ophthalmoscope [303].

intensity level in higher frame rate but the output image is still sufficient for further image analysis. [303]

The whole optical system of the VO consists of light source, detector, optical lenses, optical aperture, ophthalmic lens. The VO scheme is in **Figure 1.22**.

Light source. The light sources are characterized with different dimensions, luminosity, and dominant wavelengths. The determination of appropriate light source depends on used detector, particularly the sensitivity to specific wavelength, and Lambert-Beer law as described above.

The light source's dimensions must be minimal as it can't obstruct the optical path. The intensity of the light source must be sufficient but non-irritating for the eye. Therefore, the LED diode of 3 mm in diameter, and of light power not exceeding 10 μW at pupil plane is used for imaging with VO. As a result, illumination of retina is 40 $\mu W/cm^2$ which meets the standards ANSI Z136.1. The LED diode is generating the light of peak wavelength 574 nm (25 nm full width at half maximum of the peak, the characteristics of the LED diode is in **Figure 1.21 B**). [303]

Detector. The detector used for the VO was CCD camera (iDS-imaging Germany) of following parameters - resolution 640x480 px, frame rate up to 75 fps with full spatial resolution or up to 135 fps with reduced spatial resolution. The standard frame rate used for data acquisition is 25 fps (≡ exposure time of 40 ms for a single image). Later, the detector was replaced with CMOS (UI-3060CP-M-GL, iDS-imaging, Germany). The output resolution was 9.3 μm/pixel. [303, 304]

Optical lenses. In the optical system of the ophthalmoscope are placed 2 achromatic and 1 ophthalmic lenses. Ophthalmic lens of 40 D (Volk Optical Inc., USA) creates aerial image in the plane of optical aperture. The apparent image is transmitted through two achromatic lenses (both of focal distance 120 mm; Quoptiq, Germany) into the detector. The angle of field of view is 20° x 15°, where OD is in the center. [303]

Optical Aperture. As indicated above, the reflected light is transmitted through the outer part of the pupil and not the central, and the incidental reflected light transmitted through central part of the pupil is eliminated with optical aperture.

In the plane of optical aperture is additionally placed the red diode representing the fixating point for the subject.

Output image. Acquired single image (with parameters - field of view 20° x 15°, resolution 640 x 480 px, where 1 px corresponds to $9.3mum^2$ of retina) is demonstrated in **Figure 1.23 B**. The whole temporal series of these images may suffer from artefacts originated from blinking or eye movements (microsaccadic movements, etc.).

Binocular modification. The binocular modification of VO was introduced in 2017. The binocular VO enables the simultaneous data acquisition of both eyes. This enables to measure (and reveal) assymetric retinal pulsations, which can be useful in diagnosis of various diseases, e.g. glacuoma [331]. The schema of binocular VO is shown in **Figure 1.23 A**). The construction is similar to the monocular version. The binocular VO contains extra OLED displays for visualization of fixating point for subjects. Both cameras of this version are precisely synchronized with a trigger

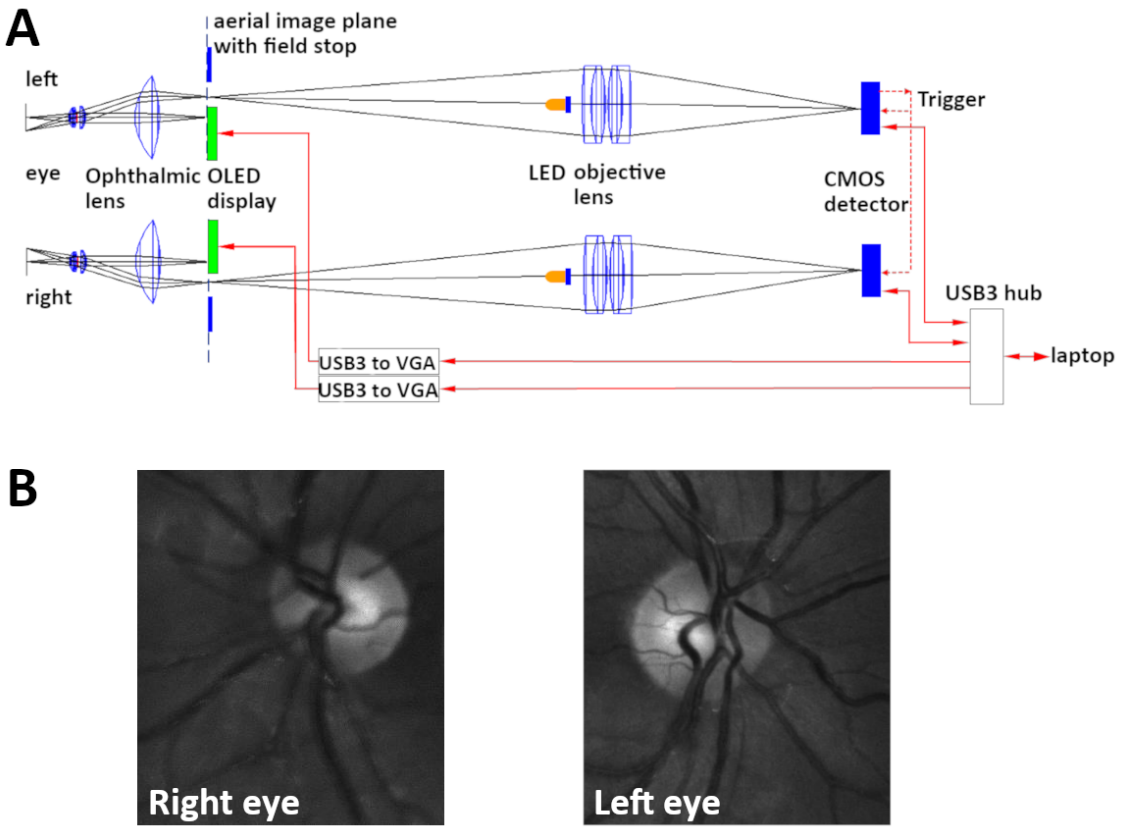

Fig. 1.23: Schema and results of binocular video-ophthalmoscopic acquisition. A, Schema of binocular video-ophthalmoscope [304]. B, Simultaneously acquired images from left and right eye with binocular ophthalmoscope.

signal generated by one of the camera. [304]

Data acquisition. The data of both monocular and binocular data were acquired within Erlangen Glaucoma Registry (NCT00494923, registered at www.clinicaltrials.gov) between years 2015-2017.

Recorded retinal pulsation phenomena. The image processing and the retinal pulsation phenomena assessment are described and discussed within the section *Results*.

1.3.6 Simultaneous acquisition of retinal video sequences and other biosignals

Through the time, the functional retinal imaging techniques (i.e. video-ophthalmoscopy, interferometry, etc.) were combined with blood pulse volume measurement [143, 158, 162, 291, 279] or electrocardiography [34, 60, 105, 162, 169, 256] to perform simultaneous data acquisition and define a temporal characteristics of retinal pulsations within a cardiac cycle. Such definition of the temporal characteristics, may help in diagnostics of diseases where vessel narrowing represents a symptom. Vessel narrowing occurs in elder people, people with hypertension or inflammation. Vessel diameter change of 3% within a cardiac cycle indicates the timing of single fundus image acquisition may be important and a proper standardization or single fundus image replacement with retinal sequence acquisition for the whole cardiac cycle may improve diagnostics. Additionally, many studies tries to clarify the timings of SVPs within a cardiac cycle. Increasing temporal resolution of simultaneous acquisitions identified the timing of retinal venous collapse within a cardiac cycle to first half of ventrical diastole within a cardiac cycle [22, 34, 162, 169] (**Figure 1.26**). Moreover, Morgan et al. tried to clarify the the timings and relationship of SVP to intracranial pressure (ICP) within his study [220] where the authors acquired simultaneous dataset of ICP and retinal sequences. However the used methodology is debatable and brings the questions about its precision (see next paragraphs). Within the experimental part of this doctoral Thesis (see chapter 3.4), a simultaneous acquisition of ICP, EKG, blood pulse volume (finger plethysmography) will be performed utilizing Kolar's solution described in the next paragraph.

History of simultaneous acquisition of retinal sequences and other biosignals. The simultaneous acquisition of retinal video-sequences and various biosignals were rarely performed in the past. Starting 1994, Chen et al. performed an experiment including the simultaneous acquisition of electrocardiogram (EKG) and retinal sequences acquired with a fundus camera [34]. Fundus camera was triggered via a time delay switch. Time delay switch was set to record eight time points during a cardiac cycle just after R-wave, i.e. a retinal photo in each 1/8th

fraction of the cardiac cycle was acquired (0/8th, 1/8th, ... 7/8th of cardiac cycle). Considering the normal heart rate between 60-100 beats per cycle, the temporal resolution of 1/8 of cardiac cycle represents 75-125 ms. [34]

In 1995, the interferograms determining time-courses of fundus pulsations were acquired simultaneously with the ear lobe photoplethysmography signal. Unfortunately, neither the synchronization of interferometer and photoplethysmograph, nor the temporal resolution was described within the paper [279].

Year after, Dumskyj et al. used purpose-built EKG synchronization unit (Historyonics, Chatham, UK) [60]. The system triggers the fundus camera in 12 subsequent intervals after EKG R-wave (1st interval 0ms, 2nd interval 120 ms, 3-12 interval 83 ms each). Thus, the temporal resolution is independent to heart rate in comparison to previous EKG-synchronized solution. As a result, this kind of synchronization provides fundus sequences through variable numbers of cardiac cycles, i.e. 12 subsequent intervals cover one cardiac cycle in a person with heart rate 60 while it may cover two cardiac cycles in a person with heart rate 120. Thus the measured vessel diameter is most likely measured in a different phase of cardiac cycle in each individual. [60]

Another EKG-synchronized retinal imaging was introduced in 1999 by D.S. Reshef [256]. Reshef et al. assembled a synchronization system utilizing a standard cardiac intensive care unit (EKG monitor) and a custom build control unit. The Intensive care unit is able to detect R-wave and produce external pulse within this detection (originally intended for cardiac defibrillation). A computerized control unit detected the external pulse, evaluated the heart rate, and determined eight equidistant time delays (1/8 of a cardiac cycle in time) according to an individual's heart rate. The camera, triggered with the control unit, acquired retinal images with the eight delays (in 0/8th, 1/8th, ... 7/8th of cardiac cycle) starting with R-wave. The number of delays determining eight segments within a cardiac cycle was inspired by the previous published work, i.e. [34], so the results could be compared. The temporal resolution is within the range of 75-125 ms.

In 2004, Knudtson et al. used a pulse synchronized ear clip trigger to acquire the fundus images in sequential order at 0%, 30% and 70% of the cardiac cycle starting at the peak of the wave at the ear lobe. Considering the heart rate 60-100 beats per second, the temporal resolution would be within the range of 150-250 ms. A detailed description of synchronization is not publically available. [158]

Five years later, Kain et al. used audio-videorecordings for synchronized acquisition of pulse oximeter and slit-lamp mounted video camera [143]. The video-camera acquired retinal sequence with a temporal resolution of 40 ms (25 fps) while microphone was recording the "beep" sound of the oximeter marking each pulse. Additionally, Kain presented the synchronized acquisition of applanation tonometer and

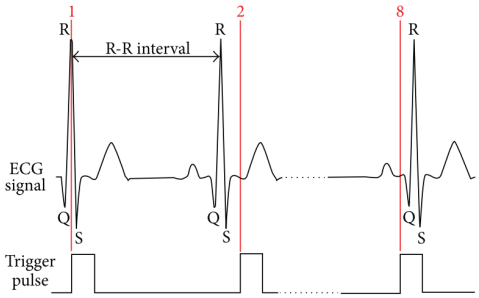

Fig. 1.24: R-wave triggering the fundus camera in eight equidistant points within cardiac cycle. The figure demonstrates the outputs of EKG and trigger signals in 1/8, 2/8...7/8 fraction of RR interval. [169]

oximetry (based on the same principle) in the subsequent experiment. Despite all the efforts, the synchronization through the audible signal of the oximeter brings doubts to its precision. [143]

In 2011, Singh et al. performed the simultaneous measurement of Fourier-Domain OCT and custom-made ear lobe pulse oximeter to assess the influence of cardiac cycle on fundus pulsation amplitude [291]. The signals from OCT CCD camera and oximeter were processed via dual-core computer with custom script in LabView (National Instruments, Austin, USA). A detailed description is not publically available. [291]

Kumar's research group in its works through years 2012-2013 [105, 169] utilized EKG R-wave (detected by EKG monitoring system) to trigger a fundus camera. Following the pattern of previous studies [34, 256], fundus images were acquired at eight distinct points within a cardiac cycle (R-R interval), i.e. in intervals 0.125 fractions starting with R-wave (as demonstrated in **Figure 1.24**). The acquisition required invariable R-R intervals. These were monitored for a 10% changes that triggered alarm. Again, this approach leads to limiting temporal resolution of sequential retinal images (i.e. 75-125 ms). Moreover, changes in heart rate up to 9% were not considered and yet may be source of erroneous trigger points. [105, 169]

In 2012, Morgan et al. acquired the retinal video sequences using the modified slit lamp simultaneously with intracranial and intraocular pressure[220]. Morgan took advantage of audio-visual recording similarly as in Kain's study. The microphone was recording the "beep" sound of the pulse oximeter device. The ICP monitor projecting the ICP values and pulses were recorded with a video-recorder. All the signals - audio signal from a microphone, visual signals from the video recorder and slit lamp detector were inputs to a audio video mixer. The authors declare a temporal precision of 0.04s.[220]

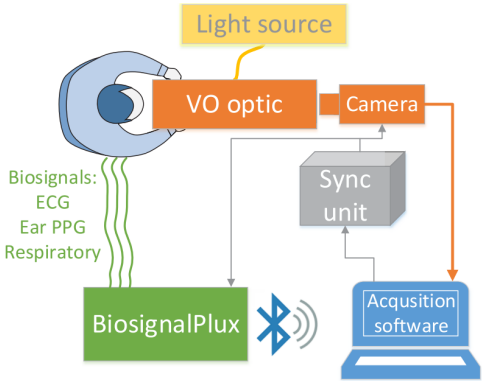

Fig. 1.25: Simultaneous acquisition of retinal video-sequences and other biosignals according to Kolar 2023 utilizing Arduino platform and biosignals plux hub to reach precise synchronization. [162]

In 2023, Kolar research group introduced an innovative hardware solution for simultaneous acquisition of retinal video-sequences and various biosignals [162]. The solution includes a video-ophthalmoscope (VO, introduced in chapter 1.3.5 and in [303]), a biosignal acquisition unit and a synchronization unit **Figure 1.25**. Synchronization unit, i.e. Arduino platform, generates a trigger signal of frequency determining also the framerate of the VO. The trigger signal is driving the detector of a video-ophthalmoscope acquiring the frames with each rising edge of the trigger signal. Biosignals acquisition unit, i.e. BiosignalsPlux hub (PLUX Wireless Biosignals S.A., Lisbon, Portugal) records both the biosignals - EKG, photoplethysmography, respiration plethysmography signals, and the trigger signal at 1kHz frequency. This setup results in precisely synchronized biosignals and retinal video-sequences. Additionaly, Kolar et al. evaluated the timings of the retinal vein collapse to the R-wave of EKG signal and compared his findings with other published work **Figure 1.26**. [162] Kolar's custom solution for precisely sychronized datasets was utilized within the experimental part of this doctoral Thesis (see chapter 3.4).

Commercially available solutions. Today, commercially available devices acquiring retinal video-sequences provides simultaneous acquisition with finger photoplethysmography or electrocardiogram with proper synchronization using its proprietary software. Semi-automatic analysis of RVA/DVA results in temporal monitoring of the diameter of selected vessel simultaneously with the finger photoplethysmography signals (e.g. as utilized in [22]). XyCam device utilizing the light of infra-red wavelength provides the simultaneous retinal blood flow monitoring along with finger plethysmography and EKG signals [37, 51]. However, the temporal resolution of these techniques reaches 25 fps which may not provide sufficient results in

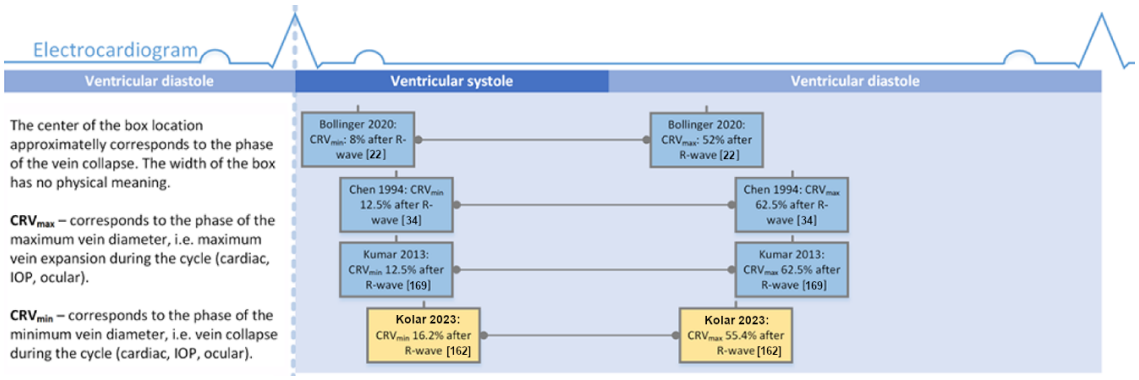

Fig. 1.26: A graphical summary of retinal vein collapse timings during a cardiac cycle (defined with R-R interval) measured in different published studies, i.e. [22, 34, 162, 169]. [162]

application to diagnostics or precisetiming identification [165].

1.3.7 Sources of physiological artifacts in retinal video-sequences and their suppression

Temporal retinal video-sequences generally suffers from artifacts originating from participant's movements regardless the used imaging technique. Such movements result in empty, blurred, distorted or/and most usually shifted images. Additionally, the images can suffer from discontinuality in images acquired with raster scanning techniques (i.e. SLO, OCT) due to eye movements.

The acquisition conditions and overall experimental procedure (common for both ophthalmoscopy-based and interferometry-based methods) eliminate or reduce the imaging distortions as follows: Placement of a participant into a sitting position eliminates large horizontal movements. Head placed into a chin holder with forehead rest reduces sub-centimeter vertical translations and rotations. Fixed positions of the chin holder and anchored imaging tool secure a stable distance eliminating variable scaling over time. [173] However, the sub-milimeter translational distortions are still possible due to fixational eye movements called physiological nystagmus that includes rapid saccades, high frequency tremor and slower drifts. These movements are characterized with amplitude 5-15 arc min and frequency 40-100 Hz, and distore the acquired video-sequence with translated or rotated frames [295]. Therefore all acquired frames need to be aligned before the subsequent analyses.

The recorded scene, i.e. the eye, composed of soft tissue is not fully rigid, it stretches due to blood filling and causes local tissue deformations (i.e., ONH axial pulsations [6, 290], vessel pulsations and displacement) that need to be corrected.

[35]

Eye-blinking presents another source of artifact in recorded video-sequences. The blinking may be partially controlled voluntarily but generally is considered as an involuntary act. Blinking produces dark or bright empty frames without retinal spatio-temporal information. In the pixel-wise time-course of local retinal haemodynamics, the eye-blinking artifact manifests as spike.

All residual motion artifacts of translational, rotational, scaling or shearing origins in the recorded retinal video-sequence needs to be supressed by the iterative image registration technique prior any subsequent video analysis. More detailed information about the state of the art of image registration methods utilized in retinal video-sequences is summarized in the chapter 1.4.2 Image Registration. If the eye-blinking spike artifact is present in an emphasized RPP time-course pattern, the artifact should be supressed by signal restoration techniques non-bluring the physiological pattern of the time-course. To the best of my knowledge there is no established method in retinal image analysis how to effectively supress the spike artifact.

1.3.8 Summary

In summary of overall estimation of pulsatile ocular/retinal hemodynamics, there is no static or dynamic gold standard technique. Each particular method evaluates parameters corresponding to a different biological atribute. If measurements are expressed in arbitrary units, a between-methodologies comparison is problematic or even impossible. Thanks to the compact size, simple and low-cost design, the video-ophthalmoscopy has a broad diagnostic potential in various diseases impacting vision, cardiovascular, neurovascular and systemic health. However, regarding the depth dimension (in a form of axial scans) and finer temporal resolution, some interferometry methods (e.g., LDH) may provide higher accuracy in assessment of the blood flow and the pulsation phenomena, but utilizing a non-compact device designs with multiple times higher purchase budgets. Every device design provides retinal video-recordings with motion-related artifacts which are mandatory to be suppressed within image analysis.

1.4 Image Analysis in Functional Retina Imaging

This chapter is focused primarily on the state of the art of image analysis in ophthalmoscopy-based functional retina imaging. It is a large field including the video/image quality assessment, image registration, segmentation of various structures of retina, RPP extraction and its parametrization or modeling.

Ophthalmoscopy-based retinal video-sequences are monomodal data of similar contrast and include intensity-based depth projection of hemodynamics over retinal surface in time. Thus the imaged scene is changing due to tissue movements or deformations, as described in previous section.

1.4.1 Video quality assessment

One of the first pre-processing step is the assessment of video quality and a decision if the retinal sequence is suitable for following analysis. In this case, each image is evaluated separately and the overall video quality level is evaluated. Manual subjective assessment is time expensive and provides significant inter-rater variability. Therefore there is a need for automated computational models that can reliably determine the quality of recorded frames in video sequences that is in agreement with a general human visual perception.

Generally, the approaches of image quality assessment can be categorized into three groups – no-reference (blind models) with no access to original image, reduced-reference and full-reference image quality measures [321].

No-reference methods can be based on precalculation of certain statistical properties as natural scene statistics (BRISQUE metrics [212]), or discrete cosine transform statistics [26, 269]. In direct application on human retina imaging, feature-based no-reference methods were utilized [77, 160]. These methods used a vessel tree as a feature to evaluate quality score or clarity as quality parameters [77, 160].

The most widespread methods are full-reference where the original undistorted image is available. This approach uses statistical error metrics (e.g. mean squared error, averaged difference, etc). Widely used quality measure is similarity index SSIM considering human visual criteria for image quality evaluation as luminance, contrast and structure [322, 323]).

The example of the full reference image quality assessment method is the utilization of the phase correlation introduced in my work [188] which is not included within the Results chapter of this Thesis. The methodology applies the normalized cross-correlation to spectral representations of reference and evaluated images. Then, the distribution of the inverse Fourier transform of the normalized cross correlation, i.e. $\delta(x, y)$ function, is parametrized and evaluated. In case that evaluated image is identical to reference image, the distribution of $\delta(x, y)$ equals to Dirac function. In case the evaluated image is identical to reference but shifted, the $\delta(x, y)$ leads to shifted Dirac function. In case of blurred, distorted images, the distribution of $\delta(x, y)$ is spread, noisy and without a visible maximum.

In general, the methodology musts consider the artifacts (physiological, technical) and diagnostic needs for quality determination if suitable, correctible, or not.

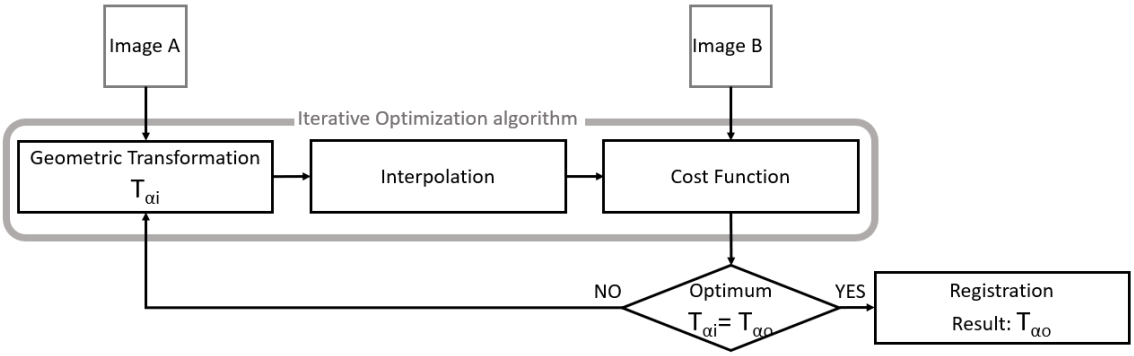

Fig. 1.27: Block diagram of image registration process.

1.4.2 Image Registration

Image registration (**Equation 1.8**) is an iterative optimization process aligning transformed image (A) to the reference image (B). Each iterative step includes three major operations, i.e., geometrical transformation (T_α), interpolation to the reference image grid, and assessment of a similarity criterion (c) between reference image and transformed image $T_\alpha(A)$. The similarity criterion is a maximized or minimized cost function depending on the character of the criterion, while coefficients of the geometrical transformation (α) are optimized. [127] Basic block diagram of the image registration process is demonstrated in **Figure 1.27**. In this section, the main image registration methodologies applied on retinal images are introduced. [127, 293]

$$\alpha_O = arg \max_{\alpha} c(B, T_\alpha(A)) \tag{1.8}$$

Regarding proper image registration, the data character and possible imaging distortions need to be identified to find optimal solution. In this case, the section is focused especially on mono modal image registration with the same imaging geometry. However, a majority of articles in the retina imaging field are focused on multi modal image fusion, thus the articles utilized multi modal image registration of images of different spatial resolutions with (full/partial) overlapping field of view.

Generally, various combinations of transformation functions, similarity criteria and optimization strategies were utilized on retinal images.

Transformation function. The number of coefficients in vector α defines degrees of freedom in the optimization process. Geometrical transformations of different degrees of freedom are necessary for different kinds of mutual image distortions. A proper selection of the geometrical transformation is essential for correct image alignment.

The very first algorithms in the field utilized cross-correlation for estimation of translation between images [227]. The computational demands of the algorithm were reduced when the search area was restricted to image areas containing retinal vessels [239]. The cross-correlation function was also utilized in order to find the parameter for rotation and scaling via log-polar mapping of the Fourier magnitude transformation [39, 38]. Algorithms estimating transformation via cross-correlation did not provide sub-pixel precision due to missing interpolation step **Figure 1.27**.

The linear image registration utilizing rigid geometrical transformation is usually sufficient enough for the eye motion artifact correction within the intra-subject functional retina imaging (i.e., the same imaging geometry over acquisition time, monomodal image character of similar field of view with inter-frame linear contrast transformation function). [161, 173].

If the optimized transformation is a linear operator providing rigid transformation, scaling and shearing, we talk about the affine image registration. The scaling may be the reason why the affine transformations were optimized within the image registration implemented in earlier commercial and custom-build imaging techniques [114, 217, 281] and other general retinal image registrations [31, 173, 198].

If the transformation operator is spatially variant, we talk about the non-linear image registration. Non-linear image registration is usually needed when the warping of the image data into a template space or into space of another subject is needed. Retinal soft tissue is not fully rigid, blood filling can cause local image deformations and necessity of a non-linear transformation within intra-subject image registration can arise [35, 54, 69, 173].

Similarity criterion. The cost function determines the similarity level via its global or local extreme. Similarity measures between two images $A(x, y)$ and $B(x, y)$ (x,y rows and columns in image) are categorized into intensity-based and feature-based.

The intensity-based approaches use image intensities and gradients. The most utilized global intensity-based similarity criteria through the literature in the field are direct intensity-based criteria, e.g. cosine criterion(**Equation 1.9**), norm-cosine criterion (i.e., correlation coefficient) and its modifications [17, 38, 39, 198, 342], and information-based criteria, e.g. mutual information [35, 261]. Cross-correlation is also a common operation in image registration in custom-build prototypes with publicly available principles [287, 324].

The main difference is that the presumption for the direct intensity-based criteria is equal or linearly dependent contrast between images. Hence it cannot be used for multi modal images. The information based criteria rely on geometrical features rather than on intensity similarity, therefore these may be used for intermodal image registration.

Considering the images A and B as gray level sets G_A and G_b of m,n gray levels in A and B respectively, the mutual information describes the amount of the information that one of the sets gives us about the other. The calculation of mutual information is based on joint histogram and is described with **Equation 1.10**, where $p(g_a)$ is the probability of particular intensity level occurring in A (**Equation 1.11**), $p(g_b)$ is the probability of particular intensity level occurring in B (**Equation 1.12**), $p(g_a, g_b)$ probability of particular intensity level occurring at matching locations in A and B (**Equation 1.13**). The probabilities are estimated based on distribution of grey levels across the overlapping part of images A and B (H is the value of the joint histogram formed from the overlapping part, N number of points in common part). [127, 261]

$$c_{cc}(A, B) = \frac{\sum_x \sum_y A(x, y)B(x, y)}{\sqrt{\sum_x \sum_y A^2(x, y)}\sqrt{\sum_x \sum_y B^2(x, y)}} \tag{1.9}$$

$$c_{MI}(A, B) = c_{MI}(G_A, G_B) = \sum_{a=1}^{m}\sum_{b=1}^{n} p(g_a, g_b)\, ln\frac{p(g_a, g_b)}{p(g_a)p(g_b)} \tag{1.10}$$

$$p(g_a, g_b) = \frac{H(g_a)}{N} \tag{1.11}$$

$$p(g_a, g_b) = \frac{H(g_b)}{N} \tag{1.12}$$

$$p(g_a, g_b) = \frac{H(g_a, g_b)}{N} \tag{1.13}$$

The next category, feature-based methods are then categorized into general image descriptor-based methods and vessel-based methods [54].

General image descriptor-based approaches extracts local invariant descriptors as image features and searching for correspondences between two sets of features. The example of such descriptors utilized in retinal imaging registration is scale invariant feature which is used in combination with RANSAC score [190] or with sum of squared differences [251], salient feature region in combination with Kullback–Leibler divergence criterion [342].

The vessel-based approaches uses the vessel tree and its characteristic descriptors (e.g. bifurcation points) as landmarks in the process of registration. The features, i.e. locations are then evaluated with statistical metrics, i.e. euclidian distances, least median of squares [31], root mean square error [173], energy cost function [69], etc.

Optimization Strategies. In the retinal field were utilized various iterative searching strategies to find the optimum of the cost function, i.e. simulated annealing with pyramid sampling [261], combination of simulated annealing and genetic algorithm [198], iterative nearest neighbour matching [190].

Open source registration tools. Besides the published algorithms, the open source tools for general registration tasks are available. The most known are Elastix (registration toolkit) and ITK (registration and segmentation toolkit). Elastix (available at https://elastix.lumc.nl/) is an open-source tool for general image registration, both rigid and elastic. Elastix provides the algorithms/protocols with parameters optimized for brain imaging [156].

Image Registration algorithms in commercial devices. All commercially available retinal function imaging devices introduced in the previous section uses its proprietary software for movement corrections and image alignment. Due to proprietary software, the used algorithms are kept unpublished. RVA/DVA image registration algorithm is based on vessel tracking and branching geometry [98]. The Automatic Real Time operation software for Spectralis HRA+OCT aligns the retinal sequences based on point-based global criteria, i.e. a set of hundreds of landmarks is determined in each image. A combinatorial algorithm matches landmarks between the images via two-dimensional affine transformation of which parameters are optimized with least square algorithm [18, 114]. The LSI Xycam camera includes also the image registration algorithm in the software, however the authors admits vascular information losses due to rapid microsaccadic movement that result into blurred images and cannot be registered [37].

1.4.3 Retinal pulsation phenomena parametrization

This section is focused on algorithms for image processing and parameter extraction from temporal retinal sequences of two dimensional images acquired with direct/ indirect ophthalmoscopy-based methods as RVA/DVA, LSI, slit lamps, fundus cameras or other experimental devices.

As noted previously, the retinal pulsation phenomena is not limited to vessel diameter alterations but it includes also the pulsations of measured atribute within both vessels and surrounding tissue. Such atribute can be the intensity of reflected light or the level of mean blur rate in case of LSI.

Evaluation of vessel diameter pulsations in functional retinal imaging. The first, structural changes (i.e., vessel diameter pulsations) were spotted already in 19th century. Through the time, these changes have been evaluated based on both subjective visual perception and objective tools measuring the diameter. Subjective visual perception methods limits the precision level of the evaluation. Some researchers categorized the vessel diameter pulsation into present/absent groups [3, 153, 286]. Other researchers [45, 46, 205, 335] used the Hedges scale [113], where the diameter pulsations were subjectively categorized into four groups (in the scale 0 to 3), where 0 was used for no collapse of a vessel, 1 for partial collapse (up

to one third of its diameter), 2 for moderate collapse (up to two thirds), and 3 for collapse greater than two thirds of the diameter.

Despite the advancements in medical retinal imaging, the subjective visual perception methods were used even in the last decade [3, 45, 46, 153, 205, 286, 335]. In focus on SVP incidence, studies with objective tools demonstrated the presence of venous diameter pulsations in 100 percent tested population [287] in comparison to lower and varying SVP incidence in literature where subjective visual perception methods were utilized [3, 113, 153, 178, 182, 218, 286]. This result highlights the importance of the utilization of objective methodologies into clinical practice.

Starting in 1994, the vessel diameter was determined based on transmittance profile of manually selected vessel as the width in half-height transmittance peak profile [34]. The same algorithm was used recently in [87], and similar approach was used in [215], where research group used a wide sliding linear fit across the transmittance profiles, yielding a smooth local slopes dividing the profiles into heights and depths. Then, the vessel diameter was determined as the distance between the intersections of transmittance profile and linear slope.

Many algorithms and image processing for structure/intensity retina analyses were utilized within general data processing tools with customized settings and protocols (Context Vision Digital Image Analysis system, Linkoping, Sweden [34]; Adobe Premiere elements version 4.0 Adobe Systems, Inc., San Jose, USA [143]; Igor Pro 6.1, WaveMetrics, Inc., Lake Oswego, USA [215]) or their combinations (ImageJ + Excel + GraphPad Prism [287]) with many manual sub-steps (e.g. vessel selection).

As introduced earlier, the only complex semi-automated ophthalmoscopy-based imaging tool RVA/DVA covering tasks from acquisition to vessel diameter evaluation (based on the vessel brightness profile in manually selected fundus area) is RVA/DVA (**Figure 1.15B**). The proprietary software and its algorithms are not publicly described.

Noteworthy are semi-automated software measuring the vessel caliber in static fundus camera images, i.e. Retinal Analysis RA (Department of Ophthalmology & Visual Science, University of Wisconsin, Madison, WI, USA), Integrative Vessel Analysis IVAN (University of Wisconsin, Madison, USA; **Figure 1.28**), Singapore I Vessel Assessment SIVA (National University of Singapore) and VAMPIRE (Vessel Assessment and Measurement Platform for Images of the REtina, project of University of Edinburgh, UK, and University of Dundee, UK). RA requires significant user input and manual tracing of the vessels. IVAN provides an automatic detection of OD and a measurement of manually marked vessels in distance from 1-2 OD diameters from the OD center. SIVA provides automated detection of OD, automated detection and identification of arterioles and venules and their measurement

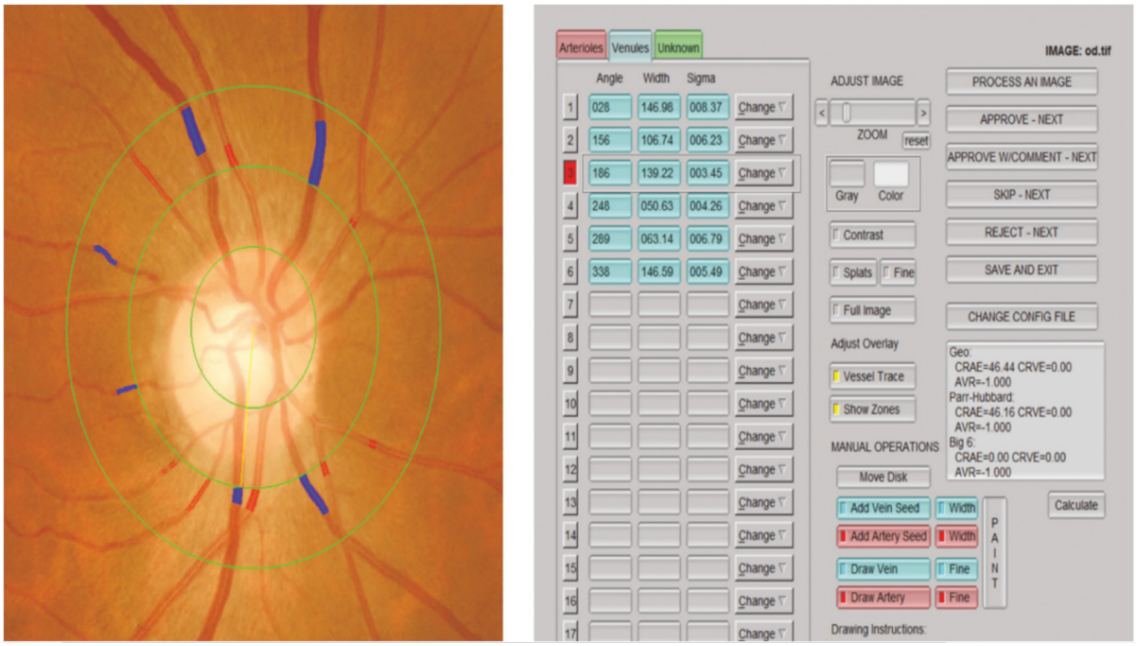

Fig. 1.28: Integrative Vessel Analysis IVAN (University of Wisconsin, Madison, USA) [312].

in the distance of 1-3 OD diameters from OD center. With a bigger computational demands, these tools has a potential to be optimized for temporal retinal sequences of fundus camera images and vessel pulsation phenomena quantification. However, these tools cannot measure the vessel diameters inside the optic disc due to frequent vessel crossing. [200, 201, 312, 338]

Similar tool for static vessel measurement is provided by Canon, In. (Tokyo, Japan) within the proprietary software of adaptive optics SLO. SLO provides automated retinal image analyser software ARIA. [9]

Manual subjective selection of the vessel for following temporal analysis is a common research practice in the field [34, 87, 143, 215, 287] including RVA/DVA [85, 284] utilization [89, 91, 165]. However, each vessel tree is unique and manual selection reduces the objectivity in evaluation. More, manual input requires the time and human resources. The full automatic algorithms for pulsation evaluations were implemented for intensity pulsations in retina.

Evaluation of intensity level pulsations in functional retinal imaging. Intensity level alterations of various retinal tissues and vessels are small, frequently non visible with eye. Thus, it excludes any subjective visual perception methods for their evaluation. The utilization of image processing methods are crucial to detect intensity changes in tissues, veins and arteries.

In dynamic ophthalmoscopy, Morgan's research moved towards automatic de-

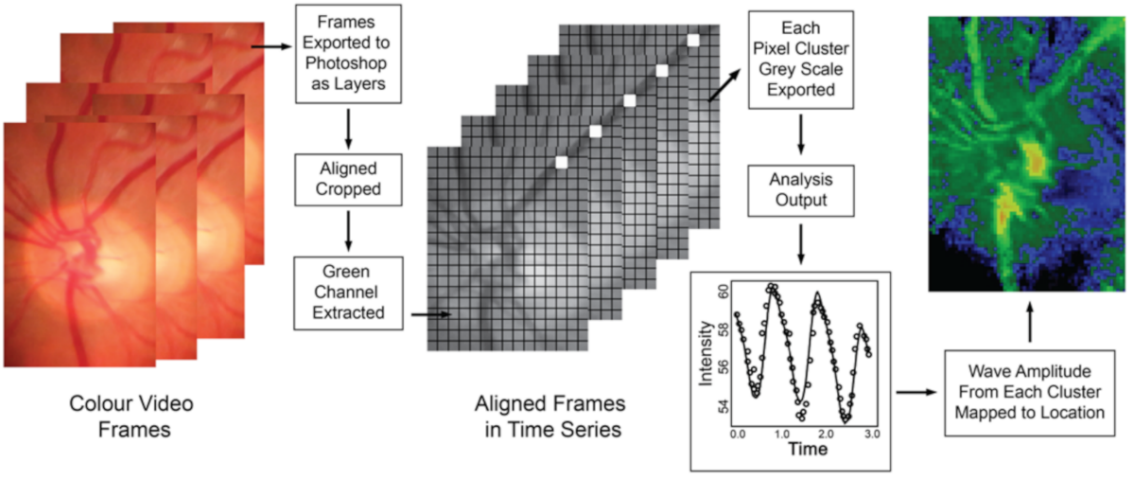

Fig. 1.29: Morgan's image processing schema for automatic detection of vessel pulsation [217].

tection of vessel pulsation mapped to corresponding location in retina [217, 219]. The detected intensity level in his measurement demonstrates the relative blood volume in the vessels. The whole schema of the image processing is in **Figure 1.29**. Morgan's research group used green channel of the detected image sequence to be processed. The separate images were divided into clusters and the intensities in clusters were locally transformed by using negative logarithm. The intensity time series of each cluster was extracted and fitted with estimated linear spline regression. The heat maps are calculated based on intensity amplitudes of each cluster. The color code corresponds to intensity amplitude level (where the intensity amplitute level range is 0-40). The heat map was thresholded with the *ideal threshold*. The level of *ideal threshold* was set to maximize specificity and sensitivity and was evaluated based on comparison with subjective mapping of vessel pulsations in images by two observers. Overall *ideal threshold* was set to 5, although the *ideal threshold* value differs in range from 2-10 over the participants. [217] In these works, the authors omits the variability in the waveforms over the retinal tissues and vessels.

In the next work, Morgan's research group designed a model to fit the extracted temporal intensity data from determined anatomical structures (lower and upper retinal vein, artery, **Figure 1.30A**) and in 5x5 px arrays across the whole image. Here, the modeled function modeling of retinal pulsation is considered as a function of three components, i.e., periodic, non-periodic and stationary error. The periodic component periodic $f_p(t)$ covers the periodic cardiac induced changes, i.e. retinal pulsation, and it is modelled using Fourier series. Non-periodic component includes temporal intensity trends (i.e., decrease, increase) and is modeled a as linear spline.

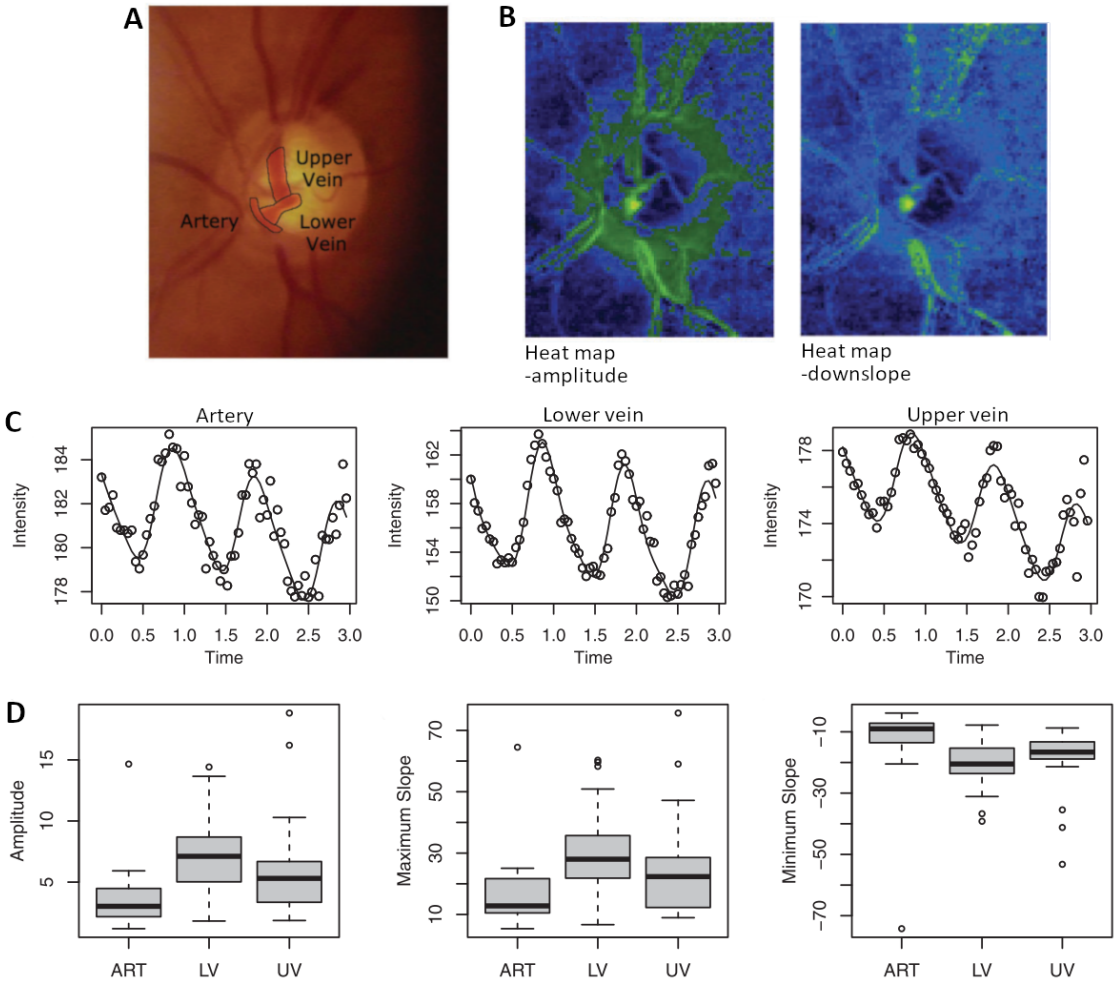

Fig. 1.30: Betz-Stablein's vessel pulsation modeling. A, Investigated anatomical structures, i.e., artery, lower and upper vein B, Heat maps generated based on pulsation amplitude and downslope C, Modeled function fitted on temporal intensity data of artery, lower and upper vein D, Amplitude, maximum and minimum slope values for artery, lower and upper vein across the dataset. [20].

[20]

The modeled function was fitted to temporal intensity data of arrays in the image and the retinal heat maps were generated based on amplitudes and slopes **Figure 1.30B,C**. The authors in this work presumed the variability of the waveforms accross the vessels. Authors fitted modeled function on temporal intensity curves of artery, lower and upper retinal vein. All three determined vessels differs in amplitude, maximum and minimum slope(**Figure 1.30D**).

It is not just the intensity level to evaluate. As noted before, LSI evaluated the size of detected speckles and gives mean blur rate, the equivalent of blood flow

velocity. The pulse-waveform analysis along with evaluated parameter (**Figure 1.31**) and the physiological interpretation was studied in the work of Luft. [196]. Luft et al. designed and evaluated parameters such as blowout time, blowout score, skew, acceleration time index, rising and falling rate, flow acceleration index and resistivity index. [196]

In summary image processing of the retina video-recordings along with the parametrization of measured atributes is still in early stages. Although the companies included further processing software in their commercially available devices, the processing tools may not meet the researchers requirements. Therefore some researchers use the qualitative and subjective methodologies [45, 285]. Other researchers using custom-built devices uses their own algorithms for the processing. Generally, there is no gold standard, universal open-source processing tool evaluating the retinal phenomena.

1.4.4 Other applied algorithms in retinal imaging field

Besides the algorithms directly processing the parameters (diameter, intensity level, ...), other operations are used in the retinal imaging field.

Regardless the measured atribute, one of commonly used preprocessing step is contrast-limited adaptive histogram equalization CLAHE [343] utilized in [87, 253, 287].

Interesting step in preprocessing is utilization of principal component analysis as filter to remove non-pulsatile dynamic features prior to temporal measurement of vessel diameter [214, 215].

1.5 Multivariate Statistics

Retina imaging field provide a unique space for utilization of various multivariate statistics algorithms. As retinal sequences are 2-dimensional data in time that may be represented by a 3D matrix of periodic and nonperiodic events, the utilization of principal or independent component analysis seems promising for extraction of these events.

1.5.1 Principal component analysis

Principal component analysis (PCA) is the most common and oldest method of the multivariate data analysis [211]. The main goal of the PCA is to reduce the dimensionality of the data therefore PCA usually represent a first step in analyzing

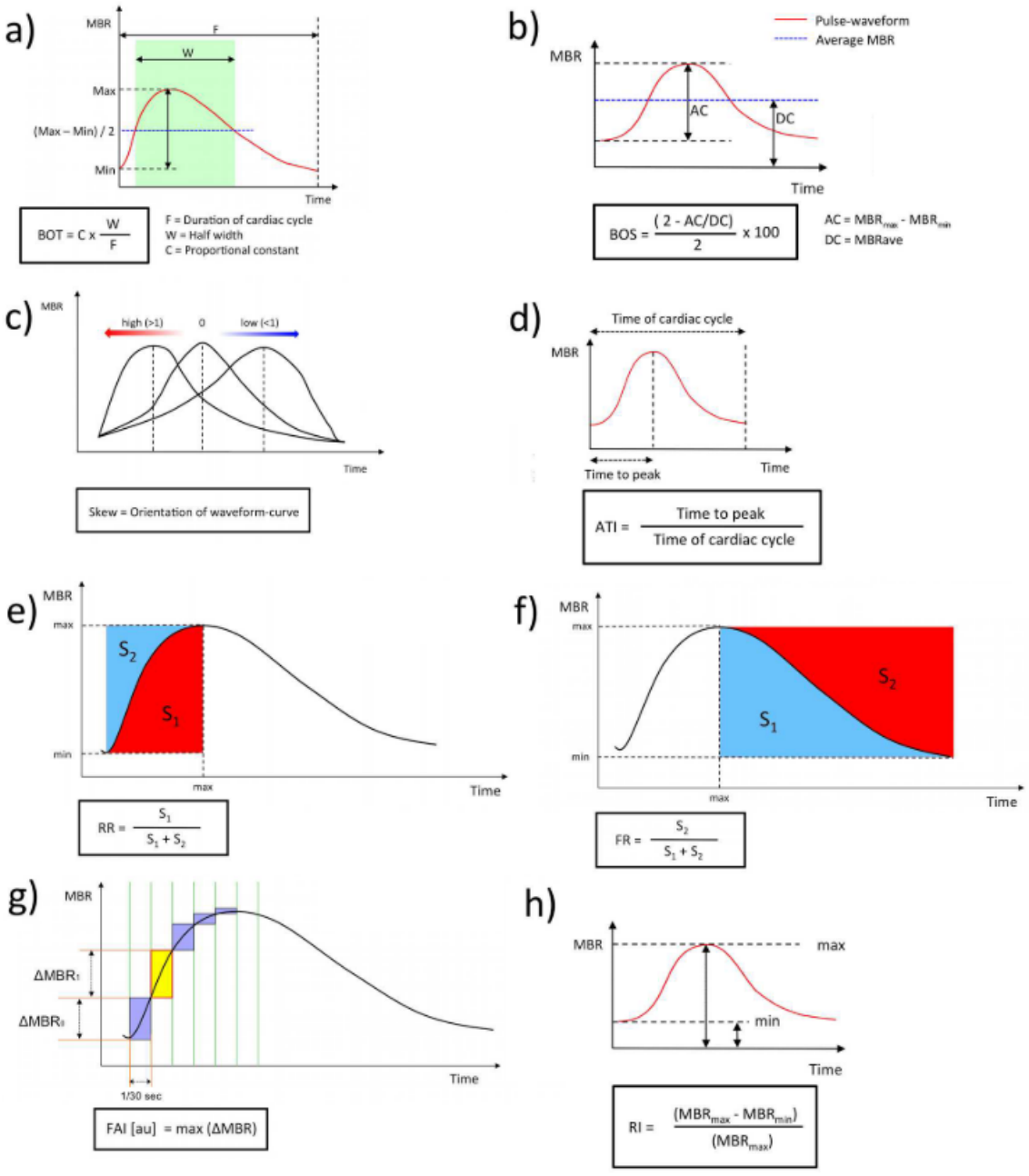

Fig. 1.31: LSI mean-blur-rate pulse-waveform analysis. BOT - blowout time is the ration of the half width to duration of a cardiac cycle. BOS - blowout score is calculated from the minimum, maximum and average mean blur rate. ATI - acceleration time index is a ration of time to peak to duration of a cardiac cycle. FAI - flow acceleration index represent highes increment between two frames. RI - resistivity index is the ration of mean blur rate peak-to-peak amplitude to mean blur rate maximum. RR - rising rate, FR - falling rate [196].

of large data sets. Additionally, PCA covers other mathematical tasks as signal denoising, blind source separation, data compression, etc. [211].

The main goal is to reduce the dimensionality of the data set consisting of interrelated variables, while preserving possibly the same amount of variation as present in the data [1, 211]. To do so, PCA computes a new set of orthogonal basis re-expresing the data so the new basis will filter out noise and help determine the important and redundant dynamics of the data [288].

PCA uses basic linear algebra and statistics. The usage of linear algebra and basic statistics only is linked to several assumptions defined prior the PCA calculation. One of the assumptions is linearity. Linearity defines a problem as a change of basis [288]. The assumption of linearity reduces a set of potential new basis to sets of basis which are a linear combination of the original set of basis. PCA also assumes the Gaussian, zero-mean, probability distribution of the dynamics of each variable. Zero-mean probability distribution can be described by mean and variance only, so the PCA can be limited to basic statistics. The third PCA assumption is that the components with large variances have important dynamics. The last, the principal components are orthogonal. [288]

As the assumptions are defined, the PCA and its goals may be described more mathematically. PCA computes the new set of basis which is a linear combination of the original set. Thus the new re-representation of data is a result of the original data matrix linearly transformed by a new set of basis. The new set of basis is chosen to reduce the noise and redundancy in the data. The noise is mathematically characterized with signal-to-noise ratio (SNR) computed as a ratio of a signal and its noise variances σ^2_{signal}, σ^2_{noise} (**Equation 1.14**). [288]

$$SNR = \frac{\sigma^2_{signal}}{\sigma^2_{noise}} \tag{1.14}$$

More importantly, PCA solves the problem of redundancy in the data. The example of the redundancy is when two variables are correlated and one can be expressed as a linear combination of another and thus can be reduced (**Figure 1.32**). Redundancy is quantified with variances within one variable (e.g. σ^2_A within a variable A), and covariances between two different variables. For variables A and B represented by its vectors $\mathbf{a}$ and $\mathbf{b}$ of length n, the covariance $\sigma^2_{\mathbf{a,b}}$ is calculated with **Equation 1.15**, where T is mathematical operation of transpose. [288]

$$\sigma^2_{\mathbf{a,b}} = \frac{1}{n-1}\mathbf{a}\mathbf{b}^T \tag{1.15}$$

Hence, for the data set X of m variables and n observations, i.e. matrix $\mathbf{X}(m, n)$, the covariance matrix $\mathbf{S_X}$ may be calculated as follows (**Equation 1.16**)

$$\mathbf{S_X} = \frac{1}{n-1}\mathbf{X}\mathbf{X}^T \tag{1.16}$$

Fig. 1.32: Example of low and high redundancy between two variables r_1 and r_2. The third is example of two highly correlated variables indicates high reduncancy (r_2 can be expressed as a linear combination of r_1, i.e., $r_2 = kr_1$) [288].

Covariance matrix $\mathbf{S_X}$ is a symmetric matrix of $m \times m$ dimensions, where variances are placed on diagonal and covariances off-diagonal. The example of $\mathbf{S_X}$ for $\mathbf{X}$ consisted of $m = 3$ variables represented by vectors $\mathbf{x}$,$\mathbf{y}$,$\mathbf{z}$ is in **Equation 1.17**, where $\sigma^2_{\mathbf{y,x}} = \sigma^2_{\mathbf{x,y}}$. It is important to note, that if $\sigma^2_{\mathbf{x,y}} = 0$, the variables x,y are entirely uncorrelated. In case of $\sigma^2_{\mathbf{x,y}} = \sigma^2_{\mathbf{x}}$, the variable $\mathbf{x} = \mathbf{y}$ and one of the variables may be reduced.

$$\mathbf{S_X} = \begin{bmatrix} \sigma^2_{\mathbf{x}} & \sigma^2_{\mathbf{x,y}} & \sigma^2_{\mathbf{x,z}} \\ \sigma^2_{\mathbf{y,x}} & \sigma^2_{\mathbf{y}} & \sigma^2_{\mathbf{y,z}} \\ \sigma^2_{\mathbf{z,x}} & \sigma^2_{\mathbf{z,y}} & \sigma^2_{\mathbf{z}} \end{bmatrix} \tag{1.17}$$

This means, to remove redundancy in the data, the covariances (off-diagonal terms) must be zero. In this case, PCA is computing a new set of orthogonal basis which transforms the original matrix $\mathbf{X}$ into a new matrix $\mathbf{Y}$ so its covariance matrix $\mathbf{S_Y}$ is diagonalized [288].

Eigenvector decomposition. The easiest way, how to diagonalize a square symmetric matrix is via eigenvector of covariance while utilizing mathematical theorems: 1) a matrix is symmetric if it is orthogonally diagonalizable and 2) a symmetric matrix $\mathbf{A}$ is diagonalized by a matrix of its orthonormal eigenvectors according to **Equation 1.18**

$$\mathbf{A} = \mathbf{EDE}^T \tag{1.18}$$

where matrix $\mathbf{E}$ includes eigenvectors and $\mathbf{D}$ is a diagonal matrix that includes eigenvalues corresponding to the eigenvectors in matrix $\mathbf{E}$ [288].

Let's have a dataset $\mathbf{X}$ with m variables and n samples each, X(m,n). Then, the new projection of data $\mathbf{Y}$ is calculated as **Equation 1.19** where P is orthonormal matrix of new set of basis while covariance matrix $\mathbf{S_Y}$ is diagonalized. The covariance matrix can be expressed using $\mathbf{PX}$ instead of $\mathbf{Y}$ (**Equation 1.20**). [288]

$$\mathbf{Y} = \mathbf{PX} \tag{1.19}$$

$$\mathbf{S_Y} = \frac{1}{n-1}\mathbf{YY}^T = \frac{1}{n-1}\mathbf{P}(\mathbf{XX}^T)\mathbf{P}^T \tag{1.20}$$

The matrix $\mathbf{XX}^T$ is a symmetric matrix diagonalizable by an orthogonal matrix of its eigenvectors according to second theorem defined in previous paragraph, i.e. there exists a diagonal matrix $\mathbf{D}$ where $\mathbf{XX}^T = \mathbf{EDE}^T$ (columns of $\mathbf{E}$ are the eigenvectors of $\mathbf{XX}^T$). The proof, that suitably selected $\mathbf{P}$ diagonalizes covariance matrix $\mathbf{S_Y}$ comes with substitution of $\mathbf{XX}^T$ with $\mathbf{EDE}^T$ where matrix $\mathbf{P}$ is to represent $\mathbf{E}^T$, hence **Equation 1.21** [288].

$$\mathbf{S_Y} = \frac{1}{n-1}\mathbf{P}(\mathbf{P}^T\mathbf{DP})\mathbf{P}^T = \frac{1}{n-1}\mathbf{D} \tag{1.21}$$

Simply, the required principal components, i.e. the new set of basis P, are eigenvectors of matrix $\mathbf{XX}^T$, i.e. $\mathbf{E}_{\mathbf{XX}^T}$.

Important to note, the eigenvector decomposition solution serves for square, positive semi-definite matrices. The most of the matrices are not even square. Fortunately, as written in previous paragraphs, the variance and mean are fully sufficient statistical description preserving all the information about the dataset that PCA needs, hence the covariance matrix can be used in place of the original dataset.

Singular value decomposition. More generalized solution of PCA is via singular value decomposition (SVD) serving also for rectangular matrices [1, 211]. SVD of dataset $\mathbf{X}$ including m variables and n samples/observations, i.e. $\mathbf{X}(n, m)$, where each variable was normalized to have zero mean (i.e. column-centered), is expressed as **Equation 1.22**.

$$\mathbf{X} = \mathbf{U\Sigma V}^T \tag{1.22}$$

where $\mathbf{U}$ and $\mathbf{V}$ are matrices with orthonormal columns while $\mathbf{U}$ is a matrix of left singular vectors of (n, n) matrix $\mathbf{XX}^T$, $\mathbf{V}$ is a matrix of right singular vectors of (m, m) matrix $\mathbf{X}^T\mathbf{X}$, and $\mathbf{\Sigma}$ is a diagonal matrix of singular values of matrix $\mathbf{X}$[1, 108, 134, 288]. The squares of singular values in $\mathbf{\Sigma}$ divided by $(n-1)$ are equivalent to eigenvalues of matrix $\mathbf{XX}^T$ and gives values of variances of final principal components. Singular values in diagonal matrix $\mathbf{\Sigma}$ are in descending order which defines also the order of corresponding columns in $\mathbf{U}$ and $\mathbf{V}$ [1, 108, 134].

SVD can be calculated in full dimensions of particular matrices $\mathbf{U}$, $\mathbf{\Sigma}$ and $\mathbf{V}$ according to **Equation 1.23**) [288], or in "economy" version (**Equation 1.24**) [108]

that removes zeros from diagonal matrix $\mathbf{\Sigma}$ along with the columns in $\mathbf{U}$ or $\mathbf{V}$ that are multiplied with zero diagonal values of $\mathbf{\Sigma}$ [134], i.e. economy PCA preserves only those columns of $\mathbf{U}$ and $\mathbf{V}$ corresponding to its non-zero eigenvalues. The economy PCA applies when there is more samples than variables in the dataset, i.e. $m < n$. In case of more variables, i.e. $m > n$, then $\mathbf{\Sigma}$ will be of $(n \times n)$ dimensions. Considering r the rank of matrix $\mathbf{X}$ while $r \leq min(n, m)$, then **Equation 1.25** is applied [134].

$$\mathbf{X}_{n\times m} = \mathbf{U}_{(n\times n)}\mathbf{\Sigma}_{(n\times m)}\mathbf{V}^T_{(m\times m)} \tag{1.23}$$

$$\mathbf{X}_{n\times m} = \mathbf{U}_{(n\times m)}\mathbf{\Sigma}_{(m\times m)}\mathbf{V}^T_{(m\times m)} \tag{1.24}$$

$$\mathbf{X}_{n\times r} = \mathbf{U}_{(n\times r)}\mathbf{\Sigma}_{(r\times r)}\mathbf{V}^T_{(m\times r)} \tag{1.25}$$

Projection of the original observations to principal component space, i.e. projection/factor score/score matrix $\mathbf{F}$, is expressed via multiplication of original data set $\mathbf{X}$ and right singular vectors in $\mathbf{V}$ **Equation 1.26**. Singular vectors in $\mathbf{V}$, also called the loadings, represents the geometrical transformation (similarly as in **Equation 1.19**) [1, 134].

$$\mathbf{F} = \mathbf{XV} = \mathbf{U\Sigma V}^T\mathbf{V} = \mathbf{U\Sigma} \tag{1.26}$$

Important to note, the original matrix can be reconstructed based on **Equation 1.26** as **Equation 1.27** (**Figure 1.33**) [1, 108].

$$\mathbf{X} = \mathbf{FV}^T \tag{1.27}$$

One of the algorithm for SVD solution is called "power iteration" [108]. This algorithm computes component by component as an iterative calculation that enumerate vectors in $\mathbf{U}$ and $\mathbf{V}$ separately for each component. Algorithm works with initial estimate for of V vector for first component and computes the estimation for corresponding vector in $\mathbf{U}$. In the next step, the estimate for $\mathbf{U}$ vector is normalized and used for optimizing the initial value of vector $\mathbf{V}$. The values of both vectors of $\mathbf{U}$ and $\mathbf{V}$ are optimized with each iteration.

Results and interpretation. Important and difficult at the same time is the interpretation of the results. SVD decomposes the data set $\mathbf{X}$ to left and right singular vectors $\mathbf{U,V}$ respectively, and singular values in $\mathbf{\Sigma}$. However, in case of PCA, the main expected results for data analysis are scores, loading and variances explained.

To summarize mathematical outputs above, squares of singular values are actually the variances of final principal components. The most important principal components are those with the biggest variances. The right singular vectors (columns in

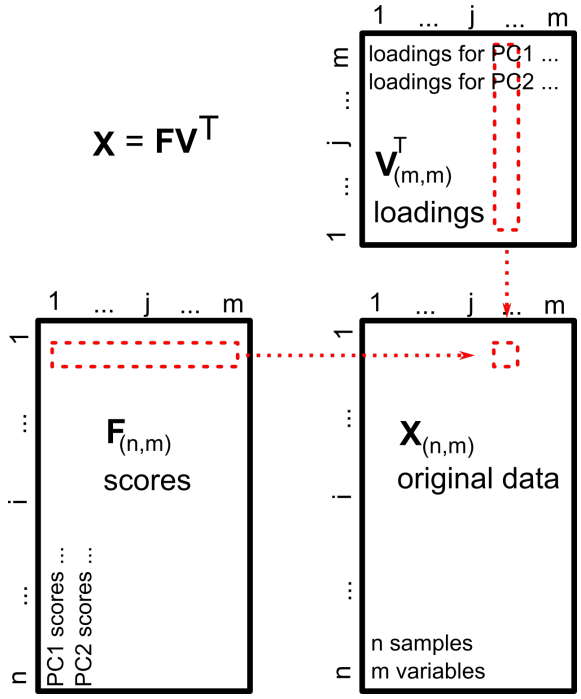

Fig. 1.33: Reconstruction of original data set matrix $\mathbf{X}$ based on SVD outputs. Element $\mathbf{X}_i, j$ as a result of a dot product of ith row in scores $\mathbf{F}$ and jth column of transposed loadings $\mathbf{V}^T$ [108].

$\mathbf{V}$) of the column-centred data matrix $\mathbf{X}$ are called loadings, i.e. principal component coefficients or the principal axis, and represent the contribution of each variable to each principal component [108]. Geometrically, loadings represent the coefficients of geometric transformation including the rotation, that projects the original dataset to a new set of basis while explaining the most variance possible (**Figure 1.34**). In a closer explanation, the loadings are defined by a cosine function, i.e. each principal component axis is defined by the cosine of its angle of rotation to relative its original axis [108].

The data $\mathbf{X}$ projected to a new set of basis are the principal components, i.e. scores $\mathbf{F}$ (projection matrix/factor scores) where the values are the positions of the samples in the new coordinate system [108]. The scores can be presented also as left singular vectors weighted by singular values (**Equation 1.26**). The mathematical relationship between the scores and original dataset is visualized in (**Figure 1.33**) demonstrating the decomposition of original data to scores and loadings.

Overall, the PCA does not use any prior knowledge about the analyzed system. This fact brings both advantages and disadvantages. One of the PCA pros is the objectivity of the results, as these were obtained without further motivation. On the other hand, the prior knowledge about the system may be used to characterize the

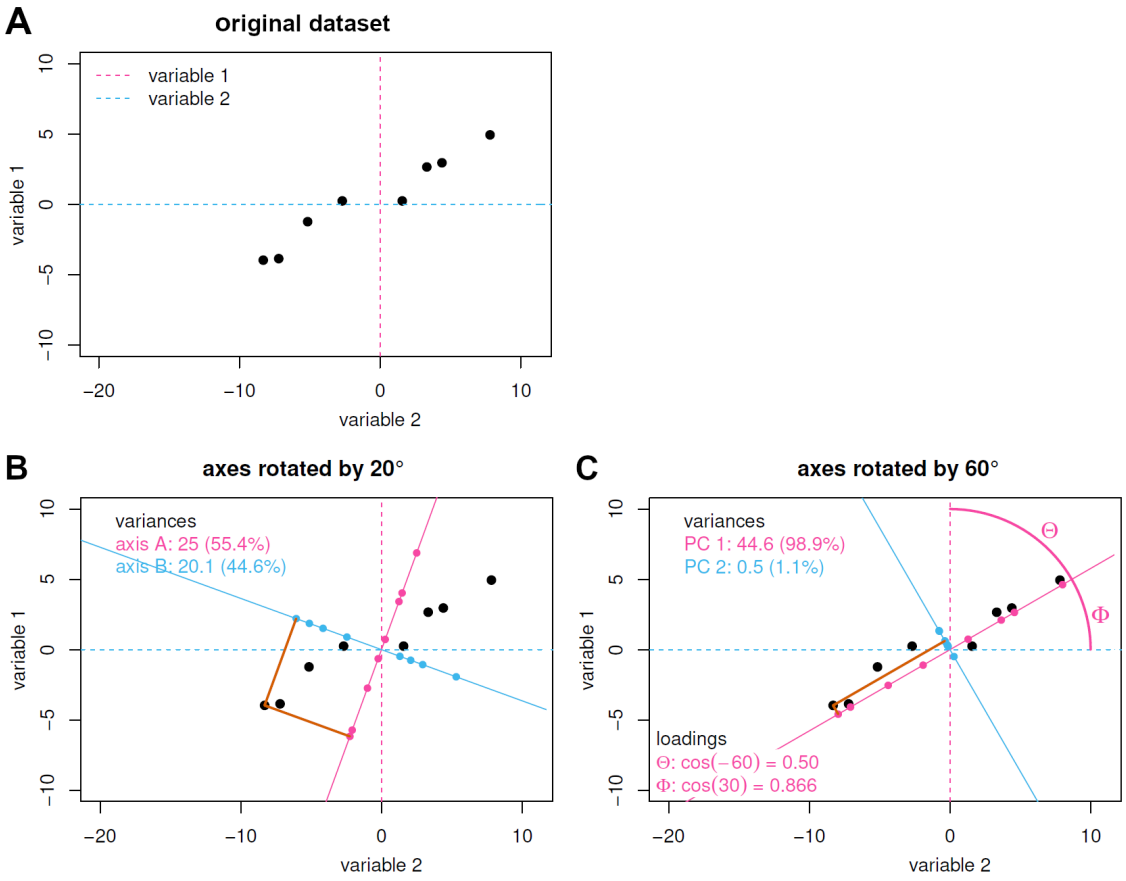

Fig. 1.34: Rotation of original axes to maximize variance along one of two axes. A, Scatterplot of original dataset B, axes A, B rotated by 20° while explained 55.4% and 20.1% variance respectively C, axes rotated by 60° marked as first and second principal component axes as it demonstrates the maximum variance, i.e. 98.9% and 1.1% for A and B respectively. [108]

new orthogonal basis which may lead to better and precise results and potentially avoid inaccurate separation. [258, 288]

Shortly, PCA reveals the hidden dynamics and reduce the dimensionality of the data. These properties of mathematical operation of PCA represents a great potential in dynamic retinal imaging which may define and localize the dynamics of retinal pulsation phenomena.

1.5.2 Independent component analysis

Except PCA, independent component analysis (ICA) is another data-driven approach method of multivariate statistics widely used for blind source separation or feature extraction.

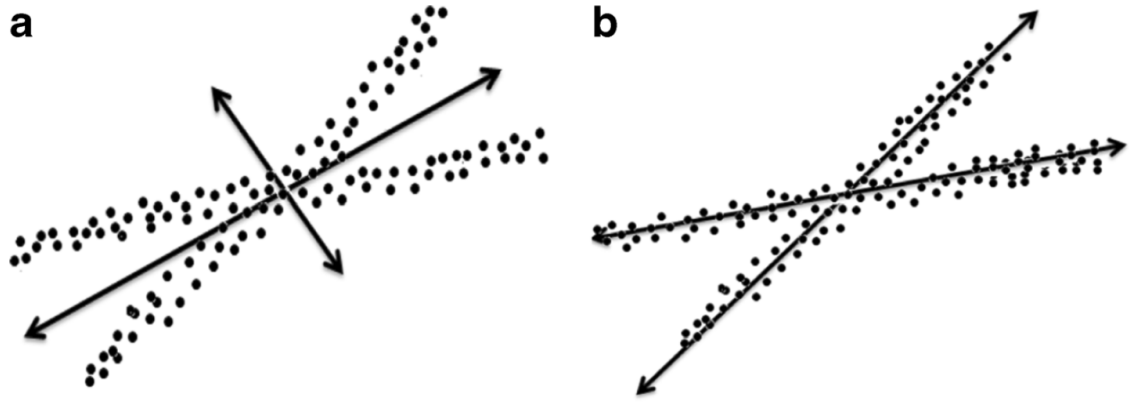

Fig. 1.35: Projections of PCA (a) and ICA (b) axes. [192]

To compare both methods shortly, both PCA and ICA removes correlations from the data however the ICA removes also higher order dependence. In other words, while PCA removes the correlations through diagonalization of covariance matrix and maximize variance (hence the 2nd order statistics), ICA uses higher order statistics to maximize mutual independence among the components through either minimization of mutual information or maximization of non-Gaussianity. As a result, the principal components are orthogonal and ordered according to explained variability (i.e. importance) while independent components do not have to be necessarily orthogonal and all the components are equally important. [121, 126, 192, 213] **Figure 1.35** demonstrates projections of PCA (a) and ICA (b) axes: PCA rebuilds the sample data according to the found unit orthogonal vector basis and in this case, PCA axes do not correspond to data well. As the ICA is not enforcing the orthogonality, ICA axes on the other hand are along with the axis of the largest statistical directions. [192, 213]

Independent component analysis is seeking the components which are not only uncorrelated but also mutually independent. Two variables are statistically independent if information of the first value of the first variable does not give any information on the value of the second variable, and vice versa [121]. In other words, the two variables are statistically independent if the joint distribution of the variables is a product of their marginal distributions. Mathematically, the independence of two variables y_1 and y_2 may be described with their probability density functions: the variables y_1 and y_2, with their marginal probability density functions $p_1(y_1)$ and $p_2(y_2)$ respectively, are independent if their joint probability density function $p(y_1, y_2)$ is factorizable as **Equation 1.28** [121].

$$p(y_1, y_2) = p_1(y_1)p_2(y_2) \tag{1.28}$$

Independent component analysis assumes the observations are generated as a

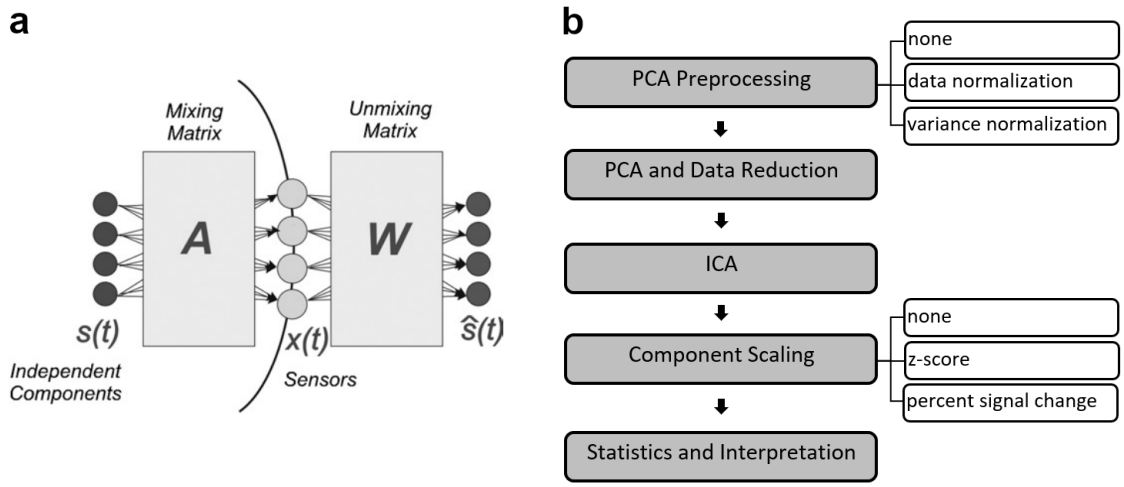

Fig. 1.36: Independent component analysis. **a,** General principle of ICA: ICA assumes the observations $\mathbf{x}(t)$ are generated as a combination of underlying independent sources $\mathbf{s}(t)$ and computes the estimates of the original sources $\hat{\boldsymbol{s}}(t)$. [126] **b,** ICA data workflow.

combination of underlying sources and computes the estimates of the original sources based on observed data only, without any prior knowledge (**Figure 1.36a**). Let's have m observations at instant time t, $\mathbf{x}(t) = [x_1(t), x_1(t), ...x_m(t)]^T$ that are results of the n underlying sources $\mathbf{s}(t) = [s_1(t), s_1(t), ...s_n(t)]^T$ combined together with a mixing matrix $\mathbf{A}$, i.e. **Equation 1.29** [126]. Independent components analysis then computes the estimates of underlying sources $\hat{\boldsymbol{s}}(t)$ and unknown de-mixing matrix $\mathbf{W}$ (**Equation 1.30**).

$$\boldsymbol{x}(t) = \boldsymbol{A}\boldsymbol{s}(t) \tag{1.29}$$

$$\hat{\boldsymbol{s}}(t) = \boldsymbol{W}\boldsymbol{x}(t) \tag{1.30}$$

Additionally, the computed estimated sources $\hat{\boldsymbol{s}}(t)$ are not ordered as in PCA so all the sources are of the same importance. As the components are not ordered and the number of sources is not known, the data reduction in form of PCA is an usual step prior to ICA. **Figure 1.36b** demonstrates data workflow while using ICA, that includes also general data preprocessing steps (i.e. mean extraction, variance normalization), PCA and data reduction. [65, 126]

To compute the estimates of the underlying sources $\hat{\boldsymbol{s}}(t)$, the most of the ICA algorithms use the basic assumptions which simplify the computation and makes the ICA more tractable [126]. The most of the assumptions are about the process of mixing the original sources $\mathbf{s}(t)$, hence the matrix $\mathbf{A}$. The mixing is supposed

to be linear, noiseless, stationary with a square mixing matrix. The assumption of linearity and noiselessness means, that the observations $\mathbf{x}(t)$ are generated by mixing the original sources using linear superposition without any additional data distortion caused by noise. The mixing process is stationary so its statistical parameters (i.e. mean, variance, etc.) are time independent. More, generally applies that the number of observations exceeds the number of sources, i.e. $m > n$. However, the most of ICA algorithms simplifies the computation with an assumption that the number of observations corresponds to the number of sources, i.e. $m = n$, hence the square mixing assumption. [126] Next assumption is the statistical independence of the sources so the sources meet the condition of independency as described earlier. Additionally, it is assumed, the distributions of the components are non-Gaussian with finite moments of any degree [7].

While computing ICA, there are another facts that must be taken into consideration: neither the variances or the order of the independent components can be determined. The explanation for these is that both $\mathbf{s}$ and $\mathbf{A}$ are being unknown. Mathematically, the coefficient multiplying the vector of observations can be weighted and also canceled by corresponding vector in matrix $\mathbf{A}$ multiplied by the same coefficient [121]. This implies the differences in magnitudes of the components. To avoid these differences, there is another assumption of unit variance of the independent components that is reached by adapting of matrix $\mathbf{A}$ to comply this restriction. [7, 121]

The ICA algorithms may be categorized into algorithms based on higher order statistics and time structure based algorithms. Furthermore, there are ICA extensions which additionally use prior knowledge about the mixing process or character of the observations. [126] Time structure based algorithms and further extensions of ICA are out of scope of this thesis, and only higher order statistics based ICA methods will be described below.

Higher order statistics based ICA methods. The general process of ICA via higher order statistics includes a postulating a certain parametric family for the marginal probability distributions followed by optimizing of a contrast function. The main criteria of statistical independence is minimization of mutual information and maximization of non-Gaussianity. The contrast function representing the mutual information are measured by Kullback–Leibler divergence or maximum entropy. The criteria of non-Gaussianity is motivated with Central limit theorem saying the sums of non-Gaussian random variables have more Gaussian distributions than the original random variables individually. The contrast function representing the non-Gaussianity is measured through kurtosis or negentropy. Besides the mutual information and non-Gaussianity, ICA may be computed based on maximum likelihood approach. [126, 213, 270]

There are many algorithms representing non-Gaussianity statistical criteria. Particularly, open source fastICA algorithm estimates independent components via kurtosis (the 4th order cumulant) in its fast fixed-point iterative algorithm. The kurtosis is zero for Gaussian distributed signals. The general equation for the kurtosis of a zero-mean random variable v is in **Equation 1.31**. The optimization of the contrast function is via the maximization of kurtosis of random variables in order to make them non-Gaussian as much as possible.

$$kurt(v) = E\{v^4\} - 3(E\{v^2\})^2 \tag{1.31}$$

In other words, fastICA algorithm is looking for a linear combination of the sphered observations $\mathbf{w}^T\mathbf{x}$ (where $\mathbf{w}$ is considered as a weight vector and x_i as observations) such that has maximal kurtosis [120]. The first step of the algorithm is to estimate one independent component. A random vector of norm 1 is set as an initial vector $\mathbf{w}(0)$ of searched $\mathbf{w}(k)$. Then, the vector $\mathbf{w}(k)$, expressed as **Equation 1.31**, is being repeatedly calculated in iterations k until $\mid \boldsymbol{w}(k)^T\boldsymbol{w}(k-1) \mid$ is close to 1.

$$\boldsymbol{w}(k) = E\{\boldsymbol{x}(\boldsymbol{w}(k-1)^T\boldsymbol{x})^3\} - 3\boldsymbol{w}(k-1) \tag{1.32}$$

The next step in fastICA algorithm estimates other independent components. This step adds orthogonalizing projection in the loop to make sure that each estimated independent component is different [120].

The another popular algorithms using the non-Gaussianity is infomax, also called Bell-Seinowski algorithm, using neural network gradient-based algorithm, and JADE using joint approximate diagonalization of eigenmatrices.

1.5.3 Concurrent multivariate statistics

Besides PCA and ICA, multivariate statistics covers far more methods including multiple regression methods, multivariate analysis of variance (e.g. analysis of variance ANOVA, analysis of covariance ANCOVA), factor and cluster analyses, etc. These methods are out of scope of this thesis except for ANCOVA that was used in statistical analysis investigating between group differences including confounding factors. [255]

Analysis of covariance. Analysis of covariance ANCOVA originates in analysis of variance ANOVA, that compares between-group variances and within-group variances, and extends ANOVA with a multiple regression analysis. ANCOVA is utilized on data that includes at least one qualitative variable (continuous dependent variable) and at least one categorical variable (i.e., independent variable; e.g., group). ANCOVA is usually used when other covariate/s is/are present. In comparison to ANOVA, ANCOVA compares one variable in two or more groups while

considering the variability of other variables. The reason is that the other variables may be related to the dependent variable. ANCOVA partitions out the variances of the related variables from the residual variance of dependent variable to increase the statistical power.

1.5.4 Multivariate statistics in the biomedical engineering field

PCA and ICA, often called the blind source separation (BSS) methods, have been widely utilized to isolate signals of orthogonal or independent sources. In electroencephalography and magnetoencephalography, the BSS proved to be useful for a suppression of physiological noise [14, 42, 53, 55, 66, 103, 310, 309], separation of distinct oscillation sources [41, 122, 170], or enhancement of event-related potentials [52, 61, 231]. In functional brain imaging, the spatial ICA is a prime method forming data-driven functional connectivity matrices [30, 133, 307]. In cardiology, BSS (ICA) is used to extract atrial activity from electrocardiogram (ECG) recording of atrial fibrilation [259], or to remove artifacts from ECG signals acquired with wearable system (i.e. biologic origin: muscle activity, and technical: electrode displacement) [210]. Additionally, BSS via ICA/PCA may be used for extraction of fetal electrocardiogram from maternal [50, 123]. In ultrasound imaging, BSS via PCA was utilized to suppress noise (random distortion, i.e. electronic noise) and cluttering (artifacts originating in deterministic sources in the area of measurement, i.e. tissue movement and multiplicative noise) [199, 330]. BSS was also utilized in dynamic positron emission tomography to reduce the noise in data time-courses [130].

Despite advancements in various biomedical fields via BSS, the BSS has only been implemented with a limited extent in the dynamic retina imaging field. Temporal PCA was shown to be capable to filter out representative time-courses [214, 215]. However, BSS power to isolate spatially orthogonal or independent sources has not been tested yet. Therefore, the presented Ph.D. thesis will extend current knowledge about spatial BSS applicability in the retina imaging field and advance the field about innovative data-driven image analysis method isolating functionally distinct patterns in the optic nerve head hemodynamics.

1.6 Pitfalls of the state of the art

Lately, dynamic retinal imaging raises in popularity as it provides both static and dynamic information. The in vivo observations of hemodynamic changes or vessel pulsatility reflect the information about the retinal condition and its local pathologies as well as the vascular condition, and even systemic neurodegenerative diseases.

However, this field of dynamic retinal imaging lacks in several points, from technical to data processing aspect.

As the retinal imaging field is still developing in both technical and clinical sides (i.e. biomarker definition), there is currently no clinical standard for dynamic retinal imaging. All various kinds of methodologies utilized in the field (described in chapter *"Functional retina imaging and ocular hemodynamic assessment"*) have its pros and cons to consider. Promising commercially available RVA/DVA provides recordings in limited fps and semi-automated analysis only, thus it partially depends on subjective evaluation. Commercially available DOCT devices provides 3D image of retina in selected region. However the DOCT devices are expensive and bulky. As the biomarkers within the dynamic retinal imaging are not established yet, the mentioned devices are used especially in experimental settings and the proprietary software often limits the research teams in progress. Promising and popular among the researchers are various kinds of low-cost custom build experimental ophthalmoscopes with targeted image analysis. However, video-opthalmoscopy is still a developing field and many tasks in techniques, imaging and data processing remains unsolved.

Proprietary software of commercially available devices provides the basic analysis. Open source algorithms for image processing of the video-ophthalmoscopic recordings (including registration, feature extraction and subsequent analysis) are limited. Till now, the subjective evaluation of retinal pulsation phenomena in video-ophthalmoscopic recordings determining presence/absence categories or four-magnitude level categories according to Hedges scale persists till present and brings potential faults into the analysis. The whole image processing often lacks the full automatization of pulsatile pattern extraction, filtering the artifacts and objective evaluation.

The method of multivariate statistics, i.e. principal component analysis and independent component analysis, are widely used in neuroscience to locate the functionally distinct anatomical parts as the sources of observed signal. Video-opthalmoscopic recordings are represented with a similar data with a potential to use in a same way and automize the process of locating the specific pulsatile patterns in the retina. Yet, these methods were applied on retinal videosequences to reduce the noise only, and were never applied in a sense of blind source separation.

The clinical biomarkers via dynamic retinal imaging are not established yet. Many experimental studies provides promising candidates for biomarkers for detection of various diseases and presents also the changes in ocular hemodynamics between healthy controls and affected groups with various progression levels. However many researchers skipped the basal research on healthy controls that may define the significant physiological factors such as heart rate, age, sex, body mass index, etc.

and their influence on RPPs. In dynamic retinal imaging field using the ophthalmoscopic methods, the researcher focused mostly on spontaneous venous pulsations or arterial pulsation and link them to specific diseases. However, the origin of SVPs is still discussed and no experimental research confirmed any model explaining the SVPs. Neither the biological factors and their influence on SVPs are fully described. Additionally, there are other pulsation phenomena to research via ophthalmoscopy methods, e.g. pulsation of optic cup tissue.

2 Aims of doctoral thesis

Dynamic imaging of retina function represents a rapidly developing biomedical field of recent years. Although a video-ophthalmoscopic initiatives are dated early after 2000, fast high-resolution dynamic imaging systems along with necessary image processing methods (e.g., image registration) started to appear between 2010-2018. Yet, automated image quality assessment of retinal frames remains underdeveloped when compared to concurrent imaging fields. A data-driven automated "functional" feature extraction from retinal videos has not been satisfactory developed and optimized. There is also plenty of space for artifact suppression. For example, eye-blinks generates signal spikes in time-courses of retinal hemodynamics and efficient spike suppressing filter has not been presented. The clinical video-ophthalmoscopy field has also number of research expectations, such as improve early diagnosis of retinal diseases, non-invasively assess early failures in systemic diseases (e.g., hypertension, diabetes mellitus), or even predict level of intracranial pressure non-invasively. However, neither clinical research task is completely solved today. Moreover, basic biological research hypotheses also remain underdeveloped and should be answered to allow reliable clinical study design.

Overall, my doctoral thesis aims to pursue five specific aims:

1. Develop automated spatial feature extraction based on mutual temporal coherence rather than based on anatomical morphology as preferably used today.
2. Develop adaptable spike suppression filter optimized for time-courses of retinal hemodynamics.
3. Utilize existing or developed image processing and biomedical engineering techniques into clinical research applications.
4. Assess basic relationships between morphology of retinal hemodynamics and other biological variables and discuss implications for clinical study designs.
5. Conceptualize and design retina imaging experiment for simultaneous imaging of video-ophthalmoscopic recordings with invasively measured intracranial pressure (ICP) and other biosignals (finger photoplethysmography, respiration plethysmography, electrocardiogram, electrooculogram), modify hardware and software solutions for the experiment, and conduct proof of concept experiment of the hardware part.

3 Results

The core of my doctoral thesis is 1) development of currently missing piece of technology in retinal imaging - automatic methodology separating different pulsatile patterns in recordings of human retina; and 2) the application of this innovative approach providing new observations advancing the basal biological knowledge.

The first section of this chapter is focused on the utilization of higher order statistics methods, i.e., PCA and ICA, in retinal imaging in effort to develop methodology that automatically separates different pulsatile patterns in recording of human retina. The presented approach includes also the spike suppression filter to effectively reduce the effects of blinking artifacts in retinal recordings. Here, this topic is presented via published article (*IEEE Transactions in Medical Imaging*) and addresses the specific aims (1,2) defined in the Aims of Doctoral Thesis.

Application of the presented approach is described in the second section of this chapter via a published article (*Communications Biology*). The observation provided by utilization of the presented approach revealed the morphology of SVPs and OCPs and their relationship to biological factors - heart rate and age. These observations advance the basal biological knowledge and address the specific aims (3,4) defined in the Aims of Doctoral Thesis.

In an effort to address specific aim 5 defined in the Aims of Doctoral Thesis, I have co-designed the experiment simultaneously acquiring the retinal recordings, invasively measured ICP and other biosignals. The Design of the acqusition and acquired data are described in the third and fourth sections of this chapter. The ongoing experiment has a potential to reveal the relationship/origin of retinal pulsation phenomena and ICP.

During my doctoral studies I have partially focused on image quality assessment issue in retinal imaging. My outcomes were presented as a research article (*Electrorevue*), and a conference paper. However this topic does not represent a major outcome and it is not included in chapter *Results*. Additionally, I have also contributed to a clinical experiment in glaucoma research that utilize developed image processing techniques. This topic address the specific aim (3) defined in the Aims of Doctoral Thesis. Neither this topic is included in the chapter *Results* as it does not represent the major outcome.

3.1 PCA and ICA utilization in Retinal dynamic imaging

The application of higher order statistics in dynamic ophthalmoscopy for blind source separation of functionally distinct anatomical parts characterized with specific pulsatile patterns was published in journal of IEEE Transactions on Medical Imaging: Labounková, Ivana, et al. Blind source separation of retinal pulsatile patterns in optic nerve head video-recordings [172]

Author's contribution and Innovation. As a first author, I have developed a methodology utilizing principle and independent component analyses for blind source separation of functionally distinct areas in retinal video-sequences, called retinal pulsatile patterns. I have identified two highly reproducible pulsatile patterns (RPPs) through out the subjects, i.e. spontaneous venous pulsations SVP and optic cup pulsations OCP. The methodology reaches high detection rate of SVP (97.5% detection rate in single eye analysis) in comparison to variable detection in other methodologies or subjective evaluation utilized in the field (varying 15-99%[113, 124, 184, 335, 205]). The methodology revealed the influence of respiration on RPPs. I have participated on results interpretation and written the significant part of the manuscript.

The developed methods and presented pipeline are incorporated in Retina Imaging Toolbox which is publicly available at
https://github.com/umn-milab/retinaimagingtoolbox.

The authors's accepted version of the article is attached in the next pages of this Thesis (

Blind Source Separation of Retinal Pulsatile Patterns in Optic Nerve Head Video-Recordings

Ivana Labounkova, *Member, IEEE EMB*, Rene Labounek, *Member, IEEE EMB,* Igor Nestrasil, Jan Odstrcilik, Ralf P. Tornow and Radim Kolar

***Abstract*— Dynamic optical imaging of retinal hemodynamics is a rapidly evolving technique in vision and eye-disease research. Video-recording, which may be readily accessible and affordable, captures several distinct functional phenomena such as the spontaneous venous pulsations (SVP) of central vein or local arterial blood supply etc. These phenomena display specific dynamic patterns that have been detected using manual or semi-automated methods. We propose a pioneering concept in retina video-imaging using blind source separation (BSS) serving as an automated localizer of distinct areas with temporally synchronized hemodynamics. The feasibility of BSS techniques (such as spatial principal component analysis and spatial independent component analysis) and K-means based post-processing method were successfully tested on the monocular and binocular video-ophthalmoscopic (VO) recordings of optic nerve head (ONH) in healthy subjects. BSSs automatically detected three spatially distinct reproducible areas, i.e. SVP, optic cup pulsations (OCP) that included areas of larger vessels in the nasal part of ONH, and "other" pulsations (OP). The K-means post-processing reduced a spike noise from the patterns' dynamics while high linear dependence between the non-filtered and post-processed signals was preserved. Although the dynamics of all patterns were heart rate related, the morphology analysis demonstrated significant phase shifts between SVP and OCP, and between SVP and OP. In addition, we detected low frequency oscillations that may represent respiratory-induced effects in time-courses of the VO recordings.**

***Index Terms*—Blind Source Separation; ICA; Independent Component Analysis; Optic Nerve Head; PCA; Principal Component Analysis; Retina; Video-ophthalmoscopy; Spontaneous Venous Pulsations**

I. Introduction

EXAMINING the retinal hemodynamic changes is an emerging approach with many research and clinical applications not only in ophthalmology (e.g. diabetic retinopathy [1], glaucoma [2], [3]) but also in other medical fields such as neurology (e.g. Alzheimer disease [4], multiple sclerosis [5]) or cardiology (e.g. arterial stiffness [6], hypertension [7], diabetes [7]). The focus on the optic nerve head (ONH) hemodynamics represents a challenging task due to its extreme vascular complexity. Two arterial systems branching off the ophthalmic artery provide blood supply to ONH. The main source is the posterior ciliary artery supplying deeper layers of ONH and choroid via choroidal vessels. The central retinal artery (CRA) supplies the surface nerve fiber layer via retinal branches [8], [9]. Venous drainage of ONH is mainly carried out via the central retinal vein (CRV) and its tributaries [10], [11].

Several retinal hemodynamic phenomena related to the complex retinal vascular tree are observable as spatially specific dynamic patterns, which can be captured by various recording techniques. Spontaneous venous pulsations (SVP) of the CRV are the most obvious dynamic pattern. The SVP correspond to a sudden vein emptying that is observed as a vein collapse during systole and a subsequent vein dilation (i.e. refilling) during diastole [12]. SVP are detected along the retinal vein while it traverses the lamina cribrosa sclerae [13], [14]. SVP are influenced by subtle changes in the local pressure gradient between the intraocular pressure (IOP) within the eyeball and intracranial pressure (ICP) within the intravaginal space along optic nerve filled with cerebrospinal fluid [13]. Two other observable phenomena that were previously reported are venous pulsations due to diameter changes but without an observable vein collapse [15] and arterial pulsations with arterial bending, i.e. serpentine pulsations/movements [12], [15]–[17]. Both these blood vessel pulsations (BVP) are influenced by many factors such as systolic pressure, wall stiffness, vessel tortuosity, peripheral resistance, etc. [16]. Lastly, pulsatile variations of the ONH tissue were studied [17]–[21] and interpreted as changes of blood volume [22] or velocity [23] in the underlying microvessels, specifically in the optic cup [24]. Here, we name this phenomenon as the optic cup pulsations (OCP).

Theoretically, each of these phenomena may be detected in functionally distinct areas of ONH with heterogeneous retinal hemodynamic properties [24]–[27] and this was one of the hypotheses we tested here. Retinal hemodynamic may be characterized by quantitative markers (e.g. blood flow, blood

Manuscript received March 16, 2020; revised September 13, 2020; accepted November 16, 2020. Research was supported by Brno University of Technology grant n. FEKT-S-17-4487, Czech Health Research Council grant n. NV17-29452A, and by Department of Pediatrics, University of Minnesota with "Progressive" grant. *(Corresponding author: Radim Kolar)*

I. Labounkova is with the Department of Biomedical Engineering, Brno University of Technology, Brno, 612 00, Czech Republic, and with the Department of Pediatrics, University of Minnesota, MN 55414, USA (e-mail: xliber00@stud.feec.vutbr.cz; ilabounk@umn.edu).

R. Labounek, was with Department of Neurology, Palacky University in Olomouc, Czech Republic. He is now with the Department of Pediatrics, University of Minnesota, MN 55414, USA.

I. Nestrasil is with the Department of Pediatrics and the Center for Magnetic Resonance Research, University of Minnesota, MN 55414, USA.

J. Odstrcilik, R. Kolar (email: kolarr@vutbr.cz) are with the Department of Biomedical Engineering, Brno University of Technology, Brno, 612 00, Czech Republic.

R. P. Tornow is with Department of Ophthalmology, Friedrich-Alexander University of Erlangen-Nuremberg, Erlangen, Germany.

velocity, blood vessel density, etc.) using various approaches (e.g. ophthalmodynamometry, optical angiography, retinal Doppler techniques, and others) [2], [28]. Retinal video-recording (RVR) techniques were also proposed for *in-vivo* acquisition of local hemodynamic changes with varying spatial and temporal resolutions. The relatively basic principle utilized a slit lamp connected to a video detector [29], [30]. Several experiments acquired RVRs with classic [31] or scanning laser ophthalmoscopes [15]. Despite a sufficient spatial resolution, low temporal sampling and/or short time acquisition represented limitations of aforementioned techniques. Next, retinal vessel analyzer (RVA) acquires video-sequences with fundus camera and provides a semi-automated processing of temporal changes in vessel diameter and blood flow [32], [33]. XyCAM RI™ camera (*Vasoptic Medical Inc.*) relies on infrared light laser speckle imaging for a local blood flow acquisition followed by velocity analysis [34]–[37]. Laser Doppler methods are another approach to record retinal local blood flow velocity [38], [39]. All devices acquire the RVRs with high spatiotemporal resolution [33], [37]–[40], but cannot simultaneously record the RVR in both eyes. Also, most devices used relatively high retinal illumination intensity, which can cause discomfort to an examined subject and may change venular caliber and ONH blood flow [41].

Recently, monocular [18] and binocular [22], [42] video-ophthalmoscopes (VOs) using a low intensity non-coherent monochromatic light have been introduced. The VO measures the intensity change in the light absorption that corresponds to the blood volume variation in the retina [22]. VOs offer an "unlimited" temporal video-acquisition of retinal hemodynamics with a sufficient spatiotemporal resolution. The challenging factor is a limited signal to noise ratio due to eye safety considerations opting for a low light power source setup.

The analysis of specific dynamic patterns in RVRs has been performed by manual or semi-automated selections of the specific area of interest [15], [17], [18], [30], [32], [33], [43]. This approach is prone to subject-related bias that can potentially decrease the data analysis reliability and reproducibility. Despite the current knowledge in RVR, an automated algorithm separating RVR into functionally distinct areas is limited to spatiotemporal singular value decomposition (SVD) achieved with Doppler holography technique [44]. Automated algorithms provide reliable and reproducible analysis across subjects. As the spatiotemporal SVD may be seen as a high-computational-demand BSS technique, we propose BSS as an automated separator tool for RVR with low computational demands. Previously reported applications of similar BSS approaches have been limited to artifact suppression [15], [17]. In our preliminary studies on monocular [45] and binocular [46] RVR VO data we have outlined the utilization of two concurrent BSSs, i.e. spatial principal component analysis (sPCA) and spatial independent component analysis (sICA).

In the current study, we present a full description of the algorithm utilizing sPCA or sICA for the automated separation of functionally distinct ONH areas from mono/binocular VO data. We also examine presence of low frequency respiratory-induced effects in RVR. These effects have not been reported in previous retinal hemodynamic studies [15], [17], [43], [47], [48], [22], [30], [32], [33], [35]–[37], [40] but are well known in classic plethysmography [49]. Finally, we propose a novel adaptive non-linear K-means post-processing of retinal pulsatile pattern (RPP) dynamics and evaluate detection success rate for each expected RPP and delays between their dynamics.

II. Methods

A. Data approval, License statement & Experimental design

All participants were healthy subjects with physiological IOP values who signed an informed consent form approved by the ethical committee at the Friedrich-Alexander University of Erlangen-Nürnberg, in concordance with the Declaration of Helsinki. The subjects are part of the Erlangen Glaucoma Registry cohort (www.clinicaltrials.gov, NCT00494923) founded in 1991. All data analyses were performed with MATLAB R2017b (*MathWorks, Natick, USA*) and with its licensed or publicly available toolboxes, including our proposed open-source **Retina Imaging Toolbox** (RIT, ***Appendix A***).

Each subject was examined while comfortably sitting with head rested and positioned on a VO chin holder to limit subject's motion. Each subject was asked to fixate the eyesight at the target presented as red LED in VO.

B. Monocular VO data acquisition

Retinal video-sequences were acquired from the left eye in six participants (age 64±14 years, four females, IOP in range 14-21 mmHg; more physiological info in ***Appendix B***) with in-house invented monocular VO [18]. Briefly, the VO consists of one optical lens system (40D ophthalmic lens, 2 achromatic lenses), one monochrome CCD camera (UI-2210 SE-M-GL, USB interface, iDS, Germany), red LED forming the fixation target and LED monochromatic low power light source (wavelength λ=575nm) illuminating retina with 30μW/cm^2. Hemoglobin absorbs the highest light power for the used monochromatic wavelength and the reflected light changes are therefore modulated due to blood volume changes during the cardiac cycle [18]. The acquired 10s video sequences were saved in non-compressed AVI format with 25fps and matrix size 640×480px covering 20°×15° field of view (i.e. 1 pixel ≈ 9.3×9.3μm^2).

C. Binocular VO data acquisition

Retinal video-sequences were acquired simultaneously from both eyes in seven healthy subjects (age 69±14 years, four females, IOP in range 12-21 mmHg; more physiological info in ***Appendix B***) with in-house invented experimental binocular VO [22], [42], which is an extension of the monocular VO. The difference was in the camera type as two CMOS cameras (UI-3060 Rev 2, USB 3.0, iDS, Germany) were used. The device allows acquisition of two separated precisely synchronized video-sequences (one from each eye). Sequences were 10s long with 25fps and matrix size 1000×770px covering 20°×15° field of view (i.e. 1 pixel ≈ 6.0×6.0μm^2). The mono- and binocular groups were fully disjunctive except for one subject.

D. VO data preprocessing

For each mono- and binocular RVR, eyeball movements during an acquisition (in spite of a target fixation) were

eliminated via rigid image registration method using the first video frame as the reference image (output examples shown in ***Appendix A***) [50]. Due to the limited field of view (20°×15°) of our VOs and the presence of surrounding artifacts (e.g. time marks, specular light reflection), we limited the analysis to ONH and peripapillary area (i.e., area adjacent to ONH aka optic papilla). This region-of-interest (ROI) was delineated by a manually drawn mask. For a both-eye BSS, the preprocessed single-eye RVRs were merged into one binocular RVR.

E. Blind Source Separation of retinal pulsatile patterns

Regardless of monocular or binocular VO RVRs, a variable $\boldsymbol{X}$ represented a 2D matrix (of dimensions $\boldsymbol{X(T,P)}$ where $P>>T$) containing the full preprocessed and ONH segmented video-recording of one mono/binocular dataset. Each row of matrix $\boldsymbol{X}$ consisted of P pixels from ONH at one time point t (T is the number of frames). While $P>>T$, sPCA [51] or sICA [52], [53] can be estimated for the matrix $\boldsymbol{X}$ whose dimensions are similar to those in functional magnetic resonance imaging (fMRI). Since both BSSs have been widely utilized in fMRI analyses [53], [54] we have applied them in the RVR data analysis.

For sPCA, a covariance matrix $\boldsymbol{\Sigma_X}$ of $\boldsymbol{X}$ served as an input subsequently decomposed with singular value decomposition (Eq. 1) at matrix of eigenvectors $\boldsymbol{F}$ of dimensions $\boldsymbol{F(T,T)}$, and diagonal matrix of eigenvalues $\boldsymbol{\Lambda}$ of dimensions $\boldsymbol{\Lambda(T,T)}$ [51], [53]. The first four principal components (PCs) $\boldsymbol{X^*}$ of dimensions $\boldsymbol{X^*(4,P)}$ estimated as back-projection of the first four eigenvectors $\boldsymbol{F_{14}}$ into the input dataset $\boldsymbol{X}$ (Eq. 2) were considered as the result of the sPCA. The number of four components was set based on our assumption that there are three expected sources of spatially distinct phenomena (SVP, BVP or OCP) and a noise component.

$$\boldsymbol{\Sigma_X} = [\boldsymbol{F}_{14} \quad \boldsymbol{F}_{1T}] \begin{bmatrix} \boldsymbol{\Lambda}_{14} & 0 \\ 0 & \boldsymbol{\Lambda}_{5T} \end{bmatrix} [\boldsymbol{F}_{14}^T \quad \boldsymbol{F}_{1T}^T] \tag{1}$$

$$\boldsymbol{X^*} = \boldsymbol{F}_{14}^T \boldsymbol{X}. \tag{2}$$

Column eigenvectors of T samples in matrix $\boldsymbol{F_{14}}$ represent temporal fluctuations (i.e. time-courses) of these PCs. Each row vector of P samples in $\boldsymbol{X^*}$ was transformed to Z-scores and represented one of four observed spatially orthogonal PCs, which can be thresholded and rescaled back into the original anatomical space. All pixels where $|\boldsymbol{X^*}|<1$ ($p<0.3174$) were thresholded to 0. This threshold segments each component into an area of about 31.74% of the whole ROI. The three expected physiological orthogonal components would be then fully disjunctive and the expected "three-component" segmented area would cover about 95% of the whole ROI. The thresholded PCs defined distinct statistical parametric maps with potential different functional dynamics defined by eigenvectors in matrix $\boldsymbol{F_{14}}$. The levels of linear dependence between eigenvector and distinct local dynamics are proportional to local $|\boldsymbol{X^*}|$ values.

The sPCA output served as the input, with reduced data dimensionality and kept high explained data variance [51], [53] into the sICA that is optimized to separate spatially independent non-Gaussian sources better than sPCA, which is expecting Gaussian sources [52], [53]. Spatial ICA (Eq. 3) was estimated with FastICA optimizing algorithm [55].

$$\boldsymbol{X^*} = \boldsymbol{AS} \tag{3}$$

Matrix $\boldsymbol{S}$ with dimensions $\boldsymbol{S(4,P)}$ was the source matrix of spatially independent components. Same as for the matrix $\boldsymbol{X^*}$ from sPCA, each row of matrix $\boldsymbol{S}$ was transformed to Z-scores, thresholded and rescaled back into the original anatomical space. Statistical parametric maps in matrix $\boldsymbol{S}$ were thresholded to 0 in pixels $|\boldsymbol{S}|<1$ for the same reasons as used for $\boldsymbol{X^*}$ values in sPCA. Columns of mixing matrix $\boldsymbol{A}$ of dimensions $\boldsymbol{A(T,4)}$ characterized the dynamics of observed ICs.

Both BSSs were applied independently as follows: on monocular data for left eye RVR; on binocular data – for left and right eye RVRs separately; and for merged both-eye RVR.

Visual inspection of principle components matrix $\boldsymbol{X^*}$ and source matrices $\boldsymbol{S}$ discovered three reproducible spatial distinct patterns across right/left eyes and across subjects. Plus/minus signs in Z-score maps of the corresponding morphological spatial area varied across subjects and eyes. Therefore, the plus/minus signs of Z-scores of classified spatial areas had to be manually adjusted for all participants and eyes to be uniform to assure the proper analysis. If the sign was changed in spatial pattern of the principal or independent component, then it was also changed in the time-course where the DC component was subtracted first and again added afterward.

Counts, minimum Z-score, maximum Z-score, mean of suprathreshold positive/negative Z-scores, and relative areas of suprathreshold positive/negative Z-score maps were evaluated over all participants of all detected reproducible spatial patterns in estimated and sign uniformed matrices $\boldsymbol{X^*}$ or $\boldsymbol{S}$.

F. Post-processing of separated RPP time-courses

As the resulting time-courses of the RPP dynamics are often disrupted by random spikes corresponding to strong eye movements and/or blinks, we have designed the adaptive signal restoration technique utilizing a single-vector K-means clustering [56] at two classes with following local adaptive temporal interpolation of the disrupted signal samples.

After the BSS, an absolute gradient $\boldsymbol{g}$ of each RPP time-course vector $\boldsymbol{u}$ (i.e. $\boldsymbol{u}$ is a column of matrix $\boldsymbol{F_{14}}$ or $\boldsymbol{A}$) was estimated with a convolution formula (Eq. 4), where $\boldsymbol{h}=[1\ -2\ 1]$ is a finite impulse response function kernel approximating a local first derivative operator.

$$\boldsymbol{g} = |\boldsymbol{u} * \boldsymbol{h}| \tag{4}$$

This gradient signal was used as an input to K-means unsupervised method in order to separate samples into "undistorted" and "distorted" class. A total of 300 runs with random two-clusters initialization was used and the most frequent and reproducible result was interpreted as the final and "optimal" solution. Signal values classified as distorted were replaced with interpolated values utilizing one-dimensional cubic spline. Then, the output filtered signal was detrended and the gradient estimation with following 300 separate K-means clustering and cubic spline interpolation was repeated one more time to effectively suppress spikes of lower magnitude.

To test whether there was a change in linear dependence between non-filtered and filtered signals we evaluated Pearson correlation coefficients and power ratios between both signals.

G. Morphology analysis of RPP time-course phase shifts

A matrix ***M*** was built for the post-processed time-courses (details in the ***Appendix C***). The matrix ***M*** consisted of groups with five subsequent control points defining one period of the RPP. The first control point 1 is the beginning of the period. The control point 2 is the maximal positive peak (without the DC component in the signal) of the period. The control point 3 is the middle period zero-crossing point (without DC). The control point 4 is the minimal negative peak (without DC) of the period. The control point 5 is the ending zero-crossing point (without DC) of the period, which is simultaneously the control point 1 of the following RPP period. The control points were estimated and visually inspected for time-courses of all physiologically classified orthogonal and independent components. If necessary, manual corrections were done in the classification and non-harmonic parts of specific sequence were excluded.

The control points were used for evaluation of phase delay or synchronicity of the different physiological RPPs between themselves. For each subject and BSS technique, a mean heart rate period and a mean delay between the same type of control points were estimated. The delays were normalized with the mean heart rate period. To determine whether positions of some control points or all control points were "phase shifted", we applied a one-tail one-sample t-test rejecting the null hypothesis that the delay was ≥0. Multiple comparison corrections were not used due to low sample sizes. In this proof of concept study, the hypothesis that BSS can blindly separate spatially distinct, reproducible and phase shifted RPPs, was tested with significance $p \leq 0.05$. Single-subject mean amplitudes of RPP time-courses were estimated as mean difference between y-coordinates of control points 2 and 4.

H. RPP time-courses in negatively suprathreshold pixels

Source matrices ***X**** and ***S*** yielded both positive and negative suprathreshold Z-scores. We tested the relationship between the temporal dynamics of positive and negative suprathreshold pixels for all three patterns and both BSSs as follows. For both positive and negative suprathreshold pixels that were identified, the averaged intensity temporal dynamics were expressed and these pairs were visually assessed and compared to the BSS-identified time-courses from matrices ***F*** or ***A***.

III. Results

A. Monocular VO

Spatial PCA and sICA, demonstrated three reproducible spatially distinct patterns in their orthogonal and/or independent components. The patterns are SVP of CRV, OCP with larger diameter vessels localized in ONH nasal part and the third group that we labeled as "other". A representative single-subject example of detected patterns with temporal dynamics is shown in **Fig. 1a**. The SVP and OCP were detected in almost all participants with both BSSs. The "other" pattern demonstrated limited inter-subject reproducibility (**Table 1**).

Group averaged maximal/minimal/mean Z-scores, mean positive/negative suprathreshold areas and total suprathreshold areas are listed in **Table 1**, together with group standard deviations for both BSS methods. The spatial PCA detected larger suprathreshold areas than sICA (**Table 1**). All obtained values were comparable to binocular dataset results (**Table 1**).

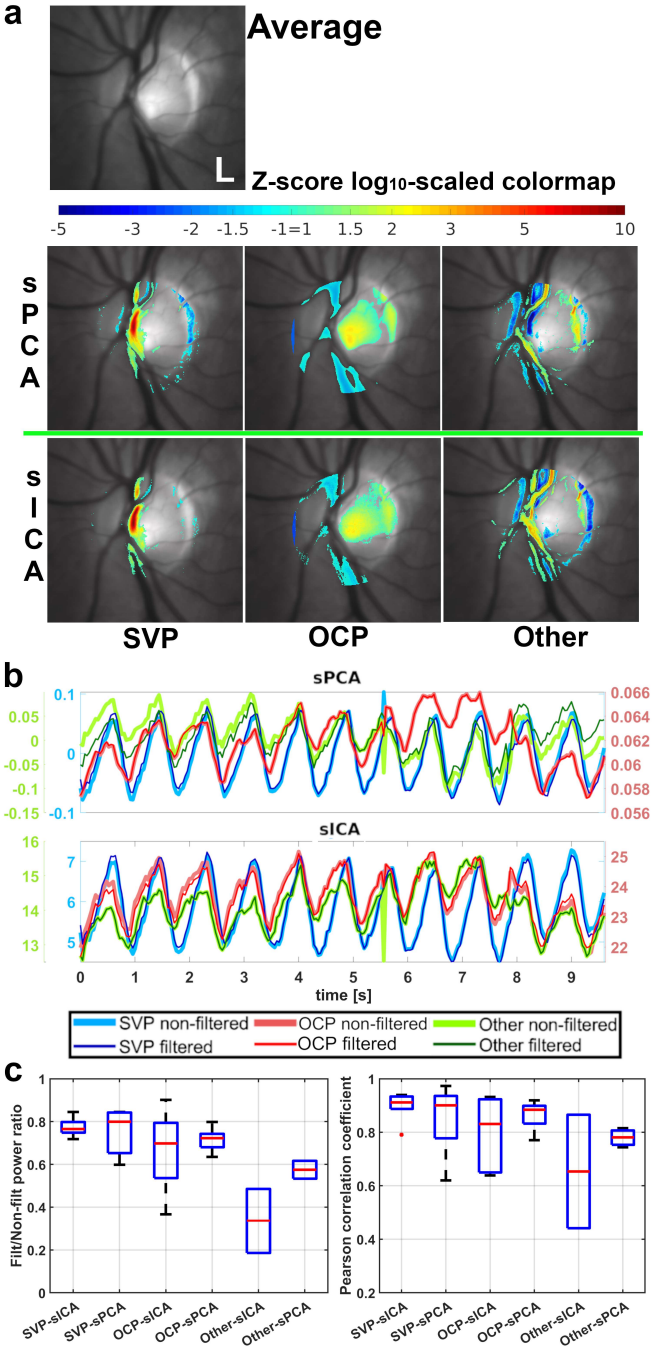

Fig. 1. Orthogonal and independent RPPs (**a**) with example of separated time-courses (**b**) and statistical evaluation of time-course filtration success (**c**) from monocular VO recordings of the left eye.
(**a**) Single-subject example of averaged image overlaid with three reproducible spatial patterns, i.e. SVP, OCP, and "other" pulsations detected with sPCA and sICA. Color-coded statistical parametric maps show thresholded coefficients of **X*** matrix for sPCA and **S** matrix for sICA. Both map types were thresholded to zero for all $|\mathbf{X}^*|<1$, $|\mathbf{S}|<1$, respectively. Colormap is $\log_{10}$ scaled. Visualizations done with `rit_showmap` (***Appendix A***). (**b**) Single subject non-filtered and filtered time-courses of the spatial patterns, i.e. columns of matrices $\mathbf{F}_{14}$ and **A**. Axis scale color-coding is matched to patterns (plotted with the `addaxis` [57]). (**c**) Distribution of filtered/non-filtered signal power ratios (left) and the Pearson correlation coefficients (right) over different RPPs and BSS techniques.

Visually, the filtered/non-filtered time-courses in **Fig. 1b** were phase shifted over different RPPs with an expected plausible pulsatile heart rate and had different time-course amplitudes for specific RPPs and BSSs.

Time-courses from sPCA-SVP and sICA-other demonstrated that the post-processing method filtered out signal spikes (**Fig. 1b**), particularly for time-courses in binocular data (**Fig. 3b**).

Within the post-processing of sPCA or sICA time-courses, sPCA demonstrated lower power of noise in raw non-filtered time-courses and higher linear dependence between filtered and non-filtered time-courses for all RPPs (**Fig. 1c**).

The heart rate was estimated from control points of the filtered RPP time-courses at 69±5 min^{-1} and was stable and reproducible over all RPP classes and both BSSs (**Table 2**).

Time-course amplitudes varied over the BSSs and over the RPPs. The sICA estimated larger mixing matrix coefficients in "mean" ranges 0.789-1.509 over RPPs. The sPCA eigenvector mean values were in ranges 0.003-0.105 (**Table 2**).

The OCP were demonstrated to be significantly phase shifted in comparison to SVP when evaluated either for all control points at once or for each separate control point (Fig. 1c and **Table 2**). The OCP preceded the SVP by 10.4±8.6% of heart cycle period for sICA and by 9.5±6.2% for sPCA. Mean p-values of observed significance in phase shifts were 0.023±0.013 for the sICA and 0.006±0.004 for the sPCA.

The "other" pulsations were not significantly phase shifted to SVP or OCP (**Table 2**) while using sICA, whereas the sPCA results demonstrated significant shifts between "other" pulsations and OCP at two control points (**Table 2**).

B. Binocular VO

Comparably to monocular VO, sPCA and sICA demonstrated the same three reproducible spatially distinct patterns (i.e. SVP, OCP and "other" pulsations). A representative single-subject example of detected patterns is shown in **Fig. 2** for four different BSS strategies (i.e. both eye sPCA/sICA or separate left and right eye sPCA/sICA) at binocular data. Filtered and non-filtered time-courses are shown in **Fig. 3a**. Pattern detection heartrates for each separate strategy are listed in **Table 1.**

The "other" pulsations demonstrated the lowest detection compared to SVP and OCP. Group averaged maximal/minimal/ /mean Z-scores, mean positive/negative suprathreshold areas and total suprathreshold areas are listed in **Table 1,** together with their group standard deviations for all used BSS strategies. Both mean and standard deviation of the parameters were comparable over BSS strategies without any obvious differences (**Table 1**).

Mean segmented and classified total area of the entire ONH was in a range of 79-85% with averaged standard deviation of 9%. It was lower than 95% of segmented area as originally expected suggesting that the last non-classified "noise" component is of a larger power than 5% of spatial variance. sPCA detected larger suprathreshold areas than sICA (**Table 1**). Visually, all filtered/non-filtered time-courses in **Fig. 3a** were phase shifted over different RPPs with an expected plausible pulsatile heart rate and had different time-course amplitudes over different RPPs and used BSS strategies. The implemented K-means post-processing filtering method of BSS outputting

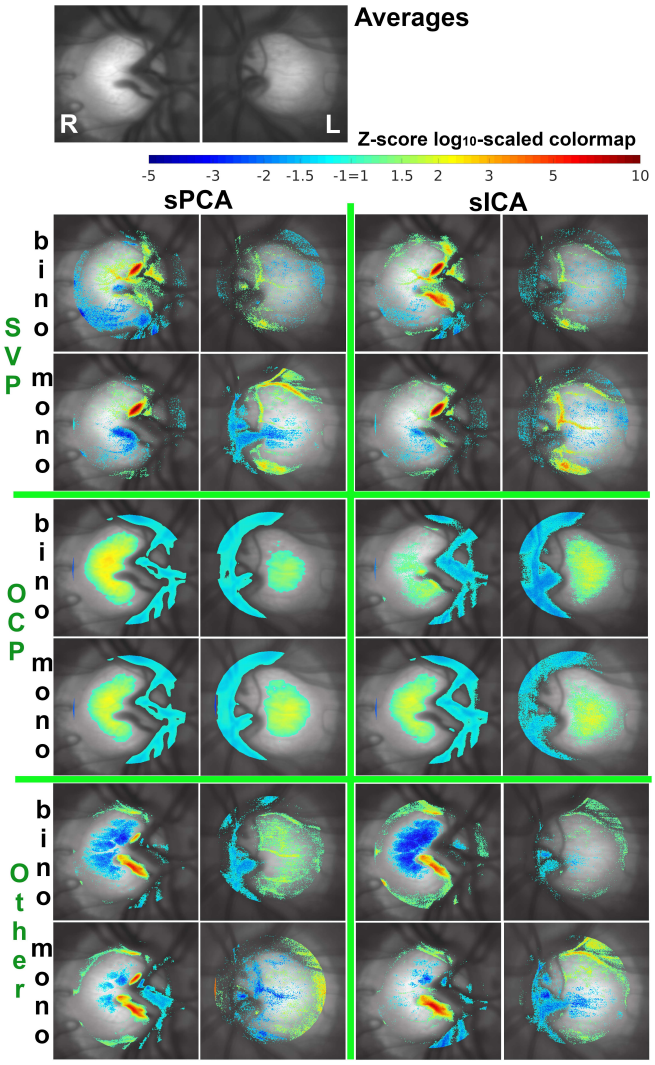

Fig. 2. Orthogonal and independent spatial patterns derived from four different BSS strategies from binocular VO recordings.
Single-subject example of averaged image overlaid with three reproducible different spatial patterns, i.e. SVP, OCP, and "other" pulsations detected with all BSS techniques, i.e. both eyes sPCA/sICA (bino), left eye sPCA/sICA (mono), and right eye sPCA/sICA (mono), respectively. Right-left orientation is the same as shown in the averaged image. Color-coded statistical parametric maps are thresholded coefficients of **X*** matrix for sPCA or S matrix for sICA. Both map types were thresholded to zero for all |**X***|<1, |**S**|<1, respectively. Colormap is log_{10} scaled. Time-courses of suprathreshold locations of this subject shown in **Fig. 3a**. Visualizations done with `rit_showmap` (***Appendix A***).

time-courses did not change the physiological pulsatile pattern character in time-courses with a low noise power level (**Fig. 3a**) but even if high-power noise spikes were present (**Fig. 3b**). The sICA method demonstrated lower power of noise in the raw output non-filtered time-courses and higher amount of linear dependence between post-processed and non-filtered time-courses for SVP and OCP patterns in comparison to sPCA results (**Fig. 3c**). After the post-processing, control points defining the full pulsatile pattern periods were automatically detected (***Appendix C***) and manually corrected if necessary. A representative example of marked time-courses of three RPPs is shown in **Fig. 4a** with a quantitative delay measurement between OCP and SVP control points 4, which was used for a mean single-subject delay estimation.

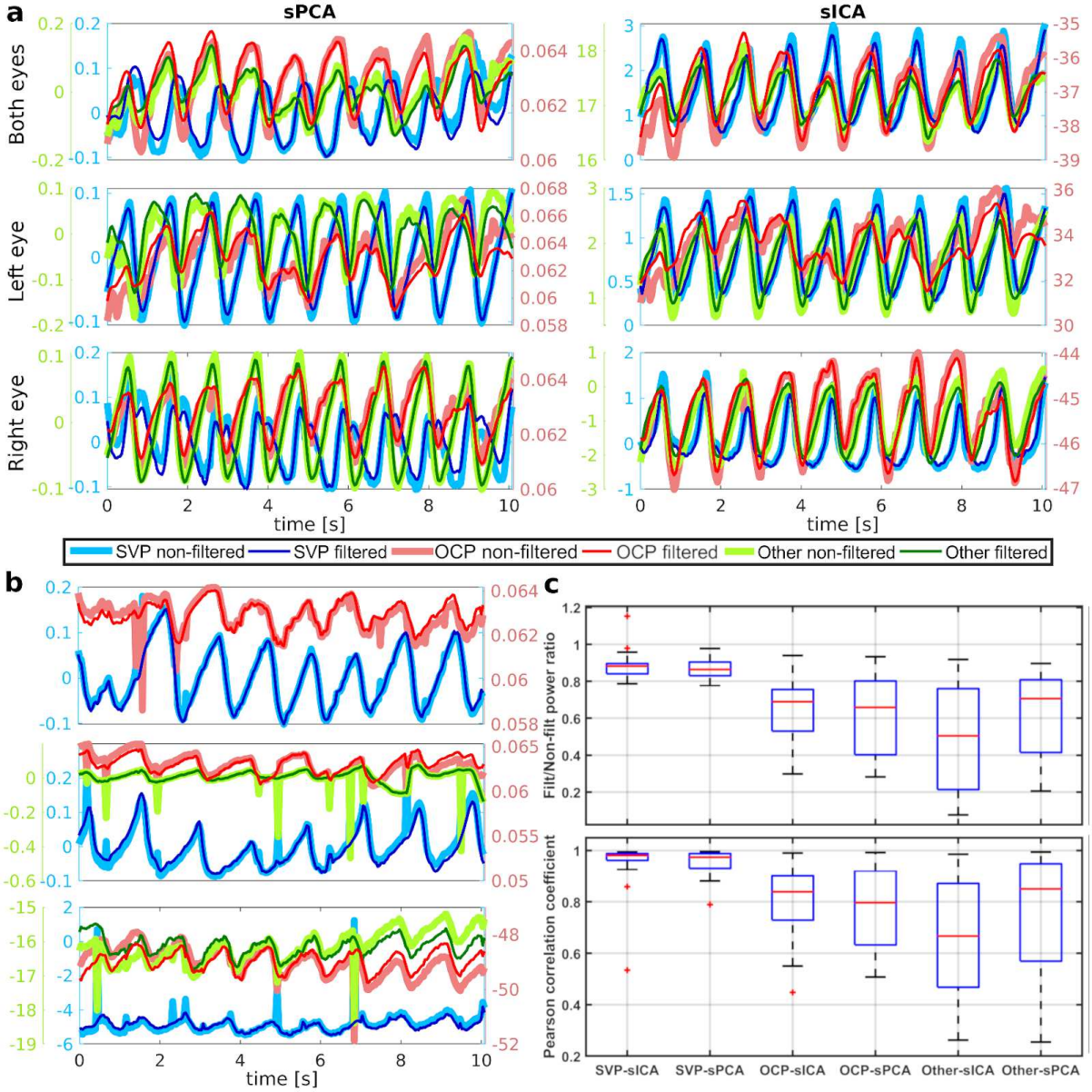

Fig. 3. Non-filtered and filtered RPPs time-courses derived from binocular VO recordings.
(a) Single-subject example of non-filtered and filtered time-courses of orthogonal and independent spatial patterns that are shown in **Fig. 2**. Y-axes represent coefficients of eigenvectors **F** (Eq. 1) for sPCA results and columns of mixing matrix **A** (Eq. 3) for sICA. Color-coded intensity scales correspond to curve pairs with matching color. Minimal amplitude peaks of ONH cup and "other" pulsations precede minimal amplitude peaks of SVP. (**b**) Y-axes description and color-codings are the same as in **a**. Representative examples of K-means filtering approach keeping and not disrupting the physiological pulsatile signal but suppressing "high-power" spike noise, which is typical and commonly present in sPCA/sICA output time-courses derived from VO recordings, are shown. (**c**) Distribution of filtered/non-filtered signal power ratios (up) and the Pearson correlation coefficients (bottom) over different RPPs and BSS techniques. Data of both/left/right sPCA/sICA were concatenated into one boxplot because of the low sample sizes, i.e. maximal number of samples for one pattern and BSS technique is 21 at present. Boxplots for "other-sICA" were only derived from 15 samples, and "other-sPCA" only from 12 samples. In power ratio boxplots, one sample with the lowest power ratio was excluded before generating the boxplot. Trends within boxplots for power ratios and Pearson correlation coefficients are similar and consistent. Generally, the filtered and non-filtered signals remain highly linearly dependent, while Q1-Q3 boxplot intervals mostly do not interfere below correlation coefficient of 0.6, even when the filtered signal has about 40% of a non-filtered signal power. Blue curves in bottom graph of **b** are SVP where Pearson correlation coefficient between post-processed and non-filtered signal is outlying 0.54 for SVP-sICA group in **c**. Graphs in **a**, **b** were plotted with the `addaxis` toolbox [57].

Minor manual corrections of incorrectly detected points 1, 2, 3, 4 or 5 were necessary to be done in 36 cases of 75 of total estimated time-courses, i.e. a full success rate of the proposed automated morphologic method was 52%. The frequent error, which needed manual edits, was overdetection of zero-crosses and peak points in OCP or "other" time-courses. The method worked without errors for 98% of all detected SVP time-courses.

The mean heartrate of 54±5min^{-1} was estimated from time-courses and was stable and reproducible over all RPP classes and both BSSs (**Table 2**). The estimated heartrate values are in physiological range for healthy subjects in well physical condition. Time-course amplitudes varied over BSSs and RPPs. The sICA estimated larger mixing matrix coefficient in 'mean' range of 1.123-2.632 over RPPs, sPCA eigenvector mean values were in range of 0.003-0.162 (**Table 2**). Optic cup pulsations were significantly phase shifted compared to SVP (**Table 2**).

TABLE I
GROUP SPATIAL STATISTICS OVER ALL INVESTIGATED BSSS

	MONOCULAR DATA		BINOCULAR DATA					
	L_sICA	L_sPCA	B_sICA	L_sICA	R_sICA	B_sPCA	L_sPCA	R_sPCA
SVP-det	6/6	6/6	6/7	7/7	6/7	6/7	7/7	7/7
OCP-det	5/6	6/6	6/7	7/7	7/7	7/7	7/7	7/7
Others-det	2/6	3/6	4/7	6/7	5/7	4/7	5/7	3/7
SVP -Z-Max	9.17±4.02	8.26±3.70	12.23±2.99	9.13±3.58	9.82±2.36	11.74±3.13	8.82±3.69	8.03±2.17
OCP-Z-Max	3.45±0.74	2.89±0.41	3.34±0.73	2.96±0.38	3.34±1.42	2.69±0.23	2.31±0.24	2.54±0.35
Others-Z-Max	3.92±0.37	6.25±1.68	4.80±0.65	4.74±1.30	4.88±1.69	5.41±0.60	4.63±0.50	5.52±2.12
SVP -Z-Min	-3.02±1.11	-3.91±1.01	-2.69±0.28	-2.45±0.59	-2.78±0.44	-2.95±0.66	-2.53±0.57	-3.45±1.17
OCP-Z-Min	-3.10±1.03	-2.80±0.94	-3.37±1.25	-2.67±0.64	-2.87±0.63	-3.03±1.23	-3.25±1.69	-3.26±1.45
Others-Z-Min	-4.64±0.22	-4.73±1.88	-4.11±0.90	-4.20±0.63	-4.21±0.60	-4.50±0.32	-4.58±0.98	-3.74±2.06
SVP -Z-P-Mean	2.14±0.52	1.98±0.34	2.34±0.31	2.42±0.33	2.32±0.15	2.26±0.38	2.33±0.38	1.97±0.35
OCP-Z-P-Mean	1.54±0.10	1.65±0.14	1.57±0.19	1.49±0.08	1.48±0.22	1.58±0.05	1.50±0.08	1.54±0.08
Others-Z-P-Mean	1.56±0.17	1.69±0.08	1.62±0.14	1.62±0.23	1.58±0.33	1.56±0.06	1.58±0.06	1.65±0.20
SVP -Z-N-Mean	-1.34±0.17	-1.45±0.07	-1.27±0.06	-1.26±0.10	-1.26±0.08	-1.32±0.08	-1.28±0.11	-1.40±0.17
OCP-Z-N-Mean	-1.38±0.10	-1.28±0.08	-1.30±0.06	-1.32±0.14	-1.31±0.10	-1.29±0.13	-1.28±0.13	-1.26±0.12
Others-Z-N-Mean	-1.71±0.01	-1.52±0.12	-1.60±0.20	-1.55±0.13	-1.61±0.16	-1.53±0.09	-1.56±0.12	-1.41±0.19
SVP -Z-P-Area	0.10±0.04	0.11±0.03	0.09±0.02	0.10±0.03	0.09±0.01	0.09±0.02	0.10±0.03	0.11±0.03
OCP-Z-P-Area	0.18±0.03	0.17±0.02	0.18±0.02	0.19±0.02	0.19±0.04	0.18±0.01	0.20±0.02	0.19±0.03
Others-Z-P-Area	0.13±0.02	0.14±0.03	0.14±0.02	0.14±0.03	0.13±0.03	0.15±0.01	0.15±0.02	0.15±0.05
SVP -Z-N-Area	0.09±0.06	0.10±0.05	0.05±0.04	0.04±0.04	0.06±0.01	0.07±0.05	0.06±0.05	0.11±0.04
OCP-Z-N-Area	0.15±0.03	0.15±0.04	0.17±0.05	0.18±0.05	0.20±0.04	0.17±0.03	0.19±0.03	0.18±0.02
Others-Z-N-Area	0.14±0.01	0.13±0.02	0.14±0.01	0.15±0.03	0.15±0.03	0.15±0.01	0.14±0.02	0.14±0.02
Total Area	0.79±0.14	0.77±0.14	0.79±0.06	0.80±0.13	0.79±0.11	0.85±0.13	0.83±0.15	0.83±0.02

det pattern incidence, **Z** Z-score, **P** positive, **N** negative, **Max** maximum, **Min** minimum. **L sICA** or **L sPCA** spatial ICA or PCA estimated from the left eye. Similarly, **B** from both eyes in one analysis, and **R** from the right eye. All area values represent the partial area of the ONH where the area of the ONH is equal to 1. All maximum, minimum, or mean Z-score values and detected counts have no units. All values are group averages and group standard deviations.

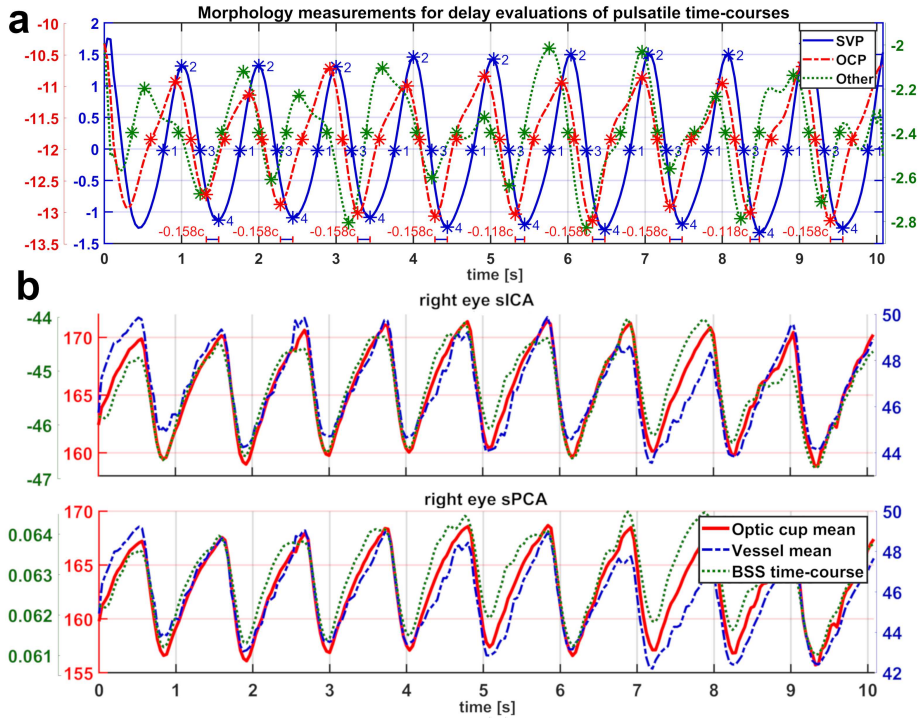

Fig. 4. RPP time-courses derived from binocular VO recordings.
All shown graphs are single-subject and single-BSS representative examples generalizable for both monocular or binocular datasets. (**a**) BSS-derived RPP time-courses divided at four representative time points (1 - pulsatile period begin/end, 2 - period's maximal peak, 3 - period's "middle", 4 - period's minimal peak, as demonstrated in the graph for the SVP curve) classified with a proposed semi-automated method. On the graph's bottom, an example of pulsatile phase shift quantitative evaluation between number 4 points of SVP and disc cup pulsations expressed in ratios of mean period/cycle (c) duration (i.e. -0.158c means about -15.8% cycle earlier phase shift) is shown. All values in y-axes are coefficients from sICA mixing matrix $\boldsymbol{A}$. (**b**) Mean pulsatile dynamics derived from positive/negative (i.e. disc cup / vessel areas) suprathreshold voxels of the BSS-derived disc cup RPP component and the BSS-derived time-course of the component. Axis scale color-coding is matched to patterns time-courses: red for intensity values of the VO recording in the disc cup area, blue for intensity values of the VO recording in the vessel area, and green for coefficients of mixing matrix $\boldsymbol{A}$ for the sICA or of eigenvector matrix $\boldsymbol{F}_{14}$ for the sPCA. Graphs plotted with the `addaxis` toolbox [57]

The OCP preceded the SVP in average 13.6±7.6% of heart cycle period for sICA, and 13.9±9.0% for sPCA. The spatial ICA demonstrated the expected signal shift of −3.1±1.8 samples (averaged p-values=0.0036±0.0063) for subjects with a heartrate ≈55min^{-1} with signal framerate 25fps. The spatial PCA demonstrated shift about −3.2±2.1 samples (p=0.0056±0.0067).

"Other" pulsations were significantly phase shifted in comparison to SVP when evaluated for all control points at once but partly when evaluated for each separate control point (**Table 2**). The "other" pulsations preceded the SVP by 12.0±7.8% of heart cycle period for sICA and 17.1±16.7% for sPCA. The spatial ICA demonstrated the expected signal shift of −2.7±1.8 samples (p=0.0403±0.0694) for subjects with a heart rate ≈55min^{-1} with the signal framerate 25 fps. The spatial PCA demonstrated shift of −3.9±3.8 samples (p=0.0834±0.0841).

Any significant time difference between "other" pulsations

TABLE II
GROUP STATISTICAL EVALUATION OF TIME-COURSE DYNAMICS

MONO	Left eye sICA	Left eye sPCA
SVP-HR	69±5	68±5
OCP-HR	70±5	69±5
Other-HR	68±6	69±4
SVP-Am	1.509±0.469	0.105±0.024
OCP-Am	1.224±0.479	0.003±0.001
Other-Am	0.789±0.540	0.090±0.010
OCP1-SVP1	**-0.095±0.087**	**-0.094±0.061**
OCP2-SVP2	**-0.109±0.087**	**-0.089±0.066**
OCP3-SVP3	**-0.105±0.085**	**-0.092±0.069**
OCP4-SVP4	**-0.108±0.090**	**-0.103±0.057**
OCP-SVP	**-0.104±0.080**	**-0.95±0.059**
Other1-SVP1	-0.176±0.102	0.039±0.105
Other2-SVP2	-0.189±0.114	0.022±0.126
Other3-SVP3	-0.175±0.089	0.026±0.115
Other4-SVP4	-0.174±0.099	0.022±0.115
Other-SVP	**-0.179±0.077**	0.027±0.099
Other1-OCP1	-0.058±0.082	0.174±0.138
Other2-OCP2	-0.055±0.072	0.167±0.139
Other3-OCP3	-0.032±0.052	0.170±0.129
Other4-OCP4	-0.028±0.058	0.169±0.139
Other-OCP	-0.043±0.053	**0.170±0.116**

Legend:
MONO monocular
BINO binocular
HR heart rate; min^{-1}
Am amplitude
1, 2, 3, 4 control point indexes
OCP1-SVP1, etc. express the portion of heart cycle as described in the Fig. 4 legend.
Values are group averages and group standard deviations. Statistically significant values according to p-values derived from Wilcoxon rank-sum test or one tailed t-tests depending on variable are shown in bold (more detail in Methods).

BINO sICA	Both eyes	Left eye	Right eye
SVP-HR	54±4	53±5	54±6
ODP-HR	55±4	54±6	54±6
Other-HR	56±4	53±6	54±6
SVP-Am	2.636±1.064	2.811±1.050	2.651±1.547
ODP-Am	1.526±0.517	1.610±0.536	1.764±0.845
Other-Am	1.107±0.506	1.171±0.400	1.123±0.682
OCP1-SVP1	**-0.164±0.083**	**-0.168±0.078**	**-0.171±0.056**
OCP2-SVP2	**-0.141±0.134**	**-0.158±0.099**	**-0.101±0.061**
OCP3-SVP3	**-0.112±0.068**	**-0.132±0.059**	**-0.103±0.049**
OCP4-SVP4	**-0.117±0.064**	**-0.124±0.066**	**-0.144±0.095**
OCP-SVP	**-0.134±0.088**	**-0.145±0.075**	**-0.130±0.070**
Other1-SVP1	-0.093±0.102	**-0.193±0.073**	**-0.155±0.058**
Other2-SVP2	-0.073±0,160	**-0.137±0.069**	**-0.086±0.025**
Other3-SVP3	-0.063±0.113	**-0.143±0.061**	**-0.107±0.035**
Other4-SVP4	-0.074±0.090	**-0.145±0.071**	**-0.166±0.078**
Other-SVP	**-0.076±0.107**	**-0.155±0.068**	**-0.128±0.059**
Other1-OCP1	0.105±0.096	-0.026±0.095	-0.016±0.114
Other2-OCP2	0.110±0.105	0.028±0.139	-0.020±0.057
Other3-OCP3	0.079±0.099	-0.007±0.073	-0.020±0.081
Other4-OCP4	0.073±0.090	-0.017±0.068	-0.021±0.087
Other-OCP	**0.092±0.089**	-0.005±0.094	-0.019±0.078

BINO sPCA	Both eyes	Left eye	Right eye
SVP-HR	56±3	54±5	53±6
ODP-HR	54±5	54±5	54±5
Other-HR	59±2	54±6	57±3
SVP-Am	0.160±0.011	0.162±0.013	0.159±0.013
ODP-Am	0.003±0.002	0.003±0.002	0.003±0.002
Other-Am	0.076±0.047	0.123±0.043	0.130±0.059
OCP1-SVP1	**-0.187±0.096**	**-0.152±0.045**	**-0.165±0.111**
OCP2-SVP2	**-0.150±0.101**	**-0.122±0.084**	**-0.106±0.098**
OCP3-SVP3	**-0.145±0.089**	**-0.113±0.045**	**-0.131±0.121**
OCP4-SVP4	**-0.156±0.107**	**-0.104±0.052**	**-0.131±0.137**
OCP-SVP	**-0.159±0.093**	**-0.12±0.0583**	**-0.133±0.113**
Other1-SVP1	-0.160±0.227	**-0.212±0.102**	-0.192±0.136
Other2-SVP2	-0.130±0.212	**-0.199±0.147**	-0.198±0.195
Other3-SVP3	-0.122±0.213	**-0.161±0.090**	-0.188±0.159
Other4-SVP4	-0.143±0.272	**-0.147±0.114**	-0.201±0.181
Other-SVP	**-0.139±0.199**	**-0.180±0.109**	**-0.1950.144**
Other1-OCP1	0.040±0.228	-0.053±0.109	0.053±0.191
Other2-OCP2	0.004±0.208	-0.066±0.185	-0.010±0.295
Other3-OCP3	0.040±0.155	-0.039±0.080	0.041±0.156
Other4-OCP4	0.043±0.188	-0.033±0.089	0.036±0.136
Other-OCP	0.032±0.169	-0.048±0.113	0.030±0.176

and OCP was not detected (**Table 2**).

For all three patterns, the mean temporal dynamics of negatively suprathreshold pixels and positively suprathreshold pixels were highly positively correlated for both BSSs (**Fig. 4b**) and the same results were obtained for the monocular dataset.

C. Respiratory-induced effects in VO recordings

Three reproducible components (i.e. SVP, OCP or OP) did not show respiratory-induced effects (i.e. ≈0.2Hz oscillations). In contrast, both-eyes sPCA or sICA demonstrated 4th separate component with ≈0.2Hz oscillations in four out of seven subjects in binocular datasets (**Fig. 5**). The oscillations might represent respiratory-induced effects. Spatial pattern was manifested homogeneously across the subjects (**Fig. 5**).

IV. DISCUSSION

A. Study novelty and medical imaging impact

We applied BSS techniques to mono- and binocular RVRs. This approach provided a blind and data-driven separation of three RPPs. The SVP and OCP patterns were uniformly captured across all subjects whereas the pulsations that we labeled "other" were observable across most subjects. We described the methodology in detail and supplied robust feasibility data for the use of BSSs in retina imaging. Moreover, in direct comparison to our preliminary binocular study [46], the current study extends the methodology with a modified adaptive K-means post-processing restoration of the pulsatile pattern dynamics and quantitatively evaluates RPP delays for both mono- and binocular video-recordings. We detected low frequency RPP with homogeneous spatial pattern across subjects. These oscillations may represent respiratory-induced effects.

Practical impact: The proposed methods represent next step to an automated analysis tool for the evaluation and segmentation of functional zones inside the OD. This method bears a major potential impact spanning from plentiful scientific applications (e.g. physiology of retinal hemodynamics) to a vast use in many clinical scenarios such as diagnostics, prediction, or monitoring of disorders where retinal hemodynamics may be altered. These disorders include conditions with an impairment of vascular elasticity (arterial stiffness due to arteriosclerosis, diabetes mellitus or metabolic syndrome, chronic renal disease, neurodegenerative disorders such as Parkinson's disease, Alzheimer's disease or other types of dementia, traumatic brain injury etc. [1], [4], [58]–[63]), blood composition (e.g. hyperviscosity syndrome [64]), and flow alteration (cardiovascular diseases, pulmonary hypertension, carotid artery stenosis, myopia) [6], [65]–[67], BP (e.g., arterial hypertension) [18], [68]–[70], IOP (e.g., glaucoma) [2], [3] or ICP (e.g., pseudotumor cerebri or intracranial pathologies increasing ICP) [71]. Both BSSs quantified spatial statistical parametric maps of patterns and significant between-pattern phase shifts. The generated maps' magnitudes and the reported time shifts in temporal dynamics corresponding to RPPs can be regarded as potential new biomarkers. The proposed method proved to be feasible in the VO data, but, in principal, can be applicable for other techniques assessing retinal hemodynamics (i.e. RVA

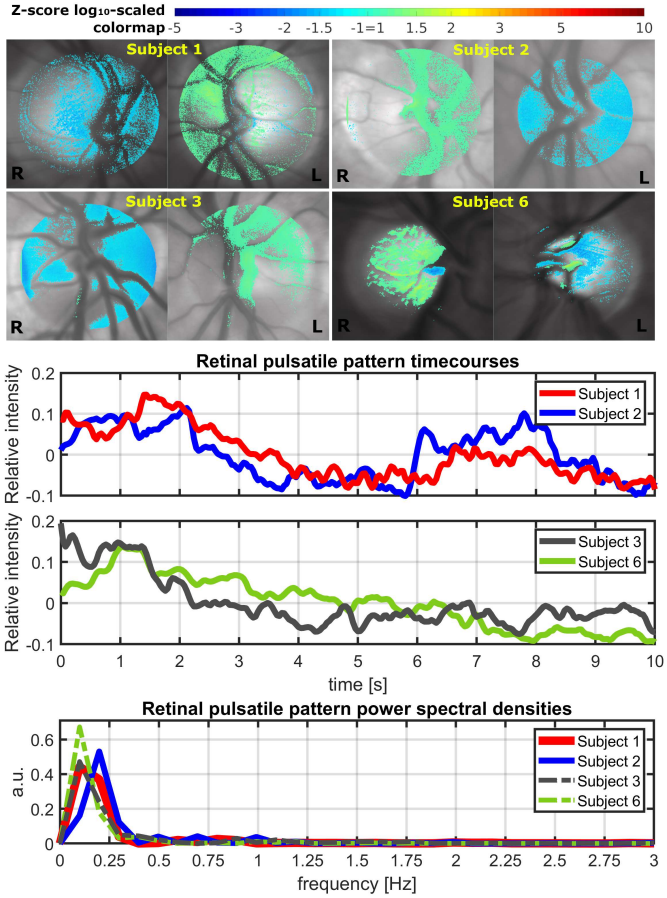

Fig. 5. Retinal pulsatile patterns considered to be respiratory-induced effects. Spatial maps, time-courses and power spectral densities are shown for the sPCA results. Letter **L** in spatial maps express left eye, **R** right eye, **a.u.** means arbitrary units. Time-courses were k-means post-processed but not detrended.

[32], [33], XyCam RI™ [34]–[37], Doppler OCT [44], [48], etc.). Given the importance and success of BSS in neuroimaging [53], [54], [72], the application of BSS in retina imaging, has a tremendous potential for future vision or eye-disease research.

Potential novel clinical applications: SVP are influenced by the pressure gradient between IOP and ICP. Therefore, there are many potential applications in conditions with altered IOP or ICP [73] [13], [14], [31]. The interpretation of IOP-SVP-ICP gradients providing a mathematical model describing the interplay between these pressures remains to be defined. BSS of SVP with high reproducibility represents a new avenue to explore and potentially define these relationships. SVP correlated to the thickness of retinal nerve fiber layer (RNFL) in a recent observation of glaucoma and glaucoma suspect patients [40], [74]. RNFL thinning was well described in glaucoma [75] or arterial hypertension [76], and in several neurological diseases such as Alzheimer's and Parkinson's disease [77]–[79], multiple sclerosis or even in rare disorders, e.g. adrenoleuko-dystrophy [80]. Hence, an examination of a relationship between SVP automatically isolated by BSS and RNFL thickness is another interesting area of future research that can lead to novel clinical applications. Finally, the presented BSSs can facilitate an investigation of the reproducible OCP and its alteration in various disease conditions affecting retinal hemodynamics.

B. Physiologic interpretation of pulsatile pattern dynamics

A local image intensity decrease in our RVR represents a local blood compartment volume increase, because the light is maximally absorbed within the blood volume peak [22].Thus, dynamics of three detected phase shifted RPPs correspond to local blood volume changes of different *blood volume compartments*. The OCP compartment preceded the SVP across all control points. The underlying physiology that would explain why the "other" pulsations are preceding SVP remains unclear.

The SVP in CRV represent the most pronounced and detectable retina compartment by VO. The SVP are caused by the vein collapse and refilling during cardiac cycle [12], [13] and it is believed that SVP dynamics is conditioned by the local pressure gradient [13], [14]. SVP are detected in the area where CRV traverses the lamina *cribrosa sclerae* [19], [20] and manifest as a strong image intensity change characterized by a specific time-course and spatial distribution.

The OCP pattern was spatially detected in the temporal part of ONH and in the larger vessels in the nasal part, predominantly arterial branches of CRA. The pattern in the temporal ONH part may originate from microvessels supplied from the posterior ciliary artery. The posterior ciliary artery is characterized by a different hemodynamics with higher blood velocity when compared to the central retinal artery (CRA) or CRV [25]–[27], [81]. A fluorescein angiography study presented the pre-arterial filling of the choroidal circulation, i.e. preceding the filling of major retinal arteries, and also revealed the relationship between OCP and the choroidal circulation [24]. Similar findings were shown in non-human primate studies showing the pre-arterial filling of the choroid and prelaminar region of ONH but not a filling of the retinal vascular bed [24]. These hemodynamics differences may contribute to phase shifts that we detected between specific patterns. The quantified delays between OCP and SVP dynamics are comparable to reported shifts between arteries and veins [30], [82], [83] and ONH and vessels [22].

The "other" pulsations may likely correspond to BVP that were described in the introduction. As BVP cover several physiologically different phenomena observed during ophthalmoscopic examination and each subject is characterized with a unique vessel tree, these pulsations may occur in various parts of the retina having various physiological origins. That can explain that the "other" pulsations are more variable and less reproducible across subjects than SVP and OCP. The further investigation of physiological origins of pulsations is warranted.

C. Monocular vs. binocular recording & sPCA vs. sICA

Our findings showed that both BSSs were feasible, equally useful, and comparable in temporal dynamics evaluation as well as in spatial statistics. Future studies with more participants and in subjects with altered retinal hemodynamics may determine if one method is preferable over the other. In the comparison of monocular/binocular BSS modes, we have not noticed any significant difference except for respiratory induced effects that were only observed in the binocular mode. Apart from BSS, spatiotemporal SVD has been recently introduced in Doppler holography RVR [44]. The decomposition was similar to sPCA but with higher computational demands since it optimizes two

(i.e. spatial and temporal) eigenvector matrices instead of one temporal eigenvector matrix $\boldsymbol{F}$ (Eq. 1). For monocular RVR, sPCA lasted 1.72±0.47s on a laptop computer (Intel® Core™ i5-5200U processor, RAM: 8GB 1600MHz DDR3L) and sICA took additional 0.83±0.19s. For binocular RVR, single-eye sPCA lasted 3.54±1.03s and sICA additional 2.03±0.55s; for both-eyes sPCA lasted 12.95±2.69s and sICA additional 5.11±1.52s. Linear regression is another approach fitting RPP from RVR [43]. Both BSSs overcome the regression since no prior information about model time-course or ROI is required.

D. Limitations and future work

A detected inconsistency in phase shifts of "other" pulsations to SVP and OCP might be caused by the fact that the "other" pulsations are not homogenous in its etiology and originated from spatially and anatomically differing areas.

The phase shifts between different RPP may become a novel quantitative biomarker for the type of diseases where retinal blood flow and perfusion are affected, i.e. plaque in the carotid artery influencing the ONH blood flow circulation [6], or glaucoma [84], [85]. Due to low sampling rate of 25fps the detected time shifts between RPP spanned a limited number of time samples. These findings might then be distorted in subjects whose heart rate is >75min^{-1}. Optimizing the data acquisition with a higher sampling rate will be the scope of the future study.

Low detection rate and reproducibility of respiratory-induced RPP may be caused by the following factors. First, participants were instructed to focus and not blink, which may result in slowing or even holding the breath during the examination in some subjects. Second, considering breath frequency ≈0.2Hz, acquisition of 10s enables to detect two full periods. Longer recordings may be required to assess the effect of breathing. Third, respiratory-induced RPP might be isolated in principal components with index>4, and so may be omitted.

In our RVR setup, the light absorption due to blood volume changes prevail over effects of ONH longitudinal movement variations reported in other studies as heartrate fundamental [86], [87] or higher-order harmonic oscillations [88]–[90]. We observed a high-frequency signal in components with index>4 but the deeper analysis was beyond the study scope.

Although BP, IOP or ICP influence the perfusion pressure in retinal vasculature [25] blood pressure and ICP measurements were not available for our cohort. Along with the limited number of participants, the evaluation of physiological effects and relationships to these pressures was precluded in our study.

BSS multi-subject extensions estimating a group aggregated components were reported in MRI field [53], [54], [72] but appear non-applicable in retina-imaging at present. Data normalized in a template space is fundamental for such approach but a retina template invention is a quite challenging task due to inter-individual & inter-eye difference in the retinal vasculature.

APPENDIX A

The **Retina Imaging Toolbox** (**RIT**) is publicly available at: https://github.com/ivanalabounkova/retinaimagingtoolbox

Example of co-registered monocular retinal video-recording is publicly available at: https://youtu.be/-CABIpjWX8Y and the binocular at: https://youtu.be/4anapI0TZTQ

APPENDIX B

CLINICAL INFORMATION OF THE PARTICIPANTS

	Age year	Sex	HR min^{-1}	IOP mmH	Refraction D	Vision	Perimetry	RNFL µm
MONOCULAR DATASET								
1	76	M	71	15	1.4	0.7	1.6	103
2	57	F	65	N/A	-1.3	1.3	0.9	94
3	66	F	65	15	2.9	1.0	-1.2	110
4	83	F	76	21	1.5	0.7	0.8	79
5	45	F	72	14	-3.9	1.0	0.9	86
6	56	M	63	19	-1.9	0.8	2.1	76
BINOCULAR DATASET (LEFT/RIGHT EYE)								
1	83	F	57	16/20	1.5/0.5	0.7/0.7	0.8/1.4	79/85
2	73	F	59	14/15	1.6/1.9	1.0/1.0	-1.3/-1.9	114/111
3	72	M	52	14/14	2.6/2.5	1.0/1.0	0.1/-0.9	95/99
4	77	F	57	12/12	-2.1/-1.8	0.7/0.8	1.4/0.4	89/90
5	45	M	45	15/15	-3.8/-3.0	1.0/1.0	-0.5/-1.1	89/91
6	55	M	56	14/13	-2.4/-3.0	1.0/1.0	-0.6/-2.2	89/90
7	80	F	49	13/14	0.3/0.5	1.0/1.0	0.5/0.3	93/86

F female; **M** male; **HR** heart rate; **IOP** intraocular pressure; D diopters, RNFL retinal nerve fiber layer; **N/A** not available. Values were measured prior to VO acquisition on the same day. HR was estimated as a mean from all isolated subject's RPPs. Vision corresponds to the best corrected visual acuity. All subjects had clear optical eye components. RNFL thickness was measured using Spectralis OCT (*Heidelberg Engineering, Germany*), IOP using Goldman contact tonometry, white-on-white perimetry with computerized static projection perimeter (*Octopus 500; Haag-Streit*).

APPENDIX C

The post-processed time-course was normalized to mean 0 and variance 1 and band-passed filtered in Fourier domain at frequency range 0.5-2.0Hz at $\boldsymbol{u}_f$. Local maxima/minima were detected as follows. The normalized and band-passed signal $\boldsymbol{u}_f$ was smoothed and local extremes were transformed to zero-crossing points in output vector $\boldsymbol{v}$ with two consecutive linear convolutions with kernels $\boldsymbol{s}=[1\ 1\ 1\ 1\ 1]/5$ and $\boldsymbol{d}=[1\ -1]$ as written in Eq. C1. Then, signal values $|v(t)|<0.08$ were identified as numbers 1 in a binary vector $\boldsymbol{b}$ at positions t. Each point of the binary vector was multiplied with a corresponding value of the signal to get a signal's values $e(t)$ suspected to be local extrema (Eq. C2). Peaks in the vector $\boldsymbol{e}$ were found with the function *findpeaks(abs(**e**))*. The detected positive/negative peak values and their temporal positions were stored in two column matrix $\boldsymbol{K}$ where 1st column represented a position and 2nd column a peak value with added mean $\boldsymbol{u}_f$ value.

$$\mathbf{v} = (\boldsymbol{u}_f * \boldsymbol{s}) * \boldsymbol{d} \quad \text{(C1)}$$

$$e(t) = b(t) \cdot u_f(t) \quad \text{(C2)}$$

Local zero-crossing points were detected from the normalized band-passed signal $\boldsymbol{u}_f$ after its transformation with Eq. C3 at variable $\boldsymbol{q}$. Values q were thresholded to 0 at each position where $\boldsymbol{q}<0$, and thresholded $\boldsymbol{q}$ was smoothed at $\boldsymbol{q}_s$ with convolution kernel $\boldsymbol{r}=[1\ 1\ 1]/3$ (Eq. C4). Peaks in $\boldsymbol{q}_s$ defining positions of zero-crossing points were found with the function *findpeaks(**q**$_s$)*. The detected zero values and their temporal positions were stored in two column matrix $\boldsymbol{L}$ where 1st column represented a position and 2nd column a zero value with added mean $\boldsymbol{u}_f$ value.

$$q(t) = log_{10}\left|\frac{1}{u_f(t)}\right| \quad \text{(C3)}$$

$$\boldsymbol{q_s} = \boldsymbol{q} * \boldsymbol{r} \quad \text{(C4)}$$

Matrix $\boldsymbol{M}$ was built from matrices $\boldsymbol{K}$ and $\boldsymbol{L}$ as shown in Eq. C5 where $\boldsymbol{K_1}$ and $\boldsymbol{L_1}$ are the 1st columns of the corresponding matrices, and similarly $\boldsymbol{K_2}$ and $\boldsymbol{L_2}$ are the 2nd columns.

$$\boldsymbol{M} = \begin{bmatrix} \boldsymbol{K}_1 & \boldsymbol{K}_2 \\ \boldsymbol{L}_1 & \boldsymbol{L}_2 \end{bmatrix} \quad \text{(C5)}$$

If there were two rows in matrix $\boldsymbol{M}$ whose temporal difference was lower than 0.2s, then the "2nd" row was deleted from matrix $\boldsymbol{M}$. Rows of matrix $\boldsymbol{M}$ were rearranged in increasing order of its 1st column and several "logic" post-processing steps were executed exactly in the same order as they are written below. If there were detected two consecutive rows where both $|m_2|>0$, then only the row with higher $|m_2|$ value was kept. If the m_2 values in the 1st or the last row of the matrix $\boldsymbol{M}$ were not equal to 0, then those rows were discarded. If the $m_2<0$ in the 2nd row and if the $m_2=0$ in the 1st row, then 1st and 2nd rows of matrix $\boldsymbol{M}$ were discarded. If the $m_2>0$ in the penultimate row and if the $m_2=0$ in the last row, penultimate and last rows of matrix $\boldsymbol{M}$ were discarded. If the $m_2=0$ in the penultimate row and if the $m_2=0$ in the last row, the last row of matrix $\boldsymbol{M}$ was discarded.

ACKNOWLEDGMENT

The authors thank to Drs. Jiří Chmelík and Roman Jakubíček from Department of Biomedical Engineering, Brno University of Technology, for discussion and advice about spike suppression via K-means. We thank Drs. Dara Koozekanani and Collin McClelland from Department of Ophthalmology at University of Minnesota for the guidance on the interpretation of our results and their practical impact. Center for Magnetic Resonance Research, Department of Radiology; Center for Neurobehavioral Development, Department of Pediatrics; and Minnesota Supercomputing Institute; all part of University of Minnesota provided lab space and computational support.

REFERENCES

[1] D. Guven, H. Ozdemir, and B. Hasanreisoglu, "Hemodynamic alterations in diabetic retinopathy," *Ophthalmology*, vol. 103, no. 8, pp. 1245–1249, 1996.
[2] J. Flammer, S. Orgül, V. P. Costa, et al. "The impact of ocular blood flow in glaucoma," *Prog. Retin. Eye Res.*, vol. 21, no. 4, pp. 359–393, 2002.
[3] X. Wang, C. Jiang, T. Ko, et al."Correlation between optic disc perfusion and glaucomatous severity in patients with open-angle glaucoma : an optical coherence tomography angiography study," *Graefe's Arch. Clin. Exp. Ophthalmol.*, vol. 253, no. 9, pp. 1557–1564, 2015.
[4] G. T. Feke, B. T. Hyman, R. A. Stern, and L. R. Pasquale, "Retinal blood flow in mild cognitive impairment and Alzheimer's disease," *Alzheimer's Dement. Diagnosis, Assess. Dis. Monit.*, vol. 1, no. 2, pp. 144–151, 2015.
[5] R. I. Spain, L. Liu, X. Zhang, et al. "Optical coherence tomography angiography enhances the detection of optic nerve damage in multiple sclerosis Rebecca," *Br J Ophthalmol*, vol. 102, no. 4, pp. 520–524, 2018.
[6] M. Rina, T. Shiba, M. Takahashi, and Y. Hori, "Pulse waveform analysis of optic nerve head circulation for predicting carotid atherosclerotic changes," *Graefes Arch Clin Exp Ophthalmol*, vol. 253, pp. 2285–2291, 2015.
[7] R. Heitmar and R. J. Summers, "Assessing vascular function using dynamic retinal diameter measurements: A new insight on the endothelium," *Thromb. Haemost.*, vol. 107, no. 6, pp. 1019–1026, 2012.
[8] F. Vosborg, L. Malmqvist, and S. Hamann, "Non-invasive measurement techniques for quantitative assessment of optic nerve head blood flow," *Eur. J. Ophthalmol.*, vol. 30, no. 2, pp. 235–244, 2020.
[9] S. S. Hayreh, "The blood supply of the optic nerve head and the evaluation of it - myth and reality," *Prog Retin Eye Res*, vol. 20, no. 5, 2001.
[10] S. S. Hayreh, "Blood flow in the optic nerve head and factors that may influence it," *Prog. Retin. Eye Res.*, vol. 20, no. 5, pp. 595–624, 2001.
[11] G. A. Cioffi and E. M. Buskirk, "Microvasculature of the anterior optic nerve," *Surv. Ophthalmol.*, vol. 38, no. Supplement May, 1994.
[12] H. Davson, *The Physilogy of the Eye*, New York: Academic Press, 1972.
[13] D. N. Levine, "Spontaneous Pulsation of the Retinal Veins," *Microvasc. Res.*, vol. 56, no. 3, pp. 154–165, 1998.
[14] A. S. Jacks and N. R. Miller, "Spontaneous retinal venous pulsation: Aetiology and significance," *J. Neurol. Neurosurg. Psych*, vol. 74, 2003.
[15] F. Moret, C. M. Reiff, W. A. Lagrèze, and M. Bach, "Quantitative Analysis of Fundus-Image Sequences Reveals Phase of Spontaneous Venous Pulsations," *Transl. Vis. Sci. Technol.*, vol. 4, no. 5, p. 3, 2015.
[16] J. S. Friedenwald, "Retinal Vascular Dynamics," *Am. J. Ophthalmol.*, vol. 17, no. 5, pp. 387–395, 1934.
[17] F. Moret, C. M. Poloschek, W. A. Lagrèze, and M. Bach, "Visualization of fundus vessel pulsation using principal component analysis," *Investig. Ophthalmol. Vis. Sci.*, vol. 52, no. 8, pp. 5457–5464, 2011.
[18] R. P. Tornow, R. Kolář, and J. Odstrčilík, "Non-mydriatic video ophthalmoscope to measure fast temporal changes of the human retina," in *Europ Conf on Biomed Optics. Optical Society of America*, 2015, vol. 9540.
[19] J. V. Lovasik, M. Gagnon, and H. Kergoat, "A novel noninvasive videographic method for quantifying changes in the chromaticity of the optic nerve head with changes in the intraocular pressure, pulsatile choroidal blood flow and visual neural function in humans," *Surv. Ophthalmol.*, vol. 38, pp. S35–S51, 1994.
[20] L. Puyo, M. Paques, M. Fink, J.-A. Sahel, and M. Atlan, "Waveform analysis of human retinal and choroidal blood flow with laser Doppler holography," *Biomed. Opt. Express*, vol. 10, no. 10, pp. 4942–4963, 2019.
[21] L. F. Schmetterer, F. Lexer, C. J. Unfried, H. Sattmann, and A. F. Fercher, "Topical measurement of fundus pulsations," *Opt. Eng.*, vol. 34, no. 3, 1995.
[22] R.-P. Tornow, J. Odstrcilik, and R. Kolar, "Time-resolved quantitative inter-eye comparison of cardiac cycle-induced blood volume changes in the human retina," *Biomed. Opt. Express*, vol. 9, no. 12, pp. 6237–54, 2018.
[23] J. E. Grunwald, J. Piltz, S. M. Hariprasad, and J. DuPont, "Optic nerve and choroidal circulation in glaucoma," *Invest. Ophtal. Vis. Sci.*, vol. 39, 1998.
[24] S. S. Hayreh, "Blood supply of the optic nerve head and its role in optic atrophy , glaucoma , and oedema of the optic disc," *Brit. J. Ophthal.*, vol. 53, pp. 721–748, 1969.
[25] A. Waliszek-Iwanicka, M. Waliszek, M. Banach, et al. "Assessment of blood flow in posterior ciliary arteries and its correlation with intraocular and arterial blood pressures in patients with open angle glaucoma," *Med Sci Monit*, vol. 16, no. 10, pp. 94–102, 2010.
[26] G. T. Dorner, E. Polska, W. Krankenanstaltenverbund, and L. Schmetterer, "Calculation of the diameter of the central retinal artery from noninvasive measurements in humans," *Curr. Eye Res.*, vol. 25, no. 6, 2002.
[27] T. H. Williamson, G. D. Lowe, and G. M. Baxter, "Influence of age, systemic blood pressure, smoking, and blood viscosity on orbital blood velocities," *Br. J. Ophthalmol.*, vol. 79, no. 1, pp. 17–22, 1995.
[28] S. M. Golzan, A. Avolio, and S. L. Graham, "Hemodynamic interactions in the eye: A review," *Ophthalmologica*, vol. 228, no. 4, pp. 214–221, 2012.
[29] B. D. Madjarov and J. W. Berger, "Automated, real time extraction of fundus images from slit lamp fundus biomicroscope video image sequences," *Br. J. Ophthalmol.*, vol. 84, no. 6, pp. 645–647, 2000.
[30] W. H. Morgan, M. L. Hazelton, B. D. Betz-Stablein, et al. "Photoplethysmographic measurement of various retinal vascular pulsation parameters and measurement of the venous phase delay," *Investig. Ophthalmol. Vis. Sci.*, vol. 55, no. 9, pp. 5998–6006, 2014.
[31] W. H. Morgan, C. R. P. Lind, S. Kain, et al."Retinal vein pulsation is in phase with intracranial pressure and not intraocular pressure," *Investig. Ophthalmol. Vis. Sci.*, vol. 53, no. 8, pp. 4676–4681, 2012.
[32] B. U. Seifertl and W. Vilser, "Retinal Vessel Analyzer (RVA)-design and function.," *Biomed. Tech. (Berl).*, vol. 47 Suppl 1, pp. 678–681, 2002.
[33] G. Garhofer, T. Bek, A. G. Boehm, et al."Use of the retinal vessel analyzer in ocular blood flow research," *Acta Ophthalmol.*, vol. 88, no. 7 , 2010.
[34] J. Senarathna, A. Rege, N. Li, and N. V. Thakor, "Laser speckle contrast imaging: Theory, instrumentation and applications," *IEEE Rev. Biomed. Eng.*, vol. 6, no. January, pp. 99–110, 2013.
[35] S. Cunningham, A. Rege, K. Raje, S. Kalarn, Y. Liu, and M. Lason Brooke, "Non-invasive measurement of retinal blood flow using the XyCAM RITM retinal imaging system: Early clinical results," in *Invest. Ophthalmol. and Vis. Sci.*, 2016, vol. 57, no. 12, pp. 5927–5927.
[36] A. Rege, S. I. Cunningham, Y. Liu, et al. "Clinical Measurement of Retinal Blood Flow using the XyCAM RITM Handheld Retinal Imager," *Invest. Ophthalmol. Vis. Sci.*, vol. 57, no. 12, p. 5925, 2016.
[37] S. Kalarn, K.-A. Cho, G. Thompson, et al. "Non-Invasive Blood-Flow Measurement in the Glaucomatous Optic Nerve Head using the XyCAM RI Retinal Imaging System," *Invest. Ophthalmol. Vis. Sci.*, vol. 60, 2019.
[38] E. Logean, M. H. Geiser, and C. E. Riva, "Laser Doppler instrument to investigate retinal neural activity-induced changes in optic nerve head blood

flow," *Opt. Lasers Eng.*, vol. 43, no. 3–5, pp. 591–602, 2005.
[39] L. Puyo, M. Pacques, M. Fink, et al. "In vivo laser Doppler holography of the human retina," *Biomed. Opt. Express*, vol. 9, no. 9, p. 4113, 2018.
[40] S. Shariflou, A. Agar, K. Rose, C. Bowd et al. "Objective Quantification of Spontaneous Retinal Venous Pulsations Using a Novel Tablet-Based Ophthalmoscope," *Transl. Vis. Sci. Technol.*, vol. 9, no. 4, p. 19, 2020.
[41] T. Von Hanno, A. K. Sjølie, and E. B. Mathiesen, "Retinal vascular calibre and response to light exposure and serial imaging," *Acta Ophthalmol.*, vol. 92, no. 5, pp. 444–448, 2014.
[42] R. P. Tornow, A. Milczarek, J. Odstrcilik, and R. Kolar, "Binocular video ophthalmoscope for simultaneous recording of sequences of the human retina to compare dynamic parameters," in *Novel Biophotonics Techniques and Applications IV*, 2017, vol. 10413.
[43] B. Betz-Stablein, M. L. Hazelton, and W. H. Morgan, "Modelling retinal pulsatile blood flow from video data," *Stat. Methods Med. Res.*, vol. 27, no. 5, pp. 1575–1584, 2018.
[44] L. Puyo, M. Paques, and M. Atlan, "Spatio-temporal filtering in laser Doppler holography for retinal blood flow imaging," *Biomed. Opt. Express*, vol. 11, no. 6, pp. 3274–3287, 2020.
[45] I. Labounková, R. Labounek, J. Odstrčilík, et al. "Retinal pulsatile shift enhancement with blind source separation," *Invest. Ophthalmol. Vis. Sci.*, vol. 60, p. 173, 2019.
[46] I. Labounkova, R. Labounek, J. Odstrcilik, et al. "Blind Source Separation of Different Retinal Pulsatile Patterns from Simultaneous Long-term Binocular Ophtalmoscopic Video-records," *IEEE 41st Eng. Med. Biol. Conf.*, vol. July 23-27, pp. 4729–4731, 2019.
[47] W. H. Morgan, A. Abdul-Rahman, D. Y. Yu, et al. "Objective detection of retinal vessel pulsation," *PLoS One*, vol. 10, no. 2, pp. 1–10, 2015.
[48] A. Wartak, F. Beer, S. Desissaire, et al. "Investigating spontaneous retinal venous pulsation using Doppler optical coherence tomography," *Sci. Rep.*, vol. 9, no. 1, pp. 1–11, 2019.
[49] M. Cannesson, A. A. Awad, and K. Shelley, "Oscillations in the Plethysmographic Waveform Amplitude : Phenomenon Hides Behind Artifacts Oscillations in the Plethysmographic Waveform Amplitude : Phenomenon Hides Behind Artifacts," *Anesthesiology*, vol. 111, 2009.
[50] R. Kolar, R. P. Tornow, J. Odstrcilik, and I. Liberdova, "Registration of Retinal Sequences from New Video-Ophthalmoscopic Camera," *Biomed. Eng. Online*, vol. 15, no. 1, p. 57, 2016.
[51] J. Shlens, "A Tutorial on Principal Component Analysis," *arXiv*, 2014.
[52] C. J. James and C. W. Hesse, "Independent component analysis for biomedical signals," *Physiol. Meas.*, vol. 26, no. 1, pp. 15–39, 2005.
[53] E. B. Erhardt, S. Rachakonda, E. J. Bedrick, et al. "Comparison of multi-subject ICA methods for analysis of fMRI data," *Hum. Brain Mapp.*, vol. 32, no. 12, pp. 2075–2095, 2011.
[54] E. A. Allen, E. B. Erhardt, E. Damaraju, et al. "A baseline for the multivariate comparison of resting-state networks," *Front. Syst. Neurosci.*, vol. 5, no. 2, pp. 1–23, 2011.
[55] A. Hyvarinen and E. Oja, "A Fast Fixed-Point Alogrithm for Independent Component Analysis," *Neural Comput.*, vol. 9, pp. 1483–1492, 1997.
[56] J. A. Hartigan and M. A. Wong, "Algorithm AS 136: A K-Means Clustering Algorithm," *J. R. Stat. Soc. Ser. C (Applied Stat.)*, vol. 28, no. 1, 2009.
[57] H. Lee, "addaxis." MATLAB Central File Exchange, 2016.
[58] S. J. Zieman, V. Melenovsky, and D. A. Kass, "Mechanisms, pathophysiology, and therapy of arterial stiffness," *Arterioscler. Thromb. Vasc. Biol.*, vol. 25, no. 5, pp. 932–943, 2005.
[59] A. Avolio, M. O. Kim, A. Adji, et al. "Cerebral Haemodynamics: Effects of Systemic Arterial Pulsatile Function and Hypertension," *Curr. Hypertens. Rep.*, vol. 20, no. 3, 2018.
[60] J. Ramos-Cejudo, T. Wisniewski, C. Marmar, et al. "Traumatic Brain Injury and Alzheimer's Disease: The Cerebrovascular Link," *EBioMedicine*, vol. 28, no. April, pp. 21–30, 2018.
[61] F. F. Wei, L. Thijs, C. G. Yu, et al. "Retinal microvasculature in relation to central hemodynamics in a flemish population," *Hypertension*, vol. 74, no. 3, pp. 606–613, 2019.
[62] J. Chua, R. Sim, B. Tan, et al. "Optical Coherence Tomography Angiography in Diabetes and Diabetic Retinopathy," *J. Clin. Med.*, vol. 9, no. 6, p. 1723, 2020.
[63] T. E. Farrah, B. Dhillon, P. A. Keane, D. J. Webb, and N. Dhaun, "The eye, the kidney, and cardiovascular disease: old concepts, better tools, and new horizons," *Kidney Int.*, vol. 98, no. 2, pp. 323–342, 2020.
[64] H. Dobberstein, U. Solbach, A. Weinberger, and S. Wolf, "Correlation between retinal microcirculation and blood viscosity in patients with hyperviscosity syndrome," *Clin. Hemorheol. Microcirc.*, vol. 20, 1998.
[65] M. Zhao, A. K. C. Lam, L. N. Quin, et al. "Capillary perfusion of superficial retina and hemodynamics of central retinal artery in myopic eyes," *Invest. Ophthalmol. Vis. Sci.*, vol. 61, no. 7, p. 2676, 2020.
[66] N. Lewczuk, A. Zdebik, J. Bogusławska, et al. "Ocular manifestations of pulmonary hypertension," *Surv. Ophthalmol.*, vol. 64, no. 5, 2019.
[67] H. Wang, H. Li, X. Zhang, et al. "Ocular Image and Haemodynamic Features Associated with Different Gradings of Ipsilateral Internal Carotid Artery Stenosis," *J. Ophthalmol.*, vol. 2017, 2017.
[68] E. Agabiti-Rosei and D. Rizzoni, "Microvascular structure as a prognostically relevant endpoint," *J. Hypertens.*, vol. 35, no. 5, 2017.
[69] J. Chua, C. W. L. Chin, J. Hong, et al. "Impact of hypertension on retinal capillary microvasculature using optical coherence tomographic angiography," *J. Hypertens.*, vol. 37, no. 3, pp. 572–580, 2019.
[70] C. Sun, C. Ladores, J. Hong, et al. "Systemic hypertension associated retinal microvascular changes can be detected with optical coherence tomography angiography," *Sci. Rep.*, vol. 10, no. 1, pp. 1–9, 2020.
[71] J. B. Jonas, E. Berenshtein, and L. Holbach, "Anatomic Relationship between Lamina Cribrosa, Intraocular Space, and Cerebrospinal Fluid Space," *Investig. Ophthalmol. Vis. Sci.*, vol. 44, no. 12, 2003.
[72] V. D. Calhoun and T. Adali, "Multisubject independent component analysis of fMRI: A decade of intrinsic networks, default mode, and neurodiagnostic discovery," *IEEE Rev. Biomed. Eng.*, vol. 5, pp. 60–73, 2012.
[73] M. Golzan, S. L. Graham, J. Leaney, and A. Avolio, "Dynamic Association between Intraocular Pressure and Spontaneous Pulsations of Retinal Veins," *Curr. Eye Res.*, vol. 36, no. 1, pp. 53–59, 2011.
[74] R. P. Tornow, R. Kolar, J. Odstrcilik, I. Labounkova, and F. Horn, "Imaging Video Plethysmography Shows Reduced Signal Amplitude in Glaucoma Patients in the Area of the Microvascular Tissue of the Optic Nerve Head," *Graefes Arch Clin Exp Ophthalmol*, 2020. [In Press]
[75] C. Bowd, R. N. Weinreb, J. M. Williams, and L. M. Zangwill, "The retinal nerve fiber layer thickness in ocular hypertensive, normal, and glaucomatous eyes with optical coherence tomography," *Arch. Ophthalmol.*, vol. 118, no. 1, pp. 22–26, 2000.
[76] O. Z. Sahin, S. B. Sahin, T. Ayaz, et al. "The impact of hypertension on retinal nerve fiber layer thickness and its association with carotid intima media thickness," *Blood Press.*, vol. 24, no. 3, pp. 178–184, 2015.
[77] J.-I. Kim and B.-H. Kang, "Decreased retinal thickness in patients with Alzheimer ' s disease is correlated with disease severity," *PLoS One*, vol. 14, no. 11, pp. 1–11, 2019.
[78] A. Chrysou, N. M. Jansonius, and T. van Laar, "Retinal layers in Parkinson's disease: A meta-analysis of spectral-domain optical coherence tomography studies," *Park. Relat. Disord.*, vol. 64, no. May, 2019.
[79] M. Satue, J. Obis, M. J. Rodrigo, et al. "Optical Coherence Tomography as a Biomarker for Diagnosis, Progression, and Prognosis of Neurodegenerative Diseases," *J. Ophthalmol.*, vol. 2016, 2016.
[80] W. J. C. Van Ballegoij, S. C. Kuijpers, I. C. Huffnagel, et al. "Optical coherence tomography shows neuroretinal thinning in myelopathy of adrenoleukodystrophy," *J. Neurol.*, vol. 267, no. 3, pp. 679–687, 2020.
[81] K. M. Lee, J. M. Kim, E. J. Lee, and T. W. Kim, "Anterior Optic Nerve Head Perfusion is Dependent on Adjacent Parapapillary Choroidal perfusion," *Sci. Rep.*, vol. 9, no. 1, pp. 1–8, 2019.
[82] H. Serr, "Zur Analyse der spontanen Pulserscheinungen in den Netzhautgefäßen," *Albr. Von Græfes Arch. für Ophthalmol.*, vol. 137, no. 4, pp. 487–505, 1937.
[83] H. Spahr, D. Hillmann, C. Hain, et al. "Imaging pulse wave propagation in human retinal vessels using full-field swept-source optical coherence tomography," *Opt. Lett.*, vol. 40, no. 20, p. 4771, 2015.
[84] K. K. W. Chan, F. Tang, C. C. Y. Tham, et al. "Retinal vasculature in glaucoma : a review," *BMJ Open Ophthalmol.*, vol. 1, pp. 1–14, 2017.
[85] M. Sehi, I. Goharian, R. Konduru, et al. "Retinal Blood Flow in Glaucomatous Eyes with Single Hemifield Damage," vol. 121, no. 3, 2015.
[86] K. Singh, C. Dion, S. Costantino, M. Wajszilber, M. R. Lesk, and T. Ozaki, "Development of a novel instrument to measure the pulsatile movement of ocular tissues," *Exp. Eye Res.*, vol. 91, no. 1, pp. 63–68, 2010.
[87] N. Dragostinoff, R. M. Werkmeister, M. Gröschl, and L. Schmetterer, "Depth-resolved measurement of ocular fundus pulsations by low-coherence tissue interferometry," *J. Biomed. Opt.*, vol. 14, no. 5, 2009.
[88] H. T. Kasprzak, T. Bajraszewski, and A. Kowalczyk, "High accuracy measurement of spectral characteristics of movements of the eye elements," *Óptica Pura y Apl.*, vol. 70, no. January, pp. 7–11, 2007.
[89] K. Singh, C. Dion, M. Wajszilber, et al. "Measurement of ocular fundus pulsation in healthy subjects using a novel Fourier-domain optical coherence tomography," *Investig. Ophthalmol. Vis. Sci.*, vol. 52, no. 12, pp. 8927–8932, 2011.
[90] K. Singh, C. Dion, A. G. Godin,et al. "Pulsatile movement of the optic nerve head and the peripapillary retina in normal subjects and in glaucoma," *Investig. Ophthalmol. Vis. Sci.*, vol. 53, no. 12, pp. 7819–7824, 2012.

3.2 Impact of biological variables on clinical outcomes from retinal pulsatile pattern dynamics

This part of the Thesis is dedicated to advancements of basal knowledge resulted from the analysis of retinal sequences. The link between the intensity of SVPs and heart rate or age was proven and published in journal of Communications Biology: LABOUNKOVÁ, Ivana, et al. Heart rate and age modulate retinal pulsatile patterns. Communications biology, 2022, 5(1),582, under the open access CC BY license (Creative Commons Attribution v4.0 International License).

Author's contribution and Innovation. As a first author, I have designed and performed the analysis utilizing the blind source separation approach introduced in previous section. The analysis revealed correlation of SVP morphology (pulse amplitude, pulse total volume) with age, and SVP and OCP morphology with heart rate. Till now, the influence of heart rate was omitted in earlier clinical studies studies and most of theoretical studies modelling the SVPs. With other co-authors, I have participated on results interpretation. And, I have written the manuscript which was editted by the co-authors.

The journal article [171] is attached in the next pages of this Thesis.

communications biology

ARTICLE

https://doi.org/10.1038/s42003-022-03441-6 OPEN

Heart rate and age modulate retinal pulsatile patterns

Ivana Labounková[1,2], René Labounek[2], Radim Kolář[1], Ralf P. Tornow[3], Charles F. Babbs[4], Collin M. McClelland[5], Benjamin R. Miller[6] & Igor Nestrašil[2,7]✉

Theoretical models of retinal hemodynamics showed the modulation of retinal pulsatile patterns (RPPs) by heart rate (HR), yet in-vivo validation and scientific merit of this biological process is lacking. Such evidence is critical for result interpretation, study design, and (patho-) physiological modeling of human biology spanning applications in various medical specialties. In retinal hemodynamic video-recordings, we characterize the morphology of RPPs and assess the impact of modulation by HR or other variables. Principal component analysis isolated two RPPs, i.e., spontaneous venous pulsation (SVP) and optic cup pulsation (OCP). Heart rate modulated SVP and OCP morphology ($p_{FDR} < 0.05$); age modulated SVP morphology ($p_{FDR} < 0.05$). In addition, age and HR demonstrated the effect on between-group differences. This knowledge greatly affects future study designs, analyses of between-group differences in RPPs, and biophysical models investigating relationships between RPPs, intracranial, intraocular pressures, and cardiovascular physiology.

[1] Department of Biomedical Engineering, Brno University of Technology, Brno, Czech Republic. [2] Division of Clinical Behavioral Neuroscience, Department of Pediatrics, Masonic Institute for the Developing Brain, University of Minnesota, Minneapolis, MN, USA. [3] Department of Ophthalmology, Friedrich-Alexander University of Erlangen-Nuremberg, Erlangen, Germany. [4] Weldon School of Biomedical Engineering, Purdue University, West Lafayette, IN, USA. [5] Department of Ophthalmology and Visual Neurosciences, University of Minnesota, Minneapolis, MN, USA. [6] Department of Neurology, University of Minnesota, Minneapolis, MN, USA. [7] Center for Magnetic Resonance Research, Department of Radiology, University of Minnesota, Minneapolis, MN, USA. ✉email: nestr007@umn.edu

In vivo dynamic video-ophthalmoscopy (VO) provides a potential opportunity for a non-invasive and easily accessible evaluation of retinal hemodynamics. VO is inexpensive and well suited to become a diagnostic and disease monitoring tool for the real-time imaging of local microvascular blood supply and detecting various pathologies. VO is applicable in many fields of medicine such as ophthalmology (e.g., diabetic retinopathy[1], glaucoma[2–4]), neurology (e.g., Alzheimer disease[5], multiple sclerosis[6], stroke[7]), or cardiology (e.g., coronary heart disease[8], arterial stiffness[9–11], hypertension[12], diabetes[12,13]).

Blood flow[14,15], blood volume[4,16] and structural venous diameter changes[17–19] are the most commonly evaluated hemodynamic parameters from dynamic retinal imaging. The hemodynamic parameters are usually extracted in a manual or semi-automated fashion from specific morphological segments of a retinal vessel tree[16–18,20–23]. However, the reproducibility of the parameters remains a challenge due to the uniqueness of each individual's retinal vessel tree[24] and the bias introduced by a subjective inter-rater and inter-participant selection of analyzed morphological segments[25]. To increase the reproducibility of local retinal hemodynamics, we have recently implemented a blind source separation that automatically divided the optic nerve head (ONH) into 2-3 functionally distinct areas that emerged as specific retinal pulsatile patterns (RPPs)[26]. The reproducible RPPs were spontaneous venous pulsation (SVP) and optic cup pulsation (OCP) with mutually phase-shifted hemodynamics. OCP was postulated to represent arterial blood filling preceding the SVP outflow[26].

Spontaneous venous pulsation is the most investigated hemodynamic phenomenon over the whole retinal background with the best detection capability and highest reproducibility in the area where the central retinal vein crosses the ONH. The etiology and visibility of the ONH SVP are likely related to the gradient between intracranial pressure (ICP) and intraocular pressure (IOP) waveforms[27–30]. Limited in vivo evidence of the SVP-ICP relationship exists[30–34]. The underlying biophysics is a subject of active investigation[35].

Mathematical models, which were proposed to describe IOP-ICP-SVP relationships[35–38], have not been verified by in vivo experiments yet. Levine and Bebie's SVP-ICP theory assumes an influence of heart rate (HR) on SVP amplitude, yet without providing the in vivo evidence[37,38]. Therefore, the influence of HR on retinal intra-vessel hemodynamics deserves further investigation. In addition to HR, demographic characteristics (e.g., age or sex) were linked to vessel stiffness[39,40], vessel cross-section area[41,42], pulse pressure[39,40] or cardiac cycle parameters (e.g., filling time, preload, stroke volume) and, consequently, modify intra-vessel hemodynamics including the blood flow/volume in retinal mini- and micro-vessels[42]. Exactly how the in vivo video-ophthalmoscopic data (sensitive to blood flow or volume fluctuations) are affected by HR, age, or sex remains to be determined. If the impact of any variable is proved, a revisiting of clinical video-ophthalmoscopic outcomes demonstrating correlations between VO measurements and retinal neural fiber layer (RNFL) thickness[4,19,43] or other outcomes in populations of healthy subjects and those with disease conditions such as glaucoma is warranted.

In this study, we investigated human in vivo video-ophthalmoscopic data and the effects of HR and age on the morphology of blood-volume-specific RPPs. We isolated two RPPs (i.e., SVP and OCP) from the video-ophthalmoscopic dataset, tested SVP-OCP phase shift, evaluated RPP reproducibility and morphology, and cross-correlated the morphology with HR, age, IOP, and RNFL thickness. Finally, we estimated the effects of HR and age with between-group comparisons in resulting morphological observations.

Results

Participant characteristics. Thirty-four retinal video-recordings (RVRs) were acquired, and exclusively left-eye RVRs were used in the analysis. HR estimated from SVP and OCP of all participants was $66 \pm 13\,\mathrm{min}^{-1}$ (ranging $44–92\,\mathrm{min}^{-1}$). (Image analysis workflow estimating and segregating SVP and OCP is summarized in Fig. 1.) HR was significantly higher in patients with treated ocular hypertension (OHT) than in healthy participants and was significantly correlated with SVP and OCP morphologies (Table 1, Figs. 2, 3). Due to this finding, HR was treated as a confounding variable in further ANCOVA between-group tests. Other physiological data such as age, IOP, and RNFL demonstrated no significant between-group differences (Table 1). Refractive error, visual acuity, and perimetry were within physiological ranges without any significant pathology.

Phase shifted retinal pulsatile patterns in principal component space. In a total of 34 RVRs, we detected SVP in 33 RVRs (97%) and OCP in 31 RVRs (91%) when the first 12 principal components were visually inspected and evaluated in each RVR. Averaged SVP principal component index was 3 ± 2 (min 1; max 9), and averaged OCP principal component index was 3 ± 2 (min 1; max 11). Representative examples of SVP and OCP spatiotemporal patterns with detected and corrected control points are shown in Fig. 1a. An input-output workflow of the utilized principal component analysis (PCA) is schematically summarized in Fig. 1b.

The cross-correlation response function (Fig. 1a) demonstrated that OCP significantly preceded SVP about -3.71 ± 2.05 (min -8; max 0) samples, i.e., 148 ± 82 ms, (one sample t-test $p = 3.95e^{-11}$). With regard to the participant's heart cycle period, the preceding interval corresponded to $-16 \pm 8\%$ of the heart cycle. The Pearson correlation coefficient (r) between not-aligned OCP and SVP time-courses (i.e., corresponding PCA eigenvectors[44]; Fig. 1b) was 0.31 ± 0.39 (min -0.45; max 0.92) and increased after the delay alignment to 0.84 ± 0.08 (min 0.66; max 0.96). The linear dependence between PCA eigenvector time-course and averaged image-intensity computed from the same region of interest (ROI) corresponding to the PCA-suprathreshold ROI was 0.55 ± 0.33 (min -0.06; max 0.97) for SVP and 0.51 ± 0.29 (min -0.11; max 0.94) for OCP. Lower correlation corresponded to recordings where the averaging approach failed due to high random noise power.

Retinal pulsatile pattern morphology modulated by heart rate and age. A sketch of the morphological measurement from the segregated RPP is shown in Fig. 1a. Morphologies of SVP and OCP were significantly modulated by HR (Figs. 2, 3). SVP amplitude Ampl ($r = -0.61$, $p = 0.0002$, $p_{BH} = 0.0003$, $P_{size} = 97.8\%$; p_{BH} - Benjamini-Hochberg adjusted p-value, P_{size} – power of the result regarding the sample size), total relative pulse stroke volume V_T ($r = -0.87$, $p < 0.0001$, $p_{BH} = 0.0002$, $P_{size} = 100.0\%$), slope-up to baseline SlpU ($r = 0.46$, $p = 0.0067$, $p_{BH} = 0.0084$, $P_{size} = 79.7\%$) and time to peak t_p ($r = -0.67$, $p < 0.0001$, $p_{BH} = 0.0002$, $P_{size} = 99.5\%$) were significantly associated with HR (Fig. 2b). SVP slope-down to peak SlpD was HR independent (Fig. 2). OCP V_T ($r = -0.53$, $p = 0.0029$, $p_{BH} = 0.0073$, $P_{size} = 91.1\%$), SlpU ($r = 0.48$, $p = 0.0078$, $p_{BH} = 0.0130$, $P_{size} = 83.5\%$), t_p ($r = -0.61$, $p = 0.0004$, $p_{BH} = 0.0020$, $P_{size} = 97.8\%$) and SlpD ($r = -0.45$, $p = 0.0154$, $p_{BH} = 0.0193$, $P_{size} = 77.6\%$) were significantly correlated with HR (Fig. 3b). OCP Ampl was HR independent (Fig. 3). HR-dependent intra-participant variability is shown in Fig. 4 for three representative participants out of the four participants who underwent RVRs twice (once at monocular and one at binocular VO) with an inter-recording interval about 2 years.

HR significantly correlated with age ($r = -0.45$, $p = 0.0090$, $P_{size} = 77.6\%$). Therefore, we investigated linear dependence

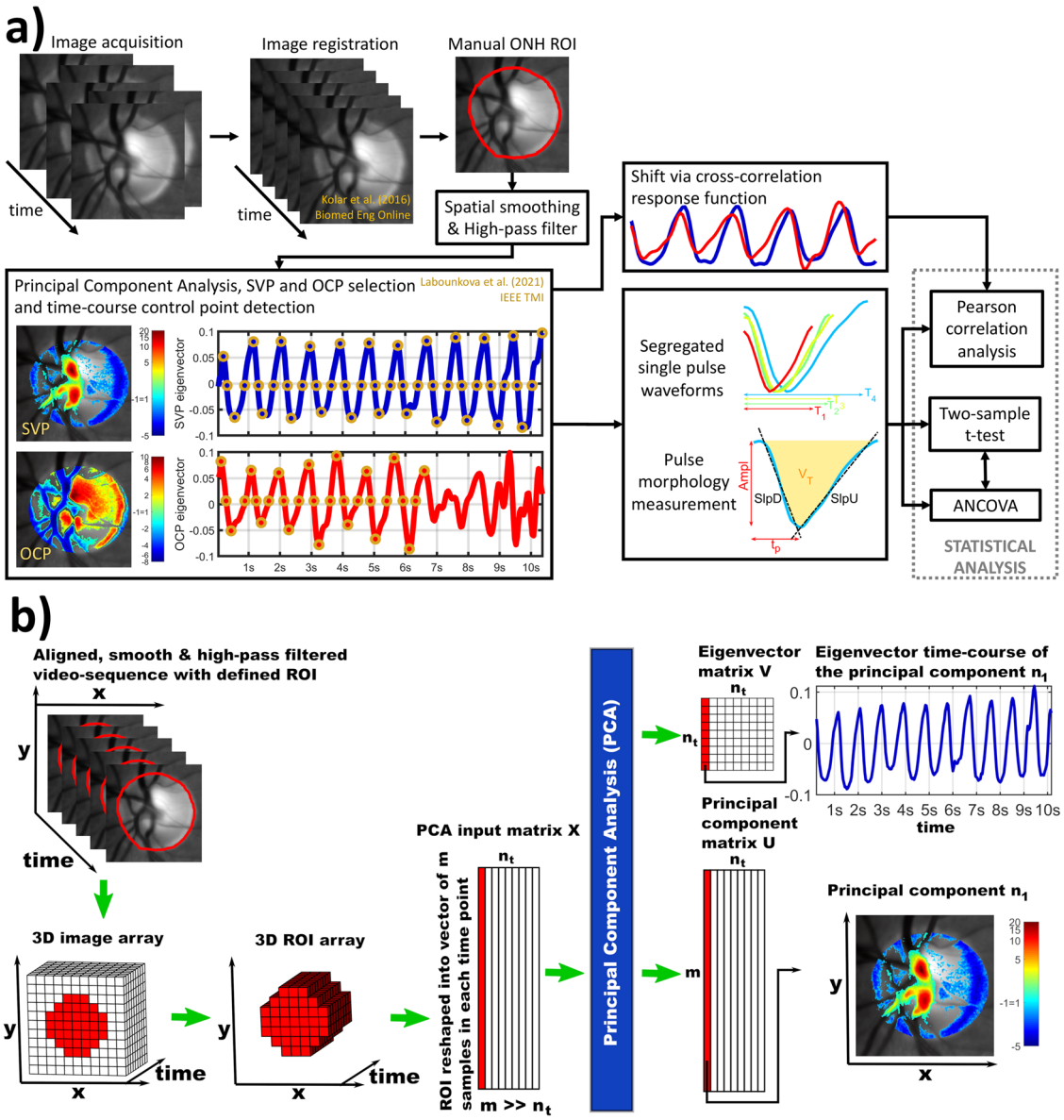

Fig. 1 Image and statistical analysis workflow. a The block diagram summarizes the whole image and statistical analysis workflow. ONH optic nerve head, ROI region of interest, SVP spontaneous venous pulsation, OCP optic cup pulsation, T period [s], Ampl amplitude, SlpD slope-down, SlpU slope-up, t_p time to peak, V_T total relative pulse stroke volume, ANCOVA analysis of covariance. **b** The block diagram summarizes the input-output system of the utilized principal component analysis (PCA). The left input side demonstrates array operations forming the PCA input matrix. The right output side demonstrates temporal and spatial extraction of the results. x, y spatial axes of images, n_t total number of time points, m total number of pixels of the ROI in one time point, n_1 index of the principal component number 1 in the output principal component and eigenvector matrices (first red-highlighted columns), and time point number 1 in the PCA input matrix. Each column in the eigenvector matrix represents an eigenvector time-course of the principal component in the corresponding column of the principal component matrix. In the right bottom corner, the thresholded n1 principal component of m-samples was reshaped back into the original xy space and overlayed the averaged anatomical background image. All images show recordings of the left eye.

between RPP morphology and additional physiological variables. SVP Ampl ($r = 0.50$, $p = 0.0026$, $p_{BH} = 0.0130$, $P_{size} = 87.0\%$) and SVP V_T ($r = 0.45$, $p = 0.0089$, $p_{BH} = 0.0223$, $P_{size} = 77.6\%$) were significantly correlated with age (Fig. 5). The modulation of SVP Ampl and V_T demonstrated a larger effect of HR than age (Figs. 2, 5). No significant correlations of RPP morphology with IOP or RNFL were detected.

Between-group differences in RPP morphology measurements. Lower SVP Ampl, SVP V_T, and OCP t_p, along with higher absolute OCP SlpD and OCP SlpU, were detected in treated OHT patients (two-sample *t*-test) (Table 1). ANCOVA with age as a confounding variable preserved all significant between-group differences in OCP morphology, but none in SVP morphology (Table 1). In contrast, ANCOVA with HR as a confounding variable only showed trends of the higher absolute OCP SlpD and the lower OCP t_p (Table 1). Group averaged OCP pulses with 25–75% confidence intervals are shown in Fig. 6 and demonstrate visible changes in group-specific pulse morphologies.

Discussion

Study novelty and practical impact. Our in vivo results demonstrate the modulation of the SVP and OCP pulse morphologies by HR and of the SVP morphology by age.

Table 1 Participant characteristics and morphology measurements of retinal pulsatile patterns.

		Age [y.o.]	HR [min^{-1}]	IOP [mmHg]	RNFL [μm]	
	p_ttest2	0.1177	***0.0182**	0.2198	0.5794	
Physiology	Healthy controls	66.0 ± 13.2	59.9 ± 9.6	15.3 ± 2.7	91.9 ± 10.5	
	OHT patients	58.7 ± 12.9	70.3 ± 13.5	16.5 ± 3.0	89.7 ± 11.6	
		Ampl	V_T	SlpD	SlpU	t_p [ms]
SVP	p_ttest2	***0.0235**	***0.0317**	0.4045	0.5110	0.3537
	p_ANCOVA_HR	0.2753	0.8049	0.2097	0.6353	0.3897
	p_ANCOVA_age	0.1057	0.1211	0.6646	0.5442	0.4962
	Healthy controls	0.143 ± 0.023	2.14 ± 0.62	−0.587 ± 0.123	0.240 ± 0.061	419 ± 66
	OHT patients	0.123 ± 0.027	1.66 ± 0.62	−0.544 ± 0.166	0.254 ± 0.059	396 ± 74
OCP	p_ttest2	0.2105	0.8740	***0.0077**	***0.0150**	***0.0047**
	p_ANCOVA_HR	0.1311	0.1532	**0.0637**	0.1299	**0.0859**
	p_ANCOVA_age	0.1070	0.7891	***0.0058**	***0.0199**	***0.0091**
	Healthy controls	0.104 ± 0.035	1.34 ± 0.42	−0.395 ± 0.199	0.174 ± 0.057	434 ± 81
	OHT patients	0.120 ± 0.031	1.31 ± 0.44	−0.590 ± 0.167	0.247 ± 0.087	355 ± 56

P-values demonstrating between-group trends ($p < 0.1$) are highlighted with bold font, and *p*-values demonstrating significant between-group differences ($p < 0.05$) are highlighted with bold font and asterisks.
Notes: OHT ocular hypertension, *SVP* spontaneous venous pulsations, *OCP* optic cup pulsations, *HR* heart rate, *IOP* intraocular pressure, *RNFL* retinal neural fiber layer thickness, *Ampl* amplitude, V_T total relative pulse stroke volume, *SlpD* slope-down, *SlpU* slope-up, t_p time to peak, *p_ttest2 p*-value of between-group difference obtained from the two-sample t-test, *p_ANCOVA_HR p*-value of between group-difference obtained from analysis of covariance where HR was confounding variable, *p_ANCOVA_age p*-value of between group-difference obtained from analysis of covariance where age was confounding variable. Values listed for HC and OHT are mean ± standard deviation. *P*-values demonstrating between-group trends ($p < 0.1$) are highlighted with bold font, and *p*-values demonstrating significant between-group differences ($p < 0.05$) are highlighted with bold font and asterisks. ANCOVA test, where two confounding variables (HR and age) would be used at once, has not been utilized because HR and age are significantly correlated pair of variables.

Therefore, the unverified biological impact of HR and age at RPP morphology was in vivo confirmed and validated. The impact of HR and age on the SVP/OCP morphology has been neglected in previous clinical research[4,19,33,34,43] and even in theoretical SVP-intracranial/intraocular pressure models[35,36]. The in vivo findings validate Levine and Bebie's theory, assuming that SVP Ampl is influenced by HR[37,38]. This discovery may also indicate descriptive vessel compliance characteristics as demonstrated by the uniformity of the SVP SlpD parameter. The studied morphology parameters should be investigated in future research as objective quantitative in vivo markers of retinal hemodynamics. Importantly, HR and age need to be considered and added as confounding variables in biological models or clinical studies evaluating between-group differences in RPP. The optimal strategy for the study design is a dataset free of between-group differences in HR and age, but such proper matching would be challenging and hardly achievable.

The analysis via spatial PCA of RVRs detected reproducible phase-shifted SVP and OCP patterns in healthy controls and treated OHT patients. SVP and OCP patterns demonstrated low inter-participant variation in eigenvector scaled time-courses, i.e., temporal pulses, and were highly reproducible. These results emphasize the feasibility of the spatial PCA for inferences achieved by RPPs and its applicability in future studies, especially those involving large population cohorts.

Although the etiology of the SVP phenomenon is still not clearly understood, the temporal uniformity in SVP SlpD can represent a novel insight into the SVP origin. This temporal uniformity may be due to similar inter-participant venous compliance characteristics that modulates venous capacitance. As the implication of vein capability to change its geometry, the vein compliance property enables a volume increase in local vein segments in response to local blood filling[45]. Since the vein resistance to local blood flow is minimal[45], the blood filling corresponding to SlpD in the SVP morphology displayed temporal uniformity over investigated population.

We revealed the significant impact of HR on the morphology of reproducible RPPs. The higher HR resulted in lower SVP Ampl, V_T, and t_p and higher SlpU. Similarly, the higher HR led to the lower OCP V_T, t_p, and SlpD and higher SlpU. This observation of changes in V_T linked to HR may reflect the impact of Starling's law. Higher HR causes a shorter period for cardiac blood filling and, consequently, lower cardiac preload leads to the lower blood volume ejected from the heart. All these characteristics of heart function imprint into the RPP morphology and may be evaluated non-invasively and in vivo with the VO.

Additionally, three SVP parameters, i.e., Ampl, SlpD, and V_T, were significantly correlated with age. Higher SVP Ampl and V_T with age can be influenced by peripheral pulse pressure pulsatility or vessel stiffening, which increase with age[11,46]. The increase of age-related vessel stiffness is directly linked to the elasticity loss[39,40] and is a potential factor underlying the steeper SVP SlpD trend observed in our older participants. Mechanistically, lesser venous capacitance leads to faster venous volume outflow. If the hypothesis is true, the SVP SlpD may become a non-invasive and fully automated measure proportional to vessel stiffness.

Previous studies showed that SVP were influenced by the IOP[28,35,37,47] and RNFL significantly correlated with RPP morphological measurements in the dataset, including population with retinal neurodegenerative disease[4,19,43]. In our participants, the IOP and RNFL did not correlate with RPP morphology. A potential explanation may lie in well-controlled OHT condition in our patient's cohort who presented with normalized IOP, so no neurodegeneration assessed by RNFL was present.

SVP morphology is believed to originate from a gradient between IOP and ICP, and many theoretical models attempted to express the SVP-IOP-ICP relationships[35–38]. However, the majority of previously reported models have not accounted for the effects of HR or age on the SVP Ampl or timings[35–38]. Therefore, the current in vivo observation represents critical information that adds another piece to the puzzle of the SVP etiology conundrum. Therefore, future models and studies evaluating SVP should account for the effects of HR and age to avoid potential erroneous conclusions.

Similar conclusions apply to the OCP assessment. Although OCP morphology demonstrated significant differences between healthy controls and OHT patients, a considerable deal of uncertainty remains as the OCP morphology changes were HR-related. The ANCOVA demonstrated the HR effect on between-group comparisons. It is important to note that the impact of HR has usually been omitted in previous clinical studies. In particular,

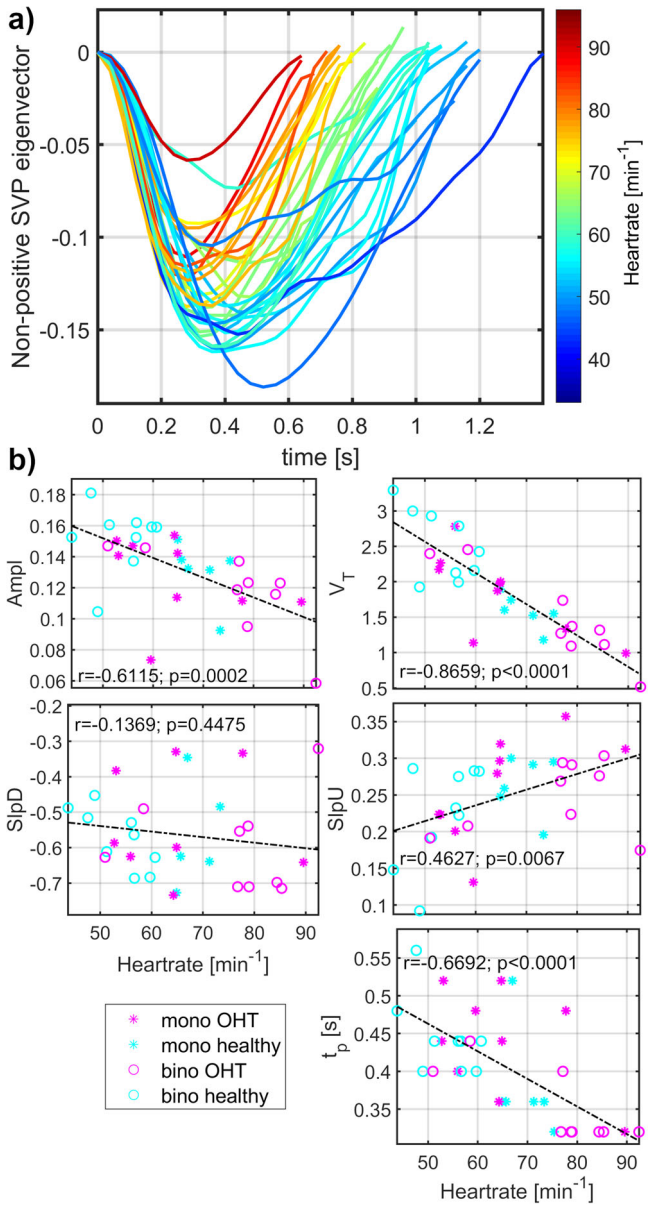

Fig. 2 Heart rate modulated morphology of spontaneous venous pulsations (SVP). a Visualization of mean single-pulses over all monocular (mono) and binocular (bino) retinal video-recordings from healthy controls and patients with medicated ocular hypertension (OHT). Graph lines are heart rate color-coded. **b** Evaluation of linear dependence between heart rate and SVP morphology measurements (Ampl amplitude of the SVP eigenvector, V_T total relative pulse stroke volume in the eigenvector measures, SlpD slope-down from the eigenvector value at the period beginning to the negative eigenvector peak ≈ peak of the maximal absolute blood volume time-point, SlpU slope-up from the negative eigenvector peak to the period end, t_p time to the negative eigenvector peak). Value r represents a corresponding Pearson correlation coefficient and value *p* the *p*-value of the correlation level.

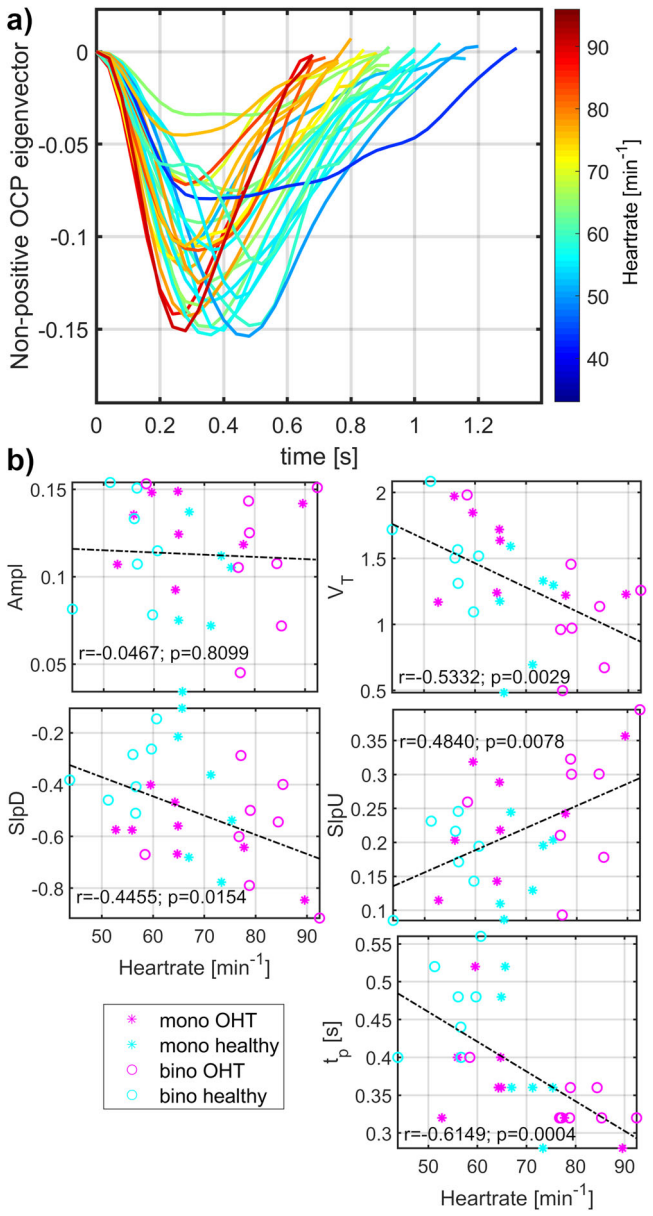

Fig. 3 Heart rate modulated morphology of optic cup pulsations (OCP). a Visualization of mean single-pulses over all monocular (mono) and binocular (bino) retinal video-recordings from healthy controls and patients with medicated ocular hypertension (OHT). Graph lines are heart rate color-coded. **b** Evaluation of linear dependence between heart rate and OCP morphology measurements (Ampl amplitude of the OCP eigenvector, V_T total relative pulse stroke volume in the eigenvector measures, SlpD slope-down from the eigenvector value at the period beginning to the negative eigenvector peak ≈ peak of the maximal absolute blood volume time-point, SlpU slope-up from the negative eigenvector peak to the period end, t_p time to the negative eigenvector peak). Value r represents a corresponding Pearson correlation coefficient and value *p* the *p*-value of the correlation level.

ICP studies[33,34] (using Hedges scale[48]) or glaucoma diagnostic studies[4,19] demonstrated qualitative or quantitative alterations in RPP morphology without considering group-specific HR distributions. Future studies may avoid potentially blurred and inaccurate outcomes by reporting or, ideally, accounting for the between-group differences in HR.

Although the PCA is an automated method, the presented data processing pipeline utilized three manual interventions with the potential impact on outcome measures. The interventions were: (i) manual ONH segmentation; (ii) identification of SVP and OCP components; and (iii) control point corrections. As PCA integrates eigen time-course for each principal component estimated from the whole ONH area, minimal imperfections in ONH segmentation should not crucially impact outcome measures. But, a further study investigating the PCA method robustness is warranted to clarify this matter. The automated

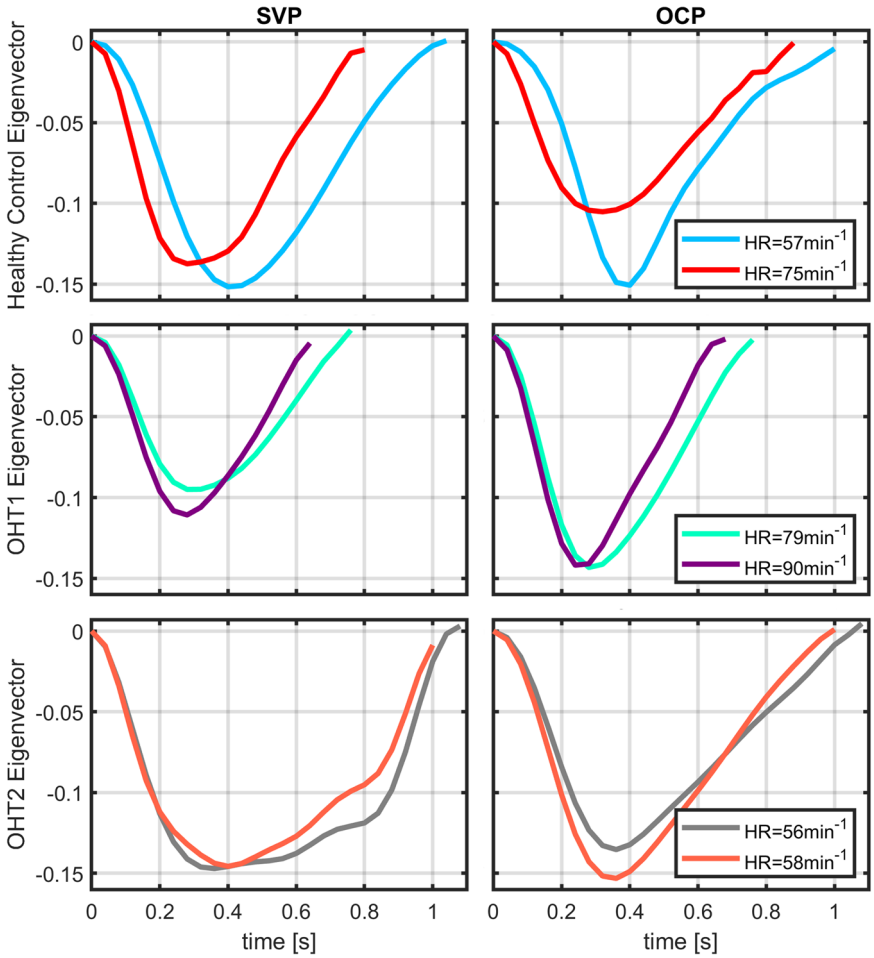

Fig. 4 Representative examples of heart rate (HR) dependent intra-participant variability of retinal pulsatile patterns in one healthy control and two medicated ocular hypertension (OHT) patients. For each participant, one retinal video-recording (RVR) was acquired with the monocular video-ophthalmoscope (VO) utilizing the CCD camera chip and one with the binocular VO utilizing the CMOS camera chip. The between-acquisition time interval was about two years for each representative participant. In healthy control and one OHT participant (OHT1), intra-participant RPP morphologies were dissimilar at different HR while RPP morphology remained unchanged for comparable HR as captured for other OHT participant (OHT2). Another OHT participant had different HR over acquisitions with similar outcomes as presented for the OHT1 participant. SVP spontaneous venous pulsations, OCP optic cup pulsations, HR heart rate.

identification of components of interest represents a challenge. We are working on the automatization of SVP and OCP identification. A wrong component selection can impact outcome measures so that morphology values are evaluated for a wrong pattern. Finally, isolated manual corrections of control points improve the precision of the averaged single pulse estimation and the precision of outcome measures.

Our study has several limitations to be addressed in future research. The sample size of our dataset is limited and should be extended to reproduce and validate our pilot observations. Still, the utilized correction for multiple comparison errors and the power analysis support that the presented correlation measures are related to the human body physiology rather than false positive observations. An optimal re-test should involve hundreds of participants with RVRs acquired at various video-ophthalmoscopes of various assembling technologies. Therefore, we would like to initialize a multi-center RVR challenge collecting 10 s RVRs to re-test the impact of HR and age at RPP morphology. Four participants who had both monocular and binocular RVR, approximately two years apart, may decrease inter-participant variability in our dataset. We consider this effect of being minimal as HR differed between the first and second RVR in three of four participants and as the intra-participant variability mostly followed dataset trends of correlation measurements. Pharmacological treatment of OHT patients may have influenced the morphology measurements, as specific drugs can alter ocular hemodynamics. The high diversity of used drugs in our OHT group and our small sample size prevented the testing post-hoc differences between the untreated group and treated subgroups (e.g., beta-blocker versus prostaglandin treatment). The differences in vessel stiffness and pulse pressure related to sex[49,50] may also play a significant role in RPP morphology. Sex effects need to be validated in the larger cohort of participants.

In conclusion, we have demonstrated the in vivo evidence that heart rate and age modulate the morphology of retinal pulsatile patterns in humans. The observation corroborates Levine and Bebie's theory. The presented study will impact the design of future biological and clinical studies, future analyses of between-group differences in morphology of RPPs, and SVP-ICP-IOP biophysical modeling by emphasizing the necessity to include heart rate and age as important confounding factors.

Methods

Experimental design. In concordance with the Declaration of Helsinki, all participants signed an informed consent approved by the ethical committee at the Friedrich-Alexander University of Erlangen-Nürnberg. The participants are part of

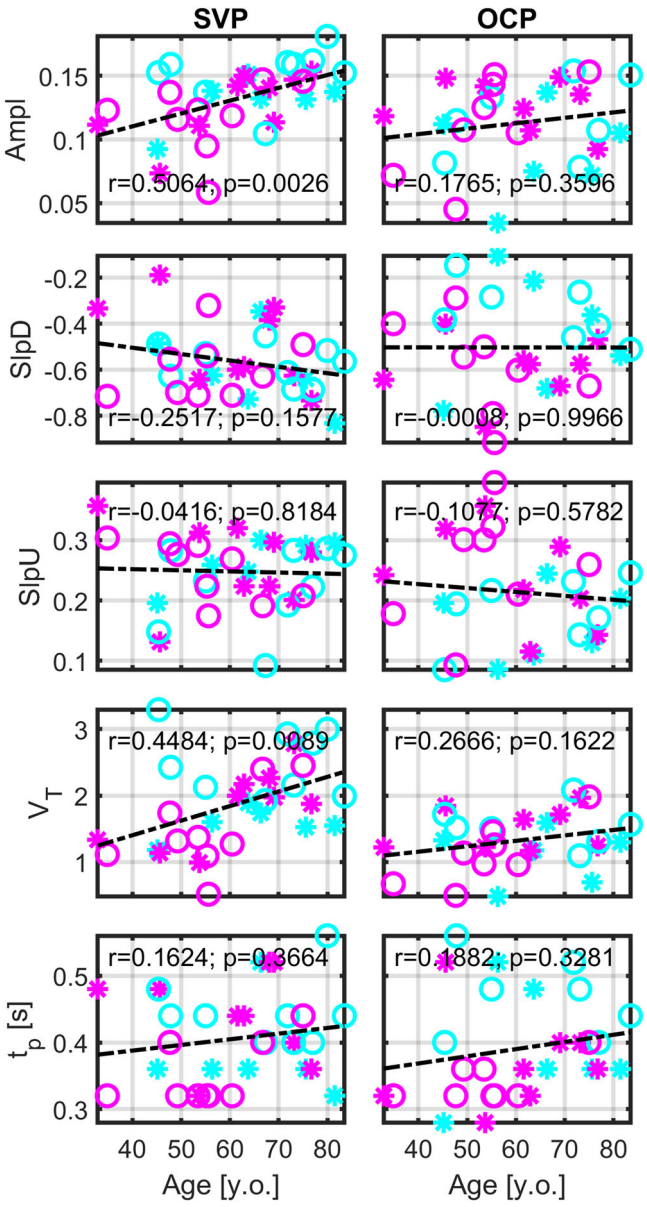

Fig. 5 Evaluation of linear dependence between age and morphology of retinal pulsatile patterns. Value r represents a corresponding Pearson correlation coefficient and value p is the *p*-value of the correlation level. SVP spontaneous venous pulsations, OCP optic cup pulsations, Ampl amplitude of the single-pulse in eigenvector space, V_T total relative pulse stroke volume in the eigenvector measures, SlpD slope-down from the eigenvector value at the period beginning to the negative eigenvector peak ≈ peak of the maximal absolute blood volume time-point, SlpU slope-up from the negative eigenvector peak to the period end, t_p time to the negative eigenvector peak.

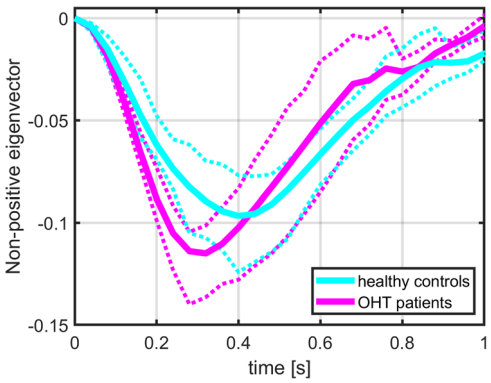

Fig. 6 Group averaged OCP pulses with 25–75% confidence intervals. Confidence intervals are visualized as color-matched dashed lines.

the Erlangen Glaucoma Registry cohort (www.clinicaltrials.gov, NCT00494923) founded in 1991.

Participants enrolled in the NCT00494923 trial met the criteria of age range 18–65, open chamber angle and corrected visual acuity 0.7 or better when entering the registry. The trial excluded people with systemic disease and potential ocular involvement (e.g., diabetes mellitus), people with myopic or hyperopic refractive error >8.0D, and people with an eye disease (except for glaucoma). From the registry, healthy controls and patients with a history of ocular hypertension (OHT; i.e., intraocular pressure IOP > 21 mmHg, normal visual field and ONH appearance) were included in this study. Pharmacological treatment along with eye surgical intervention history are described in Table 2.

Monocular or binocular retinal video-recordings (RVRs) were acquired for 16 OHT patients (age 58.7 ± 12.9 years old, seven females) and 14 healthy controls (age 66.0 ± 13.2 years old, eight females) between January 2015 and December 2017. In three OHT patients and one healthy control, two RVRs (one monocular and one binocular) were obtained approximately two years apart. In total, 34 RVRs were acquired and analyzed.

Along with RVRs, refractive error, visual acuity, perimetry, IOP, and retinal nerve fiber layer (RNFL) thickness were obtained for each eye with standard clinical devices (white-on-white perimetry with computerized static projection perimeter, Octopus 500, Haag-Streit; Goldmann tonometry; Spectralis OCT, *Heidelberg Engineering*) followed by RVR acquisition. All measurements were acquired within a one-day session.

Video-ophthalmoscopic data acquisition. Each participant was examined while comfortably sitting with head rested and positioned on a video-ophthalmoscope chin holder to minimize participant's motion. Each participant was asked to fixate the eyesight at the target presented as a red LED light or cross in the video-ophthalmoscope optical path. The principles of image acquisition were previously described[16]. In short, both available video-ophthalmoscope types (monocular and binocular) acquire images of the reflected light intensity modulated by heart rate induced attenuation changes[16,26]. Because such changes are caused by spatial-temporal retinal blood volume changes, the lowest pixel image intensity corresponds to the highest blood volume (and the highest attenuation) and vice versa.

Left eye monocular RVRs were acquired with the monocular video-ophthalmoscope consisting of the optical lens system (40D ophthalmic lens, two achromatic lenses), one monochrome CCD camera (UI-2210 SE-M-GL, USB interface, *iDS, Germany*), red LED forming the fixation target, and a low power narrow-band LED (wavelength λ = 575 nm) illuminating retina with 30 μW/cm^2. Acquired 10 s video sequences were saved in non-compressed AVI format with 25 fps (frames-per-second) and matrix size 640 × 480 pixels covering 20° × 15° field of view (i.e., 1 pixel ≈ 9.3 × 9.3 μm^2)[16,26,51].

Binocular RVRs were acquired with the binocular video-ophthalmoscope consisting of two optical lens systems, two synchronized CMOS cameras (UI-3060 Rev 2, USB 3.0, *iDS, Germany*), a green OLED display presenting a fixation target, and two narrow-band LED low-power light sources (λ = 575 nm) illuminating retina with 30 μW/cm^2. Acquired 10 s RVRs were saved in non-compressed AVI format with 25fps and matrix size 1000 × 770 pixels covering 20° × 15° field of view (i.e., 1 pixel ≈ 6.0 × 6.0 μm^2)[26,51,52]. Left eye RVRs were only used in further analyses.

Image analysis. The whole image analysis workflow is summarized in Fig. 1a. Motion artifacts in RVRs were suppressed with rigid image registration optimized for the RVRs[53]. A representative example of aligned monocular RVR is available at https://youtu.be/-CABIpjWX8Y and binocular RVR at https://youtu.be/4anapI0TZTQ. Next, the optic nerve head (ONH) area was manually segmented from the averaged aligned RVR image and defined as a region of interest (ROI) for further data analysis. Each ONH time frame was spatially smoothed with a 3 × 3 uniform convolution kernel to increase the signal-to-noise ratio (SNR) between local retinal hemodynamics and additive Gaussian noise in RVRs. Acquired relative blood volume changes were high-pass filtered in spectral domain with the cut-off frequency 0.12 Hz in each aligned pixel belonging to the ONH. The filter suppressed DC component and low-frequency drift but preserved pixel-specific pulsatile variance.

Spatial principal component analysis[26] (PCA) was estimated via singular value decomposition (Eq. 1) on each preprocessed ONH RVR.

$$\mathbf{X} = \boldsymbol{U}\boldsymbol{\Sigma}\boldsymbol{V}^{\mathrm{T}} \quad (1)$$

Formation of PCA input (i.e., ONH RVR matrix $\mathbf{X}$ of m rows and n_t columns where m is a number of analyzed pixels and n_t is a number of time points) and extraction of PCA outputs from left and right eigenvector matrices $\mathbf{U}$ and $\mathbf{V}$ are

Table 2 Eye drop medication and surgical eye intervention in each participant with ocular hypertension.

	Active substance	Class	Surgical intervention
1	Timolol Sodium hyaluronate	Non-selective beta-blocker Viscosupplementation agent	None
2	None	-	None
3	Latanoprost	Prostaglandin analogue	None
4	None	-	None
5	Timolol Dorzolamide	Non-selective beta-blocker Carbonic anhydrase inhibitor	None
6	Timolol Bimatoprost	Non-selective beta-blocker Prostaglandin analogue	None
7	Latanoprost	Prostaglandin analogue	None
8	Bimatoprost	Prostaglandin analogue	None
9	Timolol Bimatoprost	Non-selective beta-blocker Prostaglandin analogue	Selective laser trabeculoplasty
10	Pilocarpin	Non-selective muscarinic agonist *(M3 selectivity on the iris sphincter)*	None
11	Timolol Clonidine	Non-selective beta-blocker Alpha-2 adrenergic agonist *(affinitypredilection of 200:1 for α-2 versus α-1 receptors)*	Laser (chamber angle)
12	None	-	None
13	None	-	Selective laser trabeculoplasty
14	Latanoprost	Prostaglandin analogue	Selective laser trabeculoplasty
15	Timolol Latanoprost	Non-selective beta-blocker Prostaglandin analogue	None
16	None	-	Laser (other)

The table describes the active substances used to treat high intraocular pressure with the classification of the substance.

briefly summarized in Fig. 1b. Left eigenvector matrix $\boldsymbol{U}$ of m rows and n_t columns is a matrix of principal components in descending order of corresponding eigenvalues in diagonal square matrix $\boldsymbol{\Sigma}$ of dimensions n_t. One principal component is one column vector of m samples in the matrix $\boldsymbol{U}$. Square right eigenvector matrix $\boldsymbol{V}$ of dimensions n_t consists of column eigen time-courses characteristic for the principal component of a matched column in the matrix $\boldsymbol{U}$. (Illustrative lecture of these singular value decomposition basics is available online[54]).

Z-scored spatial principal components (Fig. 1b) were thresholded to zero in each pixel where $|Z| < 1$[26]. The SVP[26] and OCP[26] spatiotemporal patterns were visually identified as a single component for each pattern from a set of the first 12 principal components. PCA eigenvectors characterizing pulsation time-courses (Fig. 1b) were de-trended, and outlier values were restored utilizing the k-means clustering algorithm, as both implemented and fully described in Labounkova et al.[26]. Control points defining continuous part of an RPP time-course with high SNR (see OCP control points in Fig. 1a) were automatically identified for each SVP or OCP eigenvector[44] (Fig. 1b) characterizing the relative blood volume changes[26], and minor manual edits were done if needed. The automated identification of the control points is detailly described in the "Appendix C" of Labounkova et al.[26].

Each RVR segregated several SVP or OCP single pulse repetitions whose beginning and end were well defined by the control points (Fig. 1a). Averaged single SVP or OCP pulse waveforms were derived for each RVR, and quantitative parameters describing its morphology were evaluated. The evaluated morphology parameters were pulse amplitude (Ampl; Fig. 1a), total relative pulse stroke volume as $V_T = -\int_0^T V(t)dt$ (where $V(t)$ is a volume in non-positive eigenvector values, T is pulse period, and t is time; Fig. 1a), slope-down to peak (SlpD; Fig. 1a), slope-up to baseline (SlpU; Fig. 1a), and time to peak (t_p; Fig. 1a). The averaged RVR HR = 60/T[min^{-1}] was estimated from averaged SVP and OCP periods T[s].

The Ampl measurement is proportional to the maximum blood volume in the examined ROI during the cardiac cycle. V_T is proportional to the quantity of total blood volume change in the ROI during the cardiac cycle. SlpD is proportional to the steepness of the blood volume filling in the ROI during the cycle and SlpU to the steepness of blood volume drainage outside the ROI. t_p is proportional to the time of blood volume filling in the ROI during the cycle.

Statistics and reproducibility. Delay between overlapping high-quality SVP and OCP portions (Fig. 1a) was evaluated with maximal cross-correlation response function[55]. Pearson correlation coefficients between unaligned or aligned SVP and OCP patterns were quantified (Fig. 1a). The null hypothesis that SVP-OCP delay equals to 0 was tested with one sample t-test.

Pearson correlation coefficients and corresponding correlation p-values were evaluated between SVP or OCP morphological features (i.e., Ampl, V_T, SlpD, SlpU, and t_p; Fig. 1a) and age, HR, IOP, and average RNFL thickness, respectively. Ten correlation effects were investigated for each variable (e.g., age, HR). False discovery rate correction (p_{FDR}<0.05) was applied to the correlation p-values, and Benjamini-Hochberg adjusted p-values (p_{BH}) were computed to minimize the risk of the error type I. Due to the limited sample size, power was estimated for each significant correlation to assess the risk of error type II[56]. Two-sample t-test evaluated between-group differences in RPP morphology measurements, age, HR, IOP, and RNFL. ANCOVA (analysis of covariance) was the second statistical test evaluating between-group differences when HR or age were used as confounding variables. Results of two-sample t-tests and ANCOVA tests were compared, and the effects of HR or age on final between-group results were evaluated (Fig. 1a). Due to the limited sample size, we considered uncorrected $p < 0.05$ significant for t-tests and ANCOVA.

Reporting summary. Further information on research design is available in the Nature Research Reporting Summary linked to this article.

Data availability

De-identified data sets can be made available upon a reasonable email request to *Ivana Labounkova* (ilabounk@umn.edu), *Dr. Folkert Horn* (folkert.horn@augen.imed.uni-erlangen.de), or another responsible personnel from the *Department of Ophthalmology and University Eye Hospital, Friedrich-Alexander University Erlangen-Nürnberg at Erlangen, Erlangen, Germany*.

Code availability

The MATLAB R2017b programming environment (*MathWorks, Natick, USA*) with academic license and the open-source Retina Imaging Toolbox (https://github.com/umn-milab/retinaimagingtoolbox; GNU GPL version 3 license) were used for all image and statistical analyses and visualizations.

Received: 23 September 2021; Accepted: 3 May 2022;
Published online: 14 June 2022

References

1. Guven, D., Ozdemir, H. & Hasanreisoglu, B. Hemodynamic alterations in diabetic retinopathy. *Ophthalmology* **103**, 1245–1249 (1996).
2. Flammer, J. et al. The impact of ocular blood flow in glaucoma. *Prog. Retin. Eye Res.* **21**, 359–393 (2002).
3. Wang, X. et al. Correlation between optic disc perfusion and glaucomatous severity in patients with open-angle glaucoma: an optical coherence

tomography angiography study. *Graefes Arch. Clin. Exp. Ophthalmol.* **253**, 1557–1564 (2015).
4. Tornow, R. P., Kolar, R., Odstrcilik, J., Labounkova, I. & Horn, F. Imaging video plethysmography shows reduced signal amplitude in glaucoma patients in the area of the microvascular tissue of the optic nerve head. *Graefes Arch. Clin. Exp. Ophthalmol.* **259**, 483–494 (2021).
5. Feke, G. T., Hyman, B. T., Stern, R. A. & Pasquale, L. R. Retinal blood flow in mild cognitive impairment and Alzheimer's disease. *Alzheimers Dement. Diagnosis, Assess. Dis. Monit.* **1**, 144–151 (2015).
6. Spain, R. I. et al. Optical coherence tomography angiography enhances the detection of optic nerve damage in multiple sclerosis Rebecca. *Br. J. Ophthalmol.* **102**, 520–524 (2018).
7. Wong, T. Y. et al. Retinal microvascular abnormalities and incident stroke: the atherosclerosis risk in communities study. *Lancet* **358**, 1134–1140 (2001).
8. Wong, T. Y. et al. Retinal arteriolar narrowing and risk of coronary heart disease in men and women: the Atherosclerosis risk in communities study. *J. Am. Med. Assoc.* **287**, 1153–1159 (2002).
9. Rina, M., Shiba, T., Takahashi, M. & Hori, Y. Pulse waveform analysis of optic nerve head circulation for predicting carotid atherosclerotic changes. *Graefes Arch. Clin. Exp. Ophthalmol.* **253**, 2285–2291 (2015).
10. Holwerda, S. W. et al. Aortic stiffness is associated with changes in retinal arteriole flow pulsatility mediated by local vasodilation in healthy young/middle-age adults. *J. Appl. Physiol.* **129**, 84–93 (2020).
11. Kim, M., Kim, R. Y., Kim, J. Y. & Park, Y. H. Correlation of systemic arterial stiffness with changes in retinal and choroidal microvasculature in type 2 diabetes. *Sci. Rep.* **9**, 1–9 (2019).
12. Heitmar, R. & Summers, R. J. Assessing vascular function using dynamic retinal diameter measurements: a new insight on the endothelium. *Thromb. Haemost.* **107**, 1019–1026 (2012).
13. Wong, T. Y. et al. Retinal arteriolar narrowing and risk of diabetes mellitus in middle-aged persons. *J. Am. Med. Assoc.* **287**, 2528–2533 (2002).
14. Rege, A. et al. Noninvasive assessment of retinal blood flow using a novel handheld laser speckle contrast imager. *Transl. Vis. Sci. Technol.* **7**, 7 (2018).
15. Debuc, D. C., Rege, A. & Smiddy, W. E. Use of XyCAM RI for noninvasive visualization and analysis of retinal blood flow dynamics during clinical investigations. *Expert Rev. Med. Devices* (2021). https://doi.org/10.1080/17434440.2021.1892486
16. Tornow, R. P., Kolář, R. & Odstrčilík, J. Non-mydriatic video ophthalmoscope to measure fast temporal changes of the human retina. *Eur. Conf. Biomed. Opt. Opt. Soc. Am.* **9540**, 954006 (2015).
17. Garhofer, G. et al. Use of the retinal vessel analyzer in ocular blood flow research. *Acta Ophthalmol.* **88**, 717–722 (2010).
18. Seifertl, B. U. & Vilser, W. Retinal vessel analyzer (RVA)-design and function. *Biomed. Tech.* **47**, 678–681 (2002).
19. Shariflou, S., Agar, A., Rose, K., Bowd, C. & Golzan, S. M. Objective quantification of spontaneous retinal venous pulsations using a novel tablet-based ophthalmoscope. *Transl. Vis. Sci. Technol.* **9**, 19 (2020).
20. Moret, F., Poloschek, C. M., Lagrèze, W. A. & Bach, M. Visualization of fundus vessel pulsation using principal component analysis. *Investig. Ophthalmol. Vis. Sci.* **52**, 5457–5464 (2011).
21. Morgan, W. H. et al. Photoplethysmographic measurement of various retinal vascular pulsation parameters and measurement of the venous phase delay. *Investig. Ophthalmol. Vis. Sci.* **55**, 5998–6006 (2014).
22. Moret, F., Reiff, C. M., Lagrèze, W. A. & Bach, M. Quantitative analysis of fundus-image sequences reveals phase of spontaneous venous pulsations. *Transl. Vis. Sci. Technol.* **4**, 3 (2015).
23. Betz-Stablein, B., Hazelton, M. L. & Morgan, W. H. Modelling retinal pulsatile blood flow from video data. *Stat. Methods Med. Res.* **27**, 1575–1584 (2018).
24. Qamber, S., Waheed, Z. & Akram, M. U. Personal identification system based on vascular pattern of human retina. In *International Biomedical Engineering Conference (CIBEC)* 64–67 (IEEE, 2012). https://doi.org/10.1109/CIBEC.2012.6473297
25. Jan, J., Odstrcilik, J., Gazarek, J. & Kolar, R. Retinal image analysis aimed at blood vessel tree segmentation and early detection of neural-layer deterioration. *Comput. Med. Imaging Graph.* **36**, 431–441 (2012).
26. Labounkova, I. et al. Blind source separation of retinal pulsatile patterns in optic nerve head video-recordings. *IEEE Trans. Med. Imaging* **40**, 852–864 (2021).
27. Levin, B. E. The clinical significance of spontaneous pulsations of the retinal vein. *Arch. Neurol.* **35**, 37–40 (1978).
28. Jacks, A. S. & Miller, N. R. Spontaneous retinal venous pulsation: aetiology and significance. *J. Neurol. Neurosurg. Psychiatry* **74**, 7–9 (2003).
29. Zhang, X. et al. Invasive and noninvasive means of measuring intracranial pressure: a review. *Physiol. Meas.* **38**, R143–R182 (2017).
30. Golzan, S. M., Kim, M. O., Seddighi, A. S., Avolio, A. & Graham, S. L. Non-invasive estimation of cerebrospinal fluid pressure waveforms by means of retinal venous pulsatility and central aortic blood pressure. *Ann. Biomed. Eng.* **40**, 1940–1948 (2012).
31. Morgan, W. H. et al. Retinal vein pulsation is in phase with intracranial pressure and not intraocular pressure. *Investig. Ophthalmol. Vis. Sci.* **53**, 4676–4681 (2012).
32. Wong, S. H. & White, R. P. The clinical validity of the spontaneous retinal venous pulsation. *J. Neuro-Ophthalmol.* **33**, 17–20 (2013).
33. D'Antona, L. et al. Association of intracranial pressure and spontaneous retinal venous pulsation. *JAMA Neurol.* **76**, 1502–1505 (2019).
34. D'Antona, L. et al. Brain MRI and ophthalmic biomarkers of intracranial pressure. *Neurology* **96**, e2714–e2723 (2021).
35. Babbs, C. Biomechanics of retinal venous pulsations as indicators of intracranial pressure. *Weldon Sch. Biomed. Eng. Fac. Work. Pap.* (2016). https://doi.org/10.1039/C5RA18353G
36. Guidoboni, G. et al. Intraocular pressure, blood pressure, and retinal blood flow autoregulation: a mathematical model to clarify their relationship and clinical relevance. *Investig. Ophthalmol. Vis. Sci.* **55**, 4105–4118 (2014).
37. Levine, D. N. Spontaneous pulsation of the retinal veins. *Microvasc. Res.* **56**, 154–165 (1998).
38. Levine, D. N. & Bebie, H. Phase and amplitude of spontaneous retinal vein pulsations: an extended constant inflow and variable outflow model. *Microvasc. Res.* **106**, 67–79 (2016).
39. Shirwany, N. A. & Zou, M. H. Arterial stiffness: a brief review. *Acta Pharmacol. Sin.* **31**, 1267–1276 (2010).
40. Steppan, J., Barodka, V., Berkowitz, D. E. & Nyhan, D. Vascular stiffness and increased pulse pressure in the aging cardiovascular system. *Cardiol. Res. Pract.* 10.4061/2011/263585 (2011).
41. Wong, T. Y., Klein, R., Klein, B. E. K., Meuer, S. M. & Hubbard, L. D. Retinal vessel diameters and their associations with age and blood pressure. *Investig. Ophthalmol. Vis. Sci.* **44**, 4644–4650 (2003).
42. Wong, T. Y. et al. The prevalence and risk factors of retinal microvascular abnormalities in older persons: the cardiovascular health study. *Ophthalmology* **110**, 658–666 (2003).
43. Golzan, S. M., Morgan, W. H., Georgevsky, D. & Graham, S. L. Correlation of retinal nerve fibre layer thickness and spontaneous retinal venous pulsations in glaucoma and normal controls. *PLoS ONE* **10**, e0128433 (2015).
44. Shlens, J. A Tutorial on principal component analysis. *arXiv* https://doi.org/10.48550/arXiv.1404.1100 (2014).
45. Boron, W. & Boulpaep, E. In *Medical Physiology* (Elsevier, 2016).
46. Mitchell, G. F. Effects of central arterial aging on the structure and function of the peripheral vasculature: Implications for end-organ damage. *J. Appl. Physiol.* **105**, 1652–1660 (2008).
47. Golzan, M., Graham, S. L., Leaney, J. & Avolio, A. Dynamic association between intraocular pressure and spontaneous pulsations of retinal veins. *Curr. Eye Res.* **36**, 53–59 (2011).
48. Hedges, T. R. J., Baron, E. M., Hedges, T. R. I. & Sinclair, S. H. The retinal venous pulse: its relation to optic disc characteristics and choroidal pulse. *Ophthalmology* **101**, 542–547 (1993).
49. Lee, H. Y. & Oh, B. H. Aging and arterial stiffness. *Circ. J.* **74**, 2257–2262 (2010).
50. Kim, J.-Y. et al. Gender difference in arterial stiffness in a multicenter cross-sectional study: the Korean arterial aging study (KAAS). *Pulse* **2**, 11–17 (2014).
51. Tornow, R.-P., Odstrcilik, J. & Kolar, R. Time-resolved quantitative inter-eye comparison of cardiac cycle-induced blood volume changes in the human retina. *Biomed. Opt. Express* **9**, 6237–6254 (2018).
52. Tornow, R. P., Milczarek, A., Odstrcilik, J. & Kolar, R. Binocular video ophthalmoscope for simultaneous recording of sequences of the human retina to compare dynamic parameters. In: European Conference on Biomedical Optics. Optical Society of America, p. 1041309 (2017).
53. Kolar, R., Tornow, R. P., Odstrcilik, J. & Liberdova, I. Registration of retinal sequences from new video-ophthalmoscopic camera. *Biomed. Eng. Online* **15**, 57 (2016).
54. Brunton, S. Singular Value Decomposition (SVD): Mathematical overview. *YouTube* https://www.youtube.com/watch?v=nbBvuuNVfco (2020).
55. Jan, J. *Digital signal filtering, analysis and restoration* (IET, 2000).
56. Hulley, S. B., Cummings, S. R., Browher, W. S., Grady, D. G. & Newman, T. B. *Designing Clinical Research: An Epidemiological Approach* (Lippincott Williams & Wilkins, 2007).

Acknowledgements

The authors thank Dr. Folkert Horn and other staff of the Department of Ophthalmology and University Eye Hospital, Friedrich-Alexander University Erlangen-Nürnberg at Erlangen for their clinical support and information provided to our research team during this study. Also, the authors thank the Center for Behavioral Development and the Center for Magnetic Resonance Research (CMRR) at the University of Minnesota for providing the lab space and computational support. The study was supported by several grand awards: Brno University of Technology grant n. FEKT-S-17-4487, Czech Science Foundation, project no. 21-18578 S, Deutsche Forschungsgemeinschaft (DFG) grant number DFG TO 115/3-1, and "Progressive" grant, stage 3 from the Department of

Pediatrics and the Winston & Maxine Wallin Neuroscience Discovery Fund, University of Minnesota. All funding is highly acknowledged.

Author contributions

I.L. designed analysis, analyzed data, interpreted results, designed figures, drafted and revised manuscript. R.L. designed analysis, analyzed data, interpreted results, designed figures, drafted and revised manuscript. R.K. designed the study, provided materials, revised and proofed the manuscript. R.P.T. designed the study, acquired and provided data, revised and proofed the manuscript. C.F.B. verified, interpreted, and discussed physiology of results, revised and proofed manuscript. C.M.M. verified study design, discussed potential ophthalmological impact and applications, revised and proofed manuscript. B.R.M. discussed potential cerebrovascular impact and applications, revised and proofed manuscript. I.N. supervised and organized the whole team, provided materials, led the discussion, drafted and revised the manuscript.

Competing interests

The authors declare no competing interests.

Additional information

Supplementary information The online version contains supplementary material available at https://doi.org/10.1038/s42003-022-03441-6.

Correspondence and requests for materials should be addressed to Igor Nestrašil.

Peer review information *Communications Biology* thanks Delia Cabrera DeBuc, William Morgan, and Fion Bremner for their contribution to the peer review of this work. Primary Handling Editor: Karli Montague-Cardoso. Peer reviewer reports are available.

3.3 Simultaneous Acquisition of Retinal Video-sequences and Other Biosignals

This part of the Thesis is focused on simultaneous acquisition of retinal video-sequences and other biosignals including electrocardiography, finger photoplethysmography, respiration plethysmography and electrooculography. The innovative approach utilizing Biopac System unit and signal from external generator triggering the CCD detector was introduced in 2017 at EEICT conference proceedings. The conference proceeding summarized the design of the simultaneous system, experiment realization, data acquisition and outcomes in: Liberdová Ivana et al. Simultaneous ECG, Finger and Retinal Photoplethysmography Measurement. Proceedings of The 23rd Conference STUDENT EEICT 2017,2017, 2:329-333, which is included in following pages.

Author's contribution. As a first author, I was testing the acquisition system and acquired the datasets. I have designed and performed the data analysis pipeline (including video processing, retinal plethysmographic signal extraction, biosignals alignment) and wrote the conference paper.

Innovation. The first realization of precisely synchronized acquisition of retinal video-sequences and biosignals (electrocardiography, finger photoplethysmography, respiration plethysmography, electrooculography) with temporal resolution equal to camera framerate (25 or 50 fps), i.e. exposure time of 40 ms or 20 ms. To my knowledge, no such experiment was introduced earlier. Earlier studies presented the simultaneous acquisition of retinal video-sequences with either finger/ear lobe plethysmography signal or electrocardiography via technical solutions providing poor temporal resolution [34, 60, 105, 158, 169, 256]. Current commercial devices (XyCam, RVA/DVA) provide simultaneous acquisition or retinal video-sequences and finger photoplethysmography in framerate 25 fps (40 ms exposition time) [37, 51, 85, 284]. The experiment also demonstrated the timing of events in measured biosignals, i.e. retinal blood filling precedes the finger blood filling.

SIMULTANEOUS ECG, FINGER AND RETINAL PHOTOPLETHYSMOGRAPHY MEASUREMENT

Ivana Liberdova

Doctoral Degree Programme (2), FEEC BUT

E-mail: xliber00@stud.feec.vutbr.cz

Supervised by: Radim Kolar

E-mail: kolarr@feec.vutbr.cz

Abstract: This document is focused on simultaneous ECG, finger and retinal plethysmography method development. Document describes certain parts of measurement hardware and also subsequent data processing. There is also described retinal plethysmography extraction from video records and its data processing. The result of proposed methodology is providing simultaneous signals of ECG, finger and retinal plethysmography and their comparison.

Keywords: video-ophthalmoscope, retinal plethysmography, ECG, PPG

1. INTRODUCTION

Ophthalmoscopy is the most frequent medical diagnostic method for diseases such as macular degeneration, diabetic rethinopathy or glaucoma etc [1]. For the most of these diseases especially for glaucoma is very important early diagnosis that current ophthalmoscopy does not include. The early diagnostics of glaucomatic diseases could be settled by exploring hemodynamical changes and its dynamic parameters in ocular fundus [2].

For measuring retinal temporal changes there was developed new type of ophtalmoscopic instrument non-mydriatic video-ophthalmoscope (VO, described in [3]) that provides long term video records of ocular fundus, its hemodynamical changes and retinal blood supply as well. All these changes are depending on cardiac cycle [4] as the heart beat induces changing blood volume. Then the blood volume changes in retina – retinal plethysmography (R-PG), can be seen as the reflectance change of retinal cells. This can provide important information about microcirculation physical condition of glaucomatic or diabetic patients.

The blood supply is usually measured by the finger or other photoplethysmography method (PPG). To compare the R-PG and finger PPG is also used ECG measurement as the reference and control of cardiac cycle. There are many works comparing the ECG and PPG signals for classifying PPG parameters such as pulse transit time (PTT) or pulse arrival time (PAT) or others [5] or also for heart rate variability parameters [6]. Considering PPG parameters there are both shape and time differences between various distal and proximal PPG measurements mainly in PAT.

Considering these facts there is an assumption retinal plethysmography (R-PG) as measurement of microcirculation blood supply will be also shifted that way PAT of R-PPG will be smaller than the other PPG measurement. This methodology could detect pathology in ophthalmoscopic records then.

2. MEASUREMENT METHODOLOGY

Whole methodology for simultaneous measurement of ECG, PPG and the R-PG was realized by connected system of components including video-ophthalmoscope with CMOS camera, signal generator, set of Biopac system with its components (ECG electrodes, finger PPG) and computer with appropriate software. Schema of whole system is in the Figure 1.

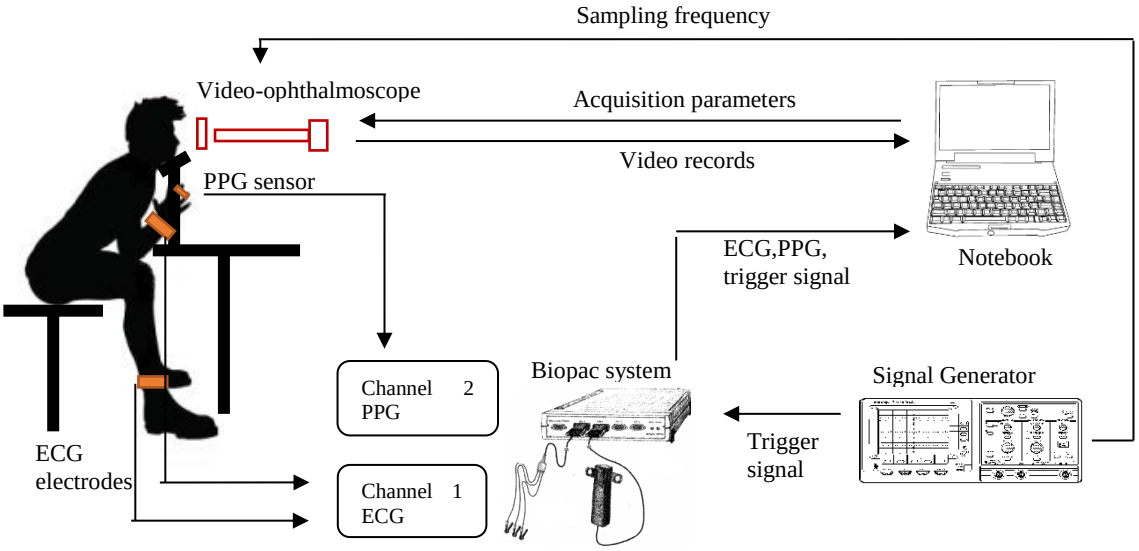

Figure 1: Schema of the simultaneous ECG, PPG and R-PG measurement

Video-ophthalmoscope – VO (Figure 2, described in [3]) is optical system including ophthalmic (40 D) as an objective len, LED source of low illumination level and wavelength 550 nm. It uses CMOS camera (UI-3060CP-M-GL, iDS-imaging, Germany). Video records were acquired with spatial resolution of 1024x1280 px and framerate both 25 and 50 fps.

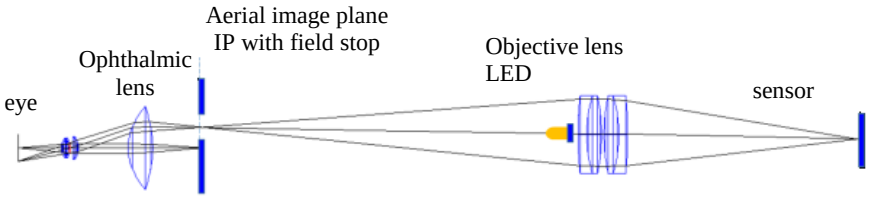

Figure 2: Video-ophthalmoscope used for retinal video sequences acquisition

Biopac system – Biopac system MP35 is used for PPG and ECG measurement with sample frequency (F_s) 50 kHz.

Signal generator – Agilent 33220A is used for rectangular trigger signal generation (F_s 50 kHz) that provides whole system synchronization for subsequent data processing and it is also used for CMOS camera settings (acquisition frequency) and acquisition start.

PPG, ECG and trigger signal is acquired into Biopac software. Due to dependency CMOS recording on trigger signal generation, the video record starts with rectangular triggered signal.

Human stability and head fixation is needed for the measurement that is why the next important part of the system is also chin rest.

3. DATA PROCESSING

3.1. PREPROCESSING

There are four types of measured data – PPG, ECG and triggered signal (recording by Biopac SW) and video records (CMOS camera). The triggered signal is a help signal where the first and last rising edge is marking the start and end of CMOS camera record and simultaneously the first and last PPG and ECG valid sample also. Exact rising edge detection is possible thanks to high F_s=50 kHz. Data need to be preprocessed as selection of valid samples only.

Due to different F_s of data, the next preprocessing step is to unify them. The Biopac signals of F_s 50 kHz need to be decimate 200 times. On the other hand video record interpolation need to be done after video processing steps (described below).

3.2. PPG SIGNAL

Besides pulsatile component in the vessels depending on cardiac cycle, the PPG signal is influenced also by artifacts due to motion or breathing. There are many methods to eliminate the mentioned artifacts e.g. moving average filter, wavelet transform or others. In this case simple highpass filtering with limit frequency 0.5 Hz to eliminate DC component (representing motion artifacts) is fully sufficient.

3.3. ECG SIGNAL

The ECG signal measurement is affected by various types of influences – breathing (DC component), muscle activity (high-frequency electromyographic noise) and others. Therefore there are also many methods for ECG filtering based on e.g. adaptive filtering etc. In this case the bandpass filer is used with limit frequencies 0.5 Hz and 45 Hz.

3.4. RETINAL VIDEO RECORDS

Schema of the video record processing is in Figure 3.

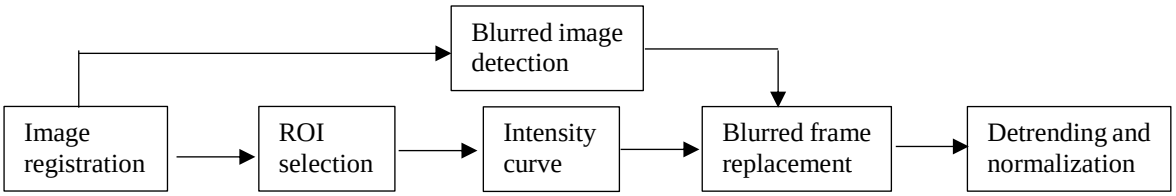

Figure 3: Video record processing schema

Due to eye movements during the fixation on target, the first step in retinal video records processing is image registration to have stable record for subsequent processing. For image registration is used method described in [7]. The method covers spatial transformation – shift, rotation and scaling. This method is based on phase correlation using the selected video record frame as the reference. Alignment of the frames is based on anatomical tracking points selection and Lucas-Kanade tracking then.

Video records include (except sharp frames) also blurred and empty images due to eye saccadic movements and blinking (see in Figure 4), that are unsuitable for the analysis. Therefore the detection of these distorted images is needed as the next step. For distorted frames detection, the reference image method using phase correlation is used as described in [8], where the reference image is the best video record frame enhanced on entropy base.

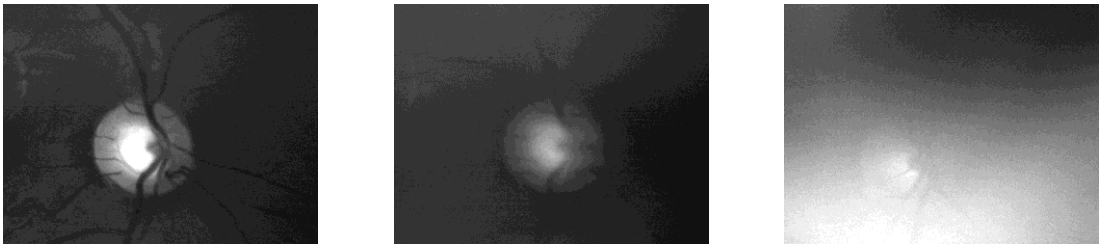

a b c

Figure 4: Example of frames in video-records: a, sharp frame b, blurred frame (eye movement) c, empty frame (blinking)

As the distorted frames are marked, the intensity curve in time can be extracted as the mean value of the selected region of interest (ROI) in frames. The ROI in this case represent the cup in optic disc (OD, see in Figure 5), where the biggest changes in blood supply can be observed. These changes modulate the reflected intensity in VO records. The reason of reverse intensity axis in intensity curve graph representing retinal plethysmography is that the increase of OD blood supply decreases OD reflectance therefore the intensity either.

The intensity curve R-PG still includes damaged frames (blinking, eye saccadic movements). These frames marked before are replaced by spline interpolated value.

The last step of video record processing is to eliminate trend line caused by human subject movements. The trend filtered and normalized R-PG is computed as intensity curve divided by trend enhanced by Savitzky-Golay algorithm with window length of three cardiac cycles computed on base of R-PG spectrum. The resulted normalized curve of specific ROI is in Figure 5.

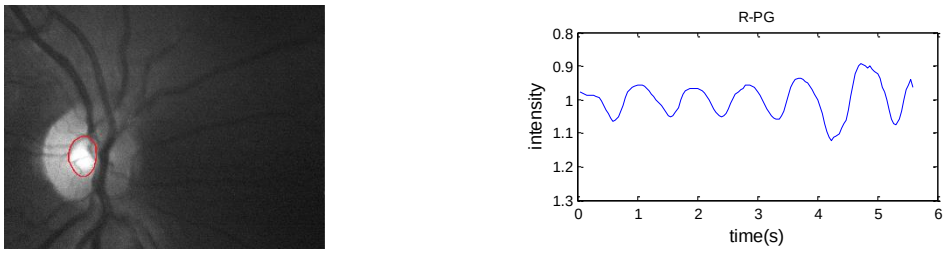

a b

Figure 5: R-PG of certain retinal video-record: a, selected ROI in retinal frame b, R-PG

4. RESULTS AND DISCUSSION

Results of simultaneous PPG, ECG and R-PG measurements are in Figure 6, where are simultaneously visualized plethysmography curves representing blood supply of retina and finger due to cardiac cycles substituted by ECG signal.

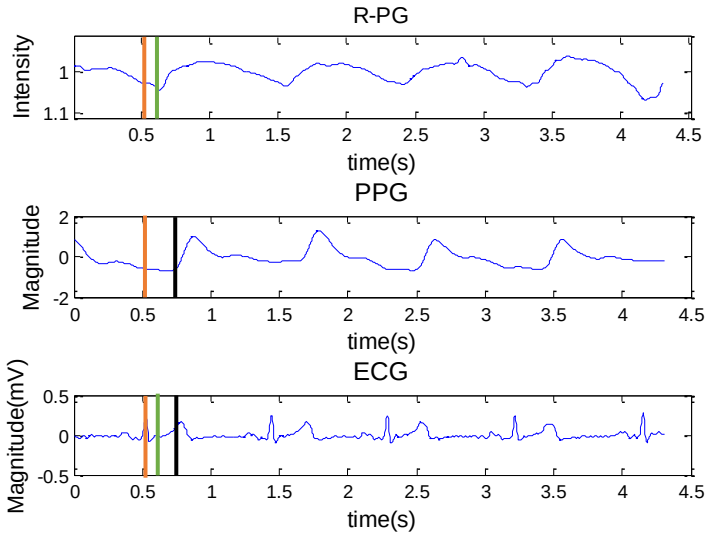

Figure 6: Resulted graphs of PPG, ECG and R-PG simultaneous measurement (red line – R wave as cardiac cycle start, green line – first R-PG rising edge sample, black line – first PPG rising edge sample)

This measurement allows data compare and measuring plethysmography parameters as PAT or PTT due to cardiac cycle. Considering PAT time, the R-PG PAT was smaller in comparison to finger PPG PAT in measured dataset, see in Figure 6, where the red line marks start of cardiac cycle and PAT interval start also, the green line marks R-PG rising edge sample and end of R-PG PAT interval, the black line marks PPG rising edge sample and end of PPG PAT interval. Study of these parameters and their changes can be promising in retinal diseases diagnostics.

The R-PG signal is very sensitive to ambient lighting, subject movements, eye saccadic movement and other influences. Moreover there are other artifacts caused by intraocular fluid or certain proteins in retina that usually damage R-PG signal.

5. CONCLUSION

The methodology of simultaneous PPG, ECG and retinal pletysmography measurement was introduced. There were used different approaches to process retinal video records to extract intensity curve representing blood supply of ocular fundus, other words retinal plethysmography. The R-PG is very sensitive to various influences and the method could be improved in measurement hardware as well as in data processing to eliminate retinal artifacts. The resulted R-PG is corresponding to cardiac cycle and can provide useful information about microcirculation physical condition.

REFERENCES

[1] Benbassat, J.,Polak, B., Ja-Vitt,J.: Objectives of teaching direct ophthalmoscopy to medical students. *Acta ophthalmologica*, 2012, 90.6:503-507

[2] Hayreh, S.: Blood supply oft he optic nerve head and ist role in optic atrophy, glaucoma and oedema oft he optic disc. *British Journal of Ophthalmology*, 1969, 53:721-748.

[3] Tornow, R. at al.: Ophthalmoscope measures fast temporal changes in the human retina. *SPIE Newsroom*. 2015. DOI: 10.1117/2.1201509.006061. ISSN18182259

[4] Lovasik, J.V., Gagnon, M., Kergoat, H.: A novel noninvasive videographic method for quantifying changes in the chromacity of the optic nerve head with changes in the intraocular pressure, pulsatile choroidal blood flow and visual neural function in humans. *Surv Ophthalmol*, 1994. 38 Suppl: p. S35-51.

[5] Mingwu, G. at al.: Comparison of noninvasive pulse transit time estimates as markers of blood pressure using invasive pulse transit time measurements as a reference. *Physiological Reports*. 2016. DOI: 10.14814/phy2.12768

[6] Ping S. at al.: A preliminary attempt to understand compatibility of photoplethysmographic pulse rate variability with electrocardiogramic heart rate variability. *Journal of medical and biological engineering*. 2008, 28(4):173-180

[7] Kolar, R. at al.: Registration of retinal sequences from new video-ophthalmoscopic camera. *Biomedical engineering online*, 2016, 15.1: 1.

[8] Liberdova, I. at al.: Image quality assessment of ophthalmologic videosequences using phase correlation. *Electrorevue*. 2016, 18(5):153-159.ISSN:1213-1539.

3.4 Simultaneous Acquisition of Retinal Video-sequences and Other Biosignals Including Intracranial Pressure

The multimodal acquisition system described in previous chapter (chapter *State of the Art*, subchapter *Simultaneous acquisition of retinal video-sequences and other biosignals*) has been upgraded to provide more comfortable acquisition. This new setup is described in [162] and it is based on Biosignal Plux unit and synchronization unit (Arduino Uno).

In collaboration with University of Minnesota (UMN), USA, and under Dr. Nestrasil's academic supervision, I have co-designed the project "Non-invasive and non-contact intracranial pressure waveform recording utilizing dynamic video ophthalmoscopy" where the upgraded simultaneous acquisition system [162] was utilized with further upgrades enabling data recording in seriously ill patients hospitalized at intensive care units. So far, the project has been awarded with departmental Progressive Grant and UMN Winston and Maxine Wallin Neuroscience Discovery Fund. Both grants primarily served to secure funds for adjustments getting the imaging system into the state when it can acquire retinal video-sequences with simultaneous non-invasive (i.e. electrocardiography EKG, blood volume pulse BVP via finger photoplethysmography, respiration pletysmography RPG and electrooculography EOG) and invasive (i.e., intracranial pressure ICP, arterial blood pressure ABP) biosignals in patients lying or sitting in the hospital bed. Final phase of the Walling grant focused on preliminary data acquisition. The schema of the simultaneous experiment is in **Figure 3.1**.

Nowadays, the only way how to measure the intracranial pressure is invasively via an implanted probe into a patient skull within one of three locations - ventricular, parenchymal or epidural. The probe is connected to a pressure transducer **Figure 3.2e**(top) that converts the pressure signal into electrical signal that is measured and visualized at intensive care unit (ICU) monitors **Figure 3.2g**. The experiment of the simultaneous acquisition suggests a recruitment of participants from a cohort of hospitalized patients at the ICU, Department of Neurosurgery, UMN with already implanted probe for ICP monitoring. The recruited participants are conscious, collaborating and monitored for the whole duration of experiment. The experiment has been approved by the Institutional Review Board at UMN since the Progressive Grant.

To proceed with the simultaneous acquisition, following aims were accomplished:

1. **Design and assembly of a bedside cart with an articulating arm and motorized VO milimeter-precision positioning**. I have participated on

design and assembly of a mobile bedside cart with an articulating arm holding the video-ophthalmoscope unit meeting all the requirements for the bedside data acquisition **Figure 3.2a**. The cart is mobile, steady, and height adjustable. Three articulating arms hold (i) motorized positioning with attached VO unit; (ii) keyboard; and (iii) acquisition laptop. All arms are long and flexible enough to precisely reach the patient's retina at the limited space of the ICU room. Additionally, the VO holder can rotate; thus, the whole positioning system with VO objective can be oriented in any direction from horizontal to vertical imaging system optical path. Thus, we can acquire data in sitting, Fowler's (half-sitting) and supine (lying on back) positions **Figure 3.2b-d**. The operator needs to reach the optimal position to record retinal pulsatile patterns in the optic nerve head (ONH) and keep the ONH centered within the camera field of view. The optimal position is secured with the joystick-controlled 3-dimensional positioning with a millimeter scale precision. Positioning joysticks are located at the table holding the keyboard and mouse.

2. **Development of customized signal splitter**. In a collaboration with a third-party company, I have participated on development of signal splitter **Figure 3.2e**. The splitter is an essential inter-piece as it provides signal transfer from the pressure transducer into the experimental acquisition system without any interruption of ICU monitoring securing the patients' safety.

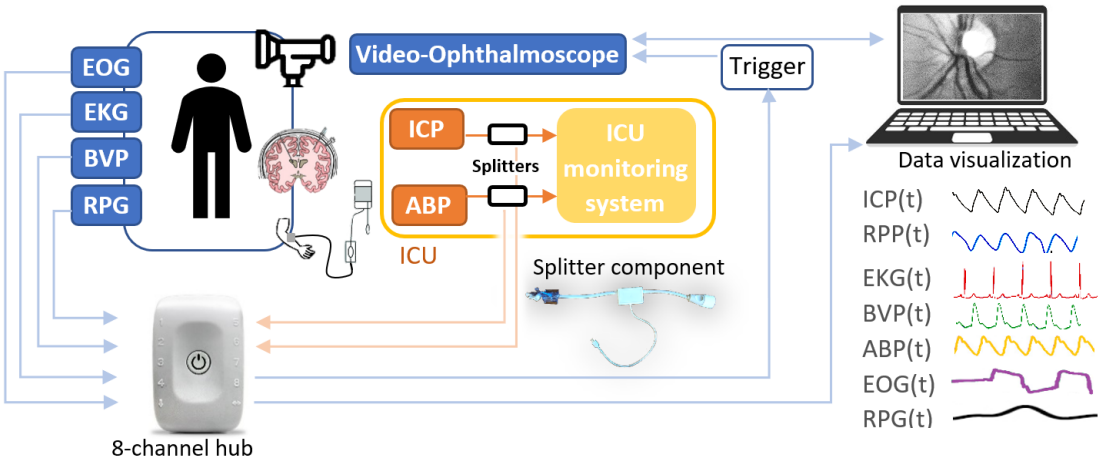

Fig. 3.1: Schema of simultaneous acquisition of retinal video-sequences, intracranial pressure and other biosignals (electrooculography EOG, electrocardiography EKG, blood volume pulse BVP via finger photoplethysmography, respiration plethysmography RPG). The schema demonstrates the possibility to acquire the invasive arterial blood pressure (ABP). The whole system utilize the 8-channel hub (Biosignals Plux) for the signal acquisition including the ICP signal. ICP signal is recorded via customized splitter sending the signal into the experimental acquisition system without any interruption of ICU monitoring

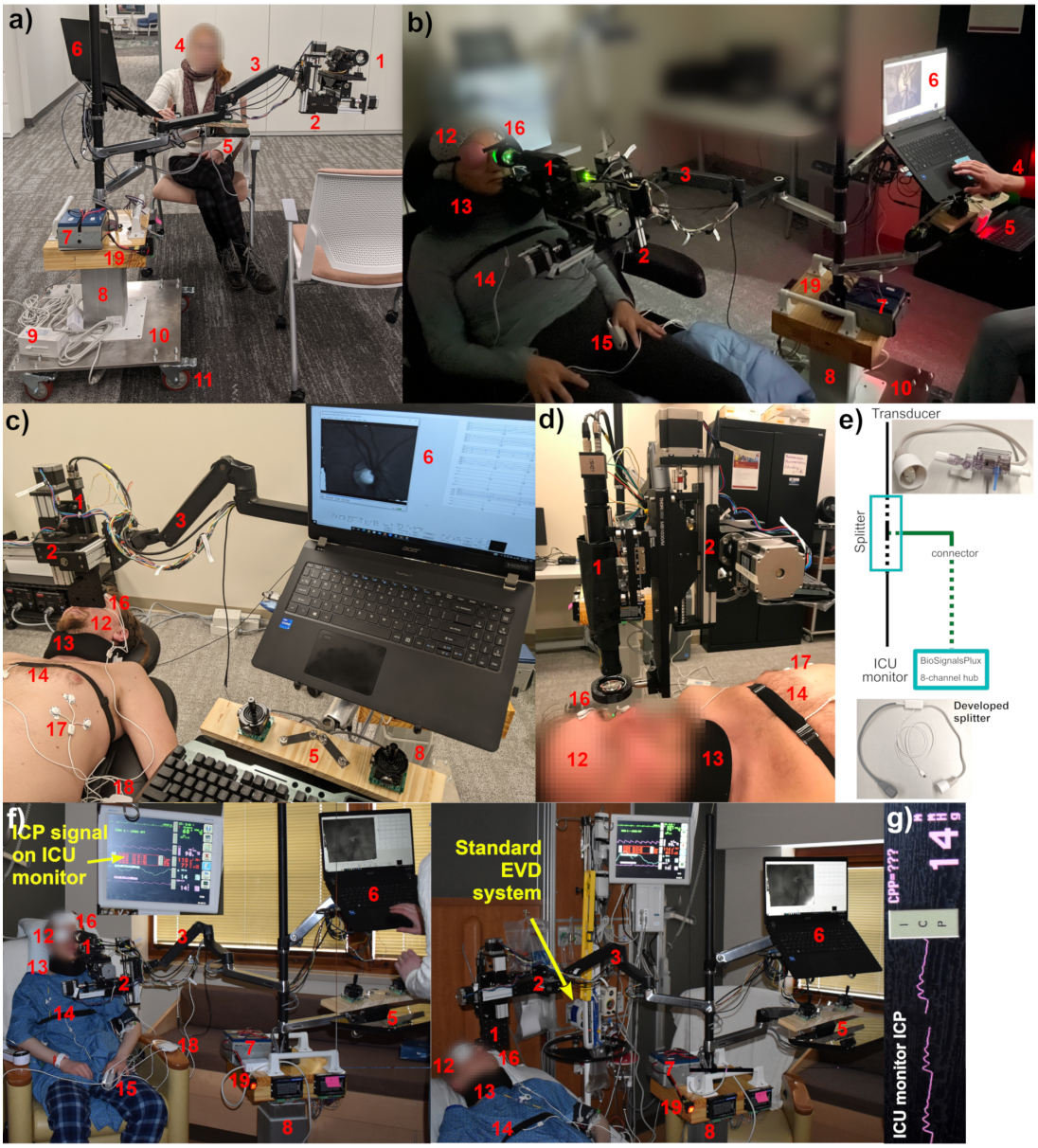

Fig. 3.2: Simultaneous and synchronized acquisition of retinal video-sequences, intracranial pressure and other biosignals (electrocardiography EKG, blood volume pulse BVP via finger photoplethysmography, respiration plethysmography RPG, electrooculography EOG). **a,** Detail of the mobile bedside multi-position video-ophthalmoscope prototype; **b,** synchronized data acquisition in a Fowler's position (135° recline) on a reclining chair; **c,** VO position detail during supine position; **d,** synchronized data acquisition in a supine position on a reclining chair; **e,** developed signal splitter for synchronized acquisition of invasive ICP or arterial blood pressure or venous blood pressure for uninterrupted clinical vital sign monitoring; **f,** bedside acquisition at intensive care unit; **g,** demonstration of ICP measured via ICU monitoring. Continue on next page.

Fig. 3.2: (Previous page.) **Label numbers**: **1** VO; **2** automated 3D XYZ positioning; **3** mobile arm enabling vertical modulation and rotation of the whole XYZ positioning; **4** device operator; **5** arm holding keyboard, mouse and joysticks for the XYZ positioning; **6** acquisition laptop; **7** battery as 24V power source for the XYZ positioning; **8** height adjustable table leg; **9** power supply and controlling unit for the table leg; **10** 65-pound stainless steel base; **11** heavy duty castors; **12** volunteer; **13** neck fixation collar; **14** respiration sensor; **15** finger blood volume pulse sensor; **16** electrooculography sensors; **17** electrocardiogram sensor; **18** 8-channel hub collecting all synchronized biosignals; **19** wood table.

Simultaneous data acquisition. Within the preliminary data acquisition, the experimental system acquired the data of two cohorts of participants - healhty controls excluding the invasive signals and hospitalized ICU patients with invasive ICP monitoring.

1. **Simultaneous data acquisition in healthy controls.** The data sets (including the retinal video-sequences, EOG, EKG, BVP and RPG) of eight healthy controls were acquired at Masonic Institute for the Developing Brain, University of Minnesota, Minneapolis, USA, utilizing the simultaneous acquisition system [162] installed at the developed bed-cart. The data sets were processed and analyzed utilizing the developed image processing pipelines (section *PCA and ICA utilization in retinal dynamic imaging*) [171, 172]. The representative example of the data set is visualized in **Figure 3.3**. Analysis of pulse morphology of identified spatiotemporal retinal pulsatile patterns corroborates correlation trends with heart rate and age that were reported on data acquired at Friedrich-Alexander University of Erlangen-Nuremberg, Germany, in Labounkova et al. 2022 [171], as shown in **Figure 3.4** .
2. **Simultaneous data acquisition in ICU patients.** The simultaneous acquisition of retinal video-sequence, other biosignals including the ICP was performed on a hospitalized patients with already implanted probe and ICP monitoring at the ICU of Department of Neurosurgery, M Health Fairview Clinic, Minneapolis **Figure 3.2f-g**. Patients were fully conscious, compliant and without any life-threatening risks during the measurement. Simultaneous data set of retinal video-sequence, EKG, EOG, BVP, RPG and ICP is demonstrated in **Figure 3.5**. Up to date, we have acquired data in 3 hospitalized patients without any complications and with 100% patients' compliance during the experiment.

Innovation. The first precisely synchronized simultaneous acquisition of retinal video-sequences, ICP and other biosignals were performed.

Significance. The developed device for simultaneous video and biosignal acquisition provides the opportunity to study the exact timing of events (CRV collapse in retinal video-sequences in relation to ICP waveform peaks etc.), has a potential to explain the origin of spontaneous venous pulsations and thereby confirm or deny previous models. Another potential of these data sets is in estimation of intracranial pressure based on retinal video-sequences. According to anatomy of retinal vessel tree, ONH and ON retrobulbar segment as described in chapter *State of the Art*, retinal vessels (both CRA and CRV) are influenced by cerebrospinal fluid in subarachnoidal spaces of ON retrobulbar segment which is of the same pressure level as intracranial pressure. Thus, the influence of intracranial pressure may be imprinted to retinal hemodynamics. Particularly, SVP are suggested to be a result of a pressure gradient between intraocular and intracranial pressure. Many clinical experiments studied the link between the intracranial pressure and SVPs before. Moreover, Morgan et al. [216, 220] estimated the intracranial pressure based on SVP collapse and ophthalmodynamometry utilizing questionable signal synchronization system via VHS-based ICU monitor recording. Precisely synchronized simultaneous data sets offer the opportunity to utilize various mathematical approaches (both linear and non-linear) that may potentially estimate intracranial pressure non-invasively based on retinal video-sequences. Promising may be the utilization of deconvolution methods similarly as in Evensen et al. [67] who estimated the ICP waveform based on continuous arterial blood pressure signal (invasive measurement) via deconvolution approach. Additionally, these data sets have a potential to optimize deterministic multi-compartment Windkessel models simulating eye hemodynamics to estimate ICP.

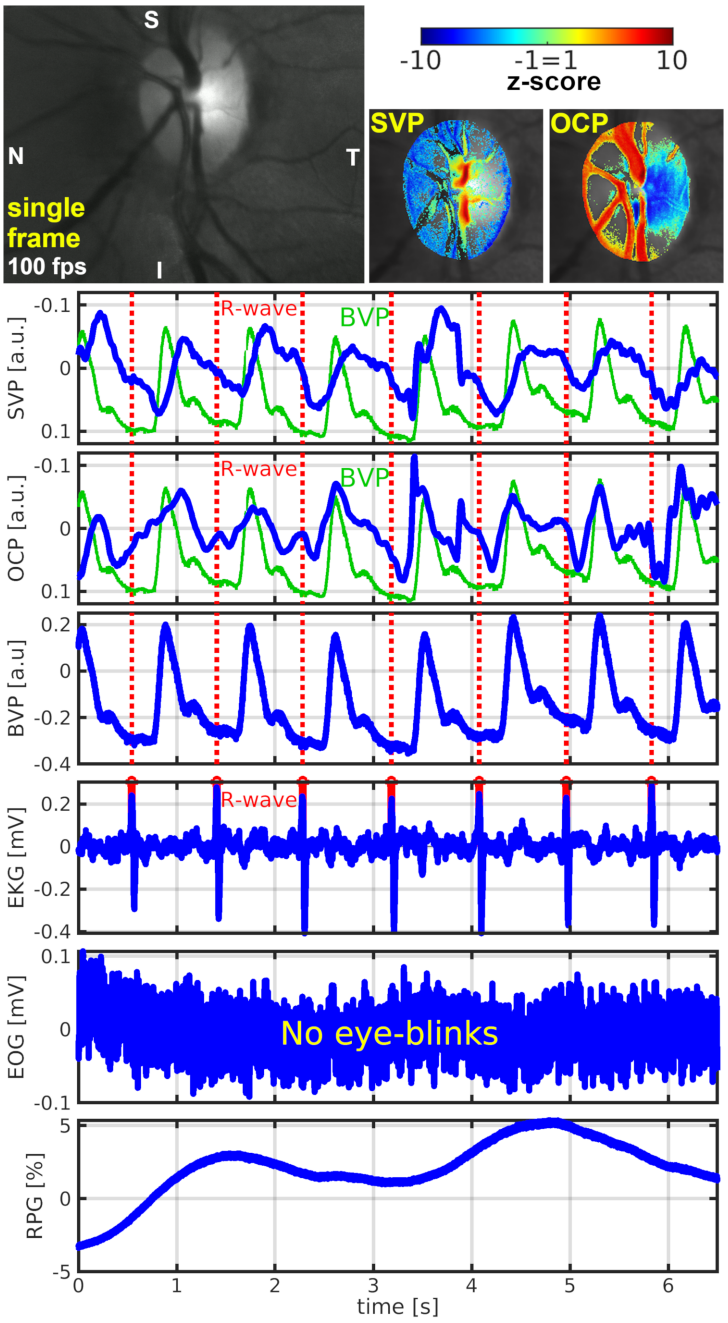

Fig. 3.3: An example of acquired biosignal and data analysis of a healthy subject. The figure visualizes the identified spatiotemporal retinal pulsatile patterns (i.e. SVP and OCP) and their time-courses with the other biosignals (EKG, BVP, RPG, EOG).

S - superior, I - inferior, N - nasal, T - temporal, SVP - spontaneous venous pulsation, OCP - optic cup pulsation

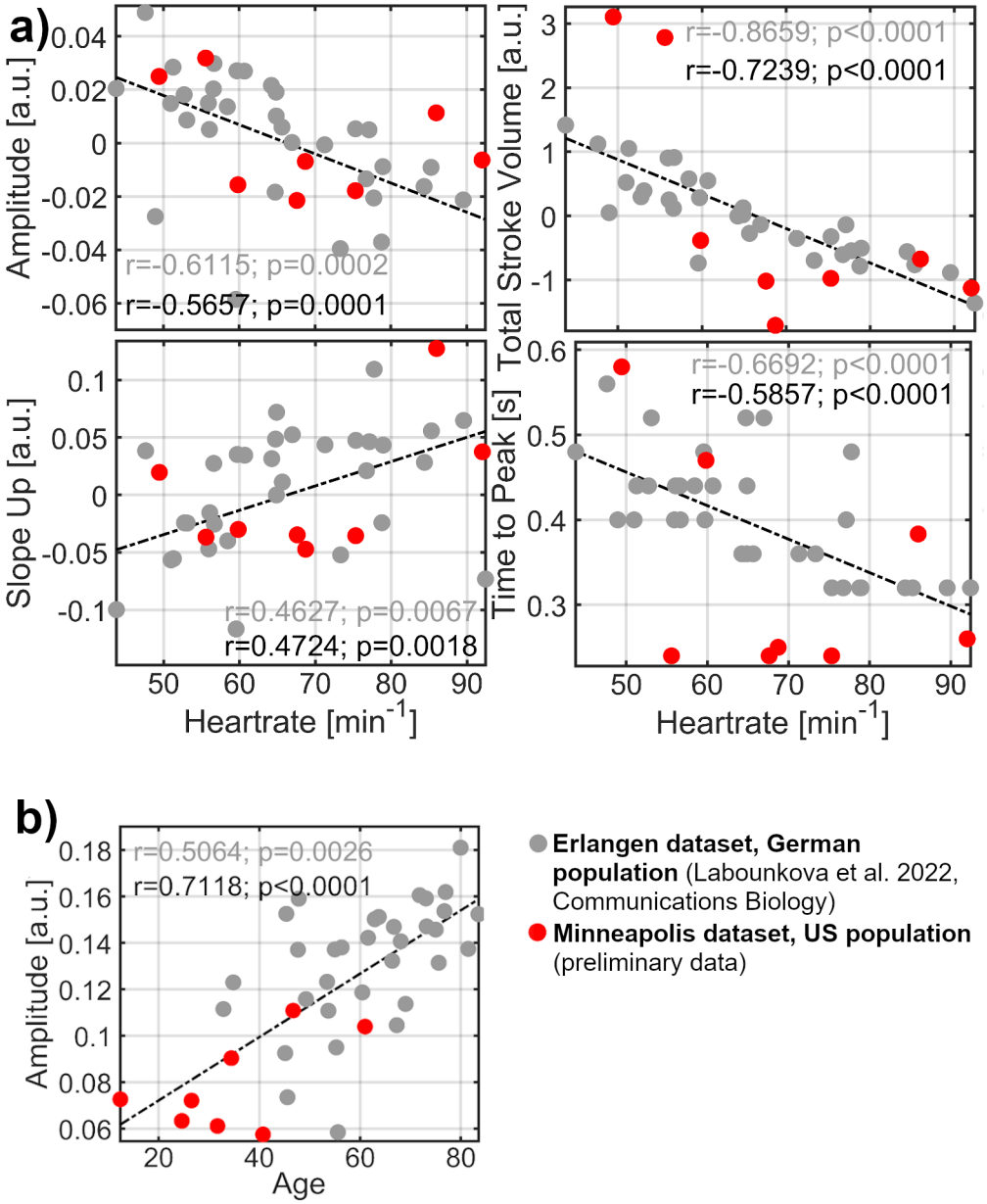

Fig. 3.4: Retinal pulse morphology measurements assessed in Minneapolis data set (grey dots) follows the measurements and trends assessed in German data set (red dots). **a,** SVP pulse morphology measurement (i.e. amplitude, stotal stroke volume, slope up and time to peak) depending on heart rate. Center specific mean was subtracted from amplitude, slope up and total stroke volume measures before the correlation analysis. **b,** SVP amplitude depending on age.
Grey Pearson correlation coefficients (r) and p-values (p) are values reported in the Communications Biology. The black r and p are values after adding 8 red UMN data points.

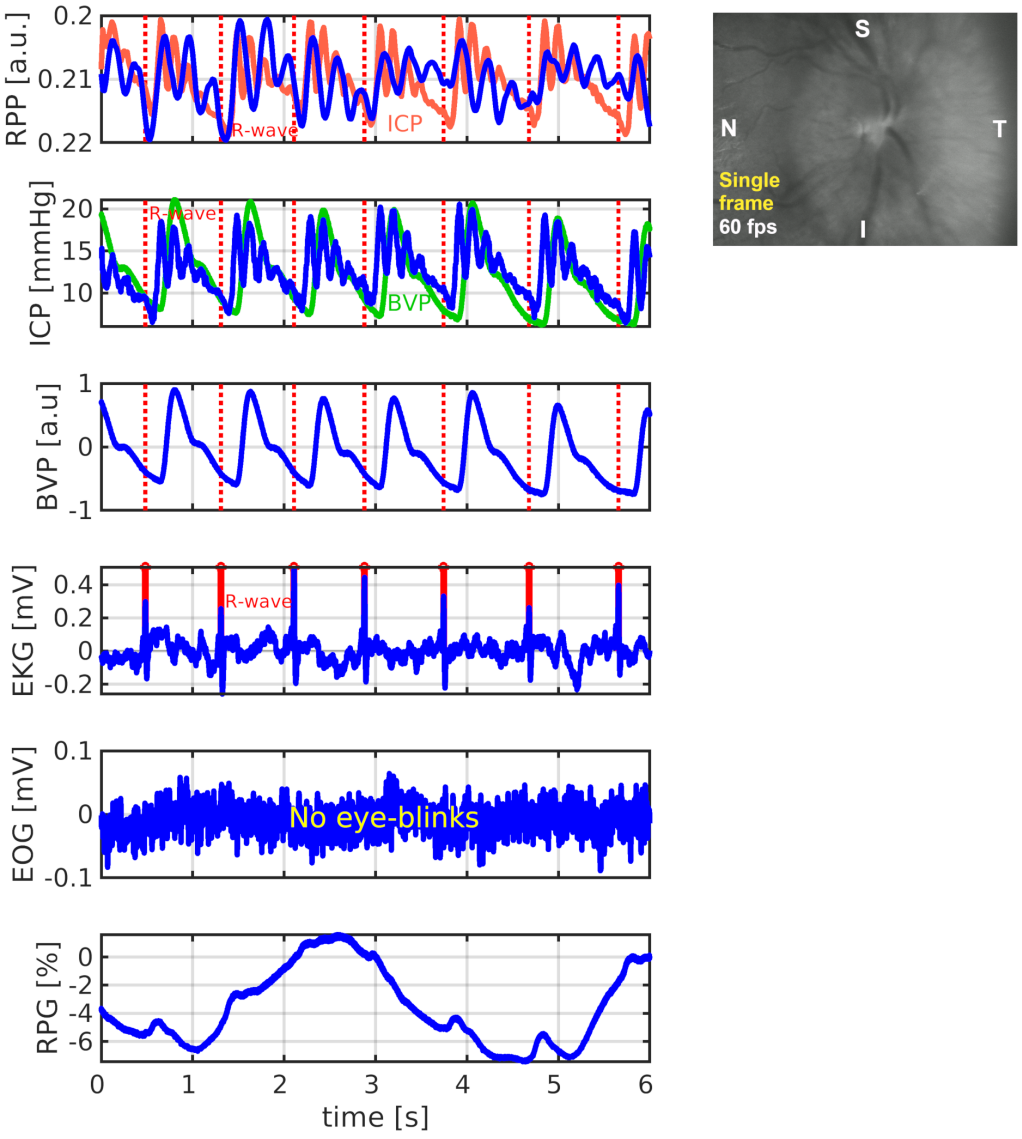

Fig. 3.5: An example of acquired biosignals (retinal video-sequences, ICP, EKG, BVP, RPG, EOG) and data analysis of a neuro-ICU patient with papilledema. The patient's papilledema (optic disc swelling due to previous long termed increase of intracranial pressure) is the reason why the only one retinal pulsatile pattern in the ONH area was identified and used for visualization. The patient's intracranial pressure was physiological in the day of the measurement.
S - superior, I - inferior, N - nasal, T - temporal, RPP retinal pulsatile pattern, ICP intracranial pressure, BVP blood pulse volume via finger photoplethysmography, EKG electrocardiogram, EOG electrooculogram, RPG respiration plethysmography

Conclusion

This Thesis aimed to advance the emerging field of functional retina imaging and fill the gaps in its current state of the art. Comprehensive introduction to the various aspects of the field provided with: (i) the knowledge of the basic anatomy and physiology of human retina including the spontaneous venous pulsation (SVP) phenomena and its origin; (ii) the principles and methodologies utilized for functional retinal imaging; (iii) image processing methods utilized in the field.

The introduction helped to understand the current state of the art and specified the gaps for improvements within the field. The Thesis proposed five specific aims in effort to fill the gaps and advance the image processing methods for the functional retina imaging. Specific aims were defined as follows: (i) to develop automated spatial feature extraction based on mutual temporal coherence; (ii) to develop adaptable spike suppression filter optimized for time-courses of retinal hemodynamics; (iii) to utilize developed image processing and engineering techniques into clinical research applications; (iv) to assess basic relationships between morphology of retinal hemodynamics and other biological variables; (v) to conceptualize and design retinal imaging experiment for simultaneous imaging of video-ophthalmoscopic recordings with invasively measured intracranial pressure. All specific aims have been addressed within the four sections in the chapter *Results*.

The first experimental section was focused on an automated spatial feature extraction from retinal image sequences via automatic, and data driven approach based on mutual temporal coherence in effort to replace manual or semi-automated feature extraction using human factor/judgement and efforts. Here, the thesis presented a novel implementation of higher order statistics, i.e. spatial principal (sPCA) and independent (sICA) component analyses, for automated separation of functionally distinct parts of human retina characterized with temporally shifted hemodynamics. The methodology was successfully utilized on mono-/bino-cular retinal image sequences acquired with experimental video-ophthalmoscope. In combination with newly introduced k-means filtering of temporal spikes in retinal hemodynamics, both sPCA and sICA separated at least two reproducible spatial patterns with mutually shifted hemodynamics in their time domains, i.e. SVP and optic cup pulsations (OCP). Evaluated shift showed that OCP hemodynamics precede SVP hemodynamics. Additionally, the analyses revealed a data-driven separation of respiration imprint into human retina and provided with a demonstration. Although introduced methodology was originally applied to video-ophthalmoscopic data, the publicly available algorithm represents a versatile tool that can be utilized in retinal image sequences of various characters acquired with various devices acquiring video-sequences of spatially stable retinal patterns.

The second experimental section utilized the developed methodology, assessed SVP and OCP morphology and identified biological and demographic factors affecting SVP/OCP morphology. The analysis confirmed the age as a factor affecting the morphological measurement of SVP. Moreover, heart rate was proven to be a factor modulating morphology of both SVP and OCP patterns. The section indicates and highlights the importance of heart rate as an important confounding variable for future clinical studies focusing on functional retina imaging.

The third and fourth section provided design and demonstration of simultaneous acquisition of retinal image sequences, other non-invasive biosignals, and invasive intracranial and arterial pressures. The experiment and overall methodology established a unique, precisely synchronized and complex dataset that represents a milestone for studies focusing on SVP etiology and non-invasive measurement of intracranial pressure based on retinal image sequences.

These four sections successfully addressed all specific aims and advanced the field of functional retinal imaging with original contributions innovating technological approach, basal knowledge about retinal pulsatile phenomena, and experimental setup that may potentially lead to development of novel non-invasive diagnostic techniques.

Bibliography

[1] Hervé Abdi. *Coefficient of Variation.* *Encyclopedia of research design*, pages 169–171, 2010.

[2] Anmar Abdul-Rahman, William Morgan, and Dao Yi Yu. *Measurement of normal retinal vascular pulse wave attenuation using modified photoplethysmography.* *PLoS ONE*, 15(5):1–28, 2020. Available from: `http://dx.doi.org/10.1371/journal.pone.0232523`.

[3] Luís Abegão Pinto, Evelien Vandewalle, Eline De Clerck, Carlos Marques-Neves, and Ingeborg Stalmans. *Lack of spontaneous venous pulsation: Possible risk indicator in normal tension glaucoma?* *Acta Ophthalmologica*, 91(6):514–520, 2013.

[4] Harish C. Agarwal, Viney Gupta, Ramanjit Sihota, and Kulwant Singh. *Pulsatile ocular blood flow among normal subjects and patients with high tension glaucoma.* *Indian Journal of Ophthalmology*, 51(2):133–138, 2003.

[5] Daniel M. Albert, Joan W. Miller, Frederick A. Jakobiec, Dimitri T. Azar, Evangelos S. Gragoudas, Barbara A. Blodi, Susan M. Power, and Nancy L. Robinson. *Retinal and choroidal circulations.* In *Albert & Jakobiec's Principles & Practice of Ophthalmology*, chapter 126. Saunders/Elsevier, Philadelphia, United States, 2008.

[6] Lin An, Jennifer Chao, Murray Johnstone, and Ruikang K Wang. *Noninvasive imaging of pulsatile movements of the optic nerve head in normal human subjects using phase-sensitive spectral domain optical coherence tomography.* *Optics Letters*, 38(9):1512–1514, 2013.

[7] Zhenyi An. *Different Estimation Methods for the Basic Independent Component Analysis.* Graduate School of Washington University, Saint Louis, 2018.

[8] Nicolas Arej, Vivien Vasseur, Elyse Jabbour, Anthony Manassero, Celine Giraud, Sebastien Bruneau, Yannick Le Mer, and Martine Mauget-Faysse. *Assessment of Spontaneous Retinal Arterial Pulsations in Acute Central Retinal Vein Occlusions.* *Journal of Ophthalmology*, 2020, 2020.

[9] Shigeta Arichika, Akihito Uji, Sotaro Ooto, Yuki Muraoka, and Nagahisa Yoshimura. *Comparison of retinal vessel measurements using adaptive optics scanning laser ophthalmoscopy and optical coherence tomography.* *Japanese Journal of Ophthalmology*, 60(3):166–171, 2016.

[10] Alberto P Avolio, Mark Butlin, and Andrew Walsh. *Arterial blood pressure measurement and pulse wave analysis — their role in enhancing cardiovascular assessment Arterial blood pressure measurement and pulse wave analysis — their role in enhancing cardiovascular assessment.* *Physiological Measurement*, 31, 2010.

[11] Charles Babbs. *Biomechanics of Retinal Venous Pulsations as Indicators of Intracranial Pressure.* *Weldon School of Biomedical Engineering Faculty Working Papers*, 2016. Available from: `https://docs.lib.purdue.edu/bmewp/1`.

[12] P. Baillart. *Circulation arte´rielle.* *Ann d'Oculist*, page 257, 1917.

[13] Chandralcumar Balaratnasingam, William H. Morgan, Martin L. Hazelton, Phillip H. House, Chris J. Barry, Hsien Chan, Stephen J. Cringle, and Dao Yi Yu. *Value of retinal vein pulsation characteristics in predicting increased optic disc excavation.* *British Journal of Ophthalmology*, 91(4):441–444, 2007.

[14] Giulia Barbati, Camillo Porcaro, Filippo Zappasodi, Paolo Maria Rossini, and Franca Tecchio. *Optimization of an independent component analysis approach for artifact identification and removal in magnetoencephalographic signals.* *Clinical Neurophysiology*, 115(5):1220–1232, 2004.

[15] M. Baurmann. *Übur die Entschung und klinische Bedeutung des Netzhautvenenpulses.* *Dtsch Ophthalmol Ges*, 45:53–59, 1925.

[16] Toke Bek, Peter Jeppesen, and Jørgen K. Kanters. *Spontaneous high frequency diameter oscillations of larger retinal arterioles are reduced in type 2 diabetes mellitus.* *Investigative Ophthalmology and Visual Science*, 54(1):636–640, 2013.

[17] Giovana A Benvenuto, Marilaine Colnago, Maurício A Dias, Rogério G Negri, Erivaldo A Silva, and Wallace Casaca. *A Fully Unsupervised Deep Learning Framework for Non-Rigid Fundus Image Registration.* *Bioengineering*, 9(369):1–17, 2022.

[18] Ciara Bergin, David F. Garway-Heath, and David P. Crabb. *Evaluating the effect of the new alignment algorithm for longitudinal series of Heidelberg retina tomography images.* *Acta ophthalmologica*, 86(2):207–214, 2008.

[19] Joseph C. Besharse and Dean Bok, editors. *The Retina and its Disorders.* Academic Press, 2011.

[20] Brigid Betz-Stablein, Martin L. Hazelton, and William H. Morgan. *Modelling retinal pulsatile blood flow from video data.* *Statistical Methods in Medical Research*, 27(5):1575–1584, 2018.

[21] Cedric Blatter, Séverine Coquoz, Branislav Grajciar, Amardeep S. G. Singh, Marco Bonesi, René M. Werkmeister, Leopold Schmetterer, and Rainer A. Leitgeb. *Dove prism based rotating dual beam bidirectional Doppler OCT.* *Biomedical Optics Express*, 4(7):1188, 2013.

[22] Olivia Bollinger, Yasemin Saruhan, and Konstantin Gugleta. *Analysis of Retinal Vessel Pulsations with Electrocardiographic Gating.* *Klinische Monatsblatter fur Augenheilkunde*, 237(4):464–468, 2020.

[23] Agnes Boltz, Doreen Schmidl, M Werkmeister, Michael Lasta, Semira Kaya, Stefan Palkovits, and Reinhard Told. *Regulation of optic nerve head blood flow during combined changes in intraocular pressure and arterial blood pressure.* *Journal of Cerebral Blood Flow & Metabolism*, 33:1850–1856, 2013.

[24] R.F. Bonner and R. Nossal. *Principles of laser-Doppler flowmetry.* In A.P. Shepherd and P.A. Oberg, editors, *Developments of cardiovascular medicine*, volume 107, chapter Laser-Dopp, pages 17–45. Kluwe Academic Publishers, Boston, 1990.

[25] Walter Boron and Emile Boulpaep. *Elastic Properties of Blood Vessels.* In *Medical Physiology*. Elsevier, 3rd edition, 2016.

[26] Tomás Brandão and Maria Paula Queluz. *No-reference image quality assessment based on DCT domain statistics.* *Signal Processing*, 88(4):822–833, 2008.

[27] Ernest E. Braxton. *Apparatus and method for non-invasive measurement of intracranial pressure.* *US 2006/0206037 A1*, 2006.

[28] Zvia Burgansky–Eliash, Hila Barash, Darin Nelson, Amiram Grinvald, Alina Sorkin, Anat Loewenstein, and Adiel Barak. *Retinal Blood Flow Velocity in Patients with Age-Related Macular Degeneration.* *Current Eye Research*, 39(3):304–311, 2014.

[29] Zvia Burgansky–Eliash, Elisha Bartov, Adiel Barak, Amiram Grinvald, and Dan Gaton. *Blood-Flow Velocity in Glaucoma Patients Measured with the Retinal Function Imager.* *Current Eye Research*, 41(7):965–970, 2016.

[30] V. D. Calhoun, T. Adali, G. D. Pearlson, and J. J. Pekar. *A method for making group inferences from functional mri data using independent component analysis.* *Human Brain Mapping*, 16(2):131, 2001.

[31] Ali Can, Charles V. Stewart, Badrinath Roysam, and Howard L. Tanenbaum. *A feature-based technique for joint, linear estimation of high-order image-to-Mosaic transformations: Mosaicing the curved human retina.* *IEEE Transactions on Pattern Analysis and Machine Intelligence*, 24(3):412–419, 2002.

[32] C. G. Caro, T. J. Pedley, R. C. Schroter, and W. A. Seed. *The Mechanics of the Circulation.* Cambridge University Press, 2012.

[33] Elizabeth Chen, Wilson Luu, Rosalie Chen, Ahmed Rafik, Yo Ryu, Barbara Zangerl, Juno Kim, and Juno Kim. *Virtual Reality Improves Clinical Assessment of the Optic Nerve.* *Frontiers in Virtual Reality*, 1:1–14, 2020.

[34] Hean C Chen, Vinod Patel, Jutta Wiek, Salwan M Rassam, and E V A M Kohner. *Vessel Diameter Changes During The Cardiac Cycle.* *Eye*, 8:97–103, 1994.

[35] Li Chen, Yang Xiang, Yao Jie Chen, and Xiao Long Zhang. *Retinal image registration using bifurcation structures.* In *18th IEEE International Conference on Image Processing, ICIP*, pages 2169–2172. IEEE, 2011.

[36] Jay Chhablani, Dirk-uwe Bartsch, Lingyun Cheng, Laura Gomez, Rayan A. Alshareef, Sami S. Rezeq, Sunir J. Garg, Zvia Burgansky–Eliash, and William R. Freeman. *Segmental reproducibility of retinal blood flow velocity measurements using retinal function imager.* *Graefes Arch Clin Exp Ophthalmol*, 251:2665–2670, 2013.

[37] Kyoung A. Cho, Abhishek Rege, Yici Jing, Akash Chaurasia, Amit Guruprasad, Edmund Arthur, and Delia Cabrera DeBuc. *Portable, non-invasive video imaging of retinal blood flow dynamics.* *Scientific Reports*, 10(1):1–12, 2020. Available from: `https://doi.org/10.1038/s41598-020-76407-5`.

[38] Artur V. Cideciyan. *Registration of Ocular Fundus Images.* *IEEE Engineering in Medicine and Biology Magazine*, 14(1):52–58, 1995.

[39] Artur V. Cideciyan, Samuel G. Jacobson, Colin M. Kemp, Robert W. Knighton, and Joachim H. Nagel. *Registration of high-resolution images of the retina.* In *Medical Imaging VI: Image Processing*, volume 1652, pages 310–322, 1992.

[40] T.A Ciulla, C.D. Regillo, and A. Harris. *Retina and optic nerve imaging*. Lippcincott Williams & Wilkins, 2003.

[41] Marco Congedo, Roy E. John, Dirk De Ridder, and Leslie Prichep. *Group independent component analysis of resting state EEG in large normative samples*. *International Journal of Psychophysiology*, 78(2):89–99, 2010.

[42] Maite Crespo-Garcia, Mercedes Atienza, and Jose L. Cantero. *Muscle artifact removal from human sleep EEG by using independent component analysis*. *Annals of Biomedical Engineering*, 36(3):467–475, 2008.

[43] Anthony J. Cunningham and Peter Barry. *Intraocular pressure -physiology and implications for anaesthetic management*. *Canadian Anaesthetists' Society Journal*, 33(2):195–208, 1986.

[44] S. Cunningham, A. Rege, K. Raje, S. Kalarn, Y. Liu, and M. Lason Brooke. *Non-invasive measurement of retinal blood flow using the Xy-CAM RITM retinal imaging system: Early clinical results*. In *Investigative Ophthalmology and Visual Science*, volume 57, pages 5927–5927, 2016. Available from: `http://iovs.arvojournals.org/article.aspx?articleid=2557438{%}0Ahttp://0-ovidsp.ovid.com.wam.city.ac.uk/ovidweb.cgi?T=JS{&}PAGE=reference{&}D=emed17{&}NEWS=N{&}AN=616036617`.

[45] Linda DAntona, Hasan Asif, Claudia Louise Craven, James Alexander McHugh, Anna Vassiliou, Lewis Thorne, Manjit Singh Matharu, Laurence Dale Watkins, Fion Bremner, and Ahmed Kassem Toma. *Brain MRI and Ophthalmic Biomarkers of Intracranial Pressure*. *Neurology*, 96(22):e2714–e2723, 2021.

[46] Linda DAntona, James A. McHugh, Federico Ricciardi, Lewis W. Thorne, Manjit S. Matharu, Laurence D. Watkins, Ahmed K. Toma, and Fion D. Bremner. *Association of Intracranial Pressure and Spontaneous Retinal Venous Pulsation*. *JAMA Neurology*, 76(12):1502–1505, 2019.

[47] Anna I Dastiridou, Harilaos Ginis, Miltiadis Tsilimbaris, Nikos Karyotakis, Efstathios Detorakis, Charalambos Siganos, Pierros Cholevas, Evangelia E Tsironi, and Ioannis G Pallikaris. *Ocular Rigidity , Ocular Pulse Amplitude , and Pulsatile Ocular Blood Flow : The Effect of Axial Length*. *Investigative Ophthalmology & Visual Science*, 54(3):2087–2092, 2013.

[48] Anna I. Dastiridou, Harilaos S. Ginis, Dirk de Brouwere, Miltiadis K. Tsilimbaris, and Ioannis G. Pallikaris. *Ocular rigidity, ocular pulse amplitude, and pulsatile ocular blood flow: The effect of intraocular pressure.* *Investigative Ophthalmology and Visual Science*, 50(12):5718–5722, 2009.

[49] Hugh Davson. *The Physilogy of the Eye.* Academic Press, New York, 3 edition, 1972.

[50] Lieven De Lathauwer, Bart De Moor, and Joos Vandewalle. *Fetal electrocardiogram extraction by blind source subspace separation.* *IEEE Transactions on Biomedical Engineering*, 47(5):567–572, 2000.

[51] Delia Cabrera Debuc, Abhishek Rege, and William E Smiddy. *Use of Xy-CAM RI for Noninvasive Visualization and Analysis of Retinal Blood Flow Dynamics During Clinical Investigations.* *Expert Review of Medical Devices*, 2021.

[52] Arnaud Delorme and Scott Makeig. *EEGLAB: An open source toolbox for analysis of single-trial EEG dynamics including independent component analysis.* *Journal of Neuroscience Methods*, 134(1):9–21, 2004.

[53] Arnaud Delorme, Terrence Sejnowski, and Scott Makeig. *Enhanced detection of artifacts in EEG data using higher-order statistics and independent component analysis.* *NeuroImage*, 34(4):1443–1449, 2007.

[54] Kexin Deng, Jie Tian, Jian Zheng, Xing Zhang, Xiaoqian Dai, and Min Xu. *Retinal fundus image registration via vascular structure graph matching.* *International Journal of Biomedical Imaging*, 2010, 2010.

[55] Stéphanie Devuyst, Thierry Dutoit, Patricia Stenuit, Myriam Kerkhofs, and Etienne Stanus. *Cancelling ECG artifacts in EEG using a modified independent component analysis approach.* *Eurasip Journal on Advances in Signal Processing*, page 747325, 2008.

[56] H.H. Do, H.K. Kang, and P.E. Beaumont. *Prognostic Significance of Fluorescein Angiography in Central Retinal Vein Occlusion.* *ARVO Annual Meeting Abstract*, 49(May):5438, 2008.

[57] Veronika Doblhoff-Dier, Leopold Schmetterer, Walthard Vilser, Gerhard Garhöfer, Martin Gröschl, Rainer A. Leitgeb, and René M. Werkmeister. *Measurement of the total retinal blood flow using dual beam Fourier-domain Doppler optical coherence tomography with orthogonal detection planes.* *Biomedical Optics Express*, 5(2):630, 2014.

[58] Guido T. Dorner, Elzbieta Polska, Gerhard Garhöfer, Claudia Zawinka, Barbara Frank, and Leopold Schmetterer. *Calculation of the diameter of the central retinal artery from noninvasive measurements in humans.* *Current Eye Research*, 25(6):341–345, 2002.

[59] W.S. Duke-Elder. *The venous pressure of the eye and its relation to the intra-ocular pressure.* *J Physiol*, 63:409–418, 1926.

[60] Martin J. Dumskyj, Stephen J. Aldington, Caroline J. Doré, and Eva M. Kohner. *The accurate assessment of changes in retinal vessel diameter using multiple frame electrocardiograph synchronised fundus photography.* *Current Eye Research*, 15(6):625–632, 1996.

[61] Tom Eichele, Srinivas Rachakonda, Brage Brakedal, Rune Eikeland, and Vince D. Calhoun. *EEGIFT: Group independent component analysis for event-related EEG data.* *Computational Intelligence and Neuroscience*, page 129365, 2011.

[62] R.H. Elliot. *The Retinal Pulse.* *The British journal of ophthalmology*, 1921.

[63] S. J. Embleton, S. L. Hosking, E. J. Roff Hilton, and I. A. Cunliffe. *Effect of senescence on ocular blood flow in the retina, neuroretinal rim and lamina cribrosa, using scanning laser Doppler flowmetry.* *Eye*, 16(2):156–162, 2002.

[64] S. Engel. *Venous pulsation as a symptom of early glaucoma.* *Am J Ophthalmol*, 29:1446–1448, 1946.

[65] Erik Barry Erhardt, Srinivas Rachakonda, Edward J. Bedrick, Elena A. Allen, Tülay Adali, and Vince D. Calhoun. *Comparison of multi-subject ICA methods for analysis of fMRI data.* *Human Brain Mapping*, 32(12):2075–2095, 2011.

[66] Javier Escudero, Roberto Hornero, Daniel Abasolo, Alberto Fernandez, and Miguel Lopez-Coronado. *Artifact removal in magnetoencephalogram background activity with independent component analysis.* *IEEE Transactions on Biomedical Engineering*, 54(11):1965–1973, 2007.

[67] Karen Brastad Evensen, Michael O'Rourke, Fabrice Prieur, Sverre Holm, and Per Kristian Eide. *Non-invasive Estimation of the Intracranial Pressure Waveform from the Central Arterial Blood Pressure Waveform in Idiopathic Normal Pressure Hydrocephalus Patients.* *Scientific Reports*, 8(1):1–11, 2018.

[68] T J Fallon, D Maxwell, and E M Kohner. *Autoregulation in Conditions of Hyperoxia and Hypoxia Using the Blue Field Entoptic Phenomenon.* *Ophthalmology*, 92(5):701–705, 1985. Available from: `http://dx.doi.org/10.1016/S0161-6420(85)33978-7`.

[69] Bin Fang and Yuan Yan Tang. *Elastic registration for retinal images based on reconstructed vascular trees.* *IEEE Transactions on Biomedical Engineering*, 53(6):1183–1187, 2006.

[70] G. T. Feke, H. Tagawa, D. M. Deupree, D. G. Goger, J. Sebag, and J. J. Weiter. *Blood flow in the normal human retina.* *Investigative Ophthalmology and Visual Science*, 30(1):58–65, 1989.

[71] Gilbert T. Feke, Bradley T. Hyman, Robert A. Stern, and Louis R. Pasquale. *Retinal blood flow in mild cognitive impairment and Alzheimer's disease.* *Alzheimer's and Dementia: Diagnosis, Assessment and Disease Monitoring*, 1(2):144–151, 2015. Available from: `http://dx.doi.org/10.1016/j.dadm.2015.01.004`.

[72] A. F. Fercher, K. Mengedoht, and W. Werner. *Eye-length measurement by interferometry with partially coherent light.* *Optics Letters*, 13(3):186–188, 1988.

[73] A.F. Fercher and J.D. Briers. *Flow Visualization by Means of Single-exposure Speckle Photography.* *Optics Communications*, 37(5):326–330, 1981.

[74] H. Ferdinand, A. Duijm, Thomas J.T.P. van den Berg, and Erik L. Greve. *A Comparison of Retinal and Choroidal Hemodynamics in Patients With Primary Open-angle Glaucoma and Normal-pressure Glaucoma.* *American Journal of Ophthalmology*, 123(5):644–656, 1997. Available from: `http://www.sciencedirect.com/science/article/pii/S0002939414710773`.

[75] Oliver Findl, Georg Rainer, Susanne Dallinger, Guido Dorner, Kaija Polak, Barbara Kiss, Michael Georgopoulos, Clemens Vass, and Leopold Schmetterer. *Assessment of optic disk blood flow in patients with open-angle glaucoma.* *American Journal of Ophthalmology*, 130(5):589–596, 2000.

[76] Josef Flammer, Selim Orgül, Vital P. Costa, Nicola Orzalesi, Günter K. Krieglstein, Luis Metzner Serra, Jean Paul Renard, and Einar Stefánsson. *The impact of ocular blood flow in glaucoma.* *Progress in Retinal and Eye Research*, 21(4):359–393, 2002.

[77] Alan D. Fleming, Sam Philip, Keith A. Goatman, John A. Olson, and Peter F. Sharp. *Automated assessment of diabetic retinal image quality based on clarity and field definition.* Investigative Ophthalmology and Visual Science, 47(3):1120–1125, 2006.

[78] John V. Forrester, Andrew D. Dick, Paul G. McMenamin, Fiona Roberts, and Eric Pearlman. *The Eye: Chapter 4 - Biochemistry and cell biology.* pages 162–274.e6. Elsevier, London, 5th editio edition, 2021.

[79] J. Francois and A. Neetens. *VASCULARIZATION OF THE OPTIC PATHWAY * publications and monographs on the subject have been sporadic , though a logical processes is very important in providing objective proofs of anatomical.* Brit. J. Ophthal., 38:472–488, 1954.

[80] Jonas S. Friedenwald. *Retinal Vascular Dynamics.* American Journal of Ophthalmology, 17(5):387–395, 1934.

[81] Y.C. Fung. *Biomechanics Circulation.* Springer Science+Business Media, New York, 2nd editio edition, 1997.

[82] Michelle L. Gabriele, Gadi Wollstein, Hiroshi Ishikawa, Larry Kagemann, Juan Xu, Lindsey S. Folio, and Joel S. Schuman. *Optical coherence tomography: History, current status, and laboratory work.* Investigative Ophthalmology and Visual Science, 52(5):2425–2436, 2011.

[83] Andrew W. Gardner and Donald E. Parker. *Association Between Arterial Compliance and Age in Subjects 9 to 77 Years Old.* Angiology, 61(1):37–41, 2010.

[84] G. Garhöfer, C. Zawinka, H. Resch, P. Kothy, L. Schmetterer, and G. T. Dorner. *Response of Retinal Vessel Diameters to Flicker Stimulation in Patients with Early Open Angle Glaucoma.* J Glaucoma, 13(4):340–344, 2004.

[85] Gerhard Garhofer, Toke Bek, Andreas G. Boehm, Doina Gherghel, Juan Grunwald, Peter Jeppesen, Hélène Kergoat, Konstantin Kotliar, Ines Lanzl, John V. Lovasik, Edgar Nagel, Walthard Vilser, Selim Orgul, and Leopold Schmetterer. *Use of the retinal vessel analyzer in ocular blood flow research.* Acta Ophthalmologica, 88(7):717–722, 2010.

[86] Gerhard Garhofer, Rene Werkmeister, Nikolaus Dragostinoff, and Leopold Schmetterer. *Retinal Blood Flow in Healthy Young Subjects.* Investigative Ophthalmology & Visual Science, 53(2):698–703, 2012.

[87] Dana Georgevsky, Sumudu V.S. Gangoda, and Seyyed Mojtaba Golzan. *Postural effects on spontaneous retinal venous pulsations in healthy individuals.* *Acta Ophthalmologica*, 97(6):e839–e843, 2019.

[88] Diana L. Glennie, Joseph E. Hayward, and Thomas J. Farrell. *Non-invasive photoacoustic microscopy of methemoglobin in vivo Noninvasive photoacoustic microscopy of methemoglobin in vivo.* *Journal of Biomedical Optics*, 20(3):9, 2015.

[89] Mojtaba Golzan, Stuart L. Graham, John Leaney, and Alberto Avolio. *Dynamic Association between Intraocular Pressure and Spontaneous Pulsations of Retinal Veins.* *Current Eye Research*, 36(1):53–59, 2011.

[90] S. Mojtaba Golzan, Alberto Avolio, and Stuart L. Graham. *Hemodynamic interactions in the eye: A review.* *Ophthalmologica*, 228(4):214–221, 2012.

[91] S. Mojtaba Golzan, Mi Ok Kim, Amir Saied Seddighi, Alberto Avolio, and Stuart L. Graham. *Non-invasive estimation of cerebrospinal fluid pressure waveforms by means of retinal venous pulsatility and central aortic blood pressure.* *Annals of Biomedical Engineering*, 40(9):1940–1948, 2012.

[92] S Mojtaba Golzan, William H Morgan, Dana Georgevsky, and Stuart L Graham. *Correlation of Retinal Nerve Fibre Layer Thickness and Spontaneous Retinal Venous Pulsations in Glaucoma and Normal Controls.* *PLoS ONE*, 10(6), 2015.

[93] Matthias C. Grieshaber, Maneli Mozaffarieh, and Josef Flammer. *What Is the Link Between Vascular Dysregulation and Glaucoma?* *Survey of Ophthalmology*, 52(SUPPL. 2):S144–S154, 2007.

[94] Amiram Grinvald, Tobias Bonhoeffer, Ivo Vanzetta, Ayala Pollack, Eyal Aloni, Ron Ofri, and Darin Nelson. *High-resolution functional optical imaging : from the neocortex to the eye Related papers.* *Ophthalmology Clinics of North America*, 17:53–67, 2004.

[95] Amiram Grinvald, Edmund Lieke, Ron D. Frostig, Charles D. Gilbert, and Torsten N. Wiesel. *Functional architecture of cortex revealed by optical imaging of intrinsic signals.* *Nature*, 324:361–364, 1986.

[96] Juan E Grunwald, Seenu M Hariprasad, Joan Dupont, Maureen G Maguire, Stuart L Fine, Alexander J Brucker, Albert M Maguire, and Allen C Ho. *Foveolar Choroidal Blood Flow in Age-Related Macular Degeneration.* *Investigative Ophthalmology & Visual Science*, 39(2):385–390, 1998.

[97] Juan E. Grunwald, Jody Piltz, Seenu M. Hariprasad, and Joan DuPont. *Optic nerve and choroidal circulation in glaucoma.* *Investigative Ophthalmology and Visual Science*, 39(12):2329–2336, 1998.

[98] K. Gugleta, A. Kochkorov, N. Waldmann, A. Polunina, R. Katamay, J. Flammer, and S. Orgul. *Dynamics of retinal vessel response to flicker light in glaucoma patients and ocular hypertensives.* *Graefe's Archive for Clinical and Experimental Ophthalmology*, 250(4):589–594, 2012.

[99] Konstantin Gugleta, Asan Kochkorov, Robert Katamay, and Claudia Zawinka. *On Pulse-Wave Propagation in the Ocular Circulation.* *Investigative Ophthalmology & Visual Science*, 47(9):4019–4025, 2006.

[100] Giovanna Guidoboni, Alon Harris, Simone Cassani, Julia Arciero, Brent Siesky, Annahita Amireskandari, Leslie Tobe, Patrick Egan, Ingrida Januleviciene, and Joshua Park. *Intraocular pressure, blood pressure, and retinal blood flow autoregulation: A mathematical model to clarify their relationship and clinical relevance.* *Investigative Ophthalmology and Visual Science*, 55(7):4105–4118, 2014.

[101] Mrinali Patel Gupta, Alexandra A. Herzlich, Theodor Sauer, and Chi-Chao Chan. *Retinal Anatomy and Pathology.* *Retinal Pharmacotherapeutics*, 55:7–17, 2016.

[102] D. Guven, H. Ozdemir, and B. Hasanreisoglu. *Hemodynamic alterations in diabetic retinopathy.* *Ophthalmology*, 103(8):1245–1249, 1996.

[103] Mehdi Bagheri Hamaneh, Numthip Chitravas, Kitti Kaiboriboon, Samden D. Lhatoo, and Kenneth A. Loparo. *Automated removal of EKG artifact from EEG data using independent component analysis and continuous wavelet transformation.* *IEEE Transactions on Biomedical Engineering*, 61(6):1634–1641, 2014.

[104] Hai-Chao Han, Jennifer K. W. Chesnutt, Justin R. Garcia, Qin Liu, and Qi Wen. *Artery Buckling : New Phenotypes , Models , and Applications.* *Annals of Biomedical Engineering*, 41(7):1399–1410, 2013.

[105] Hao Hao, Muhammad B. Sasongko, Tien Y. Wong, Mohd Zulfaezal Che Azemin, Behzad Aliahmad, Lauren Hodgson, Ryo Kawasaki, Carol Y. Cheung, Jie Jin Wang, and Dinesh K. Kumar. *Does retinal vascular geometry vary with cardiac cycle?* *Investigative Ophthalmology and Visual Science*, 53(9):5799–5805, 2012.

[106] Alon Harris, Thomas A. Ciulla, Hak Sung Chung, and Bruce Martin. *Regulation of Retinal and Optic Nerve Blood Flow.* *Arch Oph*, 116:1491–1495, 1998.

[107] Alon Harris, Larry Kagemann, Rita Ehrlich, Carlos Rospigliosi, Danny Moore, and Brent Siesky. *Measuring and interpreting ocular blood flow and metabolism in glaucoma.* *Canadian journal of ophthalmology. Journal canadien d'ophtalmologie*, 43(3):328–336, 2008. Available from: `http://dx.doi.org/10.3129/i08-051`.

[108] David T. Harvey and Bryan A. Hanson. *LearnPCA: Functions, Data Sets and Vignettes to Aid in Learning Principal Components Analysis (PCA)*, 2022.

[109] S S Hayreh. *The blood supply of the optic nerve head and the evaluation of it - myth and reality.* *Prog Retin Eye Res*, 20(5):563–593, 2001. Available from: `http://www.ncbi.nlm.nih.gov/pubmed/11470451`.

[110] Sohan Singh Hayreh. *Blood supply of the optic nerve head and its role in optic atrophy , glaucoma , and oedema of the optic disc.* *Brit. J. Ophthal.*, 53:721–748, 1969.

[111] Sohan Singh Hayreh. *Ocular Vascular Occlusive Disorders.* Springer, 2015.

[112] S.S Hayreh. *Orbital vascular anatomy.* *Eye*, 20:1130–1144, 2006.

[113] Thomas R. Jr. Hedges, Edward M. Baron, Thomas R III Hedges, and Stephen H. Sinclair. *The Retinal Venous Pulse: Its Relation to Optic Disc Characteristics and Choroidal Pulse.* *Ophthalmology*, 101(3):542–547, 1994.

[114] Hans Martin Helb, Peter Charbel Issa, Monika Fleckenstein, Steffen Schmitz-Valckenberg, Hendrik P.N. Scholl, Carsten H. Meyer, Nicole Eter, and Frank G. Holz. *Clinical evaluation of simultaneous confocal scanning laser ophthalmoscopy imaging combined with high-resolution, spectral-domain optical coherence tomography.* *Acta Ophthalmologica*, 88(8):842–849, 2010.

[115] John B. Hickham and Regina Frayser. *Studies of the Retinal Circulation in Difference , and Mean Circulation Time.* *Circulation*, 33:302–316, 1966.

[116] Esther M. Hoffmann, Franz H. Grus, and Norbert Pfeiffer. *Intraocular pressure and ocular pulse amplitude using dynamic contour tonometry and contact lens tonometry.* *BMC Ophthalmology*, 4(1):1–7, 2004.

[117] Seth W. Holwerda, Randy H. Kardon, Ryuya Hashimoto, Jan M. Full, Julie K. Nellis, Lyndsey E. DuBose, Jess G. Fiedorowicz, and Gary L. Pierce. *Aortic stiffness is associated with changes in retinal arteriole flow pulsatility mediated by local vasodilation in healthy young/middle-age adults.* *Journal of Applied Physiology*, 129(1):84–93, 2020.

[118] D. Huang, E.A. Swanson, C.P. Lin, Joel S. Schuman, William G. Stinson, Warren Chang, Michael R. Hee, Thomas Flotte, Kenton Gregory, Carmen Puliafito, and James G. Fujimoto. *Optical coherence tomography.* *Science*, 254(5035):1178–1181, 1991.

[119] Shenghai Huang, Meixiao Shen, Dexi Zhu, Qi Chen, Ce Shi, Zhongping Chen, and Fan Lu. *In vivo imaging of retinal hemodynamics with OCT angiography and Doppler OCT.* *Biomedical Optics Express*, 7(2):663, 2016.

[120] Aapo Hyvarinen and Erkki Oja. *A Fast Fixed-Point Alogrithm for Independent Component Analysis.* *Neural Computation*, 9:1483–1492, 1997.

[121] AApo Hyvarinen and Erkki Oja. *Independent Component Analysis: Algorithms and Applications.* *Neural Networks*, 13(4-5):411–430, 2000.

[122] Aapo Hyvärinen, Pavan Ramkumar, Lauri Parkkonen, and Riitta Hari. *Independent component analysis of short-time Fourier transforms for spontaneous EEG/MEG analysis.* *NeuroImage*, 49(1):257–271, 2010.

[123] Rumana Islam and Mohammed Tarique. *Blind Source Separation Of Fetal ECG Using Fast Independent Component Analysis And Principle Component Analysis.* *International Journal of Scientific and Technology Research*, 9(11):80–95, 2020. Available from: `https://www.researchgate.net/profile/Mohammed-Tarique-2/publication/346574344{_}Blind{_}Source{_}Separation{_}Of{_}Fetal{_}ECG{_}Using{_}Fast{_}links/5fc7ffb5299bf188d4e997ac/Blind-Source-Separation-Of-Fetal-E`.

[124] Andrew S. Jacks and N. R. Miller. *Spontaneous retinal venous pulsation: Aetiology and significance.* *Journal of Neurology Neurosurgery and Psychiatry*, 74(1):7–9, 2003.

[125] Glenn J. Jaffe and Joseph Caprioli. *Optical coherence tomography to detect and manage retinal disease and glaucoma.* *American Journal of Ophthalmology*, 137(1):156–169, 2004.

[126] Christopher J. James and Christian W. Hesse. *Independent component analysis for biomedical signals.* *Physiological Measurement*, 26(1):15–39, 2005.

[127] Jiri Jan. *Medical Image Processing , Reconstruction and Restoration Concepts and Methods Ji˘*. 2006.

[128] B. Jani and C. Rajkumar. *Ageing and vascular ageing*. *Postgraduate Medical Journal*, 82(968):357–362, 2006.

[129] Peter Jeppesen, Pernille A. Gregersen, and Toke Bek. *The age-dependent decrease in the myogenic response of retinal arterioles as studied with the Retinal Vessel Analyzer*. *Graefe's Archive for Clinical and Experimental Ophthalmology*, 242(11):914–919, 2004.

[130] Ci Ren Jiang, John A.D. Aston, and Jane Ling Wang. *Smoothing dynamic positron emission tomography time courses using functional principal components*. *NeuroImage*, 47(1):184–193, 2009.

[131] Yuejiao Jin, Xiaofei Wang, Sylvi Febriana Rachmawati Irnadiastputri, Rosmin Elsa Mohan, Tin Aung, Shamira A Perera, Craig Boote, Jost B Jonas, Leopold Schmetterer, and Michaël J A Girard. *Effect of Changing Heart Rate on the Ocular Pulse and Dynamic Biomechanical Behavior of the Optic Nerve*. *Invest Ophthalmol Vis Sci*, 61(4), 2020.

[132] Panitha Jindahra, Thomas R. Hedges, Carlos E. Mendoza-Santiesteban, and Gordon T. Plant. *Optical coherence tomography of the retina: Applications in neurology*. *Current Opinion in Neurology*, 23(1):16–23, 2010.

[133] Suresh E. Joel, Brian S. Caffo, Peter C.M. Van Zijl, and James J. Pekar. *On the relationship between seed-based and ICA-based measures of functional connectivity*. *Magnetic Resonance in Medicine*, 66(3):644–657, 2011.

[134] Ian T. Jollife and Jorge Cadima. *Principal component analysis: A review and recent developments*. *Philosophical Transactions of the Royal Society A: Mathematical, Physical and Engineering Sciences*, 374:20150202, 2016.

[135] J.B. Jonas. *Central retinal artery and vein collapse pressure in eyes with chronic open angle glaucoma*. *Br J Ophthalmol*, 87:949–951, 2003.

[136] J.B. Jonas. *Reproducibility of ophthalmodynamometric measurements of central retinal artery and vein collapse pressure*. *Br J Ophthalmol*, 87:577–579, 2003.

[137] J.B. Jonas and B. Harder. *Central retinal artery and vein collapse pressure in giant cell arteritis versus nonarteritic anterior ischaemic optic neuropathy*. *Eye*, 22:556–558, 2008.

[138] Jost B. Jonas. *Ophthalmodynamometric assessment of the central retinal vein collapse pressure in eyes with retinal vein stasis or occlusion.* *Graefe's Archive for Clinical and Experimental Ophthalmology*, 241(5):367–370, 2003.

[139] Jost B. Jonas. *Ophthalmodynamometric Measurement of Orbital Tissue Pressure in Thyroid-associated Orbitopathy.* *Acta Ophthalmologica Scandinavica*, Letters to:239, 2004.

[140] Jost B. Jonas and Bjoern Harder. *Ophthalmodynamometric Differences Between Ischemic vs Nonischemic Retinal Vein Occlusion.* *American Journal of Ophthalmology*, 143(1):112–116, 2007.

[141] Jost Bruno Jonas, Gabriele Charlotte Gusek, and Otto Gottfried Helmut Naumann. *Optic Disc , Cup and Neurorefinal Rim Size , Configuration ond Correlations in Normal Eyes.* *Investigative Ophthalmology & Visual Science*, 29(7):1151–1158, 1988.

[142] E. A. Kahn and G.R. Cherry. *The clinical importance of spontaneous retinal venous pulsations.* In *Univ Mich Med Bull*, volume 16, pages 305–308, 1950.

[143] Sam Kain, William Huxley Morgan, and Dao-yi Yu. *New observations concerning the nature of central retinal vein pulsation.* *British Journal of Ophthalmology*, 94:854–857, 2009.

[144] Hedwig J. Kaiser, Josef Flammer, and Phillip Hendrickson. *Ocular blood flow: new insights into the pathogenesis of ocular diseases.* Karger Medical and Scientific Publishers, Basel, 1996.

[145] S. Kalarn, K-A Cho, G. Thompson, A. Guruprasad, Y. Jing, A. Rege, and O. Saeedi. *Non-Invasive Blood-Flow Measurement in the Glaucomatous Optic Nerve Head using the XyCAM RI Retinal Imaging System.* *Investigative Ophthalmology & Visual Science*, 60(July):5616–5616, 2019.

[146] Necip Kara, Yusuf Yildirim, Ali Ismet Tekirdag, Gonca Yetkin Yildirim, Vuslat Lale Bakir, Bekir Gulac, Gokce Yilmaz, and Aysun Fendal. *Effect of body posture on intraocular pressure and ocular perfusion pressure in nonglaucomatous pregnant women.* *Current Eye Research*, 38(1):80–85, jan 2013.

[147] Remzi Karadag, Zeynel Arslanyilmaz, Bahri Aydin, and Ibrahim F. Hepsen. *Effects of body mass index on intraocular pressure and ocular pulse amplitude.* *International Journal of Ophthalmology*, 5(5):605–608, 2012.

[148] K.H. Kaschke, M. Donnerhacke and M.S. Rill. *Optical devices in ophthalmology and optometry: Technology, design principles and clinical applications.* Wiley-VCH, 2014.

[149] Henryk T Kasprzak, Tomasz Bajraszewski, and Andrzej Kowalczyk. *High accuracy measurement of spectral characteristics of movements of the eye elements.* *Óptica Pura y Aplicada*, 70(January):7–11, 2007.

[150] Dermot J. Kelly and Sinéad M. Farrell. *Physiology and role of intraocular pressure in contemporary anesthesia.* *Anesthesia and Analgesia*, 126(5):1551–1562, 2018.

[151] Jan Kerr, Patricia Nelson, and Colm O'Brien. *Pulsatile ocular blood flow in primary open-angle glaucoma and ocular hypertension.* *American Journal of Ophthalmology*, 136(6):1106–1113, 2003.

[152] J.W. Kiel. *Choroidal Myogenic Autoregulation and Intraocular Pressure.* *Exp. Eye Res.*, 58:529–544, 1994.

[153] Mijin Kim, Eun Ji Lee, Je Hyun Seo, and Tae Woo Kim. *Relationship of spontaneous retinal vein pulsation with ocular circulatory cycle.* *PLoS ONE*, 9(5):1–5, 2014.

[154] W Kinsner and Y Yan. *A Model of the Sarotid Vascular System with Stenosis at the Carotid Bifurcation.* In *Proc. 7th Conf. on Mathematical and Computer Modelling*, volume 14, pages 582–585, 1990.

[155] Barbara Kiss, Elzbieta Polska, Guido Dorner, Kaija Polak, Oliver Findl, Gabriele Fuchsja, Michael Wolzt, and Leopold Schmetterer. *Retinal Blood Flow during Hyperoxia in Humans Revisited : Concerted Results Using Different Measurement Techniques.* *Microvascular Research*, 64:75–85, 2002.

[156] Stefan Klein, Marius Staring, Keelin Murphy, Max A. Viergever, and Josien P.W. Pluim. *Elastix: A toolbox for intensity-based medical image registration.* *IEEE Transactions on Medical Imaging*, 29(1):196–205, 2010.

[157] Pascal B. Knecht, Moreno Menghini, Lucas M. Bachmann, Ralf W. Baumgartner, and Klara Landau. *The ocular pulse amplitude as a noninvasive parameter for carotid artery stenosis screening: A test accuracy study.* *Ophthalmology*, 119(6):1244–1249, 2012. Available from: `http://dx.doi.org/10.1016/j.ophtha.2011.12.040`.

[158] M. D. Knudtson, B. E.K. Klein, R. Klein, T. Y. Wong, L. D. Hubbard, K. E. Lee, S. M. Meuer, and C. P. Bulla. *Variation associated with measurement of retinal vessel diameters at different points in the pulse cycle.* *British Journal of Ophthalmology*, 88(1):57–61, 2004.

[159] In-chan Ko, Kwan-soo Park, and Jae-myung Shin. *Visual Loss After Intraoral Local Anesthesia for the Removal of Circumzygomatic and Circum-Mandibular Wires : A Case Report.* *Journal of Oral Maxillofacial Surgery*, 73(10):1918.e1–1918.e6, 2015. Available from: `http://dx.doi.org/10.1016/j.joms.2015.06.178`.

[160] Thomas Köhler, Attila Budai, Martin F. Kraus, Jan Odstrčilik, Georg Michelson, and Joachim Hornegger. *Automatic no-reference quality assessment for retinal fundus images using vessel segmentation.* *Proceedings - IEEE Symposium on Computer-Based Medical Systems*, pages 95–100, 2013.

[161] Radim Kolar, Ralf. P. Tornow, Jan Odstrcilik, and Ivana Liberdova. *Registration of Retinal Sequences from New Video-Ophthalmoscopic Camera.* *BioMedical Engineering OnLine*, 15(1):57, 2016.

[162] Radim Kolar, Tomas Vicar, Jiri Chmelik, Roman Jakubicek, Jan Odstrcilik, Eva Valterova, Michal Nohel, Karolina Skorkovska, and Ralf P. Tornow. *Assessment of retinal vein pulsation through video-ophthalmoscopy and simultaneous biosignals acquisition.* *Biomedical Optics Express*, 14(6):2645, 2023.

[163] Konstantin Kotliar, Henner Hanssen, Karla Eberhardt, Walthard Vilser, Christoph Schmaderer, Martin Halle, Uwe Heemann, and Marcus Baumann. *Retinal pulse wave velocity in young male normotensive and mildly hypertensive subjects.* *Microcirculation*, 20(5):405–415, 2013.

[164] Konstantin Kotliar, Christine Hauser, Marion Ortner, Claudia Muggenthaler, Janine Diehl-Schmid, Susanne Angermann, Alexander Hapfelmeier, Christoph Schmaderer, and Timo Grimmer. *Altered neurovascular coupling as measured by optical imaging: A biomarker for Alzheimer's disease.* *Scientific Reports*, 7(1):1–11, 2017.

[165] Konstantin E Kotliar, Marcus Baumann, Walthard Vilser, and Ines M Lanzl. *Pulse wave velocity in retinal arteries of healthy volunteers.* *Br J Ophthalmol*, 95:675–679, 2011.

[166] Konstantin E. Kotliar, Bruno Mücke, Walthard Vilser, Rudolf Schilling, and Ines M. Lanzl. *Effect of aging on retinal artery blood column diameter measured along the vessel axis.* *Investigative Ophthalmology and Visual Science*, 49(5):2094–2102, 2008.

[167] Tetsuro Koyama, Nobuhiko Matsuo, Keiichi Shimizu, Masayoshi Mihara, Yozo Tsuchida, Sebastian Wolf, and Martin Reim. *Retinal circulation times in quantitative fluorescein angiography.* *Graefe's Archive for Clinical and Experimental Ophthalmology*, 228:442–446, 1990.

[168] C.E.T. Krakau. *Reports Calculation of the Pulsatile Ocular Blood Flow.* *Investigative Ophthalmology and Visual Science*, 33(9):2754–2756, 1992.

[169] Dinesh Kant Kumar, Behzad Aliahmad, Hao Hao, Mohd Zulfaezal Che Azemin, and Ryo Kawasaki. *A Method for Visualization of Fine Retinal Vascular Pulsation Using Nonmydriatic Fundus Camera Synchronized with Electrocardiogram.* *ISRN Ophthalmology*, 2013:1–9, 2013.

[170] René Labounek, David A. Bridwell, Radek Mareček, Martin Lamoš, Michal Mikl, Tomáš Slavíček, Petr Bednařík, Jaromír Baštinec, Petr Hluštík, Milan Brázdil, and Jiří Jan. *Stable Scalp EEG Spatiospectral Patterns Across Paradigms Estimated by Group ICA.* *Brain Topography*, 31(1):76–89, 2018.

[171] Ivana Labounková, René Labounek, Radim Kolář, Ralf Peter Tornow, Charles F Babbs, Collin McClelland, Benjamin Miller, and Igor Nestrašil. *Heart rate and age modulate retinal pulsatile patterns.* *Communications Biology*, 5:582, 2022.

[172] Ivana Labounkova, Rene Labounek, Igor Nestrasil, Jan Odstrcilik, Ralf-Peter Tornow, and Radim Kolar. *Blind Source Separation of Retinal Pulsatile Patterns in Optic Nerve Head Video-Recordings.* *IEEE Transactions on Medical Imaging*, 40(3):852–864, 2021.

[173] France Laliberté and Langis Gagnon. *Studies on registration and fusion of retinal images.* *Multi-Sensor Image Fusion and its Applications*, 22(5):57–106, 2003.

[174] Maurice E Langham, Richard A Farrel, Vivian O Brien, David M Silver, and Peter Schilder. *Blood flow in the human eye.* *Acta Ophthalmologica*, 67:9–13, 1989.

[175] Stéphane Laurent and Pierre Boutouyrie. *Arterial Stiffness and Hypertension in the Elderly.* Frontiers in Cardiovascular Medicine, 7:544302, 2020.

[176] Amélie Lecleire-Collet, Isabelle Audo, Mounir Aout, Jean François Girmens, Rénata Sofroni, Ali Erginay, Jean François le Gargasson, Saddek Mohand-Saïd, Taly Meas, Pierre Jean Guillausseau, Eric Vicaut, Michel Paques, and Pascale Massin. *Evaluation of retinal function and flicker light-induced retinal vascular response in normotensive patients with diabetes without retinopathy.* Investigative Ophthalmology and Visual Science, 52(6):2861–2867, 2011.

[177] Byungkun Lee, Eduardo A Novais, Nadia K Waheed, Mehreen Adhi, Talisa E De Carlo, Emily D Cole, Eric M Moult, Woojhon Choi, Mark Lane, Caroline R Baumal, Jay S Duker, and James G Fujimoto. *En Face Doppler Optical Coherence Tomography Measurement of Total Retinal Blood Flow in Diabetic Retinopathy and Diabetic Macular Edema.* JAMA Ophthalmology, 135(3):244–251, 2017.

[178] Eun Ji Lee, Tae Woo Kim, Jung Ah Kim, Ji Ah Kim, and Hyunjoong Kim. *Spontaneous retinal venous pulsation in unilateral primary open-angle glaucoma with low intraocular pressure.* Journal of Glaucoma, 26(10):896–901, 2017.

[179] Hae Young Lee and Byung Hee Oh. *Aging and arterial stiffness.* Circulation Journal, 74(11):2257–2262, 2010.

[180] Kyoung Min Lee, Joon Mo Kim, Eun Ji Lee, and Tae Woo Kim. *Anterior Optic Nerve Head Perfusion is Dependent on Adjacent Parapapillary Choroidal perfusion.* Scientific Reports, 9(1):1–8, 2019. Available from: `http://dx.doi.org/10.1038/s41598-019-47534-5`.

[181] Tae Eun Lee, Chungkwon Yoo, and Yong Yeon Kim. *Effects of different sleeping postures on intraocular pressure and ocular perfusion pressure in healthy young subjects.* Ophthalmology, 120(8):1565–1570, aug 2013.

[182] U. Legler and Jost B. Jonas. *Frequency of Spontaneous Pulsations of the Central Retinal Vein in Glaucoma.* J Glaucoma, 18(3):210–212, 2009.

[183] Rainer A. Leitgeb, René M. Werkmeister, Cedric Blatter, and Leopold Schmetterer. *Doppler Optical Coherence Tomography.* Progress in Retinal and Eye Research, 41:26–43, 2014. Available from: `http://dx.doi.org/10.1016/j.preteyeres.2014.03.004`.

[184] Barry E. Levin. *The Clinical Significance of Spontaneous Pulsations of the Retinal Vein.* *Archives of Neurology*, 35(1):37–40, 1978.

[185] David N Levine. *Spontaneous Pulsation of the Retinal Veins.* *Microvascular research*, 56(3):154–165, 1998.

[186] David N. Levine and Hans Bebie. *Phase and amplitude of spontaneous retinal vein pulsations: An extended constant inflow and variable outflow model.* *Microvascular Research*, 106:67–79, 2016.

[187] Qian Li, Lin Li, Shanhui Fan, Cuixia Dai, Xinyu Chai, and Chuanqing Zhou. *Retinal pulse wave velocity measurement using spectral-domain optical coherence tomography.* *Journal of Biophotonics*, 11:1–10, 2018.

[188] Ivana Liberdova, Radim Kolar, and Ralf P Tornow. *Image Quality Assessment of ophthalmologic videosequences using phase correlation.* *Elektrorevue*, 18(5):153–9, 2016.

[189] Laurence S. Lim, Lieng H. Ling, Peng Guan Ong, Wallace Foulds, E. Shyong Tai, Edmund Wong, Shu Yen Lee, Doric Wong, Chui Ming Gemmy Cheung, and Tien Yin Wong. *Dynamic responses in retinal vessel caliber with flicker light stimulation in eyes with diabetic retinopathy.* *Investigative Ophthalmology and Visual Science*, 55(8):5207–5213, 2014.

[190] Yuping Lin and Gérard Medioni. *Retinal image registration from 2D to 3D.* In *26th IEEE Conference on Computer Vision and Pattern Recognition, CVPR*, 2008.

[191] Junfeng Liu, Jincheng Wan, William Robert Kwapong, Wendan Tao, Chen Ye, Ming Liu, and Bo Wu. *Retinal microvasculature and cerebral hemodynamics in patients with internal carotid artery stenosis.* *BMC Neurology*, 22(386):1–9, 2022.

[192] Lan Liu, Cheng fan Li, Yong mei Lei, Jing yuan Yin, and Jun juan Zhao. *Feature extraction for hyperspectral remote sensing image using weighted PCA-ICA.* *Arabian Journal of Geosciences*, 10(14), 2017.

[193] Yingna Liu, Matilda F Chan, and Jay M Stewart. *Pulsating Cilioretinal Artery From Ocular Hypertension.* *JAMA Ophthalmology*, 139, 2021.

[194] Farina Loeper, Jantine Oosterhof, Mark Van Den Dorpel, Denise Van Der Linde, Yaxin Lu, Elizabeth Robertson, Brett Hambly, and Richmond Jeremy. *Ventricular-Vascular Coupling in Marfan and Non-Marfan Aortopathies.* *Journal of the American Heart Association*, 5(11):1–17, 2016.

[195] S.E. Lorentzen. *Incidence of spontaneous venous pulsation in the retina.* *Acta Ophthalmol (Copenh)*, 48:765–770, 1970.

[196] Nikolaus Luft, Piotr A. Wozniak, Gerold C. Aschinger, Klemens Fondi, Ahmed M. Bata, René M. Werkmeister, Doreen Schmidl, Katarzyna J. Witkowska, Matthias Bolz, Gerhard Garhöfer, and Leopold Schmetterer. *Ocular blood flow measurements in healthy white subjects using laser speckle flowgraphy.* *PLoS ONE*, 11(12):1–17, 2016.

[197] Richard H Masland. *The fundamental plan of the retina.* *Nature neuroscience*, 4(9):877–886, 2001.

[198] George K Matsopoulos, Nicolaos A Mouravliansky, Konstantinos K Delibasis, and Konstantina S Nikita. *Using Global Optimization Techniques.* *IEEE Transactions on Information Technology in Biomedicine*, 3(1):47–60, 1999.

[199] William F. Mauldin, Dan Lin, and John A. Hossack. *The Singular Value Filter: A General Filter Design Strategy for PCA-Based Signal Separation in Medical Ultrasound Imaging.* *IEEE Transactions on Medical Imaging*, 30(11):1951–1964, 2011. Available from: `https://www.ncbi.nlm.nih.gov/pmc/articles/PMC3624763/pdf/nihms412728.pdf`.

[200] Thibaud Mautuit, Pierre Cunnac, Carol Y. Cheung, Tien Y. Wong, Stephen Hogg, Emanuele Trucco, Vincent Daien, Thomas J. MacGillivray, José Labarère, and Christophe Chiquet. *Concordance between SIVA, IVAN, and VAMPIRE Software Tools for Semi-Automated Analysis of Retinal Vessel Caliber.* *Diagnostics*, 12(6):1317, 2022.

[201] Thibaud Mautuit, Rachel Semecas, Stephen Hogg, Vincent Daien, Olivier Gavard, Nicolas Chateau, Tom Macgillivray, Emanuele Trucco, and Christophe Chiquet. *Comparing Measurements of Vascular Diameter Using Adaptative Optics Imaging and Conventional Fundus Imaging.* *Diagnostics*, 12(3):1–11, 2022.

[202] Hüseyin Mayali, Beyza Tekin, Özcan Rasim Kayikçioğlu, Emin Kurt, and Süleyman Sami İlker. *Evaluation of the effect of body position on intraocular pressure measured with rebound tonometer.* *Turkish Journal of Ophthalmology*, 49(1):6–9, 2019.

[203] Ian L. McAllister, Mei H. Tan, Lynne A. Smithies, and Wan L. Wong. *The effect of central retinal venous pressure in patients with central retinal vein*

occlusion and a high mean area of nonperfusion. *Ophthalmology*, 121(11):2228–2236, 2014. Available from: http://dx.doi.org/10.1016/j.ophtha.2014.05.031.

[204] Timothy J. McCulley, Byron L. Lam, Swaraj Bose, and William J. Feuer. *The effect of optic disk edema on spontaneous venous pulsations.* *American Journal of Ophthalmology*, 135(5):706–708, 2003.

[205] James A. McHugh, Linda DAntona, Ahmed K. Toma, and Fion D. Bremner. *Spontaneous Venous Pulsations Detected With Infrared Videography.* *Journal of neuro-ophthalmology : the official journal of the North American Neuro-Ophthalmology Society*, 40(2):174–177, 2020.

[206] Gary E. McVeigh, Christopher W. Bratteli, Dennis J. Morgan, Cheryl M. Alinder, Stephen P. Glasser, Stanley M. Finkelstein, and Jay N. Cohn. *Age-related abnormalities in arterial compliance identified by pressure pulse contour analysis: Aging and arterial compliance.* *Hypertension*, 33(6):1392–1398, 1999.

[207] G Michelson, MJ Langhans, and MJ Groh. *Clinical investigation of the combination of a scanning laser ophthalmoscope and laser Doppler flowmeter.* *German Journal of Ophthalmology*, 4(6):342–349, 1995.

[208] G Michelson, B Schmauss, MJ Langhans, J Harazny, and MJ Groh. *Principle, validity, and reliability of scanning laser Doppler flowmetry.* *Journal of Glaucoma*, 5(2):99–105, 1996.

[209] Georg Michelson and Joanna Harazny. *Relationship between Ocular Pulse Pressures and Retinal Vessel Velocities.* *Ophthalmology*, 104(4):664–671, 1997.

[210] M. Milanesi, N. Vanello, V. Positano, M. F. Santarelli, R. Paradiso, D. De Rossi, and L. Landini. *Frequency domain approach to blind source separation in ECG monitoring by wearable system.* *Computers in Cardiology*, 32:767–770, 2005.

[211] Sidharth Prasad Mishra, Uttam Sarkar, Subbash Taraphder, Sanjay Datta, Devi Prasanna Swain, Reshma Saikhom, Sasmita Panda, and Menalsh Laishram. *Principal components analysis.* *International Journal of Livestock Research*, 7(5):60–78, 2017.

[212] Anish Mittal, Anush Krishna Moorthy, and Alan Conrad Bovik. *No-reference image quality assessment in the spatial domain.* *IEEE transactions on image processing : a publication of the IEEE Signal Processing Society*,

21(12):4695–708, 2012. Available from: http://www.ncbi.nlm.nih.gov/pubmed/22910118.

[213] Yulia Monakhova and Douglas Rutledge. *Independent components analysis (ICA) at the "cocktail-party" in analytical chemistry.* Talanta, 2019.

[214] Fabrice Moret, Charlotte M. Poloschek, Wolf A. Lagrèze, and Michael Bach. *Visualization of fundus vessel pulsation using principal component analysis.* *Investigative Ophthalmology and Visual Science*, 52(8):5457–5464, 2011.

[215] Fabrice Moret, Charlotte M. Reiff, Wolf A. Lagrèze, and Michael Bach. *Quantitative Analysis of Fundus-Image Sequences Reveals Phase of Spontaneous Venous Pulsations.* *Translational Vision Science & Technology*, 4(5):3, 2015.

[216] W. H. Morgan, A. Vukmirovic, A. Abdul-Rahman, Y. J. Khoo, A. G. Kermode, C. R. Lind, J. Dunuwille, and D. Y. Yu. *Zero retinal vein pulsation amplitude extrapolated model in non-invasive intracranial pressure estimation.* *Scientific Reports*, 12(1):1–9, 2022.

[217] William H. Morgan, Anmar Abdul-Rahman, Dao Yi Yu, Martin L. Hazelton, Brigid Betz-Stablein, and Christopher R P Lind. *Objective detection of retinal vessel pulsation.* *PLoS ONE*, 10(2):1–10, 2015.

[218] William H. Morgan, Martin L. Hazelton, Stacey L. Azar, Phillip H. House, Dao Yi Yu, Stephen J. Cringle, and Chandrakumar Balaratnasingam. *Retinal venous pulsation in glaucoma and glaucoma suspects.* *Ophthalmology*, 111(8):1489–1494, 2004.

[219] William H. Morgan, Martin L. Hazelton, Brigid D. Betz-Stablein, Dao Yi Yu, Christopher R.P. Lind, Vignesh Ravichandran, and Philip H. House. *Photoplethysmographic measurement of various retinal vascular pulsation parameters and measurement of the venous phase delay.* *Investigative Ophthalmology and Visual Science*, 55(9):5998–6006, 2014.

[220] William H. Morgan, Christopher R.P. Lind, Samuel Kain, Naeem Fatehee, Arul Bala, and Dao Yi Yu. *Retinal vein pulsation is in phase with intracranial pressure and not intraocular pressure.* *Investigative Ophthalmology and Visual Science*, 53(8):4676–4681, 2012.

[221] Fumihiko Mori, Suguru Konno, Taiichi Hikichi, Yiji Yamaguchi, Satoshi Ishiko, and Akitoshi Yoshida. *Pulsatile ocular blood flow in asymmetric*

exudative age related macular degeneration. British Journal of Ophthalmology, 85(12):1411–1415, 2001.

[222] John C. Morrison and Irvin P. Pollack, editors. *Glaucoma: Science and practice.* Thieme Publishers Series, New York, 2003. Available from: http://www.ncbi.nlm.nih.gov/pubmed/23552161.

[223] M Motschmann, C Müller, J Kuchenbecker, S Walter, K Schmitz, M Schütze, W Behrens-Baumann, and R Firsching. *Ophthalmodynamometry: a reliable method for measuring intracranial pressure.* Strabismus, 9(1):13–6, 2001. Available from: http://www.ncbi.nlm.nih.gov/pubmed/11262696.

[224] Frank J. Moya, Luca Brigatti, and Joseph Caprioli. *Effect of aging on optic nerve appearance: a longitudinal study.* Br J Ophthalmol, 83:567–572, 1999.

[225] R. K. Murthy, Shamim Haji, Kumar Sambhav, Sandeep Grover, and K. V. Chalam. *Clinical applications of spectral domain optical coherence tomography in retinal diseases.* Biomedical Journal, 39(2):107–120, 2016.

[226] Edgar Nagel, Walthard Vilser, and Ines Lanzl. *Age, blood pressure, and vessel diameter as factors influencing the arterial retinal flicker response.* Investigative Ophthalmology and Visual Science, 45(5):1486–1492, 2004.

[227] Paul Nagin, Bernard Schwartz, and George Reynolds. *Measurement of Fluorescein Angiograms of the Optic Disc and Retina Using Computerized Image Analysis.* Ophthalmology, 92(4):547–552, 1985.

[228] Darin A Nelson, Zvia Burgansky–Eliash, Anat Loewestein, Adiel Bara, Elisha Bartov, Tali Rock, and Amiram Grinvald. *High-resolution wide-field imaging of perfused capillaries without the use of contrast agent.* Clinical Ophthalmology, 5:1095–1106, 2011.

[229] Hoang-ton Nguyen, Eelco Van Duinkerken, Frank D Verbraak, Bettine C P Polak, Peter J Ringens, Michaela Diamant, and Annette C Moll. *Retinal blood flow is increased in type 1 diabetes mellitus patients with advanced stages of retinopathy.* BMC Endocrine Disorders, 16:25, 2016. Available from: http://dx.doi.org/10.1186/s12902-016-0105-y.

[230] Tsuneaki Omae, Youngseok Song, Takafumi Yoshioka, Tomofumi Tani, and Akitoshi Yoshida. *Effect of insulin treatment on pulsatility ratio and resistance index of the retinal artery in patients with type 2 diabetes.* PLoS ONE,

pages 1–12, 2021. Available from: http://dx.doi.org/10.1371/journal.pone.0254980.

[231] Julie Onton, Marissa Westerfield, Jeanne Townsend, and Scott Makeig. *Imaging human EEG dynamics using independent component analysis*. *Neuroscience and Biobehavioral Reviews*, 30(6):808–822, 2006.

[232] Stefan Palkovits, Michael Lasta, Reinhard Told, Doreen Schmidl, René Werkmeister, Alina Popa Cherecheanu, Gerhard Garhöfer, and Leopold Schmetterer. *Relation of retinal blood flow and retinal oxygen extraction during stimulation with diffuse luminance flicker*. *Scientific Reports*, 5:18291, 2015.

[233] Cherilyn Mae A Palochak, Hee Eun Lee, Jessica Song, Andrew Geng, Robert A Linsenmeier, Stephen A Burns, and Amani A Fawzi. *Retinal Blood Velocity and Flow in Early Diabetes and Diabetic Retinopathy Using Adaptive Optics Scanning Laser Ophthalmoscopy*. *Journal of Clinial Medicine*, 8(1165):1–16, 2019.

[234] Michel Paques, Alain Gaudric, and Bernard Levy. *Systolodiastolic variations of blood flow during central retinal vein occlusion: Exploration by dynamic angiography*. *Br J Ophthalmol*, 89:1036–1040, 2005.

[235] N Patton, T Aslam, J MacGillivray, a Pattie, Ij Deary, and B Dhillon. *Retinal vascular image analysis as a potential screening tool for cerebrovascular disease*. *Journal of Anatomy*, 206:318–348, 2005.

[236] Friedemann Paul and Alexander Ulrich Brandt. *Optical coherence tomography in neurodegenerative and other neurologic diseases*. In P. Calabresi, L. Balcer, and E. Frohman, editors, *Optical Coherence Tomography in Neurologic Diseases*, chapter 11, pages 128–144. Cambridge University Press, Cambridge, 2015.

[237] Elias Pavlatos, Yanhui Ma, Keyton Clayson, Xueliang Pan, and Jun Liu. *Regional deformation of the optic nerve head and peripapillary sclera during IOP elevation*. *Investigative Ophthalmology and Visual Science*, 59(8):3779–3788, 2018.

[238] Nathaniel G Paz and Patricia A D Amore. *Arterial versus venous endothelial cells*. *Cell Tissue Res*, 335:5–16, 2009.

[239] Eli Peli, Reed A. Augliere, and George T. Timberlake. *Feature-Based Registration of Retinal Images*. *IEEE Transactions on Medical Imaging*, 6(3):272–278, 1987.

[240] Edward S. Perkins. *The ocular pulse and intraocular pressure as a screening test for carotid artery stenosis.* *British Journal of Ophthalmology*, 69(9):676–680, 1985.

[241] Niklas Plange, Marion Kaup, Andreas Remky, and Kay Oliver Arend. *Prolonged retinal arteriovenous passage time is correlated to ocular perfusion pressure in normal tension glaucoma.* *Graefe's Archive for Clinical and Experimental Ophthalmology*, 246(8):1147–1152, 2008.

[242] Constantin J Pournaras and E Riva. *Retinal Blood Flow Evaluation.* *Ophthalmologica*, 229:61–74, 2012.

[243] Sashank Prasad and Steven L Galetta. *Anatomy and physiology of the afferent visual system*, volume 102. Elsevier B.V., 1 edition, 2011. Available from: `http://dx.doi.org/10.1016/B978-0-444-52903-9.00007-8`.

[244] Ernest Privsek, Margareta Hellgren, Lennart Rastam, Ulf Lindblad, and Bledar Daka. *Epidemiological and Clinical Implications of Blood Pressure Measured in Seated Versus Supine Position.* *Medicine*, 97(31):1–8, 2018.

[245] L. Puyo, M. Pacques, M. Fink, J.-A. Sahel, and M. Atlan. *In vivo laser Doppler holography of the human retina.* *Biomedical Optics Express*, 9(9):4113, 2018. Available from: `http://dx.doi.org/10.1364/BOE.9.004113`.

[246] Léo Puyo, Michael Paques, and Michael Atlan. *Spatio-temporal filtering in laser Doppler holography for retinal blood flow imaging.* *Biomedical Optics Express*, 11(6):3274–3287, 2020.

[247] Léo Puyo, Michael Paques, Mathias Fink, José-Alain Sahel, and Michael Atlan. *Waveform analysis of human retinal and choroidal blood flow with laser Doppler holography.* *Biomedical Optics Express*, 10(10):4942–4963, 2019.

[248] Sana Qamber, Zahra Waheed, and M. Usman Akram. *Personal identification system based on vascular pattern of human retina.* In *International Biomedical Engineering Conference (CIBEC)*, pages 64–67, Cairo, 2012. IEEE.

[249] Giuseppe Querques, Enrico Borrelli, Riccardo Sacconi, Luigi De Vitis, Letizia Leocani, Roberto Santangelo, Giuseppe Magnani, Giancarlo Comi, and Francesco Bandello. *Functional and morphological changes of the retinal vessels in Alzheimer's disease and mild cognitive impairment.* *Scientific Reports*, 9(1):1–10, 2019.

[250] Christina Raitta and Timo Sarmela. *Fluorescein angiography of the optic disc in glaucoma.* *Acta Ophthalmologica*, 48(5):331–353, 1970. Available from: http://www.ncbi.nlm.nih.gov/pubmed/5430108.

[251] Roziana Ramli, Khairunnisa Hasikin, Mohd Yamani Idna Idris, Noor Khairiah A. Karim, and Ainuddin Wahid Abdul Wahab. *Fundus image registration technique based on local feature of retinal vessels.* *Applied Sciences*, 11(23), 2021.

[252] A. Rege, S.I. Cunningham, Y. Liu, K. Raje, S. Kalarn, M.J. Brooke, and O. Saeedi. *Clinical Measurement of Retinal Blood Flow using the XyCAM RITM Handheld Retinal Imager.* *Investigative Ophthalmology & Visual Science*, 57(12):5925, 2016.

[253] Abhishek Rege, Samantha I. Cunningham, Yusi Liu, Karan Raje, Sachin Kalarn, M. Jason Brooke, Lisa Schocket, Sunni Scott, Asifa Shafi, Luis Toledo, and Osamah J. Saeedi. *Noninvasive assessment of retinal blood flow using a novel handheld laser speckle contrast imager.* *Translational Vision Science and Technology*, 7(6), 2018.

[254] Herbert A Reitsamer and Jeffrey W Kiel. *Effects of Circulatory Events on Aqueous Humor Inflow and Intraocular Pressure.* In *Current Topics in Membranes*, volume 62, pages 273–299. Academic Press, 2008.

[255] Alvin C. Rencher. *Methods of Multivariate Analysis.* Wiley & Sons, Inc., 2nd edition, 2002.

[256] Daniel Shlomo Reshef. *Evaluation of generalized arteriolar narrowing expressed as central retinal artery/vein equivalents ratio (CRAVER), using ECG-synchronized retinal photography.* The Johns Hopkins University, Baltimore, Maryland, 1999.

[257] James D. Reynolds and Scott E. Olitsky, editors. *Pediatric Retina.* Springer Berlin Heidelberg, 2011.

[258] Mark Richardson. *Principal Component Analysis.* Number May. 2009.

[259] José Joaquín Rieta, Francisco Castells, César Sánchez, Vicente Zarzoso, and José Millet. *Atrial activity extraction for atrial fibrillation analysis using blind source separation.* *IEEE Transactions on Biomedical Engineering*, 51(7):1176–1186, 2004.

[260] Muramatsu Rina, Tomoaki Shiba, Mao Takahashi, and Yuichi Hori. *Pulse waveform analysis of optic nerve head circulation for predicting carotid atherosclerotic changes.* *Graefes Arch Clin Exp Ophthalmol*, 253:2285–2291, 2015.

[261] Nicola Ritter, Robyn Owens, James Cooper, Robert H. Eikelboom, and Paul P. Van Saarloos. *Registration of stereo and temporal images of the retina.* *IEEE Transactions on Medical Imaging*, 18(5):404–418, 1999.

[262] C. Riva, B. Ross, and G. B. Benedek. *Laser Doppler measurements of blood flow in capillary tubes and retinal arteries.* *Investigative ophthalmology*, 11(11):936–944, 1972.

[263] C. E. Riva, J. E. Grunwald, S. H. Sinclair, and B. L. Petrig. *Blood velocity and volumetric flow rate in human retinal vessels.* *Investigative Ophthalmology and Visual Science*, 26(8):1124–1132, 1985.

[264] C.E. Riva, B.L. Harino, B.L. Petrig, and R.D. Shonat. *Doppler Flowmetry in the Nerve.* *Exp. Eye Res.*, 55:499–506, 1992.

[265] Charles E Riva, Juan E Grunwald, and Benno L Petrig. *Laser Doppler measurement of retinal blood velocity: validity of the single scattering model.* *Applied Optics*, 24(5):605–607, 1985.

[266] R. J. Rodeheffer, G. Gerstenblith, L. C. Becker, J. L. Fleg, M. L. Weisfeldt, and E. G. Lakatta. *Exercise cardiac output is maintained with advancing age in healthy human subjects: Cardiac dilatation and increased stroke volume compensate for a diminished heart rate.* *Circulation*, 69(2):203–213, 1984.

[267] David Rosenbaum, Nadjia Kachenoura, Edouard Koch, Michel Paques, Philippe Cluzel, Alban Redheuil, and Xavier Girerd. *Relationships between retinal arteriole anatomy and aortic geometry and function and peripheral resistance in hypertensives.* *Hypertensio Research*, 39:536–542, 2016.

[268] Yue Ruan, Tobias Böhmer, Subao Jiang, and Adrian Gericke. *The Role of Adrenoceptors in the Retina.* *Cells*, 9:1–21, 2020.

[269] Michele A. Saad, Alan C. Bovik, and Christophe Charrier. *A DCT statistics-based blind image quality index.* *IEEE Signal Processing Letters*, 17(6):583–586, 2010.

[270] Richard J. Samworth and Ming Yuan. *Independent Component Analysis via nonparametric maximum likelihood estimation*. *Annals of Statistics*, 40(6):2973–3002, 2012.

[271] Irene Sanchez and Raul Martin. *Advances in diagnostic applications for monitoring intraocular pressure in Glaucoma: A review*. *Journal of Optometry*, 12(4):211–221, 2019. Available from: `https://doi.org/10.1016/j.optom.2018.12.003`.

[272] Paul N. Schacknow and John R. Samples, editors. *The Glaucoma Book: A Practical, Evidence-Based Approach to Patient Care*. Springer Science & Business Media, 2010.

[273] Sven Schippling. *Basic principles of optical coherence tomography*. In P. Calabresi, L. Balcer, and E. Frohman, editors, *Optical Coherence Tomography in Neurologic Diseases*, chapter 2, pages 4–13. Cambridge University Press, Cambridge, 2015.

[274] Leopold Schmetterer, Susanne Dallinger, Oliver Findl, Hans-Georg Eichler, and Michael Wolzt. *A comparison between laser interferometric measurement of fundus pulsation and measurement of pulsatile ocular blood*. *Eye*, 14:39–45, 2000.

[275] Leopold Schmetterer and Jeffrey W. Kiel. *Ocular Blood Flow*. Springer, 2012.

[276] Leopold Schmetterer, Andreas Kruger, Oliver Findl, Helene Breiteneder, Hans-Georg Eichler, and Michael Wolzt. *Topical fundus pulsation measurements in age-related macular degeneration*. *Graefe's Archive for Clinical and Experimental Ophthalmology*, 236:160–163, 1998.

[277] Leopold Schmetterer, Franz Lexer, Oliver Findl, Ursula Graselli, Hans-Georg Eichler, and Michael Wolzt. *The Effect of Inhalation of Different Mixtures of O2 and CO2 on Ocular Fundus Pulsations*. *Experimental Eye Research*, 63:351–355, 1996.

[278] Leopold Schmetterer, Alex Salomon, Alexander Rheinberger, Christian Unfried, Franz Lexer, and Michael Wolzt. *Fundus pulsation measurements in diabetic retinopathy*. *Graefe's Archive for Clinical and Experimental Ophthalmology*, 235:283–287, 1997.

[279] Leopold F. Schmetterer, Franz Lexer, Christian J. Unfried, Harald Sattmann, and Adolf F. Fercher. *Topical measurement of fundus pulsations*. *Optical Engineering*, 34(3):711–716, 1995.

[280] K. G. Schmidt, A. von Ruckmann, B. Kemkes-Matthes, and H. P. Hammes. *Ocular pulse amplitude in diabetes mellitus.* *British Journal of Ophthalmology*, 84(11):1282–1284, 2000.

[281] Tilman Schmoll and Rainer A Leitgeb. *Heart-beat-phase-coherent Doppler optical coherence tomography for measuring pulsatile ocular blood flow.* *Journal of Biophotonics*, d(3):275–282, 2013.

[282] Oliver Schwenn, R. Troost, A. Vogel, F. Grus, S. Beck, and N. Pfeiffer. *Ocular pulse amplitude in patients with open angle glaucoma, normal tension glaucoma, and ocular hypertension.* *British Journal of Ophthalmology*, 86(9):981–984, 2002.

[283] Mitra Sehi, Iman Goharian, Ranjith Konduru, Ou Tan, Sowmya Srinivas, Srinivas Sadda, Brian A. Francis, David Huang, and David S. Greenfield. *Retinal Blood Flow in Glaucomatous Eyes with Single Hemifield Damage.* *Ophthalmology*, 121(3):750–758, 2014.

[284] B. U. Seifertl and W. Vilser. *Retinal Vessel Analyzer (RVA)-design and function.* *Biomedizinische Technik. Biomedical engineering*, 47 Suppl 1:678–681, 2002.

[285] Je Hyun Seo, Tae Woo Kim, Robert N. Weinreb, Ye An Kim, and Mijin Kim. *Relationship of intraocular pressure and frequency of spontaneous retinal venous pulsation in primary open-angle glaucoma.* *Ophthalmology*, 119(11):2254–2260, 2012. Available from: `http://dx.doi.org/10.1016/j.ophtha.2012.06.007`.

[286] Je Hyun Seo, Tae Woo Kim, Robert N. Weinreb, Ye An Kim, and Mijin Kim. *Relationship of intraocular pressure and frequency of spontaneous retinal venous pulsation in primary open-angle glaucoma.* *Ophthalmology*, 119(11):2254–2260, 2012. Available from: `http://dx.doi.org/10.1016/j.ophtha.2012.06.007`.

[287] Sahar Shariflou, Ashish Agar, Kathryn Rose, Christopher Bowd, and S Mojtaba Golzan. *Objective Quantification of Spontaneous Retinal Venous Pulsations Using a Novel Tablet-Based Ophthalmoscope.* *Translational vision science & technology*, 9(4):19, 2020.

[288] Jonathon Shlens. *A Tutorial on Principal Component Analysis.* *arXiv preprint*, 2014.

[289] K. Singh, C. Dion, S. Costantino, M. Wajszilber, M. R. Lesk, and T. Ozaki. *Development of a novel instrument to measure the pulsatile movement of ocular tissues.* *Experimental Eye Research*, 91(1):63–68, 2010. Available from: `http://dx.doi.org/10.1016/j.exer.2010.03.022`.

[290] Kanwarpal Singh, Carolyne Dion, Antoine G. Godin, Faezeh Lorghaba, Denise Descovich, Marcelo Wajszilber, Tsuneyuki Ozaki, Santiago Costantino, and Mark R. Lesk. *Pulsatile movement of the optic nerve head and the peripapillary retina in normal subjects and in glaucoma.* *Investigative Ophthalmology and Visual Science*, 53(12):7819–7824, 2012.

[291] Kanwarpal Singh, Carolyne Dion, Marcelo Wajszilber, Tsuneyuki Ozaki, Mark R. Lesk, and Santiago Costantino. *Measurement of ocular fundus pulsation in healthy subjects using a novel Fourier-domain optical coherence tomography.* *Investigative Ophthalmology and Visual Science*, 52(12):8927–8932, 2011.

[292] P. Smith. *The blood-pressure in the eye and its relation to the chamber-pressure.* *Br J Ophthalmol*, 2:257–272, 1918.

[293] Guoli Song, Jianda Han, Yiwen Zhao, Zheng Wang, and Huibin Du. *A Review on Medical Image Registration as an Optimization Problem.* *Current Medical Imaging Reviews*, 13(3):274–283, 2017.

[294] Hendrik Spahr, Dierck Hillmann, Carola Hain, Clara Pfäffle, Helge Sudkamp, Gesa Franke, and Gereon Hüttmann. *Imaging pulse wave propagation in human retinal vessels using full-field swept-source optical coherence tomography.* *Optics Letters*, 40(20):4771, 2015.

[295] Scott B. Stevenson and Austin Roorda. *Correcting for miniature eye movements in high-resolution scanning laser ophthalmoscopy.* In *Event: SPIE BiOS*, number April 2005, page 12, 2005.

[296] Karin Strenn, Rupert Menapace, Georg Rainer, Oliver Findl, and Michael Wolzt. *Reproducibility and sensitivity of scanning laser Doppler flowmetry during graded changes in PO2.* *British Journal of Ophthalmology*, 81:360–364, 1997.

[297] J. P.E. Stürmer and C. Kniestedt. *Stellenwert der okulären Pulsamplitude beim Glaukom (Role of Ocular Pulse Amplitude in Glaucoma).* *Klinische Monatsblatter fur Augenheilkunde*, 232(2):162–168, 2015.

[298] Tetsuya Sugiyama, Makoto Araie, Charles E. Riva, Leopold Schmetterer, and Selim Orgul. *Use of laser speckle flowgraphy in ocular blood flow research.* *Acta Ophthalmologica*, 88(7):723–729, 2010.

[299] P. Sullivan, G.A. Cioffi, L. Wang, C.A. Johnson, E.M. van Buskirk, K.R. Sherman, and D.R. Bacon. *Scanning laser Doppler flowmetry in glaucoma.* *American Journal of Ophthalmology*, 128(1):81–87, 1999.

[300] Hiroaki Takahashi, Tetsuya Sugiyama, Hideki Tokushige, Takatoshi Maeno, Toru Nakazawa, Tsunehiko Ikeda, and Makoto Araie. *Comparison of CCD-equipped laser speckle flowgraphy with hydrogen gas clearance method in the measurement of optic nerve head microcirculation in rabbits.* *Experimental Eye Research*, 108:10–15, 2013.

[301] Dalin Tang, Chun Yang, Shunichi Kobayashi, and David N Ku. *Steady Flow and Wall Compression in Stenotic Arteries : A Three-Dimensional Thick-Wall Model With Fluid – Wall Interactions.* *Journal of Biomechanical Engineering*, 123:548–557, 2001.

[302] J Tian, GM Somfai, TR Xampagnoli, WE Smiddy, and DC DeBuc. *Interactive retinal blood flow analysis of the macular region.* *Microvascular Research*, 104:1–10, 2016.

[303] Ralf P. Tornow, Radim Kolář, and Jan Odstrčilík. *Non-mydriatic video ophthalmoscope to measure fast temporal changes of the human retina.* *European Conference on Biomedical Optics. Optical Society of America*, 9540:954006, 2015.

[304] Ralf P Tornow, Aleksandra Milczarek, Jan Odstrcilik, and Radim Kolar. *Binocular video ophthalmoscope for simultaneous recording of sequences of the human retina to compare dynamic parameters.* *Novel Biophotonics Techniques and Applications IV*, page 1041309, 2017.

[305] Ralf-Peter Tornow, Jan Odstrcilik, and Radim Kolar. *Time-resolved quantitative inter-eye comparison of cardiac cycle-induced blood volume changes in the human retina.* *Biomedical Optics Express*, 9(12):6237–54, 2018.

[306] Michael D. Twa, Cynthia J. Roberts, Huikai J. Karol, Ashraf M. Mahmoud, Paul A. Weber, and Robert H. Small. *Evaluation of a Contact Lens-Embedded Sensor for Intraocular Pressure measurement.* *J Glaucoma*, 19(6):382–390, 2010.

[307] Vincent G. Van De Ven, Elia Formisano, David Prvulovic, Christian H. Roeder, and David E.J. Linden. *Functional connectivity as revealed by spatial independent component analysis of fMRI measurements during rest.* *Human Brain Mapping*, 22(3):165–178, 2004.

[308] Luiz Carlos Viana, Marcos Faria, Heverton Pettersen, Marcos Sampaio, and Selmo Geber. *Menstrual phase-related di V erences in the pulsatility index on the central retinal artery suggest an oestrogen vasodilatation e V ect that antagonizes with progesterone.* *Arch Gynecol Obstet*, 283:569–573, 2011.

[309] Ricardo Vigário, Veikko Jousmäki, Matti Hamäläinen, Riitta Hari, and Erkki Oja. *Independent component analysis for identification of artifacts in magnetoencephalographic recordings.* *Advances in Neural Information Processing Systems*, 10:229–235, 1997.

[310] Ricardo Nuno Vigário. *Extraction of ocular artefacts from EEG using independent component analysis.* *Electroencephalography and Clinical Neurophysiology*, 103(3):395–404, 1997.

[311] Thomas J. Walsh, John W. Garden, and Brian Gallagher. *Obliteration of retinal venous pulsations. During elevation of cerebrospinal-fluid pressure.* *American Journal of Ophthalmology*, 67(6):954–956, 1969. Available from: `http://dx.doi.org/10.1016/0002-9394(69)90094-4`.

[312] Hui Wang, Hongyang Li, Xiaojie Zhang, Lanyan Qiu, Zhenchang Wang, and Yanling Wang. *Ocular Image and Haemodynamic Features Associated with Different Gradings of Ipsilateral Internal Carotid Artery Stenosis.* *Journal of Ophthalmology*, 2017:1842176, 2017.

[313] Liang Wang, Liang Wang, Hong Jiang, Amiram Grinvald, Chaitra Jayadev, and Jianhua Wang. *A Mini Review of Clinical and Research Applications of the Retinal Function Imager.* *Current Eye Research*, 43(3):273–288, 2018. Available from: `https://doi.org/10.1080/02713683.2017.1414853`.

[314] Lin Wang, Grant A. Cull, Chelsea Piper, Claude F. Burgoyne, and Brad Fortune. *Anterior and posterior optic nerve head blood flow in nonhuman primate experimental glaucoma model measured by laser speckle imaging technique and microsphere method.* *Investigative Ophthalmology and Visual Science*, 53(13):8303–8309, 2012.

[315] Xiaofei Wang, Meghna R. Beotra, Tin Aung Tun, Mani Baskaran, Shamira Perera, Tin Aung, Nicholas G. Strouthidis, Dan Milea, and

Michaël J.A. Girard. *In vivo 3-dimensional strain mapping confirms large optic nerve head deformations following horizontal eye movements.* *Investigative Ophthalmology and Visual Science*, 57(13):5825–5833, 2016.

[316] Xiaofei Wang, Meghna R Beotra, Tin Aung Tun, Mani Baskaran, Shamira Perera, J A Girard, Nicholas G Strouthidis, Dan Milea, and M.J.A. Girard. *In Vivo 3-Dimensional Strain Mapping Confirms Large Optic Nerve Head Deformations Following Horizontal Eye Movements.* *Investigative Ophthalmology & Visual Science*, 57(13):5825–5833, 2016.

[317] Xiaofei Wang, Helmut Rumpe, Winston Eng Hoe Lim, Mani Baskaran, Shamira A. Perera, Monisha E. Nongpiur, Tin Aung, Dan Milea, and Michaël J.A. Girard. *Finite element analysis predicts large optic nerve head strains during horizontal eye movements.* *Investigative Ophthalmology and Visual Science*, 57(6):2452–2462, 2016.

[318] Y. Wang, A. Lu, J. Gil-Flamer, O. Tan, J. A. Izatt, and D. Huang. *Measurement of total blood flow in the normal human retina using Doppler Fourier-domain optical coherence tomography.* *British Journal of Ophthalmology*, 93(5):634–637, 2009.

[319] Yimin Wang, Bradley A Bower, Joseph A Izatt, North Carolina, and Ou Tan. *In vivo total retinal blood flow measurement by Fourier domain Doppler optical coherence tomography.* *Journal of Biomedical Optics*, 12(4), 2007.

[320] Yimin Wang, Amani A. Fawzi, Rohit Varma, Alfredo A. Sadun, Xinbo Zhang, Ou Tan, Joseph A. Izatt, and David Huang. *Pilot study of optical coherence tomography measurement of retinal blood flow in retinal and optic nerve diseases.* *Investigative Ophthalmology and Visual Science*, 52(2):840–845, 2011.

[321] Zhou Wang and Alan C. Bovik. *Modern Image Quality assessment*, volume 3. Morgan & Claypool, 2006.

[322] Zhou Wang, Alan Conrad Bovik, Hamid Rahim Sheikh, and Eero P. Simoncelli. *Image quality assessment: From error visibility to structural similarity.* *IEEE Transactions on Image Processing*, 13(4):600–612, 2004.

[323] Zhou Wang, Ligang Lu, and Alan C. Bovik. *Video quality assessment based on structural distortion measurement.* *Signal Processing: Image Communication*, 19(2):121–132, 2004.

[324] Raymond L. Warner, Alberto de Castro, Lucie Sawides, Tom Gast, Kaitlyn Sapoznik, Ting Luo, and Stephen A. Burns. *Full-field flicker evoked changes in parafoveal retinal blood flow.* *Scientific Reports*, 10(1):1–10, 2020. Available from: https://doi.org/10.1038/s41598-020-73032-0.

[325] Andreas Wartak, Florian Beer, Sylvia Desissaire, Bernhard Baumann, Michael Pircher, and Christoph K. Hitzenberger. *Investigating spontaneous retinal venous pulsation using Doppler optical coherence tomography.* *Scientific Reports*, 9(1):4237, 2019. Available from: http://dx.doi.org/10.1038/s41598-019-40961-4.

[326] R H Webb and G W Hughes. *Scanning laser ophthalmoscope.* *IEEE transactions on bio-medical engineering*, 28(7):488–492, 1981.

[327] Xin Wei, Praveen Kumar Balne, Kenith E. Meissner, Veluchamy A. Barathi, Leopold Schmetterer, and Rupesh Agrawal. *Assessment of flow dynamics in retinal and choroidal microcirculation.* *Survey of Ophthalmology*, 63(5):646–664, 2018.

[328] P. Weinstein. *Significance of Venous Pulsation of the Eyeground.* *British Journal of Ophthalmology*, 23(6):396–398, 1939.

[329] Scott Wentz, Casey Seizys, Giovanna Guidoboni, Julia C Arciero, Katherine Hutchins, Brent Siesky, and Alon Harris. *18 . The role of blood flow in glaucoma.* pages 243–260, 2018.

[330] R. R. Wildeboer, F. Sammali, R. J.G. Van Sloun, Y. Huang, P. Chen, M. Bruce, C. Rabotti, S. Shulepov, G. Salomon, B. C. Schoot, H. Wijkstra, and M. Mischi. *Blind Source Separation for Clutter and Noise Suppression in Ultrasound Imaging: Review for Different Applications.* *IEEE Transactions on Ultrasonics, Ferroelectrics, and Frequency Control*, 67(8):1497–1512, 2020.

[331] Alice L. Williams, Srinivas Gatla, Iman Leiby, Benjamin E. Fahmy, Amitava Biswas, Rengappa de Barros, Daniela M. Ramakrishnan, Carrie Bhardwaj, Suruchi Wright, Suneeta Dubey, Jorge F. Lynch, Atilla Bayer, Parul Khandelwal, Rekha, Ichhpujani, Moataz Gheith, Ghada Siam, Robert M. Feldman, Jeffrey D. Henderer, and George L. Spaeth. *The Value of Intraocular Pressure Asymmetry in Diagnosing Glaucoma.* *Journal of Glaucoma*, 22(3):215–218, 2013.

[332] Tom H. Williamson and Alon Harris. *Ocular blood flow measurement.* *British Journal of Ophthalmology*, 78(12):939–945, 1994.

[333] F. A. Williamson-Noble. *Venous pulsation.* *Trans Ophthalmol Soc UK*, 72:317–326, 1952.

[334] Sebastian Wolf, Oliver Arend, and Martin Reim. *Measurement of retinal hemodynamics with scanning laser ophthalmoscopy: Reference values and variation.* *Survey of Ophthalmology*, 38:S95–S100, 1994.

[335] Sui Hsien Wong and Richard Patrick White. *The clinical validity of the spontaneous retinal venous pulsation.* *Journal of Neuro-Ophthalmology*, 33(1):17–20, 2013.

[336] Jiandong Xu, Ruisong Li, Haokai Xu, Yi Yang, Sheng Zhang, and Tian-Ling Ren. *Recent progress of continuous intraocular pressure monitoring.* *Nano Select*, (May):1–19, 2021.

[337] Siavash Yazdanfar and Joseph A. Rollins, Andrew M., Izatt. *In Vivo Imaging of Human Retinal Flow Dynamics by Color Doppler Optical Coherence Tomography.* *Arch Ophthalmol*, 121:235–239, 2003.

[338] Wan Fen Yip, Yih Chung Tham, Wynne Hsu, Mong Li Lee, Ronald Klein, Barbara Klein, Mohammad Kamran Ikram, Tien Yin Wong, and Carol Yim Lui Cheung. *Comparison of common retinal vessel caliber measurement software and a conversion algorithm.* *Translational Vision Science and Technology*, 5(5):1–11, 2016.

[339] Shin Yoneya, Yoshiko Komatsu, Keisuke Mori, Tatsuya Deguchi, Tamiya Saitoh, and Josephine Young-Duvall. *The improved image of indocyanine green angiography in young healthy volunteers.* *Retina*, 18(1):30–36, 1998.

[340] Kentaro Yuda, Atsuyuki Ishida, and Kenji Yuda. *Comparison of the Retinal Blood Flow Velocity Between Laser Speckle Flowgraphy and the Retinal Function Imager.* *Retina*, 37(7):1393–1399, 2017.

[341] Xuan Zhang, Joshua E. Medow, Bermans J. Iskandar, Fa Wang, Mehdi Shokoueinejad, Joyce Koueik, and John G. Webster. *Invasive and non-invasive means of measuring intracranial pressure: A review.* *Physiological Measurement*, 38(8):R143–R182, 2017.

[342] Jian Zheng, Jie Tian, Kexin Deng, Xiaoqian Dai, Xing Zhang, and Min Xu. *Salient feature region: A new method for retinal image registration.* *IEEE Transactions on Information Technology in Biomedicine*, 15(2):221–232, 2011.

[343] Karel Zuiderveld. *Contrast limited adaptive histogram equalization.* In *Graphic Gems IV*, pages 474–485. Academic Press Professional, Inc., 1994.

Symbols and abbreviations

A-scan	Axial scan
ABP	Arterial blood pressure
ANCOVA	analysis of covariance
ANOVA	analysis of variance
BP_{syst}	systolic blood pressure
BP_{diast}	diastolic blood pressure
BSS	blind source separation
BVP	blood volume pulse
CCD	charge coupled device
C/D ratio	cup to disc ratio
CIVO	constant inflow - variable outflow
CRA	central retinal artery
CRV	central retinal vein
CSF	cerebrospinal fluid
CSFP	cerebrospinal fluid pressure
$CSFP_A$	cerebrospinal fluid pressure amplitude
DOCT	Doppler optical coherence tomography
DVA	Dynamic Vessel Analyzer
EKG	electro-cardiogram
EOG	electro-oculogram
fps	frames per second
fRI	functional retinal imaging
FPA	fundus pulsation amplitude
HRA	Heidelberg Retinal Angiography

HRT Heidelberg Retinal Tomography

Hz Herz

ICA independent component analysis

ICG angiography indocyanine green angiography

ICP intra-cranial pressure

ICU intensive care unit

IOP intra-ocular pressure

LDH laser doppler holography

LED light emitting diode

LSI laser speckle imaging

MAP mean arterial pressure

OC optic cup

OCT optical coherence tomography

OCP optic cup pulsation

OD optic disc

ONH optic nerve head

OPP ocular perfusion pressure

OZH Zinn-Haller circle

PCA principal component analysis

PCAr posterior ciliary artery

RBC Red blood cells

RPP retinal pulsation pattern

RFI Retinal Funcion Imager

RNFL retinal nerve fiber layer

RVA Retina Vessel Analyzer

SD-LCI	spectral domain low coherence innterferometry
SD-OCT	spectral domain optical coherence tomography
SS-OCT	swept source optical coherence tomography
SLO	scanning laser ophthalmoscope
SNR	signal to noise ratio
SVD	singular value decomposition
SVP	spontaneous venous pulsation
TD-OCT	time domain optical coherence tomography
UMN	University of Minnesota
VO	video-ophthalmoscope
$\mathbf{A}$	mixing matrix
C	venous capacitance
c	similarity criterion
$\mathbf{D}$	diagonal matrix
$\mathbf{E}$	matrix of eigenvectors
$\mathbf{F}$	projection /factor score/ score matrix
G	grey set in image
I_0	intensity of light source
l	length
$\mathbf{P}$	matrix representing $\mathbf{E}^T$
Q	blood flow
R	vascular resistance
r	vessel diameter
$\mathbf{S_X}$	covariance matrix
$p(g)$	probability of particular intensity level in image

$s(t)$	underlying sources
$\hat{s}(t)$	estimates of underlying sources
$x(t)$	observations
T	mathematical operation of transpose
T_α	geometrical transformation
t	time
$\mathbf{U}$	matrix of left singular vectors of $\mathbf{X}\mathbf{X}^T$
$\mathbf{V}$	matrix of right singular vectors of $\mathbf{X}^T\mathbf{X}$
$\mathbf{W}$	demixing matrix
η	blood viscosity
λ	wavelength
μ_a	absorption coefficient
$\mathbf{\Sigma}$	diagonal matrix of singular values
σ	variance
φ_n	phase angle

A Electronic Appendix

The electronic appendix includes electronic version of the Thesis in .pdf format, i.e. Labounkova_thesis.pdf.

The developed methods and presented pipeline are incorporated in Retina Imaging Toolbox which is publicly available at:
https://github.com/umn-milab/retinaimagingtoolbox